SAPIENZA
UNIVERSITÀ DI ROMA

Advanced perfusion quantification methods for dynamic PET and MRI data modelling

Automatica, Bioengineering and Operation Research (ABRO)

PhD program

Cycle XXXI

Department of Computer, Control and Management Engineering

'Antonio Ruberti'

Candidate

Marianna Inglese

01201218

Supervisor

Prof. Febo Cincotti

"Allora dovresti dire quello a cui credi", riprese la Lepre Marzolina.

"È quello che faccio", rispose subito Alice; *"almeno credo a quello che dico, che poi è la stessa cosa."*
"Non è affatto la stessa cosa!" disse il Cappellaio. *"Scusa, è come se tu dicessi che* vedo quello che mangio *è la stessa cosa di* mangio quello che vedo*!"*

Alice nel Paese delle Meraviglie, Lewis Carroll

Summary

The functionality of tissues is guaranteed by the capillaries, which supply the microvascular network providing a considerable surface area for exchanges between blood and tissues. Microcirculation is affected by any pathological condition and any change in the blood supply can be used as a biomarker for the diagnosis of lesions and the optimization of the treatment. Nowadays, a number of techniques for the study of perfusion in vivo and in vitro are available. Among the several imaging modalities developed for the study of microcirculation, the analysis of the tissue kinetics of intravenously injected contrast agents or tracers is the most widely used technique. Tissue kinetics can be studied using different modalities: the positive enhancement of the signal in the computed tomography and in the ultrasound dynamic contrast enhancement imaging; T1-weighted MRI or the negative enhancement of T2* weighted MRI signal for the dynamic susceptibility contrast imaging or, finally, the uptake of radiolabelled tracers in dynamic PET imaging. Here we will focus on the perfusion quantification of dynamic PET and MRI data. The kinetics of the contrast agent (or the tracer) can be analysed visually, to define qualitative criteria but, traditionally, quantitative physiological parameters are extracted with the implementation of mathematical models. Serial measurements of the concentration of the tracer (or of the contrast agent) in the tissue of interest, together with the knowledge of an arterial input function, are necessary for the calculation of blood flow or perfusion rates from the wash-in and/or wash-out kinetic rate constants. The results depend on the acquisition conditions (type of imaging device, imaging mode, frequency and total duration of the acquisition), the type of contrast agent or tracer used, the data pre-processing (motion correction, attenuation correction, correction of the signal into concentration) and the data analysis method.

As for the MRI, dynamic contrast-enhanced magnetic resonance imaging (DCE-MRI) is a non-invasive imaging technique that can be used to measure properties of tissue microvasculature. It is sensitive to differences in blood volume and vascular permeability that can be associated with tumour angiogenesis. DCE-MRI has been investigated for a range of clinical oncologic applications (breast, prostate, cervix, liver, lung, and rectum) including cancer detection, diagnosis, staging, and assessment of treatment response. Tumour microvascular measurements by DCE-MRI have been found to correlate with prognostic factors (such as tumour grade, microvessel density, and vascular endothelial growth factor expression) and with recurrence and survival outcomes. Furthermore, DCE-MRI changes measured during treatment have been shown to correlate with outcome, suggesting a role as a predictive marker. The accuracy of DCE-MRI relies on the ability to model the pharmacokinetics of an injected contrast agent using the signal intensity changes on sequential magnetic resonance images. DCE-MRI data are usually quantified with the application of the pharmacokinetic two-compartment Tofts model (also known as the standard model), which represents the system with the plasma and tissue (extravascular extracellular space) compartments and with the contrast reagent exchange rates between them. This model assumes a negligible contribution from the vascular space and considers the system in, what-is-known as, the fast exchange limit, assuming infinitely fast transcytolemmal water exchange kinetics. In general, the number, as well as any assumption about the compartments, depends on the properties of the contrast agent used (mainly gadolinium) together with the tissue physiology or pathology studied. For this reason, the choice of the model is crucial in the analysis of DCE-MRI data.

The value of PET in clinical oncology has been demonstrated with studies in a variety of cancers including colorectal carcinomas, lung tumours, head and neck tumours, primary and metastatic brain tumours, breast carcinoma, lymphoma, melanoma, bone cancers, and other soft-tissue cancers. PET studies of tumours can be performed for several reasons including the quantification of tumour perfusion, the evaluation of tumour metabolism, the tracing of radiolabelled cytostatic agents. In particular, the kinetic analysis of PET imaging has showed, in the past few years, an increasing value in tumour diagnosis, as well as in tumour therapy, through providing additional indicative parameters. Many authors have showed the benefit of kinetic analysis of anticancer drugs after labelling with radionuclide in measuring the specific therapeutic effect bringing to light the feasibility of applying the kinetic analysis to the dynamic acquisition. Quantification methods can involve visual analysis together with compartmental modelling and can be applied to a wide range of different tracers. The increased glycolysis in the most malignancies makes ^{18}F-FDG-PET the most common diagnostic method used in tumour imaging. But, PET metabolic alteration in the target tissue can depend by many other factors. For example, most types of cancer are characterized by increased choline transport and by the overexpression of choline kinase in highly proliferating cells in response to enhanced demand of phosphatidylcholine (prostate, breast, lung, ovarian and colon cancers). This effect can be diagnosed with choline-based tracers as the ^{18}F-fluoromethylcholine (^{18}F-FCH), or the even more stable ^{18}F-D4-Choline. Cellular proliferation is also imaged with ^{18}F-fluorothymidine (FLT), which is trapped within the cytosol after being mono phosphorylated by thymidine kinase-1 (TK1), a principal enzyme in the salvage pathway of DNA synthesis. ^{18}F-FLT has been found to be useful for non-invasive assessment of the proliferation rate of several types of cancer and showed high reproducibility and accuracy in breast and lung cancer tumours.

The aim of this thesis is the perfusion quantification of dynamic PET and MRI data of patients with lung, brain, liver, prostate and breast lesions with the application of advanced models. This study covers a wide range of imaging methods and applications, presenting a novel combination of MRI-based perfusion measures with PET kinetic modelling parameters in oncology. It assesses the applicability and stability of perfusion quantification methods, which are not currently used in the routine clinical practice.

The main achievements of this work include: 1) the assessment of the stability of perfusion quantification of D4-Choline and ^{18}F-FLT dynamic PET data in lung and liver lesions, respectively (first applications in the literature); 2) the development of a model selection in the analysis of DCE-MRI data of primary brain tumours (first application of the extended shutter speed model); 3) the multiparametric analysis of PET and MRI derived perfusion measurements of primary brain tumour and breast cancer together with the integration of immuohistochemical markers in the prediction of breast cancer subtype (analysis of data acquired on the hybrid PET/MRI scanner).

The thesis is structured as follows:

- *Chapter 1* is an introductive chapter on cancer biology. Basic concepts, including the causes of cancer, cancer hallmarks, available cancer treatments, are described in this first chapter. Furthermore, there are basic concepts of brain, breast, prostate and lung cancers (which are the lesions that have been analysed in this work).

- *Chapter 2* is about Positron Emission Tomography. After a brief introduction on the basics of PET imaging, together with data acquisition and reconstruction methods, the chapter focuses on PET in the clinical settings. In particular, it shows the quantification techniques of static and dynamic PET data and my results of the application of graphical methods, spectral analysis and compartmental models on dynamic ^{18}F-FDG, ^{18}F-FLT and ^{18}F-D4-Choline PET data of patients with breast, lung cancer and hepatocellular carcinoma.

- *Chapter 3* is about Magnetic Resonance Imaging. After a brief introduction on the basics of MRI, the chapter focuses on the quantification of perfusion weighted MRI data. In particular, it shows the pharmacokinetic models for the quantification of dynamic contrast enhanced MRI data and my results of the application of the Tofts, the extended Tofts, the shutter speed and the extended shutter speed models on a dataset of patients with brain glioma.

- *Chapter 4* introduces the multiparametric imaging techniques, in particular the combined PET/CT and the hybrid PET/MRI systems. The last part of the chapter shows the applications of perfusion quantification techniques on a multiparametric study of breast tumour patients, who simultaneously underwent DCE-MRI and ^{18}F-FDG PET on a hybrid PET/MRI scanner. Then the results of a predictive study on the same dataset of breast tumour patients integrated with immunohistochemical markers. Furthermore, the results of a multiparametric study on DCE-MRI and ^{18}F-FCM brain data acquired both on a PET/CT scanner and on an MR scanner, separately. Finally, it will show the application of kinetic analysis in a radiomic study of patients with prostate cancer.

Contents

Abbreviations

[^{18}F]FDG	2-deoxy-2-[^{18}F] fluoro-D-glucose
[^{18}F]ICMT-11	[^{18}F](S)-1-((1-(2-fluoroethyl)-1H-[1,2,3]-triazol4-yl)methyl)-5-(2(2,4-difluorophenoxymethyl)-pyrrolidine-1-sulfonyl)
^{18}F-FCH	^{18}F-fluoromethylcholine
^{18}F-FLT	3-deoxy-3'-[^{18}F] fluorothymidine
3G	third-generation
AASLD	American Association for the Study of Liver Diseases
AC	Alternating Current
ACD	Annihilation Coincidence Detection
ADC	Apparent Diffusion Coefficient
AIC	Akaike Information Criteria
AIF	Arterial Input Function
APD	Avalanche Photodiode
ASL	Arterial Spin Labelling
ATP	Adenosine Triphosphate
AUC	Area Under the Curve
BALDERO	Blood Agent Level Dependent and Extravasation Relaxation Overview
BBB	Blood Brain Barrier
BC	Breast Cancer
BGO	Bismuth Germanate
BOLD	Blood Oxygenation Level–Dependent
BPH	Benign Prostatic Hyperplasia
BRC	Biomedical Research Centre
BSA	Body Surface Area
C_a	Arterial Blood
ChKα	Choline Chinase
CM	Compartmental Modelling
CR	Complete Response
CR	Contrast Reagent

CT	Computed Tomography
C_t	Concentration in Tissue
CV	Coefficient of Variation
CWM	Contralateral White Matter
DCE	Dynamic Contrast Enhanced
DCIS	Ductal Carcinoma in Situ
DKI	Diffusion Kurtosis Imaging
DOI	Depth Of Interaction
DSC	Dynamic Susceptibility Contrast
DWI	Diffusion-Weighted Imaging
ECM	Extracellular Matrix
EES	Extravascular Extracellular Space
ESSM	Extended Shutter Speed Model
ETL	Echo Train Length
ETM	Extended Tofts Model
FID	Free Induction Decay
FLAIR	Fluid-Attenuated Inversion-Recovery
FMC	Fluoromethylcholine
FORE	Fourier Rebinning
FOV	Field of View
FRT	Fractional Retention
FXL	Fast Exchange Limit
FXR	Fast Exchange Regime
Gd	Gadolinium
Gd-DTPA	Gadolinium-Diethylene Triaminepentacetate
GF	Growth Factors
GFR	Growth Factors Receptor
GRE	Gradient Recalled Echo
GSO(Ce) (or simply GSO)	Cerium-doped Gadolinium Oxyorthosilicate
H	Haematocrit
HCC	Hepatocellular Cancer

IBC	Inflammatory Breast Cancer
ID	Invasive Ductal
IHC	Immunohistochemistry
IRF	Impulse Response Function
IV	Intra-Venous
LBM	Lean Body Mass
LC	Lumped Constant
LOR	Line of Response
LSO(Ce) (or simply LSO)	Cerium-doped Lutetium Oxyorthosilicate
mRECIST	modified Response Evaluation Criteria in Solid Tumours
MRI	Magnetic Resonance Imaging
NaI(Tl)	Thallium-doped Sodium Iodide
NCT	Neo-adjuvant Chemotherapy
NEM	No-Exchange Model
NF	Normalization Factor
NIHR	National Institute for Health Research
NLLS	Non-Linear Least Squares
OSEM	Ordered-Subset Expectation-Maximization Algorithm
PADS	Positron Emission Tomography Based Apoptosis-Dominant Signature
PD	Progressive Disease
PET	Positron Emission Tomography
PFS	Progression Free Survival
PMT	Photomultiplier Tube
PNDS	Positron Emission Tomography based Necrosis-Dominant Signature
POB	Plasma Over Blood
PR	Partial Response
PS	Performance Status
PSA	Prostate-Ppecific Antigen
PVIS	Positron Emission Tomography based Voxel Intensity Sorting
PZ	Peripheral Zone
RB	Retinoblastoma-Associated

RF	Radiofrequency
ROI	Receiver Operating Characteristic
ROI	Region of Interest
RSS	Residual Sum of Squares
RTS	Real-Time Sorter
SA	Spectral Analysis
SARM	Selective Androgen Receptor Modulator
SCLC	Small-Cell Lung Cancer
SD	Stable Disease
SE	Spin Echo
SERM	Selective Estrogen Receptor Modulator
SI	Signal Intensity
SPECT	Single Photon Emission Computed Tomography
SSM	Shutter Speed Model
STIR	Short Time Inversion Recovery
SUV	Standardised Uptake Value
TAC	Time Activity Curve
TACE	Transarterial Chemoemobilisation
TBR	Tumour-to-Background Ratio
TE	Echo Time
TI	Inversion Time
TIC	Time Intensity Curve
TK1	Thymidine Kinase-1
TM	Tofts Model
TMA	Tissue Microarray
TNBC	Triple Negative Breast Cancers
TOF	Time of Flight
TR	Repetition Time
V_D	Distribution Volume
VOI	Volume of Interest
WHO	World Health Organization

List of figures

List of tables

Ringraziamenti

Il dottorato è stato un percorso incredibile e non so quante volte, nell'arco di questi tre anni, abbia ripetuto a me stessa che è stata tutta una follia. Lo penso ancora oggi che metto la parola fine a questa ulteriore esperienza di crescita professionale e personale.
Come spesso accade nel momento in cui si arriva al traguardo, pensare a ciò che verrà dopo è inevitabile e, in questo particolare caso, anche tanto incognito quanto eccitante.

Ci sono molte persone che sento di ringraziare, senza le quali probabilmente starei facendo marmellate a certificazione geografica controllata. Per prima, la mia piccola grande famiglia composta non solo dai miei genitori, ormai abituati ai miei borsoni, ai biglietti, ai miei silenzi, ai miei momenti (rari) di soddisfazione personale. Senza di loro, immagino, avrei avuto la stessa testa dura che mi ha permesso di perseguire tutto questo, ma con loro, d'altra parte, ho avuto la costante certezza di non essere da sola e di avere un porto sicuro al quale tornare in periodi di tempesta. Grazie.

La mia famiglia sono i miei amici, sempre presenti con una telefonata, un messaggio, un "pacco da giù". Sempre pronti ad accogliermi a braccia aperte (anche agli orari più improbabili) con un po' di pane e formaggio e una valanga di affetto, che non è mai abbastanza. Grazie.

La mia famiglia sono i miei colleghi e anche i miei professori, che mi hanno accompagnato in questo difficile percorso credendo nelle mie capacità e nella mia caparbietà. Grazie alla fetta napoletana e a quella inglese, che insieme hanno fatto quella che sono oggi: ancora una studentessa, certo, ma un pochino più consapevole.
In particolare, ringrazio il prof. Cincotti, che mi ha fatto credere che tutto questo potesse essere possibile, ringrazio il prof. Aboagye, che mi ha dato i mezzi per riuscirci ma che, soprattutto, mi ha trasmesso la gioia, la passione, la fede che in questo lavoro bisogna avere, e il NapLab, che mi ha iniziato a tutto questo. Grazie.

Ringrazio la Prof. Bertoldo e il Dott. Veronese, che con cura hanno contribuito alla versione finale di questa tesi offrendomi suggerimenti e spunti di approfondimento. Grazie.

Ed infine, in maniera davvero poco autocelebrativa, ringrazio me stessa, per la soddisfazione che ho deciso di regalarmi ancora una volta e perché' ho creduto di potercela fare, non sempre, lo ammetto, ma quel tanto che oggi mi fa essere qui a ringraziare chi ci ha creduto quanto e con me.

CHAPTER 1

Cancer biology – Basic concepts

Cancer is the second most common cause of death in the 'developed' world; only cardiovascular disease mortality exceeds that of malignancy [1]. Cancer is the disease of uncontrolled growth and proliferation and it can be considered a multi-step process which requires the accumulation of many genetic changes over time. These genetic alterations involve activation of proto-oncogenes to oncogenes, deregulation of tumour suppressor genes and DNA repair genes and 'immortalisation' [2].
Usually, the cell cycle is regulated by proteins that interact with each other in a specific sequence of events. They check that each stage of the cycle is competed correctly ensuring that incompletely replicated DNA is not passed onto daughter cells. This regulation is influenced by transcription receptors in the nucleus, which trigger the start of DNA synthesis. P53 is called the "guardian of the genome" and is able to induce apoptosis if the genomic damage is too great to be repaired. It also induces the expression of cell cycle inhibitors to prevent cell proliferation of a cell until the damage is repaired [2]. Normal mammalian somatic cells proliferate a limited number of times before undergoing senescence. Senescent cells may remain metabolically active even though they have permanently ceased proliferation. Immortalisation is an essential step in the malignant transformation of normal cells and can be attributed, in part, to the presence of telomerase, the enzyme responsible for maintaining telomeres at the ends of chromosomes. By extending telomeric DNA, telomerase is able to counter the progressive telomere shortening that would otherwise lead to cell death. Unlike normal cells that lack detectable levels of telomerase activity, approximately 90% of human tumours consist of cells that contain an active telomerase enzyme [2]. Tissue homeostasis is regulated by growth factors (GFs), which transmit signals from one cell to another. They are sensitive to specific growth factors receptors (GFR), which can activate target molecules promoting proliferation. Normal cell proliferation include:

- the binding of a GF to its specific receptor on the cell membrane
- transient and limited activation of the GFR, which, activates several signal-transducing proteins (e.g. Ras) on the inner leaflet of the plasma membrane
- transmission of the signal by signal transduction molecules, either to cytosolic targets or to the nucleus where they activate transcription of specific genes
- entry of the cell into the cell cycle, ultimately resulting in cell division.

This pathway is often derailed in cancer and allows wayward cells to generate their own internal signals that stimulate proliferation and become independent of their environments. In fact, cancer cells are able to induce their own growth stimulatory signals when mutations in the GFR gene occur, which facilitates activation in the absence of GFs or when overproduction of GFs results in an autocrine signalling loop [2]. An alternative strategy by which cancer cells can become GF independent involves constitutive activation of internal signalling components.

Carcinogenesis

The genes that have been implicated in carcinogenesis are grouped in oncogenes and tumour suppressor genes.

- Cellular oncogenes

Genes that promote autonomous cell growth in cancer cells are called oncogenes, and their normal cellular counterparts are called proto-oncogenes. Proto-oncogenes are physiologic regulators of cell proliferation and differentiation while oncogenes are characterised by the ability to promote cell growth in the absence of normal mitogenic signals. Their products, oncoproteins, resemble the normal products of proto-oncogenes with the exception that oncoproteins are devoid of important regulatory elements. Their production in the transformed cells becomes constitutive, that is, not dependent on growth factors or other external signals. Proto-oncogenes can be converted to oncogenes by several mechanisms including point mutation and gene amplification resulting in:

- Overproduction of growth factors
- Flooding of the cell with replication signals
- Uncontrolled stimulation in the intermediary pathways
- Cell growth by elevated levels of transcription factors

The RAS oncogene is the most frequently mutated oncogene in human cancer. It encodes a GTP-binding protein Ras that functions as an on-off 'switch' for a number of key signalling pathways controlling cellular proliferation [2]. Other oncogenes frequently mutated in cancer are listed in Table 1.

Table 1: Selected oncogenes and associated cancers

Category/Protein Function	Proto-oncogene	Mode of Activation	Associated Cancer
Growth Factors			
-PDGF (β chain)	SIS	Overexpression	Astrocytoma, osteosarcoma
-Fibroblast growth factors	HST-1	Overexpression	Stomach cancer
	INT-2	Amplification	Bladder and breast cancer
-Transforming growth factor α	TGFα	Overexpression	Melanoma Astrocytomas Hepatocellular carcinomas
Growth factor Receptors			
-EGF-receptor family	ERB-B1	Overexpression	SCC of the lung, gliomas
	ERB-B2	Amplification	Breast and ovarian cancers
	PDGF-R	Overexpression	Gliomas
-PDGF receptor			
-Receptor for stem cell (steel) factor	KIT	Point Mutation	Gastrointestinal stromal tumours
Proteins involved in Signal Transduction			
-GTP-binding	K-RAS	Point mutation	

	H-RAS	Point mutation	Colon, lung, pancreatic tumours
	N-RAS	Point mutation	Bladder and kidney tumours
-Non-receptor tyrosine kinase	ABL	Translocation	Melanoma, leukaemia, lymphoma
-RAS signal transduction	BRAF	Point mutation	CML, ALL
-WNT signal transduction	B-catenin	Point mutation/ Overexpression	Melanomas
			Hepatoblastomas and HCC
Nuclear Regulatory Proteins			
Transcriptional activators	C-MYC	Translocation	Burkitt lymphoma
	N-MYC	Amplification	Neuroblastoma, small cell carcinoma of lung
	L-MYC	Amplification	SCC of the lung
Cell-cycle Regulators			
Cyclins	CYCLIN D	Translocation	Mantle cell lymphoma
		Amplification	Brest and oesophageal cancers
	CYCLIN E	Overexpression	Breast cancer
		Amplification or	Glioblastoma, melanoma
Cyclin-dependent kinase	CDK4	Point mutation	sarcoma

- Tumour suppressor genes

Tumour suppressor genes (Table 2) encode proteins that are:

- receptors for secreted hormones that function to inhibit cell proliferation• negative regulators of cell cycle entry or progression
- negative regulators of growth signalling pathways (e.g. APC or PTEN)
- checkpoint-control proteins that arrest the cell cycle if DNA is damaged or chromosomes are abnormal
- proteins that promote apoptosis DNA repair enzymes.

The transformation of a normal cell to a cancer cell is accompanied by the loss of function of one or more tumour suppressor genes and both gene copies must be defective in order to promote tumour development [2].

Table 2: Examples of tumour suppressor genes

Gene	Protein function	Inherited disease	Spontaneous Tumours
APC	Negative regulator of the signalling pathway	Adenomatous polyposis coli (APC)	Most colon cancers
BRCA1 BRCA2	Components of DNA repair systems	Familial breast and ovarian cancer	Spontaneous breast cancers
CDH1	E-cadherin, a cell adhesion molecule	Hereditary diffuse gastric cancer	Many epithelial cancers
CDKN2A	INK4a, inhibitor of cyclin-dependent kinase Cdk4	Some familial melanomas	Some esophageal and pancreatic cancers
MEN1	Transcription factor and protein kinase	Multiple endocrine neoplasia	Many metastatic cancers
NF1	Neurofibromin, Ras-GTPase activation	Neurofibromatosis type 1	Some tumours of neural crest origin
PTEN	Negative regulator of PI3K growth signalling pathway	Cowden disease	30%-50% of spontaneous cancers
RB	Repression of transcription factor E2F	Retinoblastoma. osteosarcoma	Retinoblastoma, sarcomas, several cancers
SMAD4	Signal transducer in TGF-signalling	Juveline polyposis	Colon and pancreatic cancers
TP53	Transcription factor; guardian of the genome	Li-Fraumeni syndrome	Most frequently mutated in human cancers
TSC1 TSC2	Inhibitor of mTOR	Tuberous sclerosis	Rare
VHL	Ubiquitin ligase	Von Hippel-Lindau disease	Many renal cell carcinomas
WT1	Transcription factor	Wilms tumour	Some leukaemias

Causes of cancer

Cancer development is based on the accumulation of somatic mutations over lifetime. Environmental carcinogens include chemical mutagens, which modify DNA through a range of mechanisms (alkylation or deamination of DNA bases, intercalation between base pairs and formation of DNA adducts); radiation, which induces DNA double strand breaks and tumour viruses, which can be subdivided in oncogenic viruses, viral oncogenes and slowly transforming viruses. Usually, viruses tend to use one of the following mechanisms to stimulate proliferation of their host cells:

- insertion of a strong promoter in the vicinity of a host cell proto-oncogene
- expression of proteins that neutralise host cell tumour suppressor proteins
- expression of proteins that prevent or delay apoptosis

Characteristics of viral carcinogenesis include:

- Tumour viruses often establish persistent infections in the human host
- Host factors are important determinants of virus-induced carcinogenesis
- Viruses are rarely complete carcinogens; they require additional factors to fully activate carcinogenesis.

The complex micro-evolutionary process of carcinogenesis requires the accumulation of a range of genetic mutations. As a consequence, cells acquire new characteristics such as enhanced survival and invasiveness. Three are the main processes involved in carcinogenesis: malignant transformation, invasion and metastasis. An example of the early steps of carcinogenesis can be done studying colorectal cancer: genetic characterisation of a large number of early, intermediate and late adenomas and frank carcinomas led to the establishment of a 'preferred' sequence of genetic alterations during the adenoma-adenocarcinoma pathway of colorectal cancer. These include the activation of the K-ras oncogene from its cellular proto-oncogene and the loss for three tumour suppressor genes, where loss of APC (adenomatous polyposis coli) is an early event, whereas loss of p53 is normally a late event.
The spread of cancer cells to distant sites is called metastasis and is the most lethal form of disease. Metastatic cells are less adhesive than normal cells and are able to degrade and penetrate tissue barriers of surrounding connective tissue and the basement membrane of blood vessels. They can invade normal tissues at various sites in the body forming secondary colonies. Usually, the invasion – metastasis cascade involves:

1. Acquisition of local invasiveness
2. Invasion of the cell into blood/ lymph vessels (intravasation)
3. Transport through the blood/lymph vessels to distant tissue sites
4. Escape of the cancer cells from circulation (extravasation)
5. Ability to adapt to the local tissue environment and to proliferate

Cancer can be caused by other different alterations apart from tumour suppressor genes, proto-oncogenes and DNA repair genes. These include alterations of genetic mechanisms like:

- Loss of heterozygosity
- Microsatellite instability
- DNA hyper or hypomethylation

Furthermore, there are a wide range of rare familial syndromes that predispose affected family members to cancer development (usually based on mutations of tumour suppressor genes).

Cancer hallmarks

The hallmarks of cancer comprise six biological capabilities acquired during the multistep development of human tumours. The hallmarks constitute an organizing principle for rationalizing the complexities of neoplastic disease. They include sustaining proliferative signalling, evading growth suppressors, resisting cell death, enabling replicative immortality, inducing angiogenesis, and activating invasion and metastasis [3].

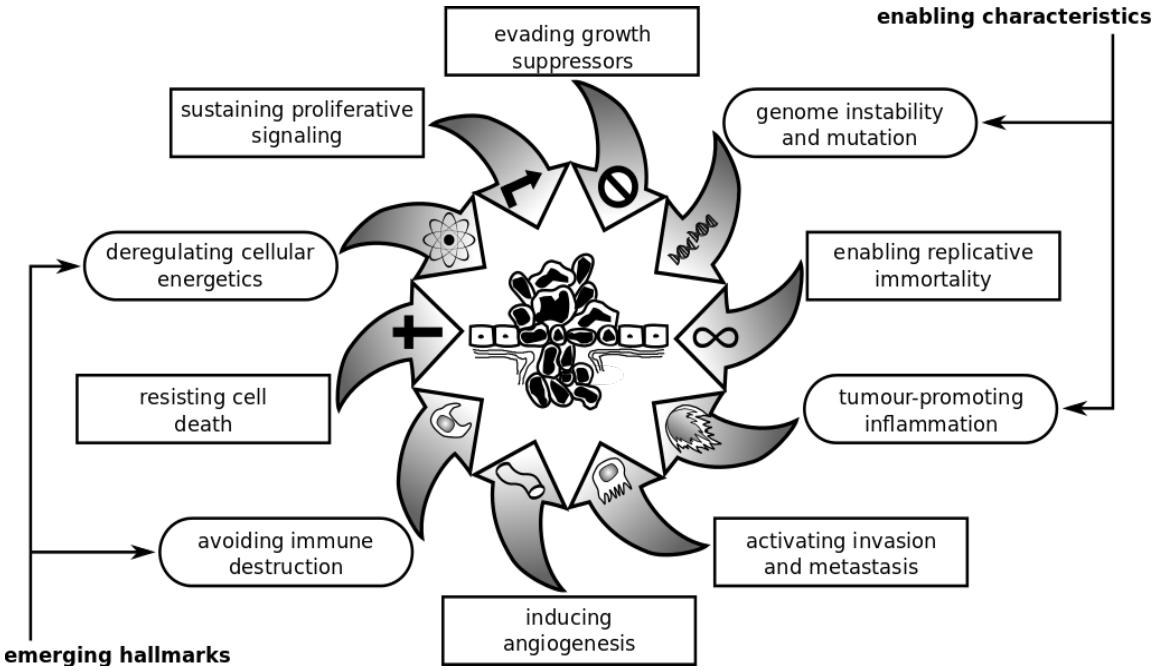

Figure 1: The hallmarks of cancer.

- Sustaining proliferative signalling: cancer cells sustain chronic proliferation deregulating signals which, in normal tissues, carefully control the production and release of growth-promoting signals ensuring homeostasis and the maintenance of normal architecture and function. Cancer cells promote proliferative signalling in many ways: they may produce growth factor ligands themselves, to which they can respond via the expression of cognate receptors, resulting in autocrine proliferative stimulation. Alternatively, cancer cells may send signals to stimulate normal cells within the supporting tumour-associated stroma, which reciprocate by supplying the cancer cells with various growth factors.
- Evading Growth Suppressors: cancer cells must also circumvent powerful programs that negatively regulate cell proliferation; many of these programs depend on the actions of tumour suppressor genes. The two prototypical tumour suppressors encode the RB (retinoblastoma-associated) and TP53 proteins, which operate as central control nodes within two key complementary cellular regulatory circuits that govern the decisions of cells to proliferate or, alternatively, activate senescence and apoptotic programs.
- Resisting Cell Death: Programmed cell death is also known as the phenomenon of apoptosis. DNA damage sensor operates via the TP53 tumour suppressor which then induces apoptosis. Cells with DNA damage die off and the cellular parts reclaimed. Tumours find ways around this apoptosis, most commonly by evolving mutations to the TP53 pathway which inactivates it. There are many similarities between the pathways apoptosis and autophagy—the cellular recycling process of sub cellular parts and organelles. Importantly, autophagy has both good and bad effects as it may potentially delay the onset of cancer, once established, and enhance cancer survival by putting it into a dormant state.
- Enabling replicative mortality: cancer cells are immortal. Normal cells can only replicate a certain number of times before they die. Telomeres protecting the end of chromosomes are crucially important in developing immortality. Regular cells have telomeres that progressively get shorter the more times they divide. Thus, over time, as telomeres

shorten, cells get old. Normal cells don't have it, and immortal cells, including cancer cells, do. This blocks aging (senescence) and apoptosis.

- Inducing angiogenesis: as the cancer grows, it requires blood vessels to bring nutrients into the centre of the tumour and to remove waste products. Without acquiring this ability to grow new blood vessels, tumours would die. This led to the development of a number of drugs that targeted and blocked specific receptors in this pathway.
- Activating Invasion and Metastasis: Tumours can invade other tissues through local invasion or metastatic spread. In local invasion, a tumour may invade the tissue surrounding it. In metastatic spread, the tumour spreads to tissues which are farther away from the original tumour.

Cancer treatment

The course of treatment depends on the type of cancer, its location, and its state of advancement. Surgery, often the first treatment, is used to remove solid tumours. It may be the only treatment necessary for early stage cancers and benign tumours. Radiation kills cancer cells with high-energy rays targeted directly to the tumour. It acts primarily by damaging DNA and preventing its replication; therefore, it preferentially kills cancer cells, which rapidly divide. It also kills some normal cells, particularly those that are dividing. Surgery and radiation treatment are often used together. Chemotherapy drugs are toxic compounds that target rapidly growing cells. Many of these drugs are designed to interfere with the synthesis of precursor molecules needed for DNA replication. Other drugs cause extensive DNA damage, which stops replication. A class of drugs called spindle inhibitors stops cell replication early in mitosis. During mitosis, chromosome separation requires spindle fibres made of microtubules; spindle inhibitors stop the synthesis of microtubules. Because most adult cells don't divide often, they are less sensitive to these drugs than are cancer cells. Chemotherapy drugs also kill certain adult cells that divide more rapidly, such as those that line the gastrointestinal tract, bone marrow cells, and hair follicles. This causes some of the side effects of chemotherapy, including gastrointestinal distress, low white blood cell count, and hair loss.

Newer therapies block the activity of hormones often required by the cell for growing. For example, some breast cancer cells require estrogen for growth. Drugs that block the binding site for estrogen can slow the growth of these cancers. These drugs are called selective estrogen receptor modulators (SERMs) or anti-estrogens. Tamoxifen and Raloxifene are examples of this type of drug. A ten-year clinical trial of these two drugs with 20,000 women began in 1999 to determine their effectiveness in preventing breast cancer. Similarly, testosterone (an androgen hormone) stimulates some prostate cancer cells. Selective androgen receptor modulators (SARMs) are drugs that block the binding of testosterone to these cancer cells, inhibiting their growth and possibly preventing prostate cancer.

Newer chemotherapeutic drugs target specific, active proteins or processes in cancer cell signal transduction pathways, such as receptors, growth factors, or kinases. Because the targets are cancer-specific proteins, the hope is that these drugs will be much less toxic to normal cells than conventional cancer drugs.

Another promising target for cancer therapy is angiogenesis. Several drugs, including some naturally occurring compounds, have the ability to inhibit angiogenesis. Two compounds in this class are angiostatin and endostatin; both are derived from naturally occurring proteins. These drugs prevent angiogenesis by tumour cells, restricting tumour growth and preventing metastasis. One important advantage of angiogenesis inhibitors is that, because they do not target the cancer cells directly, there is less chance that the cancer cells will develop resistance to the drug.

A technique called chemoimmunotherapy attaches chemotherapy drugs to antibodies that are specific for cancer cells. The antibody then delivers the drug directly to cancer cells without harming normal cells, reducing the toxic side effects of chemotherapy. These molecules contain two parts: the cancer-cell-specific antibody and a drug that is toxic once it is taken into the cancer

cell. A similar strategy, radioimmunotherapy, couples specific antibodies to radioactive atoms, thereby targeting the deadly radiation specifically to cancer cells.

1. Brain cancer

Gliomas account for more than 70% of all primary brain tumours, and of these, glioblastoma is the most frequent and malignant histologic type (World Health Organization [WHO] grade IV) [4].

Clinical classification

There are two main types of tumours: malignant or cancerous tumours and benign tumours. Cancerous tumours can be divided into primary tumours that start within the brain, and secondary tumours that have spread from elsewhere, known as brain metastasis tumours.
Glioma occurs in the brain and spinal cord and, more precisely, in glial cells, which surround and help nerve cells. Tumours can be produced by three different types of cells and gliomas are usually classified according to the type of glial cell involved in the tumour. Types of glioma include:

- astrocytomas, including astrocytoma, anaplastic strocytoma and glioblastoma,
- ependymomas, including anaplastic ependymoma, myxopapillary ependymoma and subependymoma,
- oligodendrogliomas, including oligodendroglioma, anaplastic oligodendroglioma and anaplastic oligoastrocytoma.

Secondary brain tumours are metastatic and have invaded the brain from cancers originating in other organs. They then circulate through the bloodstream, and are deposited in the brain. There, these cells continue growing and dividing, becoming another invasive neoplasm of the primary cancer's tissue. Secondary tumours of the brain are very common in the terminal phases of patients with an incurable metastasized cancer; the most common types of cancers that bring about secondary tumours of the brain are lung cancer, breast cancer, malignant melanoma, kidney cancer, and colon cancer (in decreasing order of frequency). Secondary brain tumours are more common than primary ones; in the United States there are about 170,000 new cases every year. Secondary brain tumours are the most common cause of tumours in the intracranial cavity. The skull bone structure can also be subject to a neoplasm that by its very nature reduces the volume of the intracranial cavity, and can damage the brain.

Risk factors

The cause of most brain tumours is unknown [4]. Epidemiological studies are required to determine risk factors. Aside from exposure to vinyl chloride or ionizing radiation, there are no known environmental factors associated with brain tumours [5]. Mutations and deletions of so-called tumour suppressor genes, such as P53, are thought to be the cause of some forms of brain tumour [6]. Inherited conditions, such as Von Hippel–Lindau disease, multiple endocrine neoplasia, and neurofibromatosis type 2 carry a high risk for the development of brain tumours [7]. People with celiac disease have a slightly increased risk of developing brain tumours [8]. Although studies have not shown any link between cell phone or mobile phone radiation and the occurrence of brain tumours, the World Health Organization has classified mobile phone radiation on the IARC scale into Group 2B – possibly carcinogenic [9]. Discounting claims that current cell phone usage may cause brain cancer, modern, third-generation (3G) phones emit, on average, about 1% of the energy emitted by the GSM (2G) phones that were in use when epidemiological studies that observed a slight increase in the risk for

glioma – a malignant type of brain cancer – among heavy users of wireless and cordless telephones were conducted.

2. Breast cancer

Breast cancer is the most frequently diagnosed cancer among women in 140 of 184 countries worldwide and remains the most common cause of cancer death (322,600 breast cancer deaths have been averted in US women through 2015) [10].

Clinical classification

Clinically, breast cancer classification is done on the basis of tumour morphological characteristics into different types and these include infiltrating ductal carcinoma of no special type, and a large number of 'special types' such as infiltrating lobular carcinoma, tubular, mucinous, medullary, and adenoid cystic carcinoma. Histological grade, including the degree of cellular differentiation, nuclear pleomorphism, and mitotic count help in further sub-classification of breast tumours. Breast tumours such as smaller size tubular carcinomas are typically associated with earlier stage at presentation, compared with infiltrating ductal carcinomas. It is also noted that breast tumours of high histological grade are generally large at presentation and are associated with local or distant metastasis, compared with tumours of low histological grade. Breast tumours have also been identified into five different subtypes based on the expression of estrogen receptors (ER) and progesterone receptors (PR), and Her2 oncogene. Overall, the ER positive tumours are more common than the ER-negative tumours. Also, the ER positive tumours are smaller and low grade and lymph node negative unlike the ER negative tumours [11]. Thus, there are two ER/PR-positive subgroups, Luminal A and Luminal B, and three ER-negative subgroups. One of the ER negative type is characterized by elevated expression of Her2 and related genes, and thus termed as the Her2 subtype; the second ER negative type is associated with high expression of genes normally identified with myoepithelial or basal cells, termed basal-like subtype; and a third ER negative group that shows a varied gene expression profile is termed normal-like subtype [11]. Both Her2 and basal-like subtypes of ER negative breast tumours clinically exhibit significantly poorer outcome than the luminal and normal-like groups. It has been observed that prognosis is worse in a stage-independent manner for both Her2 and basal-like subtypes of ER negative breast tumours and that both subtypes are also associated with more advanced stage at presentation [10]. Both Her2 and basal-like breast tumours were found to contain a greater percentage of stem cell-like cells, which seven may contribute to their aggressive clinical behaviour [11]. Her2 oncogene is related to epidermal growth factor receptor family and is overexpressed in approximately 20 % of the breast tumours. PR negativity among all ER positive tumours independently predicts Her2 positivity [11]. Breast tumours that do not express either ER, PR, or Her2 are called triple negative breast cancers (TNBC) and approximately 15 % of the breast cancers fall into this category. Besides the above subtypes, there is another form of breast cancer known as inflammatory breast cancer (IBC) that is clinically and biologically distinct [11].

Risk factors

For most sporadic breast cancer, age and female sex are the two key risk factors with most women diagnosed after menopause (median age 59). Family history especially in first or second-degree relatives is also important. Estrogen exposure has a role in the genesis of breast cancer, with early menarche, late menopause, and nulliparity being risk factors, and parity, history of breast feeding being protective. Although the risk of breast cancer whilst on the oral contraceptive pill is higher, the overall risk during one's lifetime is small due to the young age at which women are on the pill. Hormone replacement therapy can increase the risk of breast cancer. Other lifestyle related risk factors increase high caloric intake during childhood and adolescence, obesity and alcohol.

Some breast pathologies increase the risk of breast cancer such as ductal carcinoma in situ (DCIS), lobular carcinoma in situ and atypical ductal hyperplasia.
It is well recognized that while the breast cancer incidence is higher in developed countries and also in women of higher socioeconomic status, the mortality due to breast cancer is higher in women from poorer countries and also from lower socioeconomic status [11]. This can be partly because of the lower screening rates in poor women compared with relatively affluent women, despite much progress in increasing mammography utilization. For example, in 2008, about 21 % more non-poor women had undergone screening than the poorer women [11].

3. Lung cancer

Lung cancer is the leading cause of cancer death in the United States and around the world. Almost as many Americans die of lung cancer every year than die of prostate, breast, and colon cancer combined [12]. Globally, lung cancer is the largest contributor to new cancer diagnoses (1,350,000 new cases and 12.4% of total new cancer cases) and to death from cancer (1,180,000 deaths and 17.6% of total cancer deaths). The 5-year survival rate in the United States for lung cancer is 15.6%, and although there has been some improvement in survival during the past few decades, the survival advances that have been realized in other common malignancies have yet to be achieved in lung cancer. There has been a large relative increase in the numbers of cases of lung cancer in developing countries. Approximately half (49.9%) of the cases now occur in developing countries whereas in 1980, 69% of cases were in developed countries. The estimated numbers of lung cancer cases worldwide has increased by 51% since 1985 (a 44% increase in men and a 76% increase in women) [12].

Clinical classification

There are two broad categories of lung cancer:

1. Small-cell lung cancer (SCLC), which accounts for about 20% of all lung cancers. It has a very aggressive behaviour and is considered a “systemic” disease at diagnosis. It develops in 3-5 years and has a doubling time of 30 days. Up to 15 % of patients with limited stage SCLC will have long-term survival. The commonest location of SCLC is around the hilum and central areas of the lungs. SCLC is most frequently associated with several para-neoplastic syndromes. Small cell carcinomas arise from neuroendocrine cells and secrete many different polypeptides. Some of the polypeptides have an auto feedback loop which induces further tumour growth. Often the initial presentation of patients with SCLC is with a paraneoplastic syndrome, such as Cushing’s syndrome or Addison’s disease. SCLC is extremely aggressive and spreads very early. Surgery does not play a part in most cases. Although SCLC responds extremely well and quickly to chemotherapy and radiation therapy, even those patients who respond usually relapse within 12 months.

2. Non-small cell lung cancer, which has 3 broad categories of histology. In non-small cell lung cancer histology is now considered very important as treatment choices vary significantly between the various histologies.
- Adenocarcinoma: Now the most common non-small cell lung cancer and is the dominant lung cancer amongst females. Non-smokers with lung cancer most often have adenocarcinoma. Approximately 40% of all lung cancers would be adenocarcinoma. Adenocarcinomas are typically slow growing and take over 15 years to develop with a tumour doubling time in excess of 200 days. Adenocarcinomas are more often found peripherally and therefore often present late with distant metastases present at time of diagnosis in most patients. Adenocarcinomas arise from mucous cells in the bronchial epithelium. Adenocarcinoma involves mediastinal lymph nodes and

the pleura and spreads to bone and brain. They are sometimes confused with mesothelioma and are most likely to cause pleural effusions.

- Squamous cell: Incidence is declining and now accounts for approximately 25% of all lung cancers. There are various subtypes, with some differences in presentation, behaviour and treatments. Squamous cell cancers are somewhat more aggressive than adenocarcinoma and take 8 or more years to develop. With doubling time in excess of 100 years, squamous cell carcinomas usually cause bronchial obstruction leading to infections. Up to 10% of squamous cell carcinomas may have cavitation. The cavitation occurs due to central necrosis of tumour mass due to rapid growth of lung cancer. These cavitating lesions are often labelled as abscess or TB cavity.
- Large cell carcinoma: The least common variety accounts for about 10% of all lung cancer and is more undifferentiated with clear cell and giant cell variants. These are considered variants of adenocarcinoma and squamous cell carcinoma but because of poorly differentiated histology cannot be ascribed either. Large cell carcinomas metastasise early and have poor prognosis.
- A small number of lung cancers have mixed histology consisting either of adenocarcinoma and squamous cell carcinoma admixed or less common a combination of small cell and non-small cell variant.

Tumours arising in the main bronchi tend to present earlier than those arising peripherally and frequently are associated with haemoptysis. About 80% of lung cancers are found in the lobar bronchi; the remainder are in larger bronchi.

Risk factors

Smoking is responsible for over 90% of lung cancers. Tobacco smokes contains over 60 known carcinogens. Passive smoking increases the risk of lung cancer by 1.5 fold and possibly accounts for about 5% of lung cancers. Other risk factors include exposure to arsenic, radon, radiation, iron oxide, chromium, petroleum products and possibly coal mining.

4. Prostate cancer

Prostate cancer is the most common non-skin cancer diagnosed among American males, affecting roughly one in six men (16.15%) over the course of their lifetime. Prostate cancer is also the second leading cause of cancer-related deaths in American men. The incidence of prostate cancer spiked in the United States in the early 1990s because of the advent of more aggressive prostate-specific antigen (PSA) screening [13]. This was followed by a sharp decline from 1992 to 1995 during which incidence rates returned to a new baseline which remained approximately two and a half times the pre-PSA era rate, likely due to the fact that increased screening in prior years had successfully diagnosed much of the previously undetected prostate cancer patients in the population.

Risk factors

Advancing age is the principal risk factor for acquiring prostate cancer. From 2005 to 2009, the median age of diagnosis was 67 years, with approximately 90% of diagnoses occurring at the age of 55 years and above [13]. In addition, older men are more likely to be diagnosed with high-risk prostate cancer leading to lower overall and cancer-specific survival. Race is a major risk factor for prostate cancer, both with respect to incidence and mortality; however, reasons are less clear. African-Americans have the highest incidence of prostate cancer than any other race or ethnicity in the United States. Family history is one of the strongest risk factors when considering who will develop prostate cancer. Having an affected relative, the number of affected relatives, and the age of onset of prostate cancer in the affected relative are all risk factors for developing prostate

cancer. Risk of prostate cancer doubles for a male who has one affected first-degree relative. Other risk factors are related to cigarettes smoking, obesity, and alcohol [13].
By far the most common pathological subtype is adenocarcinoma; grading is by the Gleason system; numbered from 1-5 (from well differentiated glandular structures to anaplastic) and the scoring of the two most common histological growth patterns is added together, i.e. 4+3 = 7. Grading is a strong predictor of prognosis.

References

[1] S. Fleming, The molecular biology of cancer: the basics, Surgery-Oxford International Edition, 21 (2003) iii-vi.
[2] U.A. Bommer, K.L. Vine, Cancer biology: molecular and genetic basis, DOI (2014).
[3] D. Hanahan, R.A. Weinberg, Hallmarks of cancer: the next generation, Cell, 144 (2011) 646-674.
[4] M. Mehta, M.A. Vogelbaum, S. Chang, N. Patel, Neoplasms of the central nervous system, Cancer: principles and practice of oncology, 9 (2011) 1700-1749.
[5] M. Krishnatreya, A.C. Kataki, J.D. Sharma, M. Bhattacharyya, P. Nandy, M. Hazarika, Brief descriptive epidemiology of primary malignant brain tumors from North-East India, Asian Pacific Journal of Cancer Prevention, 15 (2014) 9871-9873.
[6] P. Kleihues, H. Ohgaki, R. Eibl, M. Reichel, L. Mariani, M. Gehring, I. Petersen, T. Höll, A. von Deimling, O. Wiestler, Type and frequency of p53 mutations in tumors of the nervous system and its coverings, Molecular Neuro-oncology and Its Impact on the Clinical Management of Brain Tumors, Springer1994, pp. 25-31.
[7] T.S. Hodgson, S.M. Nielsen, M.S. Lesniak, R.V. Lukas, Neurological Management of Von Hippel-Lindau Disease, The neurologist, 21 (2016) 73-78.
[8] C. Hourigan, The molecular basis of coeliac disease, Clinical and experimental medicine, 6 (2006) 53-59.
[9] P. Frei, A.H. Poulsen, C. Johansen, J.H. Olsen, M. Steding-Jessen, J. Schüz, Use of mobile phones and risk of brain tumours: update of Danish cohort study, Bmj, 343 (2011) d6387.
[10] C.E. DeSantis, J. Ma, A. Goding Sauer, L.A. Newman, A. Jemal, Breast cancer statistics, 2017, racial disparity in mortality by state, CA: a cancer journal for clinicians, 67 (2017) 439-448.
[11] Z. Tao, A. Shi, C. Lu, T. Song, Z. Zhang, J. Zhao, Breast Cancer: Epidemiology and Etiology, Cell Biochemistry and Biophysics, 72 (2015) 333-338.
[12] C.S. Dela Cruz, L.T. Tanoue, R.A. Matthay, Lung Cancer: Epidemiology, Etiology, and Prevention, Clinics in chest medicine, 32 (2011).
[13] A. Darves-Bornoz, J. Park, A. Katz, Y. Philippou, H. Dev, P. Sooriakumaran, J. Oxley, P.J. Cheetham, J. Richenberg, N.J. Smith, Prostate Cancer Epidemiology, Prostate Cancer: Diagnosis and clinical management, DOI (2014) 1-15.
[14] B.M. Reid, Epidemiology of ovarian cancer: a review, 14 (2017) 9-32.

CHAPTER 2

The basics of PET

Positron emission tomography is a nuclear medical imaging technique for quantitative measurement of physiologic parameters in vivo, based on the detection of small amounts of positron-emitter-labelled biologic molecules [1].

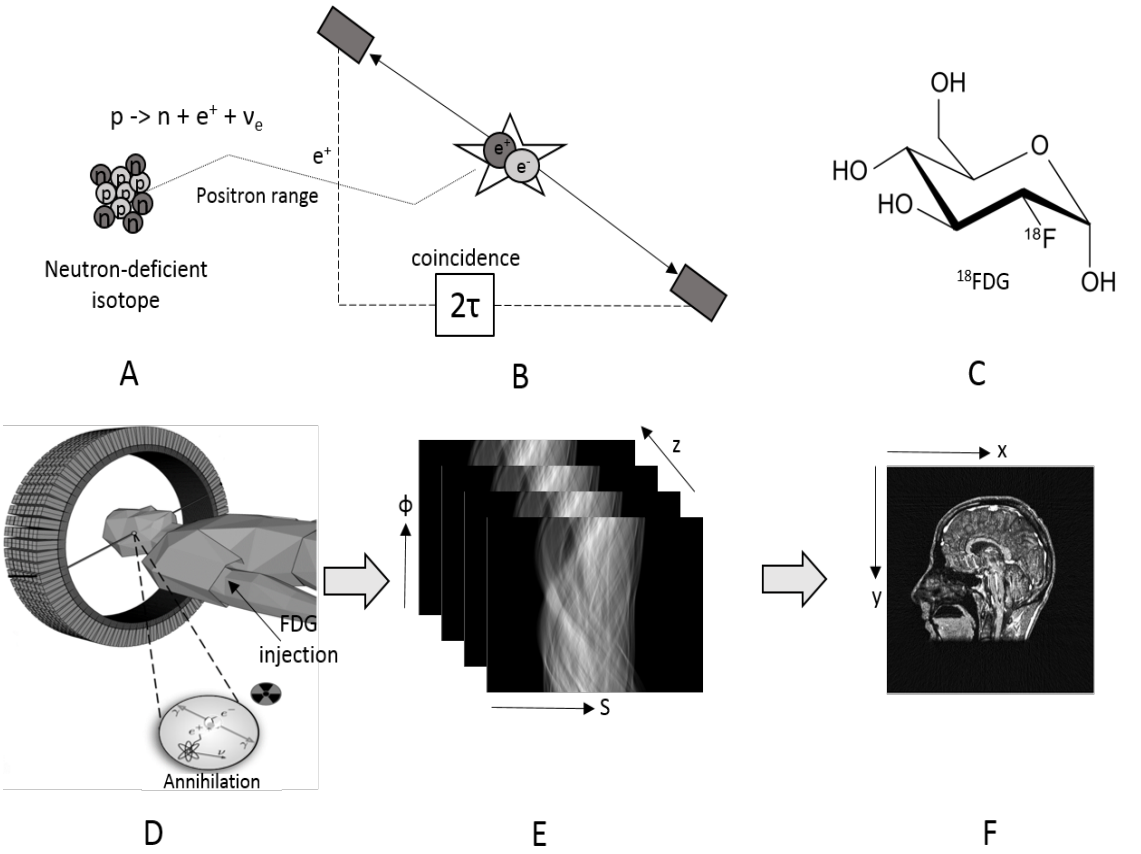

Figure 2: The principle of PET imaging shown schematically, including: (a) the decay of a neutron-deficient, positron-emitting isotope, (b) the detection in coincidence of the annihilation photons within a time window of 2τ ns, (c) the glucose analogue deoxyglucose labelled with the positron-emitter 18F to form the radiopharmaceutical FDG, (d) the injection of the labelled pharmaceutical and the detection of a pair of annihilation photons in coincidence by a multi-ring PET camera, (e) the collection of the positron annihilation events into sonograms where each element of the sonogram contains the number of annihilations in a specific projection direction and (f) a coronal section of the final, reconstructed whole-body image mapping the utilisation of glucose throughout the patient.

The most commonly used emitters are carbon-11, oxygen-15, nitrogen-13, and fluorine-18. Advantages of positron labelled substances are their very high specificity (molecular targeting), the possibility of using biological active substances without changing their behaviour by the label, and fulfilment of the tracer principle. Target structures of these molecules are e.g. glucose metabolism, receptor binding potential, catecholamine transport, amino acid transport, or protein synthesis.

PET imaging consists on several steps: 1) the selection and production of a suitable molecular probe, a pharmaceutical labelled with a positron-emitting radionuclide, 2) the administration of the probe to the patient and finally 3) the imaging of the distribution of the probe in the patient (Figure 2) [2]. Positron emitters are neutron-deficient isotopes that achieve stability through the nuclear transmutation of a proton into a neutron. The process involves the emission of a positive electron, or positron (e^+) and electron neutrino (ν_e). The energy spectrum of the emitted positron depends on the specific isotope, with typical endpoint energies varying from 0.6 MeV for 18F up to 3.4 MeV for 82Rb [2]. After emission, the positron loses energy through interactions with the surrounding tissue until it annihilates with an electron. The range the positron travels in tissue obviously depends on the energy with which it is emitted, and that, in turn, depends on the particular isotope. The annihilation produces two gamma rays, which are emitted in opposite directions and are detected in coincidence [2]. PET imaging is based on the annihilation coincidence detection (ACD) of these two collinear 511-keV gamma rays traveling in opposite directions, corresponding to equal-magnitude, opposite-sign (positive and negative) momenta.

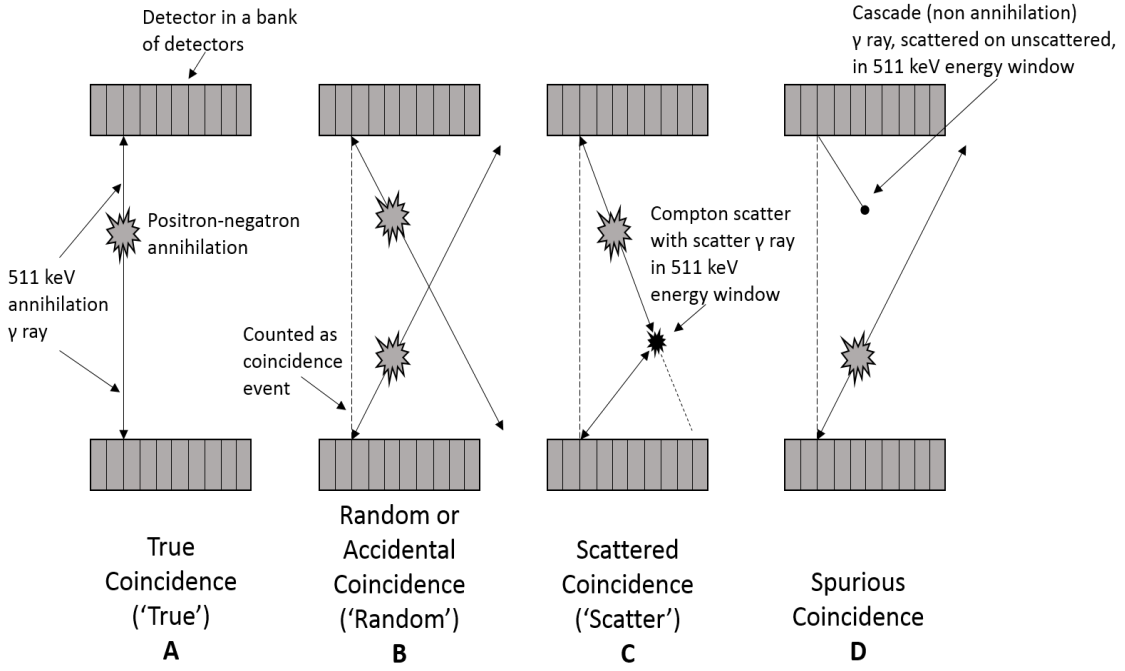

Figure 3: The various events associated with ACD of positron-emitting radionuclides, illustrated for two opposed banks of coincidence detectors and assuming only one opposed pair of detectors are in coincidence. (A) A true coincidence ("true") is counted only when each of the two 511-keV annihilation gamma-rays for a single positron-negatron annihilation are not scattered and are detected within the timing window τ of the two coincidence detectors. (B) A random or accidental coincidence ("random") is an inappropriately detected and positioned coincidence (the dashed line) that arises from two separate annihilations, with one gamma-ray from each of the two annihilations detected within the timing window τ of the coincidence-detector pair. (C) A scattered coincidence ("scatter") is a mispositioned coincidence (the dashed line) resulting from a single annihilation, with one of the gamma-rays undergoing a small-angle Compton scatter but retaining sufficient energy to fall within the 511-keV energy window. (D) A spurious coincidence is an inappropriately detected and positioned coincidence (the dashed line) which arises from an annihilation and a cascade gamma-ray, scattered or unscattered but having sufficient energy to fall within the 511-keV energy window. Spurious coincidences occur only for radionuclides which emit both positron and prompt cascade gamma-ray(s).

The pairs of coincident photons, or events, are detected by a circular configuration of detectors and are stored in matrices or sonograms where each row in the matrix represents a parallel projection p(s, φ) of the activity distribution in the patient at a specific angle (φ) and axial position (z) [2]. An output is generated only when signals from the two coincidence detectors simultaneously trigger the coincidence circuit. It is called a "true coincidence event" (or just "true"). The volume between the opposed coincidence detectors is referred to as "line of response (LOR)" and the time

interval allowed for coincidence detection is called the "coincidence timing window τ" (typically 6 to 12 ns) [3]. The finite timing window is necessitated by several considerations. First, depending on the exact position of the positron negatron annihilation, the annihilation photons reach the detectors at slightly different times. However, because these photons travel at the speed of light ($c = 3 \times 10^{10}$ cm/s), this effect is very small. Second, the transit and processing of the signal pulses through the detector circuitry is rapid but not instantaneous. Third, the light signal emitted by the scintillation detectors used in PET is emitted not instantaneously but over a finite time interval, called the "scintillation decay time", of the order of 10 to 100 ns. In addition to the true coincidence events (Figure 3A), a number of other types of events occur in PET, events that degrade quantitative accuracy as well as image quality. Random or accidental coincidence events ("randoms") occur when annihilation gamma-rays from two separate positron-negatron annihilations are detected in two different detectors within the coincidence timing window τ (Figure 3B). Randoms thus increase the detected coincidence count rate by contributing spuriously placed coincidence events [3]. Because the total activity-containing volume is typically much greater than the LOR, random coincidences are common and the randoms count rate may actually exceed the trues count rate. Clinically, the ratio of the randoms-to-true count rates range from 0.1 to 0.2 for brain imaging to greater than 1 for whole-body imaging [4]. The randoms count rate is actually proportional to the product of the singles count rate and therefore the square of the activity present [4]:

$$C_{randoms} = 2\tau C_1 C_2 \qquad 1)$$

where $C_{randoms}$ is the randoms count rate (cps), τ is the coincidence timing window (sec), and C_1 and C_2 are the detector 1 and detector 2 singles count rates (cps), respectively. Importantly, because the trues count rate is only linearly proportional to the activity, the ratio of the randoms to-trues count rates increases linearly with activity. Therefore, imaging times cannot be reduced simply by using higher and higher administered activities, as the randoms count rate will increase more rapidly than the trues count rate and at some point prohibitively degrade image quality. By using absorptive septa to restrict the activity-containing region sampled by coincidence detectors to a volume defined by the cross-sectional area of the detectors—as in two-dimensional, the randoms-to-true count rate ratio can be reduced substantially. By using "faster" detectors and therefore shorter coincidence timing windows, the randoms-to-true count rate can be reduced further [3]. Annihilation gamma-rays traveling out of an LOR may undergo Compton scatter and be re-directed back into the LOR. The scattered photon may, however, retain sufficient energy to fall within the energy window set for the 511-keV annihilation gamma-rays and produce a coincidence event. Such scatter coincidences ("scatter") result in mispositioned events. The scatter count rate as well as the trues count rate are proportional to the activity present and therefore the scatter-to-trues count rate ratio is independent of activity. Because trues and scatter each result from single annihilation events, the scatter-to-trues count rate ratio is likewise independent of the coincidence timing window. On the other hand, inter detector septa used in 2D PET reduce the scatter count rate considerably [3]. Many positron-emitting radioisotopes also emit significant numbers of high-energy prompt gamma-rays, and such gamma-rays may be in cascade with each other or with the positrons [5]. These can result in spurious coincidences which are spatially uncorrelated but nonetheless counted as true events (Figure 3D) [3]. Table 3 includes, for selected positron emitters, the energy and abundance of gamma- (and x-) rays with sufficient energy (i.e., greater than 250 keV) to fall within the 511-keV energy windows typically used to count annihilation gamma-rays in PET.

Table 3: Individual attenuation contributions and total attenuation coefficients (mass and linear) for various materials and energy levels. Water constitutes the majority of the body material and most tissue attenuation is near to that of water. BGO and LSO are commonly used scintillator material used in PET detectors. The values smaller than 10^{-3} are neglected.

Material	Radio-nuclide	Photon Energy (keV)	Scattering attenuation coefficient		Photoelectric attenuation coefficient	Total attenuation coefficient	
			Rayleigh	Compton		cm^2/g	cm^{-1}
WATER	^{125}I	27.5	0.054	0.182	0.194	0.430	
Z_{eff} = 7.89	^{99m}Tc	140	0.003	0.150	0.000	0.154	
ρ = 1 g/cm^3	PET	511	0.000	0.096	0.000	0.096	
LEAD	^{125}I	27.5	1.550	0.079	36.3	37.9	393
Z_{eff} = 82	^{99m}Tc	140	0.119	0.096	2.18	2.39	27.1
ρ = 11.35 g/cm^3	PET	511	0.011	0.067	0.078	0.156	1.77
NaI(TI)	^{125}I	27.5	0.473	0.122	5.24	5.84	21.4
Z_{eff} = 50	^{99m}Tc	140	0.032	0.117	0.332	0.481	1.76
ρ = 3.67 g/cm^3	PET	511	0.003	0.077	0.009	0.089	0.33
BGO	^{125}I	27.5	0.439	0.136	0.108	11.4	81.3
Z_{eff} = 74	^{99m}Tc	140	0.032	0.124	0.497	0.652	4.65
ρ = 7.13 g/cm^3	PET	511	0.003	0.081	0.018	0.101	0.72
LSO (Lu_2SiO_5)	^{125}I	27.5	0.376	0.140	6.34	6.85	50.7
Z_{eff} = 66	^{99m}Tc	140	0.027	0.126	0.379	0.532	3.93
ρ = 7.4 g/cm^3	PET	511	0.002	0.082	0.012	0.096	0.71

Detector materials

To date, only four detector materials, all inorganic scintillators, have been widely used in PET scanners: thallium-doped sodium iodide (NaI(Tl)), bismuth germanate (BGO), cerium-doped lutetium oxyorthosilicate (LSO(Ce) or simply LSO), and cerium-doped gadolinium oxyorthosilicate (GSO(Ce)or simply GSO) [3]. Annihilation photons interact within the scintillator through Rayleigh, Compton, and photoelectric effects. Only the latter two release energy to the detector, making the photons "detectable". Rayleigh scattering can be ignored at typical PET energies. The annihilation photon could deposit a fraction or all of its energy within the crystal. The deposition can occur in one location by photoelectric effect, or at several points within the same crystal by successive Compton interactions, or in different (usually adjacent) crystals in a pixelated matrix [6]. The absorbed energy causes the crystal lattice to make a transition to a higher energy state, from which it may undergo decay after a characteristic time by emitting lower energy photons, the "scintillation photons", which are detected by the photocathode of a photomultiplier tube. Self-absorption of the scintillation photons by the scintillator must be minimal, i.e., the attenuation length must be much longer than the crystal thickness. The amplitude of the electronic signal produced is proportional to the number of scintillation photons, and thus to the energy deposited within the crystal. Energy thresholding can then allow the rejection of a large fraction of events scattered within the patient, which have sufficiently low energy to fall below the energy discrimination window [6]. The most important practical features of scintillation detectors include high mass density (ρ) and effective atomic number (Z_{eff}), high light output, and speed (Table 4).

Table 4: Physical properties of scintillator materials commonly used for PET.

Scintillator material	Composition	density (g/cm3)	Z_{eff}	Attenuation length for 511-keV gammas (mm)	Probability of PET (%)	Light output (ph/MeV)	Decay time (ns)	Scint. emission wave length (mm)	Hygroscopic	Refractive index
BGO	$Bi_4Ge_3O_{12}$	7.1	75	10.4	40	9,000	300	480	no	2.15
LSO	Lu_2SiO_5:Ce	7.4	66	11.4	32	30,000	40	420	no	1.82
NaI:TI	NaI:TI	3.67	51	29.1	17	41,000	230	410	yes	1.85
CsI:TI	CsI:TI	4.51	52	22.9	21	66,000	900	550	slightly	1.80
GSO	Gs_2SiO_5:Ce	6.7	59	14.1	25	8,000	60	440	no	1.85
LGSO	$Lu_{1,8}O_2SiO_3$:Ce					23,000	40	420	no	
LuAP	$LuAlO_3$:Ce	8.3	64.9	10.5	30	12,000	18	365	no	1.94
YAP	$YAlO_3$:Ce	5.5	33.5	21.3	4.2	17,000	30	350	no	1.95
LPS	$Lu_2Si_2O_7$:Ce	6.2	63.8	14.1	29	30,000	30	380	no	
LuAG	$Lu_3Al_5O_{12}$:Ce	6.7	62.9	13.4	27	5,606		510	no	

A high mass number and high effective atomic number maximize the crystal stopping power (i.e., linear attenuation coefficient μ) and therefore the detection of radiations. In addition, a higher-atomic number crystal will have a higher proportion of photoelectric than Compton interactions, facilitating energy discrimination of scattered photons. High light output reduces statistical uncertainty (noise) in the scintillation and associated electronic signal and thus improves energy resolution and scatter rejection. A fast crystal (i.e., a crystal with a short scintillation decay time) allows the use of a narrow coincidence timing window, τ, reducing the randoms count rate [3]. Other detector considerations include: transparency of the crystal to its own scintillations (i.e., minimal self-absorption); matching of the index of refraction (η) of the crystal to that of the photodetector (specifically, the entrance window [$\eta = 1.5$] of a photomultiplier tube [PMT]); matching of the scintillation wavelength to the light response of the photodetector (the PMT photocathode, with maximum sensitivity in the 390-410 nm, or blue, wavelength range); and minimal hygroscopic behaviour [6]. NaI(Tl) crystals were used in the original PET scanners.

Higher-density and -effective atomic materials, such as BGO, LSO, and GSO, have emerged as the detectors of choice for PET because of their greater stopping power for 511-keV annihilation gamma-rays (Table 2). Note, for example, that the attenuation length for 511-keV gamma-rays is at least twice as long in NaI(Tl) as in BGO, GSO, or LSO. Among the latter three materials, GSO and LSO have a faster light output—nearly 10-fold faster—than BGO, with LSO having a much greater light output—approximately 3-fold greater—than either BGO or GSO. GSO has somewhat better energy resolution, and scatter rejection capability, than either BGO or LSO. A notable disadvantage of LSO is the presence of a naturally-occurring long-lived radioisotope of lutetium, lutetium-177 [3]. Lutetium-177 has an isotopic abundance of 2.6% and a half-life of ~4 x 10^{10} years and emits two prompt gamma-rays (88% abundance) of 201 and 306 keV in energy; the summed energy of 507 keV falls well within the 511-keV energy windows commonly used in PET scanners. The presence of lutetium-177 results in a measured background count rate of 240 cps/cm3 of LSO and singles and trues count rates of 100,000 and 10,000 cps, respectively, in clinical LSO PET scanners. Although the former has a negligible effect on typical emission scans, the latter would significantly increase the statistical uncertainty (noise) in single-photon transmission scans (e.g., with cesium-137) used for attenuation correction [3].

Detector configurations

Most commonly in dedicated PET scanners, detectors are arranged in rings or polygonal arrays of discrete, small-area detectors completely encircling the patient (Figure 4A–C).

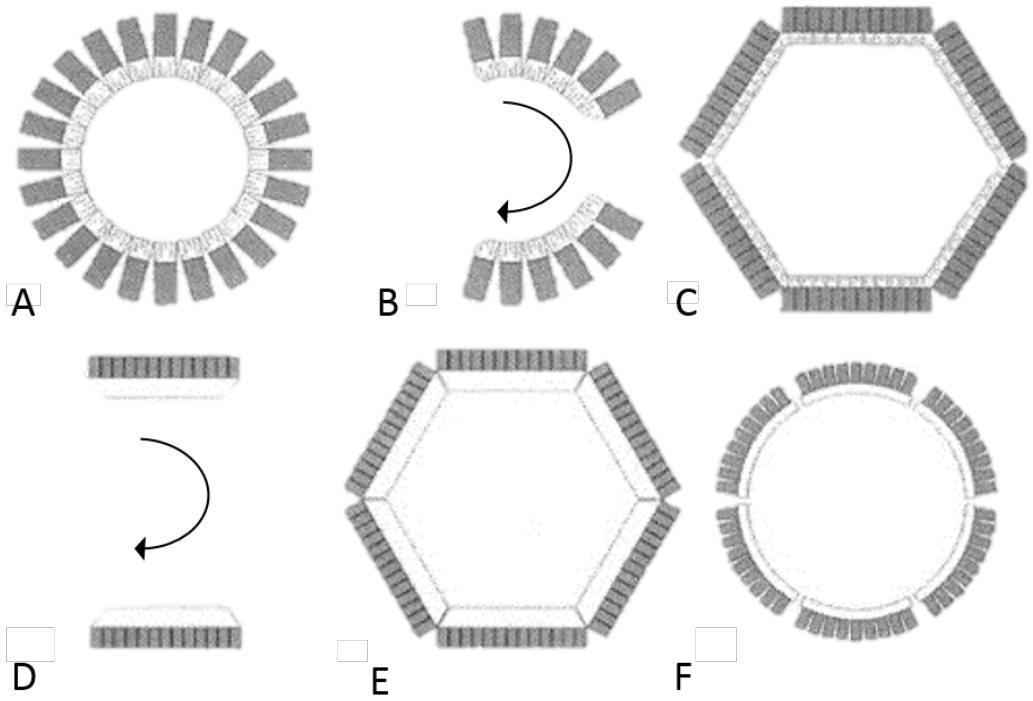

Figure 4: PET scanner detector configurations. (A) Multiple full rings of detector blocks comprised of discrete, small-area detector elements. (B) Multiple partial rings of detector blocks comprised of small-area detector elements. (C) Hexagonal array of detectors banks comprised of small-area detector elements. (D) Opposed large-area detectors such as Anger cameras. (E) Hexagonal array of large-area detectors. (F) Circular arrangement of six large-area, curved detectors. Inset: Multi-coincidence fan beam detection used in detector rings and arrays of small-area detectors. Such fan beam transverse sampling data are generally treated as parallel-beam data.

In such systems, multi-coincidence fan beam detection is used, with each detector element operated in coincidence with multiple opposed detector elements. For a ring comprised of N detector elements, a total of N/4 to N/2 fan beams is acquired. In rings, each element is typically in coincidence with about half of the total detectors in the ring and in polygonal arrays with the opposed detector bank. PET systems with only partial detector rings are less expensive but require rotation of the detector assembly about the longitudinal axis of the patient to complete acquisition of the projection data (Figure 4B). In addition, continuous, large-area detectors, have now been appropriately modified and are used for coincidence imaging of positron emitters (Figure 4D). With two or even three such detectors, rotation (180 or 120°, respectively) is required for complete angular sampling. Alternatively, large-area detectors may be arranged in a polygon (if flat) or in a circle (if curved) completely encircling the patient (Figure 4E and F); such systems have been manufactured using GSO as well as NaI(Tl) [3]. A block detector consists of a large cubic piece of scintillator (2 x 2 to 3 x 3 cm in cross section by 2 to 3 cm in depth) partially cut, or scored, depth-wise into a rectangular array of detector elements. The cuts are filled with reflective material to optically isolate the detector elements from one another and to maximize light collection efficiency by the PMTs backing the scintillator. Crystal elements with a somewhat smaller cross-section improve spatial resolution—but only to a certain point. As the cross-section of detector elements is reduced and the number of elements increased, the number of cuts and therefore the fraction of the scintillator face occupied by the filling material increase. As a result, the detector element packing fraction (i.e., the fraction of the scintillator face occupied by

scintillation material) and therefore the intrinsic sensitivity decrease [3]. In modern ring-detector PET scanners, there are typically three to four rings of 100 to 200 block detectors each. There are about 6 to 8 cuts per block detector, yielding an array of 6 x 6 x 36 to 8 x 8 x 64 elements 4 x 4 to 6 x 6 mm each. Overall, therefore, there are a total of 10,000 to 20,000 detector elements. Ring diameters range from 80 to 90 cm, the patient ports and trans axial fields of view from 50 to 70 cm, and the axial (or longitudinal) fields of view from 20 to 30 cm, typically yielding about 50 trans axial image planes each 2 to 4 mm thick [3]. A recently developed alternative to the block detector is the pixelated detector matrix [7], wherein individual small-area detectors elements (typically 4 x 6 mm in cross-section by 20 mm in depth) are fixed onto a continuous light guide backed by a close-packed array of PMTs [3].

Data acquisition

The detector block is formed by a number of crystals viewed by four PMTs. When the block is hit, a fast electronic circuit determines the start time of the pulse, which is integrated to obtain the deposited energy. Localization electronics decide which crystal in the detector block was hit and if the energy was outside or inside the energy window for each element. All this information is stored in a data block and is compared with opposite detector blocks in the detector in order to decide whether there was a coincidence or not. Most of this analysis is done by hardwired electronics, a real-time sorter (RTS). Modern electronics add the possibility to perform analysis of the depth of interaction in the crystals (DOI) and time of flight (TOF) on line [8]. Annihilation photons are randomly detected by two crystals in the tomograph. These two crystals define a coincidence channel, a straight line, through the body. However, the coincidence channels can also be organized into parallel channels which define a projection of an integrated radioactivity distribution through the object from a specific angle. Such projections taken at angles around the object are usually the input into the reconstruction algorithms. Each activated coincidence channel belongs to one such projection. Every time a coincidence is detected a scaler is incremented by one in the right projection position. Data are collected in this so-called '*histogram mode*' for a pre-set time which can vary from one second to infinity. Usually a protocol is made in advance where a number of pre-set times defines the histograms to be measured. Another way to collect the data is called '*list mode*'. The coincidences are sorted out by RTS electronics. Data characterizing one single event are registered in one data block (crystal position, running time, single rate, etc.). After the end of the data acquisition the data set can be sorted in histograms but with a free choice of sampling times [9]. In early PET systems the number of coincidence channels was usually small compared with the number of events collected during one experiment. It was an advantage to sort the data on line in histograms since it minimized the storage volume and handling times. Modern technology today allows a maximum data throughput of about 4×10^6 events per second but in most investigations the total number of counts rarely exceeds 10^7 and it is likely that list mode will be an important way to store data in the next generation of PET systems [9].

Reconstruction algorithms

In 2D systems the predominant reconstruction method is filtered back-projection, which is fast and reliable [10]. However, since it is an approximation, it also introduces some noise in the reconstructed image. It is also difficult to enter system related parameters into the algorithms. A problem with using filtered back-projection in 3D systems is that the algorithms need full 4π data sampling, which is not available (there are holes in the 4π geometry). However, the 3D sampling is an overestimation which is easily understood, since a subset of the 2D dataset can be made which is sufficient to make a three-dimensional description of the radioactivity distribution. In theory the missing data set can be calculated from this 2D reconstruction, after which we can apply the 3D algorithms. In practice the data handling is done by using different weighting factors

for different angles. A new, elegant way to perform 3D reconstruction uses the fact that the solid angle inmost 3D PETs is fairly small. In Fourier space, an approximate method to sum projections indifferent angles can be applied. This technique is called Fourier rebinning (FORE) [11] and it accurately converts a 3D data set to a 2D data set, after which a 2D statistically-based reconstruction algorithm can be applied. It is the ordered-subset expectation-maximization algorithm (OSEM) [12]. An alternative to filtered back-projection methods is to use iterative reconstruction methods. They have several advantages: there is no reconstruction noise and the physics of the PET systems related to the measured object (geometry, scatter, etc.) can be built into the algorithms [9]. Furthermore, Bayesian methods attempt to improve the quality of the reconstructed image by taking advantage of prior knowledge, which can be obtained, for example, from a co-registered anatomical image (CT or MR)[13]. This information is known a priori and is often incorporated into a maximum a posteriori (MAP) objective function. These reconstruction methods lead to improvements of contrast and noise properties of the reconstructed PET images. This a-priori known anatomical information can be introduced into the reconstruction algorithm by using probabilistic image models or similarity measures between the anatomical and the functional images[13].

Data correction

PET can give an accurate quantification of the radioactivity distribution in Bq cm^{-3} after several corrections.

Count rate correction

The total uncorrected count rate in each coincidence channel can be written as R_{tot}. From this value is subtracted the randoms, R_{random}, to obtain the number of true coincidences either by calculations or by measuring delayed coincidences. The true coincidence rate is composed by unscattered and scattered coincidences and a formula can be derived, $R_T = (T_{tot} - R_{scatter})(1 - SF)$, where R_T is the corrected count rate and SF is the scattered fraction of coincidences [9]. Randoms are easy to correct for but the scatter fraction R_T, heavily dependent on the object's geometry and the radioactivity distribution, is more difficult to estimate. Reliable corrections (e.g., the convolution method) for scatter in 2D mode have been established, but are more difficult to apply in 3D mode. A possible improvement may be obtained in 3D by using a two-energy window, i.e. to monitor scatter just outside the coincidence energy window and then to use scatter correlation between the two sets of data [14].

Attenuation correction

Since most annihilation events are scattered and the fraction varies substantially with the path length of the photons, it is important to measure the geometry and the density variation of the object [9]. The common way to do this in PET is by performing a transmission scan where one or more linear radioactive sources are rotated around the object. The radioactive source, usually $^{68}Ge/^{68}Ga$, is also a positron emitter and the coincidence rate with and without the object gives a measure of the object thickness. Only one of the annihilation photons penetrates the object but it is easily seen that this is equivalent to the emission situation where the annihilation is detected in the same coincidence channel. It is important that the transmission scan and the emission scan represent the same geometry, i.e. that the object is not moved. Alternative ways to do attenuation correction is to combine PET and morphological techniques like CT or MRI [9]. As for the CT, the attenuation values are energy dependent. Hence, the correction factors derived from a CT scan at mean photon energy of 70keV must be scaled to the PET energy of 511 keV (typically with bilinear functions) [2]. As for the MR, there are three methods available: segmentation-based methods, atlas based methods and reconstruction based methods (for more details ref [15]).

PET in the clinical setting

The value of PET in clinical oncology has been demonstrated with studies in a variety of cancers including colorectal carcinomas, lung tumours, head and neck tumours, primary and metastatic brain tumours, breast carcinoma, lymphoma, melanoma, bone cancers, and other soft-tissue cancers [16]. PET studies of tumours can be performed for several reasons including:

1. Quantification of tumour perfusion;
2. Evaluation of tumour metabolism;
3. Tracing of radiolabeled cytostatic agents.

Despite its quantitative potential, however, in daily clinical practice, PET is used almost exclusively with 2-deoxy-2-[^{18}F] fluoro-D-glucose ([^{18}F]FDG) and, in addition, [^{18}F]FDG data are normally assessed visually or using simple indices as the standardised uptake value (SUV) [17]. Quantitative assessment is superior to visual inspection as it is less user-dependent, it can be fully automated and it allows an easier comparison between centres, thus facilitating multi-centre trials. Visual assessment is normally considered adequate for initial diagnosis and staging, whereas the comparison of (semi)quantitative indices before and after treatment might be better applied o early response assessment or interim evaluation of therapeutic efficacy [17]. When PET is used for the evaluation of the pharmacokinetic properties and efficacy of drugs, only a quantitative data analysis can provide the parameters necessary to this aim, such as peak time, clearance, area-under-the-curve (AUC) in plasma, healthy tissue and tumour [17]. Furthermore, the increasing number of available tracers will allow in the future the selection of the most appropriate according to the application (type of tumour and physiological process to be monitored). In order to properly analyse data coming from a variety of tracers having different kinetic properties, visual inspection and SUV are not sufficient.

Quantification techniques

- **SUV**

The SUV is the most widely used parameter for the analysis not only of [^{18}F] FDG but also of most tracers in oncology. The SUV is the ratio between the radiotracer concentration in a certain ROI (or group of voxels) and the injected activity, divided by a normalization factor (NF):

$$SUV = \frac{radiotracer\ concentration}{\frac{injected\ activity}{NF}} \quad 2)$$

where radiotracer concentration (e.g. kBq/ml) and injected activity (e.g. MBq) indicate, respectively, the concentration measured with PET in the region or voxels of interest and the total injected activity. In Eq. 1 the radiotracer concentration is computed by scanning the patient for a short interval (typically from 5 to 15 min) after a certain predefined time (e.g. 60 min) after tracer administration. Three normalization factors are commonly used: they are body weight (BW, e.g. kilograms), body surface area (BSA) and lean body mass (LBM). The benefit of the SUV is related to the fact that no arterial cannulation is required (the scan is less expensive and less uncomfortable for the patient) [18]. On the other hand, the SUV is significantly dependent on many different factors so that it is very difficult to compare SUVs acquired in different centres when even slight differences in the experimental procedure are present. Among the factors affecting the SUV are (a) the dependency on the time interval between injection and scanning; (b) the settings characterising image acquisition (scanner, scatter and attenuation correction, reconstruction algorithm) and (c) the algorithm through which the tumour is defined [17]. Despite its limits, however, the SUV, when computed in the same centre with the same settings, has been shown

effective in assessing the response to therapy by comparing its value in a given tumour before and after treatment, especially with [^{18}F] FDG [17].

- **Compartmental modelling**

Compartmental modelling (CM), also known as kinetic modelling, is the most accurate method to analyse PET data. In CM the PET radiotracer is assumed to be exchanged between compartments, each compartment representing a homogeneous physiological or biochemical entity, and the rates at which the tracer is transferred between compartments are described by first-order differential equations [17]. Through a numerical procedure known as non-linear least squares (NLLS), the so called rate constants (aka kinetic parameters, or micro parameters)can be estimated; these parameters can be then used to obtain physiological measures of interest, such as blood flow [19], metabolic rate of glucose [20] and receptor–ligand binding [21].
CM requires dynamic scanning (multiple frames) from the time of injection and, generally, arterial blood sampling to measure the time course of tracer concentration in plasma (time activity curve, TAC), used as input function [17].

-- **One tissue compartmental model**

This model describes the bidirectional flux of tracer between blood and tissue. In kinetic modelling, flow is generally not measured in terms of volume per time, as one might expect, but rather in terms of perfusion of tissue, which is described as volume per unit time per unit volume of tissue. Thus, the words flow and perfusion are used interchangeably in PET [22].

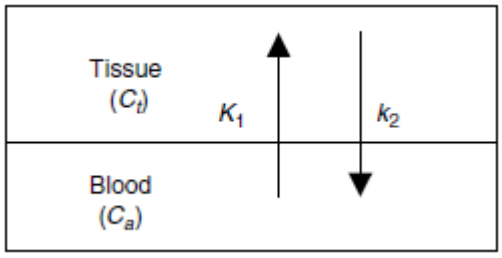

Figure 5: One tissue compartment model. It describes the bidirectional flux of tracer between the blood (C_a) and the tissue (C_t). The net tracer flux into tissue equals the flux entering the tissue (K_1C_a) minus the flux leaving the tissue (k_2C_t).

The model is characterized by the time-varying tracer concentration in tissue, $C_t(t)$, and arterial blood, $C_a(t)$ and two first-order kinetic rate constants (K_1, k_2). The tracer concentrations are measured in nano curies per millilitre (nCi/ml). Throughout the remainder of this chapter, we suppress the explicit time dependence of the concentration functions for notational simplicity. For example, $C_a(t)$ and $C_t(t)$ will be written simply as C_a and C_t. It is assumed that within each compartment (blood and tissue) the tracer is homogeneously distributed. The unidirectional tracer flux from blood to tissue is K_1C_a, and the flux from tissue to blood is k_2C_t; therefore, the net tracer flux into tissue is:

$$\frac{dC_t}{dt} = K_1C_a - k_2C_t \qquad 3)$$

This equation can be solved for C_t to obtain:

$$C_t = K_1C_a \times e^{-k_2t} \qquad 4)$$

where the symbol × denotes one-dimensional convolution. If C_a and C_t are radioactivity concentrations, then k_2, implicitly, includes a component for radioactive decay. For a PET scan, C_t is the radioactivity concentration that is measured in a given tissue region. Blood samples may be drawn during a PET scan in order to measure C_a. If the tracer distribution in a tissue region is a
d
e
q
u
a
t

$dCtdt=K1Ca-k2Ct$ 3) can be applied using standard nonlinear regression techniques to estimate the values of $K_1$and k_2 for that region [22].

K_1 is an expression of both permeability and flow. The exchange of tracer between blood and tissue occurs either via diffusion or active transport across the capillary wall. For this purpose we can apply the model in figure 4 on its smallest scale, such that the blood compartment represents a single capillary and the tissue compartment is the tissue in the immediate vicinity. Because some tracer is removed from the blood via extraction into tissue, the tracer blood concentration diminishes as it passes through the capillary [22]. K_1 is closely related to blood flow when the extraction fraction is large, but is more related to permeability when the extraction fraction is small. Accordingly, the best tracers for studying blood flow have large extraction fractions. When blood flow is expected to be higher than normal, there is an added burden on the permeability-surface area product to be high. When flow is high (provoked by the breathing of carbon dioxide), the measured K_1 of the tracer with the higher capillary permeability is better able to reflect the true flow value[22].

In the tissue, tracer will accumulate with a time course described by Eq. (3). After sufficient time the net tracer flux between compartments is zero, and the system is said to be in equilibrium. At this point the blood and tissue concentrations are constant and the ratio of these concentrations C_t /C_a is called the equilibrium volume of distribution V_D (alternatively called the distribution volume, or partition coefficient). Although V_D is a ratio of concentrations (and hence dimensionless), it is called a volume because it equals the volume of blood that contains the same activity as 1 ml of tissue. Because the net tissue flux at equilibrium is zero, V_D can be expressed as:

$$V_D = \frac{C_t}{C_a} = \frac{K_1}{k_2} \quad 5)$$

For the one-tissue model, the volume of distribution is a macroparameter equal to K_1/k_2. In general, the precise formulation of V_D in terms of the kinetic rate constants (K_1, k_2 …) depends on the particular compartmental model employed. From the physiological interpretations of K_1 (the product of blood flow and extraction) and V_D (the ratio of C_t /C_a at equilibrium), k_2 can be defined as the ratio of K_1 to V_D. In most experimental paradigms, it is easier to measure V_D than its constituent parameters, and this is often just as useful for interpreting results. A common experimental technique used to measure V_D is to deliver tracer via continuous infusion in order to maintain C_a at a constant level. Once tissue equilibrium is achieved, V_D is easily obtained from blood and tissue measurements using Eq. (5)[22].

An important application of the one-tissue model is the measurement of regional blood flow, which can be described as the volume of blood that passes through a blood vessel per unit time (e.g., ml/min) [22]. The tracer that is most commonly used to measure blood flow with PET is ^{15}O-water [23]. Because ^{15}O-water is rapidly diffusible, the tissue concentration equilibrates with the venous outflow, such that these concentrations are related by $V_D = C_t /C_v$.

-- Two tissue compartmental model – 3 rate constants

The main example of a two tissue compartmental is given by the model for the measurement of cerebral glucose with [^{18}F]FDG in a homogeneous tissue in brain, based on that of [^{14}C]DG [20].

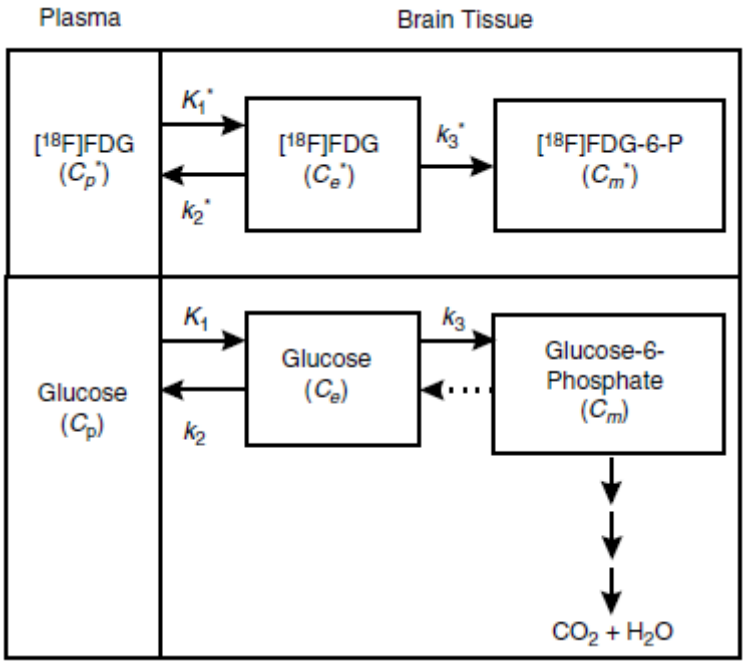

Figure 6: Model for measurement of cerebral glucose use with [^{18}F]FDG in a homogeneous tissue. Cp* and Cp represents the concentration of [^{18}F]FDG and glucose in the arterial plasma, respectively; Ce* and Ce are the concentration of [^{18}F]FDG and glucose in exchangeable pool in the tissue; Cm* and Cm are the concentrations of metabolites of [^{18}F]FDG-6-P and glucose in the tissue, respectively.

Because [^{18}F]FDG and glucose compete for the same carrier, the rate of inward transport of [^{18}F]FDG can be described by the classical Michaelis-Menten equation modified to include the influence of the competitive substrate, that is

$$v_i^*(t) = \frac{V_t^* C_p^*(t)}{K_t^*\left[1+\frac{C_p(t)}{K_t}\right]+C_p^*(t)} \qquad 6)$$

where v_i* is the velocity of inward transport; C_p^* and C_p are the concentrations of [^{18}F]FDG and glucose, respectively, in the plasma; V_t^* is the maximal velocity of [^{18}F]FDG transport; K_t^* and K_t are the apparent Michaelis-Menten constants of the carrier for [^{18}F]FDG and glucose, respectively; and t is the variable time. Because [^{18}F]FDG is administered in tracer amounts, $C_p^*(t)$ can be considered negligible compared to K_t^* [1 + $C_p(t)/K_t$]. If the glucose concentration in the plasma is constant, then the velocity of inward transport can be expressed as $K_1^* C_p^*(t)$, where $K_1^* = V_t^*/[K_t^* (1 + C_p(t)/K_t)]$ is a first-order rate constant. Once [^{18}F]FDG is in the tissue, it can either be transported back to the plasma or phosphorylated to [^{18}F]fluorodeoxyglucose-6-phosphate ([^{18}F]FDG-6-P), processes that follow Michaelis-Menten equations analogous to Eq. (6). When cerebral glucose use is in steady state, the concentration of glucose in brain (C_p) is constant and both outward transport and phosphorylation of [18F]FDG can be considered first-order processes. Thus the rate of change of the [^{18}F]FDG concentration in the exchangeable pool in the tissue can be described by the equation:

$$\frac{dC_e^*}{dt} = K_1^* C_p^*(t) - (k_2^* + k_3^*) C_e^*(t) \qquad 7)$$

where C_p^* (t) (in nCi/ml plasma) represents the concentration of [^{18}F]FDG measured in the arterial plasma t minutes after its injection into the venous blood; C_e^*(t) (in nCi/g brain tissue) is the concentration of unmetabolized tracer in the exchangeable pool in the tissue; K_1^* (in ml plasma/g brain/min) and k_2^* (in min^{-1}) represent the first order rate constants for transport of [^{18}F]FDG from plasma to tissue and back from tissue to plasma, respectively; and k_3^* (in min–1) represents the

first-order rate constant for phosphorylation of [^{18}F]FDG by hexokinase. K_1^*, k_2^*, and k_3^* are constant with respect to time, but vary regionally and with different plasma and brain concentrations of glucose [22]. The advantage of using [^{18}F]FDG rather than labelled glucose as the tracer is that the primary and secondary products of its phosphorylation, unlike those of glucose, are trapped in the tissue and accumulate where they are formed for reasonably prolonged periods of time. Therefore, the rate of change in the concentration of products of [^{18}F]FDG metabolism in the tissue, $C_m^*(t)$, is

$$\frac{dC_m^*}{dt} = k_3^* C_e^*(t) \quad 8)$$

and the total concentration of activity in the tissue, $C_i^*(t)$,is the sum of the concentrations in the precursor and product tissue pools:

$$C_i^*(t) = C_e^*(t) + C_m^*(t) \quad 9)$$

The PET scanner measures all activity in the field of view, both intra- and extravascular. Thus the total concentration of activity measured by the scanner, $C_t^*(t)$, is

$$C_i^*(t) = (1 - V_B)C_i^*(t) + V_B C_B^*(t) \quad 10)$$

where V_B is the fraction of the measured volume occupied by blood ($0 \leq V_B \leq 1$) and $C_B^*(t)$ is the concentration of label in whole blood. In the human, brain–blood volumes in grey and white matter are about 4 and 2%, respectively [24].The kinetic model for glucose uptake and metabolism in the tissue is equivalent to that of [^{18}F]FDG, except thatglucose-6-phosphate is not trapped in the tissue but continues down the glycolytic pathway eventually to CO_2 and H_2O[22].
This model allows to calculate the fractional uptake of [^{18}F]FDG [25]:

$$K = \frac{K_1 k_3}{k_2 + k_3} \quad 11)$$

Once K is known, one can then calculate the local metabolic rate of glucose by assuming a value for the lumped constant LC and by using the steady-state glucose concentration in plasma. The model was identified from [^{18}F]FDG brain data, using the measured (assumed error-free) plasma time activity curve as forcing function.

$$C_b(t) = C_p(t)(1 - 0.9H) \quad 12)$$

where H is the subject's measured haematocrit (the assumption is made that H in the capillaries equals that of the large vessels) [27].

- **Three compartmental model – four rate constants**

In 1979, Phelps et al. [24] proposed a modification of the model of [^{18}F]FDG kinetics using the observation that, following a pulse of [^{18}F]FDG, total tissue activity was observed to decline after 120 min, thus, indicating a loss of product.

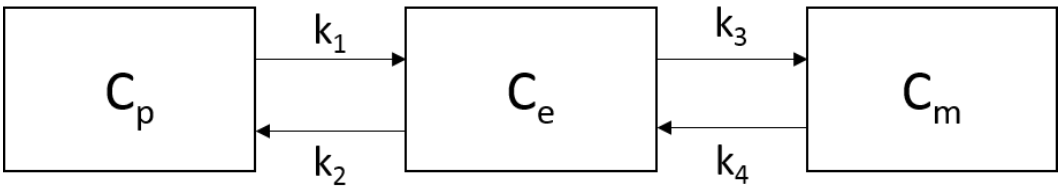

Figure 7: Three compartment – four rate constant model.

This model does not require that [^{18}F]FDG-6-P is irreversibly trapped in tissue for the whole duration of the experiment, but that it can be dephosphorylated. The model and input–output experiment equations are:

$$\frac{dC_e(t)}{dt} = k_1 C_p(t) - (k_2 + k_3) C_e(t) + k_4 C_m(t)$$
$$\frac{dC_m(t)}{dt} = k_3 C_e(t) - k_4 C_m(t) \qquad 13)$$

where k_1,k_2,k_3 and k_4 are rate constants, $C_p(t)$ is the concentration of [^{18}F]FDG in plasma, $C_e(t)$ is the concentration of [18F]FDG in tissue, and $C_m(t)$ is the concentration of [^{18}F]FDG-6-P in tissue. The PET tissue measurement equations were the same as those of the precious model. Like for the 3K model, the fractional uptake of [^{18}F]FDG is given by equation ($K = \frac{K_1 k_3}{k_2 + k_3}$ 11). All model parameters are a priori uniquely identifiable [28].

There's potentially a huge gain from including kinetic parameters in the diagnosis, staging, treatment planning, treatment monitoring and follow up of cancerous tumours. Many examples in the literature show the ability of pharmacokinetic parameters to differentiate between different lesions, to help in the diagnosis and in treatment response evaluation.
Schiepers et al.[29] showed that compartment modelling of ^{18}F-FLT PET produced a k_3 parameter that could differentiate lesions that were tumour predominant and treatment change predominant in patients with glioma and brain metastases. In another glioma ^{18}F-FLT study by Schiepers et al.[30], they found that some parameters, especially K_i, changed during the course of treatment and that changes were correlated to overall survival. Wardak et al.[31] found that the ratios of k_2, k_4, as well as the volume of distribution $V_d = K_1/(k_2 + k_3)$, before and after glioma brain tumour chemotherapy treatment could predict overall patient survival for ^{18}F-FLT. Muzi et al.[32] also looked at ^{18}F-FLT in glioma patients, and found that the influx rate constant K_{FLT} (denoted K_i in this thesis) and k_3 successfully distinguished recurrence from radionecrosis. Sugawara et al.[33] monitored patients with germ cell tumours using ^{18}F-FDG PET, and compared SUVs and 2-tissue compartment model parameters before and after chemotherapy. The authors concluded that although visual inspection or SUV calculations could differentiate viable tumours from mature teratomas and necrotic/scar tissue, these metrics did not manage the finer differentiation between mature teratomas and necrotic/scar tissue. Parametric images of the influx rate constant K_i had better contrast compared to SUV images, and parameters K_i and K_1 did manage to separate teratomas from necrosis or scar. Upon studying patients with primary central nervous system (CNS) lymphoma, Nishiyama et al.[34] found that kinetic analysis of ^{18}F-FDG, especially with respect to k_3, was helpful for diagnosis and treatment response evaluation. Doot et al.[35] concluded that kinetic parameters of the transport (K_1) and flux (K_i) of ^{18}F-fluoride was found useful for evaluating treatment response in breast cancer bone metastases, which is hard for conventional CT and MRI techniques.

- **Graphical methods**

Patlak and Logan plots are graphical analysis methods based on compartmental models. They approximate the behaviour of the tracer with two compartments: a "central" compartment, which is in rapid equilibrium with the plasma, and a "peripheral" one, where, in case of an irreversible kinetics, the net irreversible transfer of the tracer from blood to the tissue at steady state is measured [36]. This method transforms the model equations into a linear equation evaluated at multiple time points and provides fewer parameters (i.e., slope and intercept). In details, Patlak plot involves irreversible tracers while Logan plot involves reversible ones.

-- Patlak method

It assumes the presence of an irreversible compartment and a time t* after which all the reversible compartments are in equilibrium with the plasma. K_i is the unique parameter this method provides. It denotes the so-called irreversible uptake rate constant, which quantifies the rate at which the tracer is irreversibly trapped**.** The Patlak plot is given by the linearization of this expression and K_i is simply calculated as the slope of the regression line [37,38]:

$$\frac{C_{tissue}(t)}{C_p(t)} = K_i \frac{\int_0^t C_p(\tau)d\tau}{C_p(t)} + V \qquad 14)$$

The plot in Figure 8 shows an example of the Patlak graphical method applied for the analysis of an irreversible radiotracer. In particular, after a time t* = 1300 sec, the system is in equilibrium and the relationship between C_{tissue}/C_{plasma} and $\int C_{plasma}/C_{plasma}$ is linear with a K_i slope value.

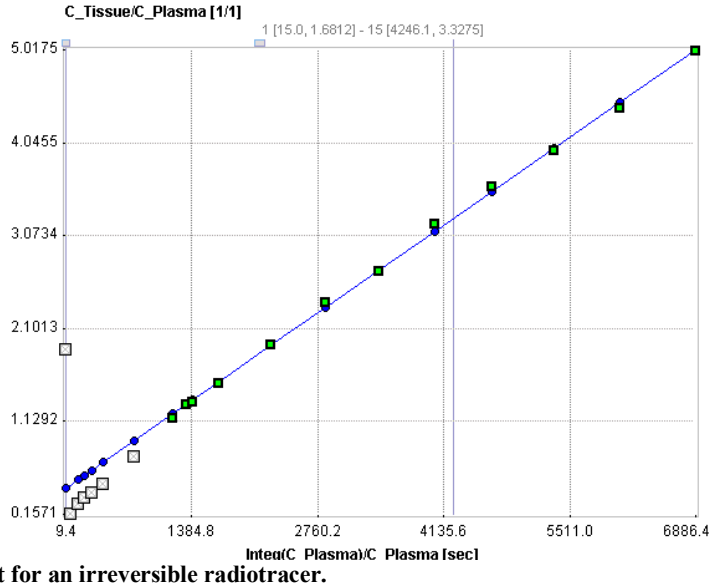

Figure 8: Patlak plot for an irreversible radiotracer.

-- **Logan method**

The Logan plot is the counterpart of the Patlak plot for reversible radiotracers. It involves the linearization of this expression stating that after a time t* the system is in equilibrium:

$$\frac{\int_0^t C_{tissue}(\tau)d\tau}{C_{tissue}(t)} = V_T \frac{\int_0^t C_p(\tau)d\tau}{C_{tissue}(t)} \qquad 15)$$

V_T is the unique parameter provided and it is the distribution volume of the tracer in the tissue. It is a measure of the overall uptake of the tracer relative to the plasma compartment [39].

The plot in Figure 9 shows an example of the Logan graphical method applied for the analysis of a reversible radiotracer. In particular, after a time t* = 900 sec, the system is in equilibrium and the relationship between $\int C_{tissue}/C_{tissue}$ and $\int C_{plasma}/C_{tissue}$ is linear with a V_T slope value.

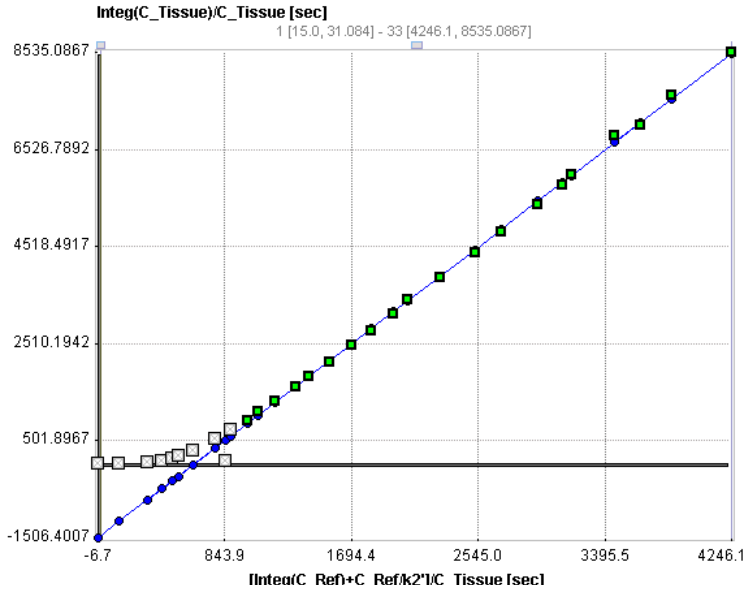

Figure 9: Logan plot for a reversible radiotracer.

- **Spectral analysis**

The spectral analysis method, introduced by Cunningham and Jones, allows the identification of the kinetic components of the tissue tracer activity without specific model assumptions. It considers the impulse response function (IRF) of the compartmental models used in PET as an analytical sum of exponentials. The tissue tracer activity in a given volume of observation at time t, $C_{tissue}(t)$, is then given by the convolution of the plasma time activity curve, $C_p(t)$, with the IRF:

$$C_{tissue}(t) = \sum_{j=0}^{M} C_p(t) \times \alpha_j e^{-b_j t} \qquad 16)$$

where α_j and b_j are assumed to be real values and nonnegative.

The idea is to fix a grid of $b_j$values that covers an appropriate spectral range and then estimate their associated amplitudes α_j, which are the spectral contents. Only a few values of $\alpha_j > 0$ are detected and they constitute the spectrum of the kinetic components of the tracer. The components of the spectrum have different meaning depending on their position in the spectrum, hence on their correspondent b_j value. Components with very large b_j are proportional to $C_p(t)$ and are seen as high frequency components, while components corresponding to $b_j = 0$ become

proportional to $\int C_p(\tau)d\tau$ and are seen as low frequency components. In other words, they account for a slower kinetic, for the trapping of the tracer in the tissue (irreversible trapping). Lastly, the components with intermediate b_j values are referred to as the equilibrating components and their number corresponds to the number of tissue compartments that exchange material with the plasma (Figure 10).

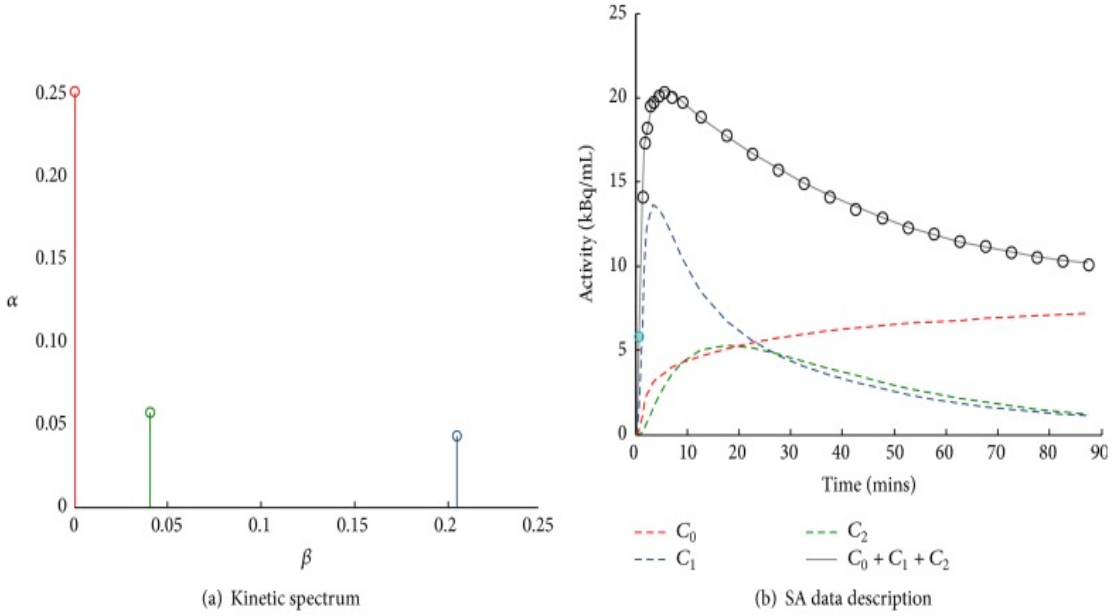

Figure 10: Example of spectral analysis quantification. (a) Representative kinetic spectrum: out of the three spectral components reported, one corresponds to the tracer trapping (red) while the remaining ones refer to two equilibrating components at different frequencies (green and blue). (b) In this example the measured tracer activity (open circles) is described by the sum of the time-activity curves of each individual component of the spectrum (red, green, and blue dashed lines) resulting in the SA data model prediction (grey line). It is important to note that different positions of the components in the spectrum correspond to different shapes of time-activity curves, with the wash-out being slower for low-frequency spectral components and faster for the high-frequency ones [34].

The information given by the spectrum allow the estimation of some macro parameters of interest. They are: the influx rate constant [mL/cm^3/min] $K_1 = \sum_{j=0}^{M} \alpha_j$; the net uptake of the tracer in the tissue [mL/cm^3/min], that, for irreversible tracers, can be derived by the limit of the IRF→ ∞, $K_i = \lim_{n\to\infty} IRF(t) = \alpha_0$, and the volume of distribution [mL/cm^3], that, for reversible tracers, can be derived as the integral of IRF, $V_T = \int_0^\infty IRF(\tau)d\tau$ [40].

The standard approach for the quantification of dynamic PET studies is represented by compartmental modelling, which requires the full mathematical description of the system under investigation [41]. It is the only method able to provide a detailed understanding of the physiological system and it is usually adopted when the compartmental structure of the system is known [42]. Graphical plots are easy to implement and give a fast solution. On the other hand, these methods are affected by several limitations: they allow the estimation of a unique macroparameter but they cannot characterize the whole kinetic profile as they rely on the assumption that the system is in equilibrium [42]. Furthermore, they don't account for a vascular component of the signal and finally, the linearization required by this model may distort the noise level of small resolution images [43].

A trade-off between CM and graphical methods is given by the spectral analysis which can be applied without any specific model configuration [42]. It is applicable only to single-input, noncyclic systems (and the majority of compartmental models use the same assumptions) (Figure 11).

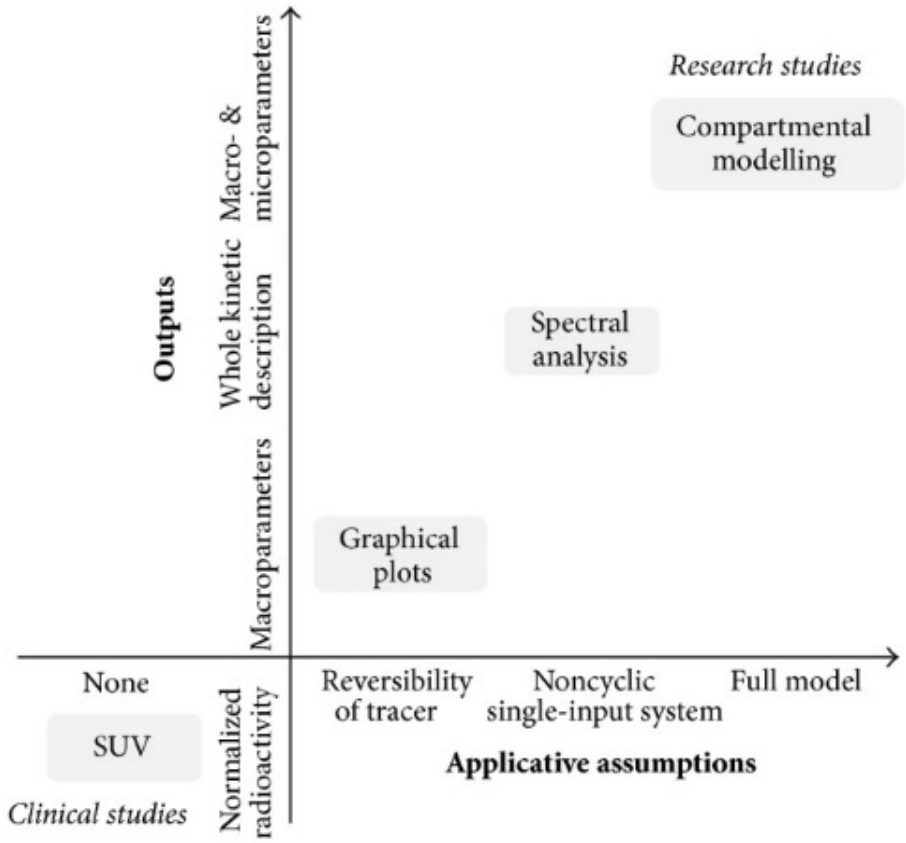

Figure 11: Quantification in Positron Emission Tomography. The figure shows a schematic summary of the major PET quantification methods organized by considering for each approach the information returned as function of the application requirements. Clinical and research PET imaging studies are separately reported. Within the diagram a diagonal distribution of the methodologies is clearly evident, indicating that more information is obtainable only at the cost of more modelling assumptions [34].

Applications

My work involved the kinetic analysis of ^{18}F-FDG, ^{18}F-FLT, ^{18}F-D4-Choline in breast and lung cancers. Graphical, spectral and compartmental modelling techniques have been implemented for these studies. In the next section I will present the results of the first kinetic analysis of D4-Choline in lung cancer patients; then I will present the combined study of FDG and FLT for the early detection of DCIS.

I. Kinetic analysis of D4-Choline in patients with lung cancer

1. Introduction

Choline is the precursor for the biosynthesis of phosphatidylcholine, a key component of the cell membrane phospholipids. It is transported intracellularly and phosphorylated by the enzyme choline chinase (ChKα) to phosphocholine and it is trapped within the cell. Most types of cancer are characterized by increased choline transport and by the overexpression of choline kinase in highly proliferating cells in response to enhanced demand of phosphatidylcholine [44-47]. In particular, this has been reported in prostate, breast, lung, ovarian and colon cancers [48-51]. ^{11}C-choline has been widely used to study metabolic activity in vivo but its short physical half-life (20.4 min) is disadvantageous for its routine clinical use. The longer half-life of ^{18}F (109.8 min) overcomes this limitation allowing also late imaging of tumours when sufficient clearance of the parent tracer in systemic circulation occurs. ^{18}F-fluoromethylcholine (^{18}F-FCH) was developed, for the first time in 2001, by DeGrado et al. [52] and has never presented any adverse effect on patients [53-55]. However, at present, another fluoro-analog choline tracer has been introduced. It is the more metabolically stable ^{18}F-fluoromethyl-[1, 2-$^{2}H_4$]-choline (^{18}F-D4-FCH or simply ^{18}F-D4-Choline) which has been preclinically validated for tumour imaging [56-58] and presented encouraging biodistribution results in healthy volunteers [59].
To our knowledge, we present the first study of ^{18}F-D4-Choline dynamic PET performed on patients affected by lung cancer. Kinetic analysis is generally carried out at the region of interest (ROI) level as it guarantees accurate results (reduced noise of the regional data) in a minimal computational time. On the other hand, biological systems, and in particular cancer tissues, are complex and heterogeneous and need to be analysed at the voxel level. In this work, we chose to perform the spectral analysis (SA) method developed by Cunningham and Jones in 1993 [40] because it can be applied to both homogeneous and heterogeneous tissues with no previous hypothesis related to the number of compartments in the tissue. We started with a ROI level analysis to look at the components of the spectrum resulted from the SA. We then compared the main voxel-wise quantification methods (spectral and graphical) applied to ^{18}F-D4-Choline PET data in lesion, vertebra, node and reference area.

2. Materials and methods

2.1 Patient population

Eleven patients (age 62.5 ± 6.5) with 11 primary tumours (7 squamous carcinomas and 4 adenocarcinomas) and 6 hilar nodes were included (Table 5). All patients fulfilled the inclusion criteria and provided written informed consent. Patient characteristics and primary treatment modalities are shown (Table 5). The mean age and weight ± SD were 64 ± 11y (range 39-84 y) and 68.9 ± 15kg (range 49.7-93.3 kg), respectively.
Patients eligible for surgery underwent either a lobectomy or pneumonectomy or wedge resection with hilar and mediastinal lymph node sampling or en bloc resection. Primary chemotherapy

consisted of combination chemotherapy with platinum (gemcitabine and cisplatin or carboplatin, pemetrexed and cisplatin). Other treatment options included radical radiotherapy, chemoradiotherapy, and palliative high–dose radiotherapy. Decision regarding treatment was made by the attending clinician as per local hospital policy.

Table 5: Patient population and histology. SqCC, squamous cell carcinoma; Adenoca, adenocarcinoma.

Patients	Sex	Age	Weight	TNM	Histology	Lesion
Pt. 1	F	60	55.2	T4N1M0	SqCC	Primary tumour, hilar node
Pt. 2	M	60	72.4	T2bN0M0	SqCC	Primary tumour, hilar node
Pt. 3	F	57	54.4	T1bN1M0	SqCC	Primary tumour, hilar node
Pt.4	M	59	68.5	T4N1M0	SqCC	Primary tumour, hilar node
Pt. 5	M	79	69.5		SqCC	Primary tumour
Pt. 6	F	58	64.8	pT1bN1M0	SqCC	Primary tumour
Pt. 7	F	64	49.7		Adenoca	Primary tumour, hilar node
Pt. 8	M	67	83	T1bN0M0	Adenoca	Primary tumour
Pt. 9	M				Adenoca	Primary tumour, hilar node
Pt. 10	M			T3N1MX	SqCC	Primary tumour
Pt. 11	F	59	49.5		Adenoca	Primary tumour

2.2 ^{18}F -D4-FCH PET imaging

[^{18}F]D4-FCH was synthesised from the precursor as described by Smith, G et al, 2011. Patients underwent routine standard imaging with CECT of chest and upper abdomen for local staging, additionally followed by an [^{18}F]FDG PET/CT for lymph node staging and a bone scan if indicated. [^{18}F]D4-FCH PET/CT was performed post routine standard investigations and prior to any therapy. Images were acquired on a Siemens Biograph 6 TruePoint PET/CT scanner (with TrueV; extended field of view) with 21.6-cm axial and 60.5-cm transaxial fields of view. An attenuation CT scan over the thorax (130 kV, exposure, exposure, 15 effective mAs; pitch, 1.5; slice thickness, 5 mm; rotation time, 0.6 s; resulting in an effective dose of 2.5 mSv) was performed for accurate anatomical localisation. This was then followed by tracer injection (a maximum dose of 370MBq of [^{18}F]D4-FCH) and dynamic imaging (single-bed position over thorax and mediastinum) over 66 mins followed by a half-body static (mid-thigh to vertex) attenuation CT and PET scan. Discrete venous bloods and plasma (at 5, 10, 15, 30, 60, p.i) were obtained for radioactivity counting and metabolite analysis.

All Dynamic [^{18}F]D4-FCH PET/CT data were reconstructed using the ordered-subsets expectation maximization algorithm (3 iterations and 21 subsets) with corrections for dead time, scatter, attenuation, and radioactive decay. All volumes of interest (VOIs) on PET/CT were outlined manually on Hermes (Hermes Diagnostics, Stockholm, Sweden) by a single investigator (SD) to avoid any interobserver variation. VOIs were drawn manually around visible primary lung tumour, and any mediastinal lymph nodes by a single investigator (SD) to avoid any interobserver variation. Whole tumour volumes were outlined. VOIs were also drawn in normal background organs using a 2cm fixed-sphere (normal lung tissue, bone (vertebral body), and muscle) and 1cm in the aorta for the use of an image derived arterial imput function[60].

2.3 Quantification of dynamic D4-choline data

Dynamic PET data has been analysed with Spectral Analysis and graphical methods as described in *Chapter 2, Quantification techniques*. We decided to apply both Patlak and Logan graphical methods since the kinetic of the tracer has not been analysed in the present literature yet.

2.4 Statistical analysis

All statistical analysis were performed using Matlab R2015b (Mathworks). The tests chosen were: the Kolmogorov - Smirnov test, to assess the normal distribution of each parameter distribution; the Wilcoxon Sum Rank test, to assess the statistically significant differences among tumour, healthy lung tissue, node and vertebra; the non-parametric Spearman test to verify the correlation between parameters evaluated with different modelling approaches. For each map, kurtosis and skewness were also evaluated for a distribution analysis [61].

2.5 Reliability analysis

Method performance was assessed in terms of reliability of the estimates. It was evaluated, for each maps, in terms of the fraction of voxel estimates associated with biologically implausible results. In details, for K_i and K_1 maps, values < 0 and > 1.5 $\mathrm{mL}/cm^3/\mathrm{min}$ were considered biologically implausible while for the V_T only negative values [62,63].

3. Results

All of the patients had measurable disease in the lung. Six of them presented also small hilar nodes. The mean dose of activity injected was 283.95 (±77.92) MBq. D4-Choline localized mainly in tumour, node and vertebra (Figure 12). Localization of radioactivity in normal tissue was generally low.

The analysis has been conducted at a region and voxel level to look both at the spectrum and the 3D parametric maps. Finally, by considering mean, kurtosis and skewness values of the K_i (Patlak), K_i (SA), K_1(SA) and V_T (Logan) estimates for the VOI voxels (tumour, healthy lung, node and vertebra), several comparisons were made within patients and among models.

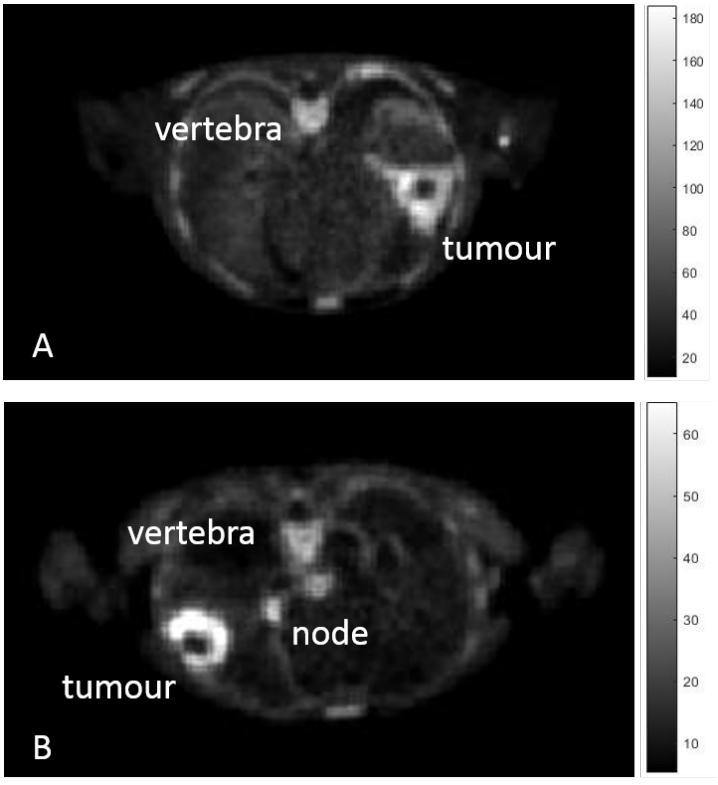

Figure 12: Axial section of summed (last six phases) PET imaging data of patient n.6 (A) and patient n.3 (B) showing high uptake of D4-Choline in tumour, node and vertebra.

3.1 Region level analysis

The spectral analysis was conducted for each patient choosing a grid of 100 components with $0.0001<b_j>1$ (the values of the grid are arbitrarily chosen, they must be included in the $[1/3T_f; 1/T_i/3]$ range where T_f is the end time of the experiment and T_i is the duration of the first scan [27,64]. Six patients presented an $\alpha_0$value (correspondent to $b_j = 0$), revealing an irreversible trapping of the tracer in the tissue during the experimental scan (Figure 13, D). The fractional retention uptake was evaluated as the ratio of the IRF at 60 minutes and at baseline. The spectral model showed that there was a retention component in the tumour but less so in normal lung and vertebra (Figure 14). The mean fractional retention of the node is comparable to the tumour one.

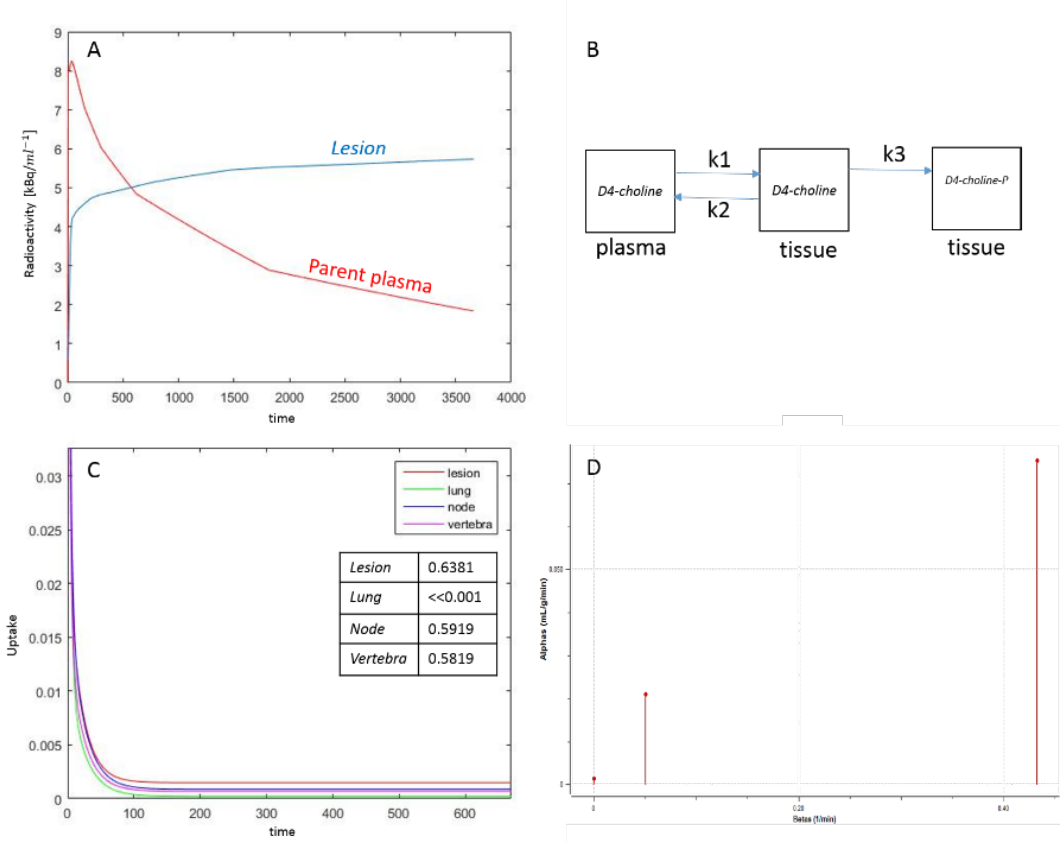

Figure 13: Patient n. 2. A, tumour time activity curve with a parent plasma input function (i.e. activity due to d4-choline); B, compartmental model used to describe the exchange of D4-choline from the plasma into the tissue; C, the unit impulse response function of tumour compared with normal lung, node and vertebra (a zoomed part) (in the tab the values of the FRTs); D, spectrum of kinetic components obtained using spectral analysis.

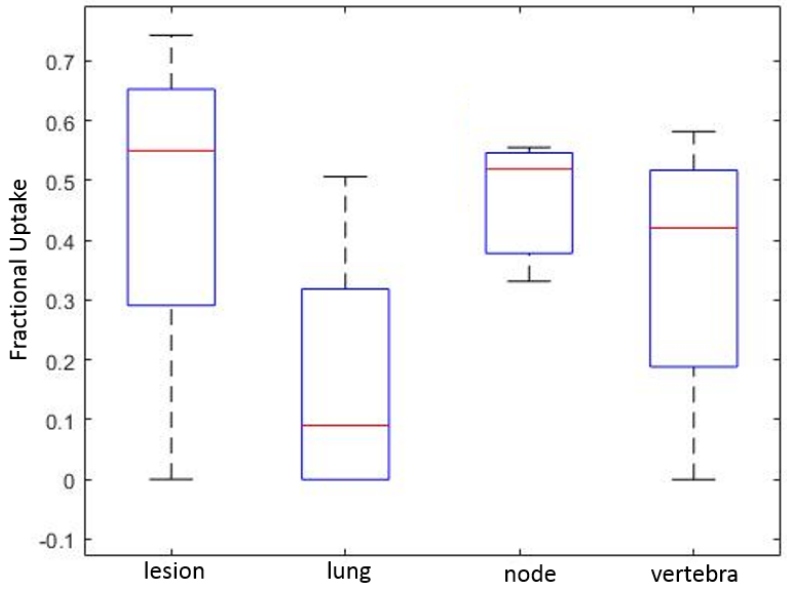

Figure 14: Fractional uptake boxplots show the highest retention component in tumour (and in the node). Less retention has been seen in the reference lung and in the vertebra.

3.2 Voxel level analysis

Spectral analysis. As for the region level, spectral analysis was conducted for each patient choosing a grid of 100 components with $0.0001<b_j>1$. It was made on a voxel level allowing the calculation of 3D parametric maps of the tumour, the reference area, the node and the vertebra. In particular, the influx rate constant [mL/cm^3/min] $K_1 = \sum_{j=0}^{M} \alpha_j$, and the $K_i = \lim_{n\to\infty} IRF(t) = \alpha_0$, that represent only the trapping component of the tumour, were evaluated. Mean values (± standard deviation) are: for the tumour, K_1= 0.82 ± 0.91 and K_i = 0.053 ± 0.091; for the reference tissue, K_1= 0.066 ± 0.062 and K_i = 0.0022 ± 0.0020; for the node, K_1= 0.85 ± 0.95 and K_i = 0.014 ± 0.0081; for the vertebra, K_1= 0.094 ± 0.11 and K_i = 0.0045 ± 0.0040. Bearing in mind that Spectral K_i maps do not cover the entire volume of the tumour (as the Patlak K_i does) and mean (as kurtosis and skewness) values resulted only by the trapping component of the tissue.

Graphical analysis. Patlak and Logan methods have been applied on tumour, reference lung tissue, node and vertebra VOI and resulted in 3D parametric maps of the irreversible uptake rate constant K_i and the distribution volume of the tracer in the tissue, V_T. The value of t* was set to 40 min after a visual inspection of Patlak (and Logan) plots. Mean values (± standard deviation) are: for the tumour, K_i = 0.021 ± 0.010 and V_T= 2.44 ± 1.46; for the healthy lung, K_i= 0.0045 ± 0.018 and V_T= 0.43 ± 0.31; for the node K_i= 0.011 ± 0.018 and V_T= 1.26 ± 0.92; for the vertebra K_i = 0.0089 ± 0.012 and V_T= 0.63 ± 0.50.

In Figure 15 an example of the evaluated 3D parametric maps in the lesion of patient n. 9.

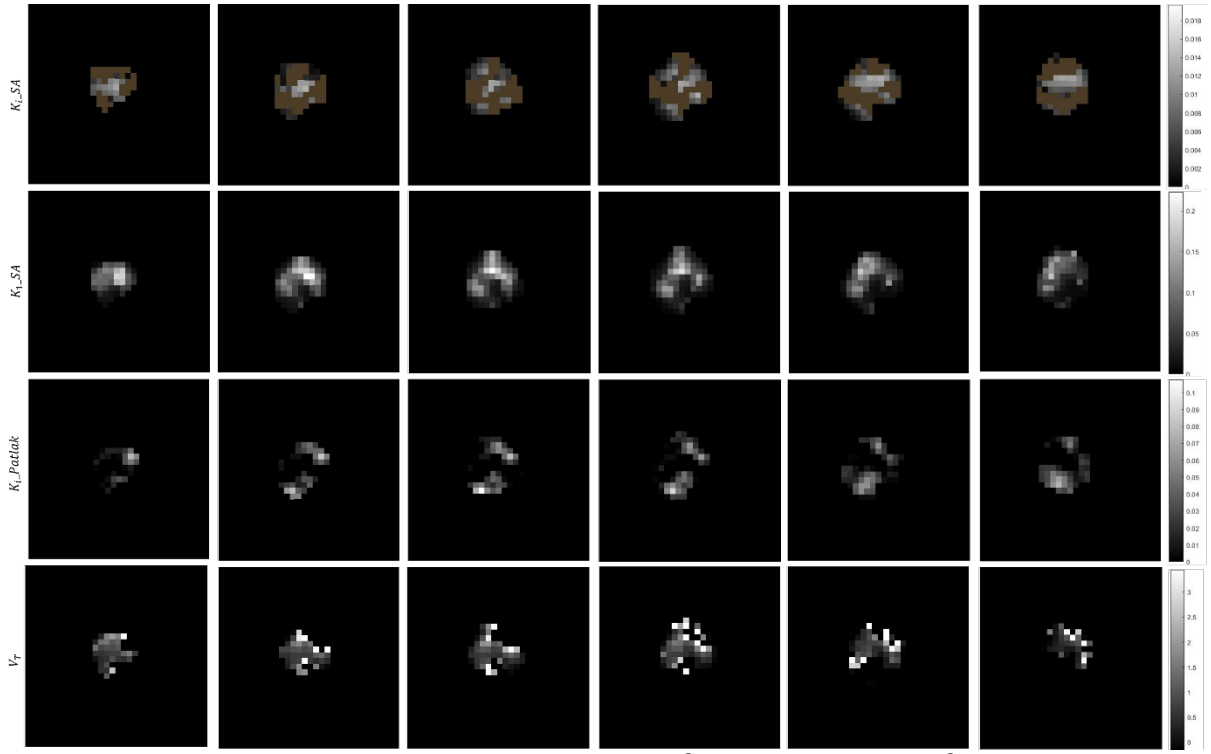

Figure 15 Patient n. 9. Parametric maps for K_i_SA [mL/cm^3/min], K_1_SA [mL/cm^3/min], K_i_Patlak [mL/cm^3/min] and V_T [mL/cm^3].

Statistical analysis. The Wilcoxon rank sum test resulted, for each map, with a good discrimination between tumour and healthy lung tissue ($p < 0.01$). In the same way, the discrimination between tumour and vertebral tissue was found statistically significant: K_1 ($p < 0.01$); K_i_SA ($p < 0.01$); K_i_Patlak ($p < 0.05$); V_T ($p < 0.01$) (Figure 16).

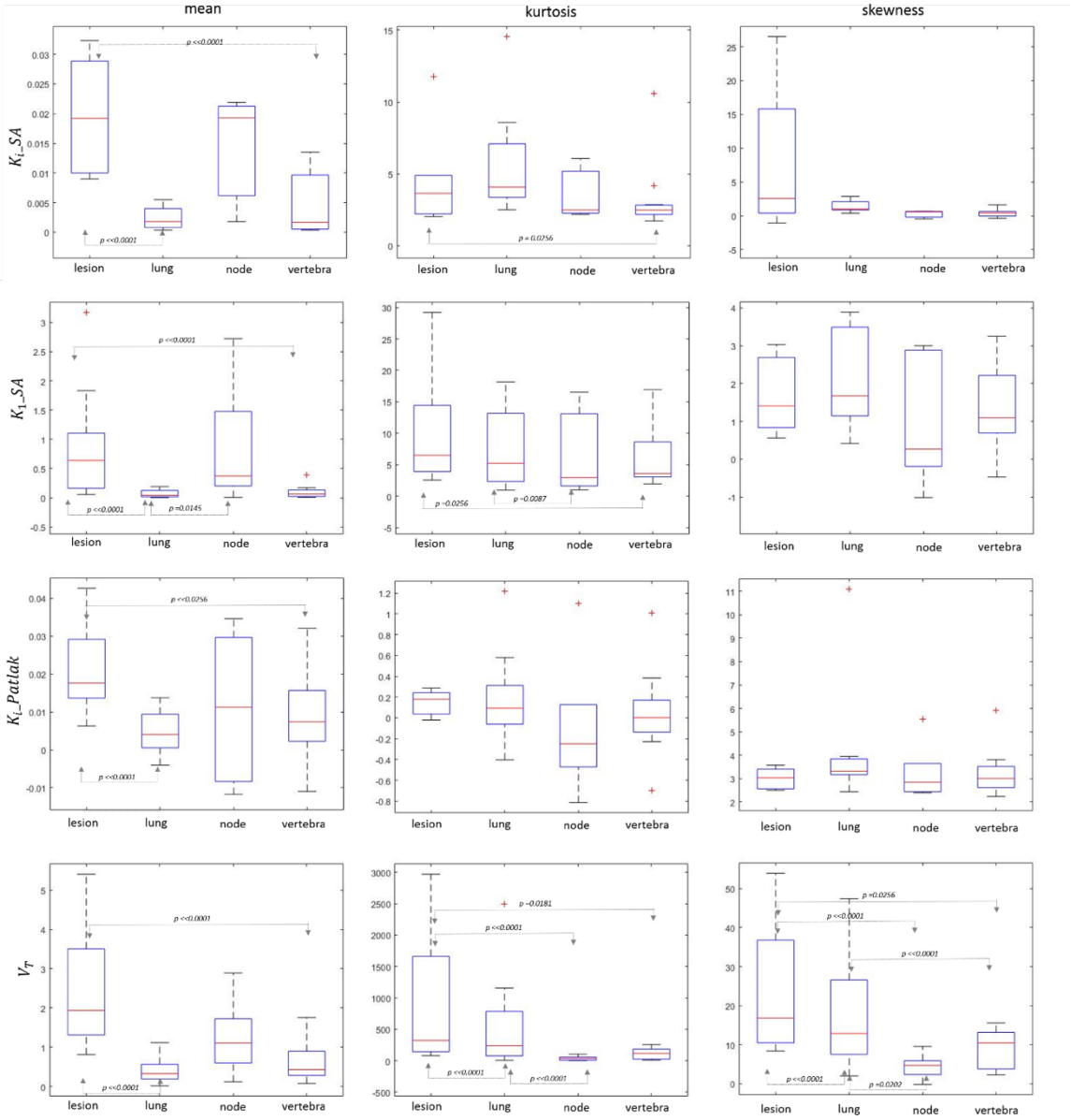

Figure 16: Boxplots of mean, kurtosis and skewness values (in columns) evaluated for each patient and for each modelling approach (in rows). Arrows point at the statistical differences resulted from the Wilcoxon test.

The Spearman test found a good correlation in the tumour between K_i of the spectral and Patlak analysis (p = 0.013, ρ = 0.74), and between K_1 and K_i_Patlak (p = 0.013, ρ = 0.74).
The distribution analysis was performed for each patient and for each modelling approach on the tumour, reference, nodular and vertebral area. In particular, in most of the analysed cases, the voxel distribution profiles were non-Gaussian. Hence, they have been modelled with the Kernel function (on the y axes, the square root of the number of elements of the input data) (Figure 17, Figure 18).

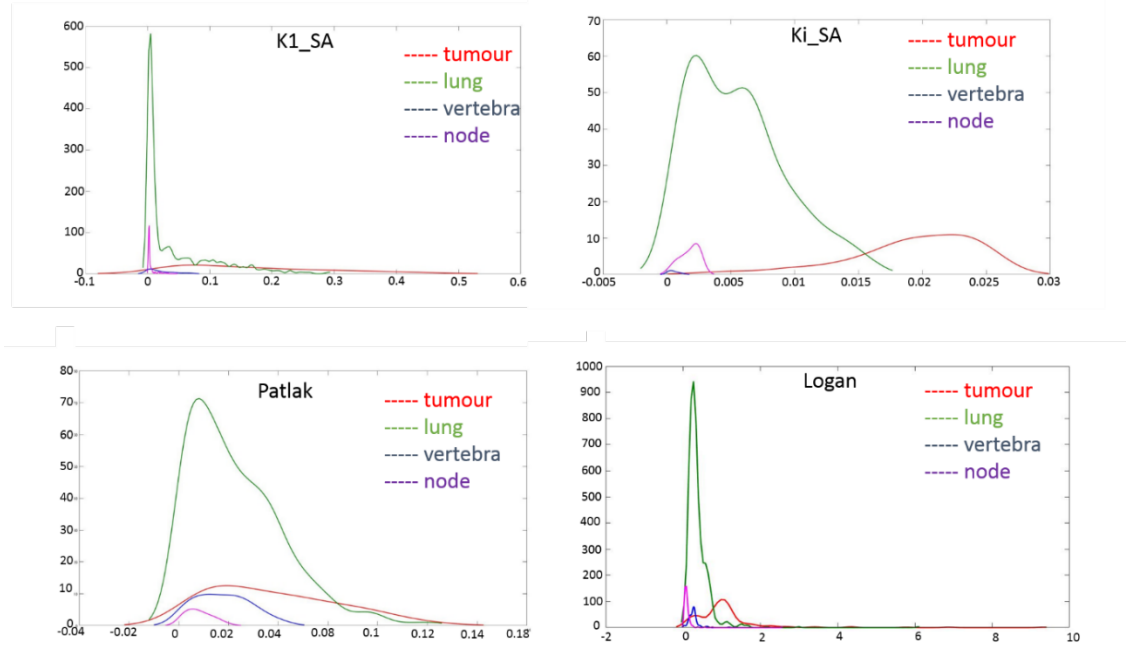

Figure 17: Patient 10. Tumour, reference lung tissue, node and vertebra Kernel distribution. On the y axes, the square root of the number of elements of the selected parameter.

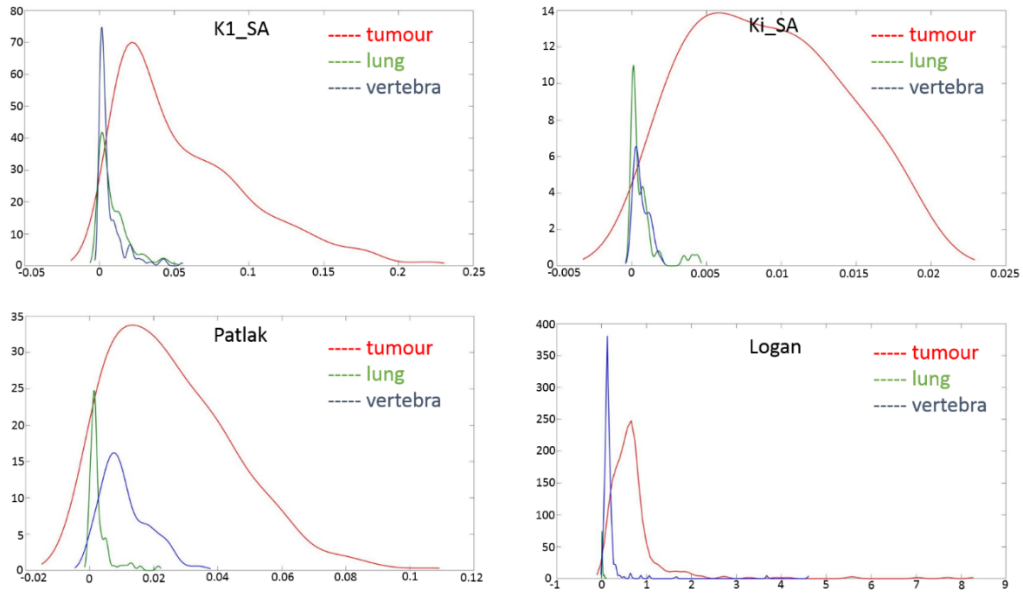

Figure 18: Distribution analysis of patient n. 9. Tumour, reference lung tissue and vertebra Kernel distribution. On the y axes, the square root of the number of elements of the selected parameter.

Reliability analysis. Among the kinetic modelling approaches, the worst performance was obtained with the Patlak analysis (reliability in the tumour 65.26%, in the reference lung 54.44 %, in the node 61.29%, in the vertebra 59.48%) while the best performance was obtained with the Logan method (reliability in tumour 90.46%, in the reference tissue 95.68%, in the node 93.45%, in the vertebra 94.32%) followed by the spectral analysis, in particular in the evaluation of the K_i maps (reliability in the tumour 99.91%, in the lung, node and vertebra 100%). All the results are shown in Table 6.

Table 6: Reliability evaluated as the percentage of biologically plausible voxel values. K_i_SA is the parametric map of the irreversible trapping component of the tissue [mL/cm^3/min], K_1_SA is the global influx rate constant [mL/ cm^3/min], **K_i _Patlak is the irreversible uptake rate constant** [mL/cm^3/min] **and V_T [mL/ cm^3] is the Logan distribution volume of the tracer in the tissue.**

Reliability (%)	tumour	healthy lung	node	vertebra
K_i_SA	99.91	100	100	100
K_1_SA	85.60	76.17	83.21	85.95
K_i_Patlak	65.26	54.44	61.29	59.48
V_T	90.46	95.68	93.45	94.32

4. Discussion

This study focused on the pharmacokinetic analysis of ^{18}F-fluoromethyl-[1, 2- $^{2}H_4$]-choline in lung cancers. Different quantification methods have been applied and compared together with the evaluation of the reliability of their estimation. Choline is the precursor for the biosynthesis of phospholipids, which are the main component of the cellular membrane. The accumulation of radiolabeled choline in tumours is associated with cellular proliferation as it is due to the overexpression of choline kinase in support of malignancy-induced increased demand for cellular membrane synthesis [65]. Compared with ^{18}F-FDG, whose uptake has been reported to be influenced by several factors, as the upregulation of glucose transporter 1 receptors [66], the number of viable tumour cells [67], microvessel density, or hexokinase expression [68], radiolabeled choline is a more selective tracer and it is not trapped in the whole tumour tissue. Figure 12 shows ^{18}F-D4-FCH summed PET images where high tumour to background contrast is present. In fact, choline kinase is up-regulated by overexpression in human lung carcinomas [69]. Uptake was also seen in the node and vertebra. The retention of the tracer was firstly studied at the *region level* with the application of the standard spectral analysis. It allows the measurement of both the impulse response function and the spectral components of the tracer in the tissue. In Figure 13 ROI analysis results, which confirmed that D4-Choline is delivered and retained to a higher degree by lung tumours (as by node and vertebra) compared with normal tissue. Furthermore, the spectrum showed, in most cases, the presence of an irreversible trapping component of the tracer in the tissue during the time of measurements (8/11 patients).

In order to have a more exhaustive physiological characterization of tumour tissues that considers the complexity and the variability of the kinetics, a voxel wise analysis was necessary. In fact, the simplified average description obtained by ROI analysis alone cannot provide a fair description of tumour heterogeneity. The *voxel level* spectral analysis resulted in two different parametric maps: K_i, that shows only the irreversible trapping part of the tissue in the whole tumour volume (Figure 15, first row), and K_1, that is the net influx rate constant (Figure 15, second row). K_i map testified that a part of the tumour tissue actually traps the tracer during the measurement time and that the trapping areas have not a preferential location (grey voxels). Reference lung tissue, node and vertebra also presented a small trapping component that K_i was able to differentiate from the lesion ($p << 0.0001$) (Figure 16). K_1 is a global parameter resulted by the sum of all the αs of the spectrum. So it is the expression of the utter kinetics of the tracer in the tissue. It was able to provide a good discrimination between lesion and reference lung ($p << 0.0001$), as between lesion and vertebra ($p << 0.0145$), and finally between healthy lung and node ($p << 0.0001$) (Figure 16). Graphical methods resulted with the Patlak K_i and the Logan V_T maps (Figure 15, last two rows) which also provided a good discrimination between tumour and reference tissue ($p < 0.05$). The rationale of applying both graphical methods is explained by the fact that the kinetic behaviour of the tracer is not known. In fact, the heterogeneous nature of the lesions presented in the study could show a different behaviour of the tracer in different areas of the tumour.

In terms of percentage of outliers in the estimated maps, the Logan method resulted the most reliable one for the lowest number of biologically implausible values detected (93.48 ± 2.20 %), immediately followed by spectral analysis (91.36 ± 9.68 %). Spearman test resulted with a good

correlation between the rate constants evaluated with these two different methods ($p = 0.013$, $\rho = 0.74$) with the SA K_i showing the best reliability. This could be due to the fact that SA K_i covers a limited part of the tumour volume since it shows only a particular kinetic behaviour of the tracer in the tissue (irreversible trapping). Patlak and Logan based parametric maps showed an interesting complementarity (Figure 15, last two rows) as these two methods describe, respectively, the irreversible and reversible behaviour of a tracer.

Perfusion maps show the presence, in tumour tissue, of lower activity spots, possibly due to hypoxia. Metabolism of choline in cancer cells is known to be sensitive to its microenvironment. Tracer studies in the mouse atrial cardiomyocyte tumour lineage, AT-1 [70], and 9L glioma allografts [71] have shown that radiolabelled choline phosphorylation and accumulation is significantly diminished in hypoxia. Furthermore, hypoxic regions in head and neck cancers, resulted with increased asymmetric distributions of the transfer constants in DCE-MRI studies[72,73]. We also studied the distribution of the parametric maps evaluated in tumour, lung, node and vertebra with both spectral and graphical methods in terms of kurtosis and skewness. Figure 17 shows the distribution analysis of patient n. 10. The flattened tumour distributions profiles testify the wider range of values covered by parametric maps as they describe a heterogeneous tissue (lower kurtosis). On the contrary, the profiles of normal lung are picked (higher kurtosis) and left located as most of the values of parametric maps evaluated in reference tissue are lower (positive skewness) and confined in a smaller range (as for homogeneous tissues). Figure 18 confirms these results even though tumour profiles are wider (and less flattened). This might be related to the different histological type of the lesion: adenocarcinoma for patient n. 9 and squamous cell carcinoma for patient n. 10 (Table 5). The Logan V_T is the only parameter for which kurtosis and skewness were found to be able to statistically differentiate among lesion, reference tissue, vertebra and node (Figure 16). The volume of distribution is not a physiological value. It is a proportionality factor as it relates the amount of the tracer in the body to its concentration measured in the plasma (amount of injected dose/concentration of tracer in the plasma). It does not derive from the other pharmacokinetic parameters since it depends on the physiological properties of the body and the physiochemical properties of the tracer itself. So, it is not a 'true' volume expression but it explains *where* in the body the tracer is distributed as, when low, it testifies a difficulty for the tracer to penetrate cell membranes and to diffuse in the tissue (it is only in the plasma) and, on the contrary, when high, the extravascular tissues are more likely to be diffused by the tracer then the intravascular ones. Boxplots in Figure 16 show higher mean, kurtosis and skewness V_T values in the lesion ($p < 0.0001$) compared to reference tissue (and vertebra and node). This could be really useful for the localization of the tracer and for the understanding of the physiochemical properties of the tracer. Higher mean V_T values in the tumour testify the presence of D4-Choline in the extravascular tissue (no trouble diffusing through cell membranes) and higher kurtosis and skewness strengthen this result adding a significant specificity to this preference.

To our knowledge, this is the first work in which the kinetics of the D4-Choline was analysed with spectral and graphical methods. The main limitation of this study is the dataset obtained from a small number of subjects. The strength of the analysis is related to the SA that can be applied to reversible/irreversible kinetics, single or multicompartment models, homogeneous or heterogeneous systems. This way, it is adaptable to different tracers without any a priori assumptions and gives a full model description of the entire data time-course.

This initial study strongly supports further evaluation of 18F-D4-FCH PET in a larger trial to fully assess the utility of D4-Choline in lung cancer and substantiate our findings.

II. Kinetic analysis of dynamic 18F-FLT PET data in the detection of ductal carcinoma in situ

1. Introduction

In the quantification of dynamic positron emission tomography (PET) data, spectral analysis (SA), unlike the other graphical and compartmental approaches, allows the identification of the kinetic components of the tissue tracer activity without specific model assumptions. It considers the impulse response function (IRF) of the compartmental models used in PET as an analytical sum of exponentials and evaluates the poles of the Laplace transform of the IRF, which can be represented as the spectrum of the kinetic components of the tracer exchanges among compartments [40]. Since its introduction in 1993, SA has been widely used in a large variety of testing conditions, both in preclinical [74-76] and clinical studies considering different tracers [77-82] and different acquisition protocols [83-86]. In particular, many applications involved breast and lung cancer patients [63,87,88].

Ductal carcinoma in situ (DCIS) of the breast is a non-invasive carcinoma with a wide spectrum of disease, ranging from low-grade to high-grade malignancy with foci of invasive malignancy. Histologically, DCIS is characterized by a proliferation of malignant cells in the ductal epithelium that are confined to the basement membrane and are not invading the normal breast parenchyma. The biological mechanisms involved in the progression of DCIS to invasive cancer are not yet fully understood but they are part of the same process that comes from the similarity in risk factors predisposing to both conditions. Gapstur and his colleagues [89] followed for 11 years 37,105 women enrolled in the Iowa Women's Health Study. They prospectively collected risk factor information and observed 1520 breast carcinomas, 175 of which were DCIS. Those who developed DCIS or invasive breast cancers had the same risk factor profiles, and the magnitude of risk conveyed by each of the risk factors was similar for both conditions[90]. Early detection is important because of the large proportion of DCIS that can progress to invasive carcinoma. The extent of DCIS involvement is frequently underestimated at mammography, which can reliably help detect only calcified DCIS; consequently, magnetic resonance imaging (MRI) evaluation can alter the course of treatment [91]. In addition to mammography, ultrasonography, and magnetic resonance imaging, ^{18}F-FDG PET has been recognized as an important modality for detecting the hyper metabolic activity of breast tumours. The sensitivity of FDG-PET for detecting primary cancer is 64.4%–89.5%. Conversely, sensitivity for the detection of DCIS has been reported at 25%–76.9% in a small number of articles [92-94]. Azuma et al. retrospectively reviewed 386 consecutive patients who underwent FDG-PET/CT diagnosing 11 pure or predominant DCIS patients. In their study they determined that tumour cell density of intraductal carcinoma appears strongly correlated with detection by FDG-PET/CT [95].

Compared with ^{18}F-FDG, whose uptake is not tumour specific, and false-positive findings can occur in inflammatory lesions [96], ^{18}F-FLT PET has been shown to image cell proliferation [97]. This tracer is trapped within the cytosol after being mono phosphorylated by thymidine kinase-1 (TK1), a principal enzyme in the salvage pathway of DNA synthesis. The accumulation of FLT is dependent on the presence of TK1, which is closely associated with cellular proliferation [98]. ^{18}F-FLT has been found to be useful for non-invasive assessment of the proliferation rate of several types of cancer and showed high reproducibility and accuracy in breast and lung cancer tumours [99-102].

In this work, a voxelwise SA approach was chosen to study 7 patients who underwent dynamic 3'-deoxy-3'-[^{18}F] fluorothymidine (^{18}F-FLT) PET scan followed by a dynamic ^{18}F-fluorodeoxyglucose (FDG) PET scan within a week. 4 of them were diagnosed with ductal carcinoma in situ (DCIS) at biopsy. The application of SA allowed the quantification of two macroparameters: the steady state irreversible flux constant K_i and the influx rate constant K_1 for the transfer of the tracer from plasma to tumour.

2. Materials and methods

2.1 Patient population

A total 12 of breast cancer patients have been enrolled to this study. Written and dated informed consent was obtained from all subjects.
Inclusion criteria comprehended a diagnosis of high grade ductal carcinoma in situ of the breast with a minimum size of 1.5cm (measured by mammography or ultrasound). The diagnosis should have been documented by a previous histological analysis of a core biopsy. Inclusion criteria were also a clinically acceptable (as judged by the investigator) haematological (haemoglobin ≥11g/dL), renal (eGFR >60ml/min) and hepatic history and physical examination at screening. Exclusion criteria comprehended pregnancy, anticoagulation therapy, chemotherapy, immunotherapy, biologic therapy or investigational therapy within 14 days or five half-lives of a drug (whichever is longer) prior to the first dose of FDG or FLT injection.

2.2 PET imaging

Subjects received a single i.v. bolus injection of 1-20 mL injection of FDG or FLT (with at least a 24 hour gap between the two radiotracers). The tracer injection was followed by a saline flush. The maximum ^{18}F activity to be administered was 370 MBq of FDG and 300 MBq of FLT.
Arterial blood samples for ^{18}F activity measurements and ^{18}F metabolite analysis were obtained from subjects with breast cancer from baseline up to 60 minutes after FDG and FLT administration. An arterial cannula was inserted in the radial artery prior to the start of the scan under local anaesthetic to allow arterial blood sampling during the scan. Continuous arterial blood sampling at 5mL/min were performed for the first 10 minutes. Discrete blood samples (5ml) from baseline to 60 minutes post administration were taken for analysis of ^{18}F metabolites. The total blood volume required for all analyses in the study did not exceed 200mls. ^{18}F activity was measured using a gamma counter according to the working instructions at the site. Volumes were adjusted to avoid counter saturation.
Aliquots of each whole blood sample were assayed for ^{18}F content. Following removal of blood for whole-blood assay, the remaining blood sample was centrifuged to obtain plasma. Immediately thereafter, the resulting supernatant (ie, plasma) was transferred to a pre-labelled tube using a fresh disposable pipette. Aliquots of each plasma sample were assayed for ^{18}F.

For each subject and each PET scan, VOIs were manually drawn by the same experienced physician on the summed PET image using Analyze image analysis software (Biomedical Imaging Resource, Mayo Foundation, Rochester, MN). For tumour segmentation, only the planes with identifiable abnormal tracer uptake were chosen.

2.3 Quantification of dynamic FLT data

Dynamic PET data has been analysed with Spectral Analysis as described in *Chapter 2, Quantification techniques*.

2.4 Statistical analysis

All statistical analysis were performed using Matlab R2015b (Mathworks). The tests chosen were: the Kolmogorov - Smirnov test, to assess the normal distribution of each parameter distribution; the Wilcoxon Sum Rank test, to assess the statistically significant differences among tumour, healthy lung tissue, node and vertebra; the non-parametric Spearman test to verify the correlation between parameters evaluated with different modelling approaches. For each map, kurtosis and skewness were also evaluated for a distribution analysis [61].

3. Results

Figure 19 shows the result of ^{18}F-FLT and FDG dynamic PET data quantification of a patient with DCIS. The uptake of the tracers in the lesion is shown in the first column while, in the following ones, parametric maps resulted from spectral and graphical analysis are shown. Maps have been evaluated on a voxel level on the whole volume (Figure 19 is representative of one single slice). In particular, they are K_i and K_1 derived from the spectral analysis.

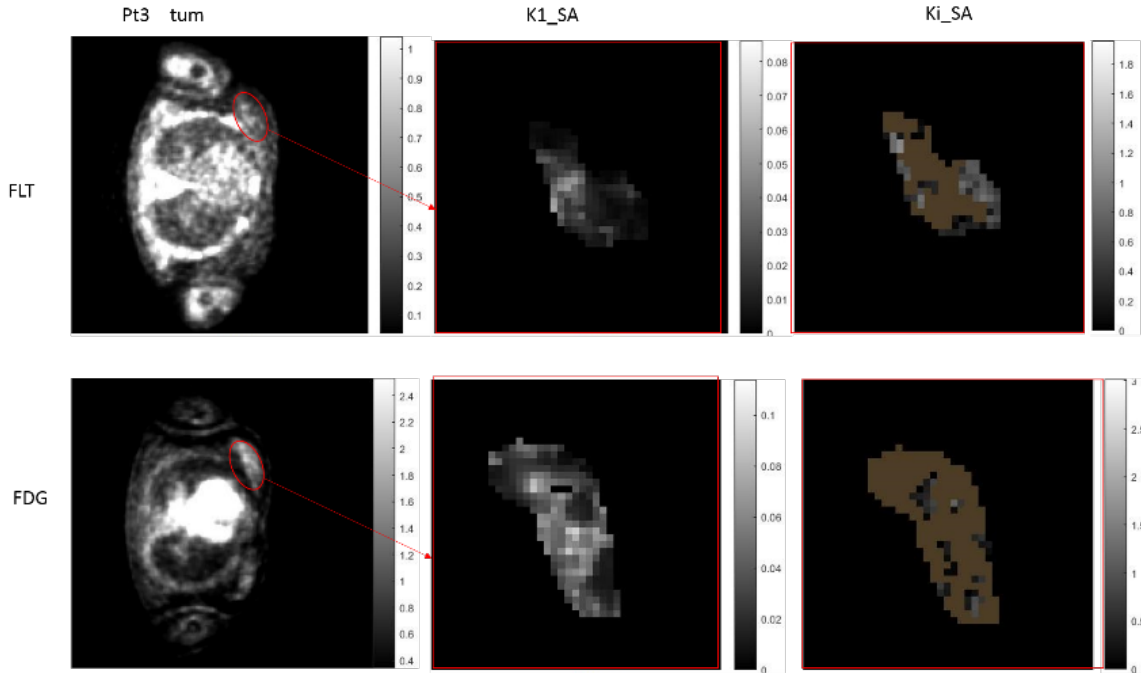

Figure 19: DCIS patient n.3. In the first row, analysis results of the dynamic FLT PET data. From left: phase n. of the PET dynamic scan, SA K_1, SA on a zoomed section of the breast. In the second row, results from the quantification of dynamic FDG PET data.

Table 7 shows the results of spectral and graphical analysis on DCIS patients in terms of mean and standard deviation.

Table 7: Spectral analysis results on ^{18}F-FLT and ^{18}F-FDG dynamic PET data of patients with DCIS. Values are expressed in terms of mean and standard deviation ($\mu \pm \sigma$).

	Spectral Analysis	
	K_i	K_1
FLT	0.0010 ± 0.00030	0.013 ± 0.011
FDG	0.00070 ± 0.00030	0.038 ± 0.035

The fractional retention (FRT) of the tracer in the tissue has been evaluated as the ratio between the IRF at 60 minutes and at baseline.

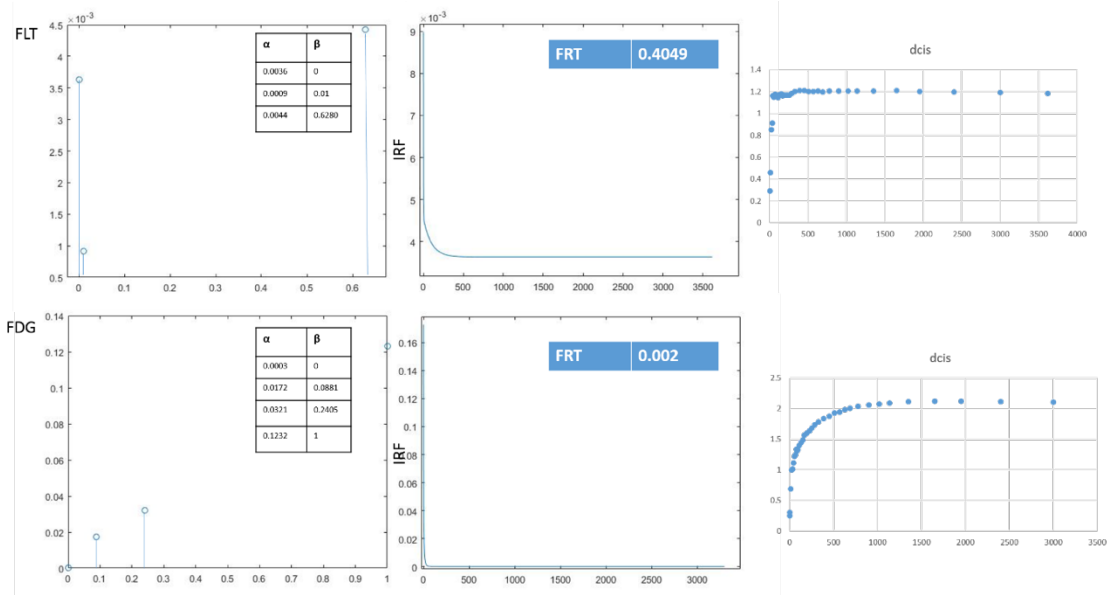

Figure 20: DCIS patient n.1: SA results. The first column shows the spectra derived from the ROI level SA applied on both FLT (first row) and FDG (second row) dynamic PET data. Both tracers presented an a0 value indicating the irreversible trapping of the tracer in the tissue during the time of experiment. The IRFs are shown in the second column with their correspondent FRT value evaluated as the ratio of the IRF at 60 minutes ad at baseline. The last column shows the tissue uptake curves of the two different tracers.

Figure 20 is representative of the results of the spectral analysis applied on an ROI level on DCIS patient n. 1. On the left side, the spectra of the kinetic components of the two different tracers in the lesion are shown. Both spectra present an α_0 value indicating the presence of an irreversible trapping component of the tracer in the tissue during the time of measurements. The FRTs are shown on their correspondent IRF curve (in the middle). On the right side of the figure, the DCIS ^{18}F-FLT and FDG tissue uptake curves are shown.

Spectral analysis was applied also on 15 patients with breast cancer who underwent dynamic ^{18}F-FLT scan before and after one or two cycle of docetaxel. Table 8 shows mean values of spectral K_i and K_1 in tumour (at baseline), DCIS and healthy breast tissue.

Table 8: Spectral K_i and K_1 mean values evaluated in breast tumour, healthy tissue and DCIS.

	Tumour (mean ± std)	Healthy Tissue(mean ± std)	DCIS (mean ± std)
K_i [mL/cm^3/min]	0.025 ± 0.014	0.0055 ± 0.0036	0.0024 ± 0.0014
K_1 [mL/cm^3/min]	0.18 ± 0.14	0.10 ± 0.097	0.016 ± 0.013

Receiver operating characteristic (ROI) curves analysis was applied on spectral K_i and K_1 mean values in tumour and healthy tissue. Results are shown in Figure 21. A cut-off value of 0.014 (sensitivity 80%, specificity 100%) resulted for the spectral K_i, with an area under the curve (AUC) of 0.90 significantly greater than 0.5.

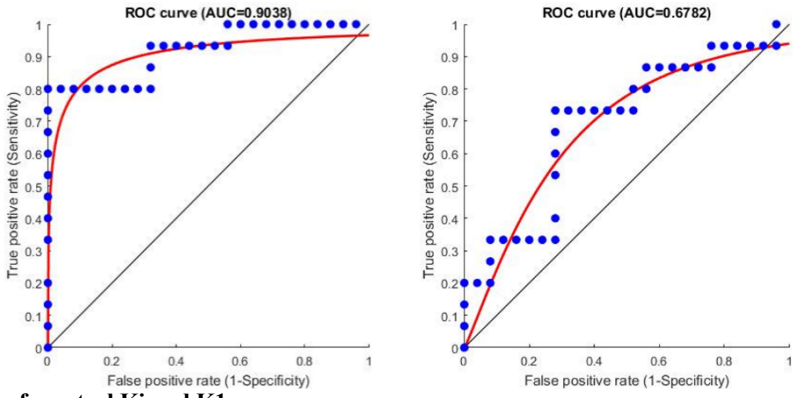

Figure 21: ROC of spectral Ki and K1.

For spectral K_1, ROC curve analysis gave a threshold value of 0.15 with a sensitivity of 71% and a specificity of 68% and an AUC of 0.6782 significantly greater than 0.5.
In order to have a more robust evaluation of cut-off values, a bootstrap analysis was applied on the spectral K_i and K_1 3D parametric maps (Figure 22). In fact, in the absence of repeated measurements, this technique has been shown to be the only consistent method for assessing uncertainty in all detected components of the tracer kinetic [103].

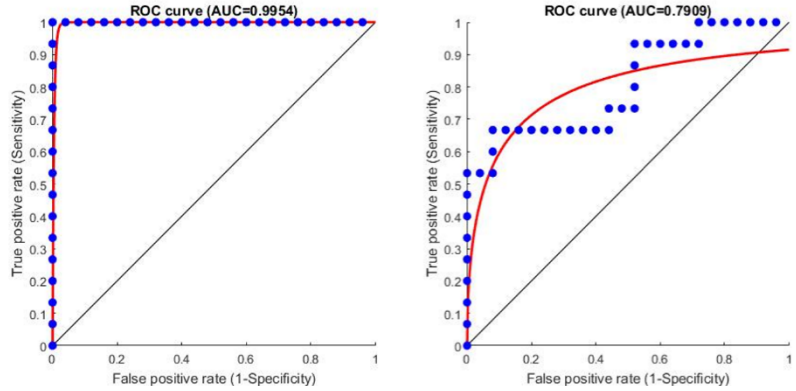

Figure 22: ROC on bootstrapped spectral Ki and K1.

ROC analysis on bootstrapped data confirmed the K_i cut-off value previously found with a resulting higher AUC (0.99). In the same way, for the spectral K_1, a 0.23 cut-off value was set with 66% sensitivity and 92% specificity and the AUC was found to be greater than 0.5 (0.79).

Neither of these value was able to differentiate DCIS as the uptake of the tracer in these areas was much lower. As a consequence, perfusion values were under the thresholds.
Table 9 shows the mean and standard deviation of SA K_i, K_1 and the ratio between these two, in tumour, healthy breast and DCIS evaluated at 60 minutes. This ratio has been displayed in Figure 23. The panel in Figure 24 shows the voxelwise analysis of patient n. 4. In particular, K_i, K_1 and K_i/K_1 ratio map for 3 slices (41, 42, and 43) of the DCIS.

Table 9: Spectral K_i and K_1 and K_i/K_1 ratio values evaluated in breast tumour, healthy tissue and DCIS.

	Tumour (mean ± std)	Healthy Tissue(mean ± std)	DCIS (mean ± std)
K_i [mL/cm^3/min]	0.025 (0.014)	0.0055 (0.0036)	0.0020 (0.0012)
K_1 [[mL/cm^3/min]	0.18 (0.14)	0.10 (0.097)	0.027 (0.017)
K_i/K_1	**0.22 (0.19)**	**0.082 (0.075)**	**0.10 (0.088)**

Figure 23: mean and 95% CI of spectral K_i/K_1 map in breast tumour (red), normal breast (green). The blue dots represent the six DCIS patients: for two of them, the K_i/K_1 ratio fell in the tumour range.

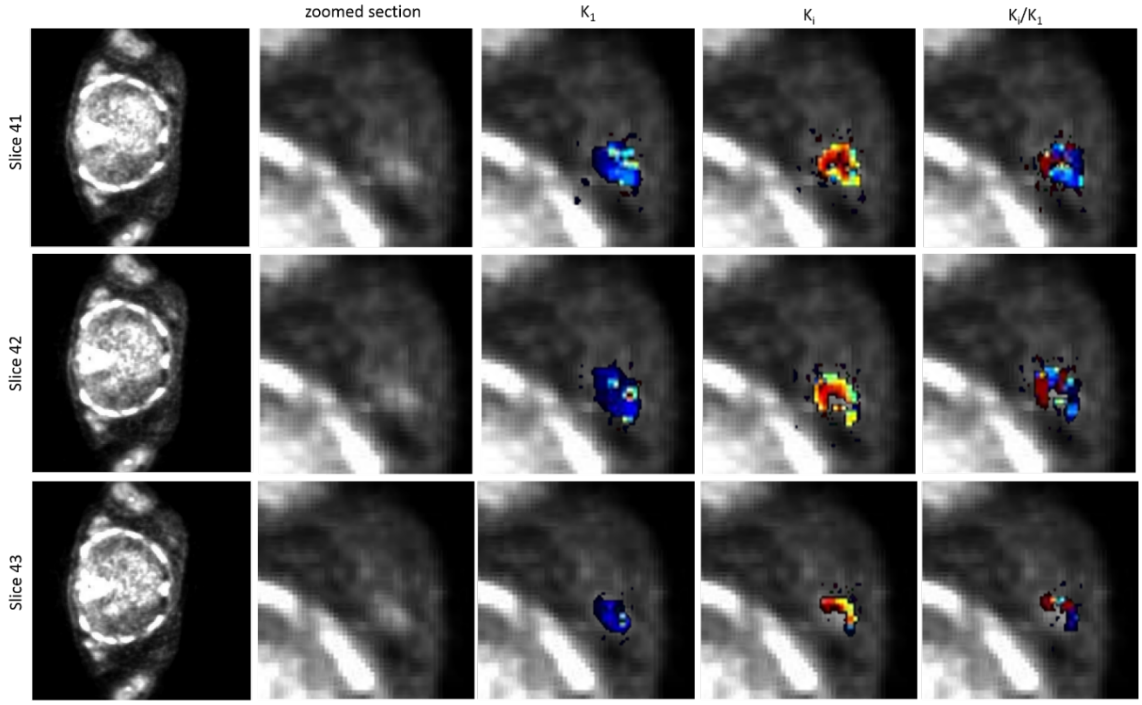

Figure 24: Patient n. 4. The panel shows the voxelwise SA results for three representative slices (in the three rows) of the DCIS of this patient. In the second column there is a zoomed section of the original PET data (first column). Third, fourth and fifth column are representative of K_1, K_i and K_i/K_1 maps.

4. Discussion

The study investigated the kinetics of the tracer in DCIS compared with breast tumour to assess the utility of SA in the early diagnosis of DCIS. A voxelwise SA approach was applied on 7 patients who underwent dynamic 3'-deoxy-3'-[^{18}F] fluorothymidine PET scan followed by a dynamic ^{18}F- fluorodeoxyglucose PET scan within a week. 4 of them were diagnosed with ductal carcinoma in situ at biopsy. SA was also applied on 15 breast cancer patients who underwent a baseline dynamic ^{18}F-FLT PET scan followed by a scan after 2 weeks after the first or second cycle of docetaxel. The application of SA allowed the quantification of two macroparameters: the steady state irreversible flux constant K_i and the influx rate constant K_1 for the transfer of the tracer from plasma to tumour.
Ductal carcinoma in situ of the breast is a non-invasive carcinoma characterized by proliferation of malignant cells in the ductal epithelium that are confined to the basement membrane and are not invading the normal breast parenchyma. Diagnosis of DCIS is primarily based on imaging results. While mammography remains the gold standard for diagnosis of breast diseases, MRI is frequently used after the detection of lesions by digital or screening mammography [104]. MRI can help guide surgical decision making among the possible options (breast conserving surgery, mastectomy, or bilateral mastectomy) and has a higher diagnostic accuracy for DCIS compared with either film or digital mammography. Riedl and colleagues studied 672 imaging rounds in a high-risk population and found that the detection rate of DCIS by mammography, ultrasound (US), and MRI were 50%, 42.9%, and 85.7%, respectively [105]. The aim of this study was the characterization of DCIS in breast with a spectral analysis approach. The segmentation of DCIS was guided by DCE MRI data as coregistration between PET and MR was not doable because data were acquired in two different spaces (patient prone in PET and supine in MRI). MR was useful for the identification of the lesion and the following segmentation. In particular, on PET data, small DCIS spots were included in a larger VOI covering the entire breast. The retention of the tracers was evaluated both at region and voxel level. ROI level SA resulted with a spectrum of the kinetic components of the tracer showing the presence of an irreversible trapping component during the time of measurements (for both ^{18}F-FLT and FDG) (Figure 20). But, the simplified average description obtained by ROI analysis alone cannot provide a fair description of tumour heterogeneity. An exhaustive physiological characterization of tumour tissues that considers the complexity and the variability of the kinetics is given by a voxel wise approach. VOI level SA gave 3D parametric maps of two perfusion parameters: K_i, the irreversible uptake rate constant and the K_1, the influx rate constant. Graphical plots were also applied on DCIS data resulting with Patlak K_1 and Logan V_t parametric maps. Figure 19 shows the uptake of the two tracers in the DCIS of patient n.3 and the parametric maps resulted from spectral and graphical analysis. Compared with ^{18}F-FDG, whose uptake has been reported to be influenced by several factors, as the upregulation of glucose transporter 1 receptors [66], the number of viable tumour cells [67], microvessel density, or hexokinase expression [68], FLT-PET has been shown to image cell proliferation. The uptake of both ^{18}F-FLT and FDG in DCIS was not statistically higher compared with the surrounding healthy tissue and the identification of DCIS was not clear. In the same way, no statistical difference was found between DCIS and healthy tissue with spectral and graphical results.

SA was applied on a dataset of 15 breast cancer patients. The mean value of both spectral K_i and K_1 in DCIS was found to be really low compared with breast tumour and resulted closer to healthy breast values (Table 9). A receiver operating characteristic curve analysis was applied on breast tumour patients' dataset to find a cut-off between lesion and healthy tissue. A more robust result was obtained with the application of the bootstrap analysis on spectral approach that resulted with a very good discrimination between healthy and tumour tissue given by the K_i (AUC = 0.99) with a cut-off of 0.014 (80% sensitivity and 100% specificity). DCIS was not identifiable by this threshold as well. This could be explained by the overall high proliferation activity of the breast

affected also by the menstrual cycle. Söderqvist and his colleagues analysed the proliferation marker Ki67/MIB-1 by immunocytochemical methods in breast epithelial cells to assess proliferation in normal breast epithelial cells from healthy women during follicular and luteal phases of the menstrual cycle. They found a higher proliferation during the luteal phase and a positive correlation with serum progesterone levels [106]. Furthermore, Hoque and his colleagues did not observe a statistically significant difference in Ki67 labeling indices between DCIS associated with invasive breast cancer and DCIS alone [107].

The periductal vascularization is important in determining transformation from in situ to invasive disease [108]. Since it can be very different among different DCIS as not all of them convert into breast tumour, we normalized our SA results by the K_1 with respect to their heterogeneous delivery mechanism. Results in Table 9 show K_1 values in tumour, healthy breast and DCIS. The latter results very low, comparable to the healthy tissue. The K_i/K_1 ratio was plotted in Figure 23 where DCIS values were compared to tumour and healthy breast. Two patients resulted to fall into the tumour range.

Our results suggest that the difficulty in the identification of DCIS is related to the proliferative activity of the normal breast. Neither spectral, nor graphical methods were useful in the diagnosis of DCIS as the uptake, and the kinetic parameters as well, resulted with very low values (almost comparable to normal breast). As the microvessel density is a key factor in the transformation of a DCIS to invasive breast cancer, and as it can be very different among different DCIS, we showed the utility of the K_1 normalization in the identification of pure DCIS.

III. [^{18}F]Fluorothymidine Positron Emission Tomography is a sensitive method for imaging hepatocellular carcinoma patients undergoing transaterial chemoembolization

1. Introduction

Hepatocellular cancer (HCC) is the most common primary hepatic malignancy worldwide and third leading cause of cancer mortality [109]. Most cases arise in the context of liver cirrhosis (>80%) secondary to hepatitis, alcohol excess and increasingly, non-alcoholic fatty liver disease. Cirrhosis is a progressive process characterised by nodules: benign regenerative nodules, dysplastic and HCC. Radiologic visualisation of HCC is dependent on typical vascular pattern on contrast enhanced-CT or MRI of arterial uptake followed by "washout" on venous phase. Multiphase contrast-enhanced CT is the most widely available imaging modality, and is considered a reliable method for assessment of tumour viability with a sensitivity 68% [110]. MRI has marginally improved sensitivity of 80%, but still underestimates pathologic staging of disease [110]. Furthermore, both CT and MRI are unable to effectively differentiate regenerating nodules from viable tumour. For intermediate stage HCC, transarterial chemoemobilisation (TACE) has been shown to improve clinical outcomes and is also used as a bridge to transplantation [111]. In a series of patients undergoing TACE prior to transplantation, response by conventional imaging was 35% (range 16% - 61%). Pathologic analysis of explanted livers suggested post-TACE necrosis in 75%, highlighting diagnostic uncertainty in response assessment by conventional radiology [110]. Moreover, there is no consensus as to the optimal imaging modality of extrahepatic disease.

PET imaging has been evaluated in HCC both for staging and in assessing response to treatment [112]. Clinically, the most widely used tracer is [^{18}F]Fluorodeoxyglucose ([^{18}F]FDG). Studies investigating the utility of [^{18}F]FDG-PET in HCC have shown limited sensitivity (50 – 70%) [113]. The reason for this limited sensitivity is likely due to less marked differential activities of glycolytic enzymes and of glucose 6-phosphatase in liver and well-differentiated HCC, resulting in almost equivalent uptake of [^{18}F]FDG and poor differentiation of tumours. Imaging with [11C]acetate and [11C]-, [18F]choline are similarly limited [114]. 3'-Deoxy-3'-[^{18}F]fluorothymidine ([^{18}F]FLT) is a surrogate marker of proliferation, with uptake reflecting the activity of thymidine kinase (TK-1), the key enzyme in the salvage pathway for thymidine monophosphate production; its expression correlating with the *S* phase of the cell cycle [115]. Unlike [^{18}F]FDG, the uptake of [18F]FLT is specific for proliferation and is not affected by the presence of inflammation[116], a particular concern in HCC, as these tumours develop in a pro-inflammatory milieu [117]. To date there has been a single study of [^{18}F]FLT-PET in HCC which indicated that only 69% of patients with HCC had uptake in the liver [118]. However, the population studied was a heterogenous group including cholangiocarcinoma and no information was given with regards to tumour stage or response to therapy. Moreover, no study has considered the differential expression of TK-1 in HCC and the surrounding cirrhotic tissue, an important consideration in developing a tracer paradigm that will effectively differentiate cirrhotic tissue and HCC.

We therefore conducted a comprehensive study of patients with intermediate stage HCC undergoing TACE therapy in order to evaluate the ability of [^{18}F]FLT-PET to visualise HCC compared to standard imaging and as a response biomarker. As an initial step we reviewed the differential expression of TK-1 in HCC and surrounding cirrhotic tissue in pathologic resection samples, and then undertook a retrospective study to illustrate the importance of response assessment in assessing treatment outcome for patients. We then undertook a prospective study using dynamic [^{18}F]FLT-PET to both visualise the tumours and as a response biomarker, incorporating comprehensive kinetic modelling.

2. Materials and Methods

2.1 Tissue Microarray

Combined primary tumor/metastasis TMA blocks were prepared as previously described (15) from separate areas of the primary tumors and matched secondary lesions to ensure maximal reproducibility. The tissue cores were re-embedded in recipient microarray blocks.
A tissue microarray (TMA) was constructed from patients (n=36) with a histological diagnosis of HCC treated at the Hammersmith Hospital, London as previously described [119]. Following marking of diagnostic H&E slides, a MTA-1 Manual Tissue Microarrayer (Beecher Instruments, USA) was used to obtain 1 mm cores of matched cores of malignant tissue and surrounding parenchyma. All primary and metastatic deposits were sampled in triplicate. Adequate sampling of the target lesions was confirmed on a freshly cut H&E section from the recipient TMA block before immunostaining. Immunohistochemistry (IHC) was performed on the TMA sections using an established methodology for TK-1 (1:100, AbCam, Cambridge) at the Department of Pathology, Hammersmith Hospital.

2.2 Study Design and participants

2.2.1 Retrospective study

We conducted a retrospective study of 148 consecutive patients with a diagnosis of HCC, treated with conventional TACE at Imperial College Healthcare NHS Trust, London (UK) between 2001 and 2018 (Table 10). TACE consisted of intrarterial infusion of doxorubicin emulsified in lipiodol followed by embolisation with gelatin sponge particles. All patients underwent a tri-phasic contrast enhanced computer tomography (CT) scan prior to and 6-8 weeks following TACE. Two hepato-biliary radiologists (P.T. and M.P.) blinded to treatment outcome reviewed CT and pre-treatment angiogram images with concordance reached over the qualification of each radiologic feature. Progression free survival (PFS) was calculated from initial TACE to the time of progression or last-documented follow-up. The local Research Ethics Committee, Imperial College Healthcare NHS Trust, approved the study.

Table 10: Eighteen patients were enrolled (16 men and 2 women). A tracer production failure meant one patient was unable to have baseline scanning and one patient withdrew consent following the first PET scan, therefore 16 patients were evaluable for treatment outcome (Table 1). Median age was 68 years (range 42 – 79years). All patients received TACE for intermediate stage disease. Three patients had had previous TACE and were undergoing retreatment. The remaining patients were treatment naïve. One patient did not have radiologic evidence of background cirrhosis. Three patients had diffuse disease on conventional imaging.

Patient No	Lesion location	$SUV_{60,ave}$ x $10^{-5}m^2mL^{-1}$ (preRx)	$SUV_{60,max}$ x $10^{-5}m^2mL^{-1}$ (preRx)	mRECIST response	Percentage Change $SUV_{60,ave}$	Percentage Change $SUV_{60,max}$
1	Diffuse disease, R lobe	3.4	5.115	PD	-12.21	13.98
2[a]		2.17	7.825	PR	-22.81	0.77
3	Segment VII	5.68	7.97	PR	-65.23	-42.60
4	Segment VI	2.75	5.515	CR	-6.00	-14.42
4[b]	Segment V	4.125	5.8		-0.97	-6.72

5	Segment II	7.535	10.335	PR	-37.36	1.35
	Segment VI[c]	7.6	9.885		10.92	-0.66
	Segment IV	7.325	9.82		15.49	26.17
	Segment IV	7.84	10.285		5.93	1.90
	Segment VIII	7.08	9.385		0.07	0.85
	Segment IV	7.8	11.295		-4.68	0.93
	Segment VIII	7.075	8.205		22.19	36.50
6		7.57	10.225	CR	-45.57	-19.02
7		10.875	14.28	CR	0.00	-100.00
8		7.83	11.46	CR	-66.41	-41.45
9		7.965	10.295	CR	-58.63	-46.09
10		8.13	20.355	SD	-71.34	-41.00
11		7.11	10.585	PR	-29.04	-21.49
12	Segment VIII	5.075	10.9	PR	-55.76	-32.84
12	Segment IV[d]	2.86	8.36		-51.57	-33.85
13		6.365	8.93	CR	-25.06	-30.01
14	Segment VII (sagittal)	5.315	7.36	PR	-33.96	-30.50
	Segment VIII	6.265	7.505		-33.52	-39.11
	Segment VII (medial)	6.62	8.015		17.15	30.88
15		7.295	10.42	SD	-52.43	-46.26
16		6.555	11.6	PR	-65.83	-24.09

[a]Incidental finding of T12 metastases not visualised on MRI. Confirmed on subsequent bone scan
[b]multiple subcentimetre lesions seen on [18F]FLT-PET
[c]Lesion untreated
[d]Photopaenic lesion

2.2.2 Prospective study

Eighteen patients with a diagnosis of HCC were included in this prospective study. Eligible patients were aged 18-85 years with histological diagnosis HCC or a diagnosis of HCC based on American Association for the Study of Liver Diseases (AASLD) criteria, had intermediate stage disease suitable for TACE, disease evaluable by modified Response Evaluation Criteria in Solid Tumours (mRECIST) and at least 1 target lesion ≥2cm, an Eastern Cooperative Oncology group performance status (PS) of 2 or less, and a life expectancy of at least 6 months [120,121].

Patients had to have adequate bone marrow function (haemoglobin concentration <90 g/L, neutrophils <1500 cells per μL, platelets <100 000 cells per μL), kidney function (creatinine <1·5 times the normal upper limit; calculated creatinine clearance ≥50 mL/min), and liver function (aspartate aminotransferase or alanine aminotransferase ≤2·5 times the normal upper limit, alkaline phosphatase ≤2·5-times the normal upper limit, total bilirubin ≤1·5 times the normal upper limit).

Patients were recruited from Hammersmith Hospital Imperial College Healthcare NHS Trust. The study was approved by the ethics committees at each institution, and all the patients provided written informed consent.

2.2.3 Study Assessments

All patients received standard TACE with liposomal doxorubicin emulsified in lipiodol followed by embolisation with gelatin sponge particles. Baseline staging included CT chest, abdomen and

pelvis or MRI liver. The same radiological tests were repeated 6-8 weeks following TACE to assess treatment response, and then 3 monthly until disease progression. Response was assessed in accordance with modified RECIST (mRECIST) for HCC [122] by a single experienced hepatobiliary radiologist (NPT).

2.2.4 Imaging protocol

[^{18}F]FLT was manufactured according to standard protocols. All patients were scanned on a Siemens Biograph 64-slice PET/CT scanner. [18F]FLT-PET imaging was carried out at baseline and at the time of follow-up imaging following TACE. In all cases, the liver was imaged in a single abdominal bed position. Patient positioning was followed by a CT scan (300 mA, 120 kVp, 1.35 pitch, 0.8 s/rotation) for both attenuation correction and co-registration with PET images, to allow anatomical visualisation and localisation of [^{18}F]FLT activity. [^{18}F]FLT, mean (±SD) 208.2 ± 10.4 MBq, was injected as a bolus intravenously, and a dynamic, list mode emission scan in the 3D mode, lasting 66 min, was undertaken [123,124].

2.3 Image analysis

Raw PET data were corrected for scatter, attenuation and reconstructed with an iterative algorithm consisting of 8 iterations and 21 subsets. The data were binned into time frames as follows: 1 * 30 (background), 6 * 10, 4 * 20, 4 * 30, 5 * 120, 4 * 180 and 4 * 600 seconds. The attenuation corrected PET images and CT data were fused and analysed on a dedicated workstation (Hermes diagnostics, Sweden) by a dual trained radiologist/ nuclear medicine physician (TDB). All SUV analyses were conducted using PET uptake parameters generated on Hermes.

Tumour lesions were defined as target lesions by mRECIST on either CT or MRI [125]. The lesions on the [^{18}F]FLT corresponding to those on the CT or MRI, showing an increased uptake were considered as target lesions. All lesions greater than 10mm on CT or MRI imaging were measured on PET/CT. The diameter of the target lesions was measured using electronic callipers on the PACS workstation. The same target lesions were used for analyses on both the PET/CT and CT or MRI, before and after treatment.

Consecutive regions of interest (ROI) were manually defined around the tumours on the summed images, employing the patient's diagnostic imaging. The ROI encompassed the whole tumour for SUV analysis. The [^{18}F]FLT radioactivity concentration within the ROIs was then normalised for injected radioactivity and body weight (grams) to obtain the mean and maximum SUV at 60 minutes ($SUV60_{mean}$, and $SUV60_{max}$) on baseline and post-treatment [^{18}F]FLT PET/CT studies. The percentage change in SUV in both SUV_{mean} and SUV_{max} was then calculated for each target lesion visible on baseline imaging as; $(SUV_{post} - SUV_{pre})/SUV_{pre}$. In each case, a 3 cm ROI was placed in the liver in a tumour free area, and the tumour/liver (T/L) ratio determined.

2.3.1 Quantitative analysis

-- ***The arterial input function***

For each patient, an additional ROI on the aorta was drawn for the implementation, in the kinetic model, of an image derived arterial input function (idAIF)[60]. Since metabolite data were available for 10 patients, the idAIF was corrected for an average metabolite and plasma-over-blood ratio for each patient. The total [^{18}F]FLT activity in each blood sample was averaged and used to fit the plasma-over-blood (POB) ratio to a mono-exponential curve to provide a continuous POB representation. A total plasma activity curve was obtained by multiplying the POB by the tissue-derived input function. Finally, the average pre- and post-treatment fraction of parent compound in each sample was fitted to obtain a continuous representation of the parent tracer concentration which was then multiplied by the total plasma function. The result was a tissue-derived parent plasma input function for each scan which was subsequently used for compartmental modelling.

-- ***The compartmental model***

The average activity within the tumour ROI was used, for each time frame of the dynamic PET imaging sequence. The regional tissue activity curves (TACs), the metabolite corrected idAIF and the whole blood activity curve were fitted to a two tissue compartmental model using the Levenberg-Marquart least-square minimization algorithm implemented in the PMOD kinetic modelling tool PKIN (PMOD version 3.703; PMOD group, Zurich, Switzerland). The two-tissue compartment model separates tracer in tissue into two exchanging compartments as described in *Chapter 2, Quantification techniques*.

2.4 Statistical Analysis

As this was a pilot study no formal power calculation was undertaken. Summary statistics of the associations between PET parameters and clinical outcome were determined. Due to the small sample size, patients were grouped as responders (complete and partial response, CR and PR) or non-responders (stable disease or progressive disease, SD and PD). ROC analysis was undertaken to determine optimal PET uptake predictive of response and progression. The relationship between kinetic parameters and response was evaluated using Wilcoxon rank tests. Survival was determined by Kaplan-Meier statistics. Chi-squared test was used to evaluate utility of the tracer pre and post TACE therapy. $p \leq 0.05$ was considered significant. All statistical analyses were conducted using SPSS statistical package version 22 (SPSS Inc., Chicago, IL, USA).

3. Results

3.1 Response to TACE is predictive of progression free survival

As PET parameters were associated with response, we evaluated the relevance and range of responses in the context of PFS within our institution. In this regard, we considered a large group of consecutive patients who had undergone TACE at our institution. Response to TACE using mRECIST was defined as CR, PR, SD, PD. Response was a significant predictor of PFS (median PFS 15.4 months, 95%CI: 9.1-21.7, $p < 0.001$).

3.2 TK-1 is upregulated in HCC compared with cirrhotic tissue

To confirm that [^{18}F]FLT is an appropriate tracer for the visualization of HCC we investigate the expression of TK-1 in HCC compared to surrounding cirrhotic tissue using a TMA of matched cores of malignant tissue and surrounding parenchyma. A significantly higher TK-1 expression in HCC compared to the surrounding parenchyma was observed confirming that [^{18}F]FLT has potential for the differentiation of HCC from the surrounding cirrhotic liver parenchyma ($p<0.05$).

3.3 HCC is visible above background liver using [^{18}F]FLT-PET imaging

On visual analysis, 25 lesions were visible above background liver uptake, and one lesion was noted to be photopenic. All liver lesions seen on standard radiologic imaging were also seen on PET imaging. One patient had a bone metastasis seen at T_{12} on PET imaging that was not visible on conventional imaging but was confirmed 3 months later on a bone scan.

All lesions were included in analysis. The mean $SUV_{60,mean}$ (±SD) and $SUV_{60,max}$ (±SD) on the baseline scan were 6.39 (±2.00) and 9.68 (±3.00), respectively. The mean $SUV_{60,mean}$ of the background liver was 6.08 (±0.97). A significant difference was observed between $SUV_{60,max}$ of the cancer compared to surrounding, non-cancerous liver tissue ($p=0.02$), with the mean tumour to liver (T/L) ratio being 1.59 (±0.39), confirming that uptake in HCC was above cirrhotic background activity thus enabling visualization on [^{18}F]FLT-PET scans.

3.4 [^{18}F]FLT uptake parameters and clinical outcome

In terms of response to TACE, according to mRECIST criteria, five patients (33%) had CR, seven patients (47%) had PR, two patients (13%) had SD and one patient (7%) PD. There was a median overall reduction in [^{18}F]FLT-PET/CT $SUV_{60,\ mean}$ ($-26.67 \pm 29.86\%$) and $SUV_{60,\ max}$ (-14.27 ± 24.83 %) following TACE. Previous test–retest reproducibility studies in breast cancer patients showed that changes in [^{18}F]FLT standardized uptake value (SUV) of more than 20% is considered significant with 95% confidence interval (SD: 10%–15%) [126]. Using a 20% reduction in $SUV_{60,\ max\ as\ response,}$, response to PET imaging was 73% (n = 11) and non-response was 27% (n = 4). As CR/PR and SD are clinically managed in a similar way, these were subsequently grouped as "responders" whilst PD was classified as "non-responders". Accordingly, 80% of patients were responders and 20% were non-responders. Using Cohen's kappa measures, there was no concordance observed between PET response and mRECIST.

3.5 Kinetic quantification of [^{18}F]FLT data

Kinetic modelling illustrates significant reduction in [^{18}F]FLT uptake and retention following TACE

Fourteen patients had bloods taken for kinetic modelling. The analysis of [^{18}F]FLT dynamic data with a two tissue compartmental model resulted in kinetic parameters consistent with physiological conditions (Table 11)[127].

Table 11: Results of the compartmental analysis done on dynamic [^{18}F]FLT data. The analysis was run on a ROI level and results show the parameters extracted from the single TAC (no standard deviation).

Patient Number	K_1 (mL/min/g)	k_2 (1/min)	k_3 (1/min)	k_4 (1/min)	v_B (mL/g)	K_i (mL/min/g)
1	0.16	0.10	0.10	0.11	0	0.082
2	0.17	0.075	0.074	0.065	0.013	0.086
3	0.31	0.40	0.24	0.039	0.019	0.11
4	0.21	0.28	0.13	0.059	0.034	0.066
5	0.34	0.16	0.096	0.039	0.030	0.12
6	0.43	0.28	0.085	0.011	0.057	0.10
8	0.27	0.28	0.13	0.024	0.045	0.089
9	0.29	0.52	0.32	0.037	0.054	0.11
11	0.41	0.51	0.16	0.020	0.073	0.10
13	0.11	0.16	0.038	0.0017	0.10	0.021
14	0.46	0.42	0.13	0.035	0.0002	0.10
15	0.58	0.69	0.13	0.024	0.066	0.090
16	0.26	0.17	0.075	0.024	0.069	0.077
18	0.23	0.19	0.092	0.023	0	0.074

Compartmental modelling provided separate estimates of both transport (K_1) and retention (K_i) of [^{18}F]FLT. There was a significant and profound reduction in mean K_1 values from baseline, 0.30±0.13 (mL/min/g), compared to post-treatment, 0.13 ± 0.054 ($p < 0.001$). This is in keeping with the abrupt cessation of blood flow to the tumour following embolization of the feeding vessels resulting in reduced transport of [^{18}F]FLT to the tumour. While all tumours showed some degree of reduction in K_1, the change in K_1 was greater in responders (66% reduction) versus non-responders (50%), p=0.034 (Figure 2A). Baseline $SUV_{60,\ mean}$ and baseline K_i were significantly correlated (Pearson's correlation coefficient 0.55, p-0.043) and a significant difference was observed in K_i at baseline 0.089 ± 0.026 (mL/min/g) compared to post-TACE imaging, 0.043 ± 0.02 ($p < 0.001$). In responders, baseline K_i and v_B were greater compared to non-responders (Figure 25B and C) ($p < 0.05$).

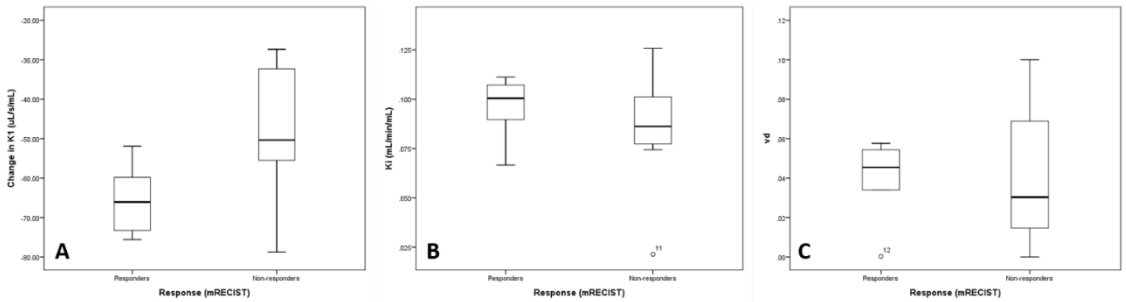

Figure 25: A) Change in K_1 in responders and non-responders; B) Baseline K_i in responders and non-responders; C) Baseline v_B in responders and non-responders.

4. Discussion

Despite numerous studies investigating the utility of PET in HCC, there is still no one tracer recommended by international guidelines for either diagnosis or response assessment [128]. The main limitation of the studied tracers has been poor tumour to background ratio which has impacted negatively on the utility of a number of PET tracers and has resulted in the use of dual tracers for visualizing HCC, which is both time-consuming for nuclear medicine departments and exposes patients to significant radiation [112-114,129]. We hypothesized, that as [^{18}F]FLT uptake is specific for proliferation, tracer uptake will not be affected by the presence of inflammation, a particular concern in HCC, as these tumours develop in a pro-inflammatory milieu [130].

In order to address this hypothesis, we firstly assessed the expression of TK-1 both in HCC and surrounding, matched cirrhotic tissue. TK-1 directly impacts on [^{18}F]FLT trapping within the cell and has been shown in a number of studies to be a surrogate marker of proliferation [131-133]. Using paired samples of tumour tissue and surrounding cirrhosis, we illustrated a marked upregulation of TK-1 in HCC, thereby suggesting that [^{18}F]FLT could be useful in differentiating HCC from surrounding background liver. Accordingly, the results of our clinical study illustrate that [^{18}F]FLT-PET was accurate in detecting intrahepatic lesions, with increase uptake above tumour background consistent with TMA findings. Moreover, in one patient with boney metastasis, [^{18}F]FLT-PET was more sensitive in detecting extra-hepatic disease compared to conventional imaging. This is in contrast with the study by Eckels and colleagues who reported only 72% sensitivity of [^{18}F]FLT in visualizing HCC [134]. The difference may be attributable to the heterogeneous study population investigated in the Eckels paper including cholangiocarcinomas. Of interest, the median SUV and T/L ratios are consistent between the two studies.

We also considered the role of dynamic [^{18}F]FLT-PET in response assessment following TACE an important clinical situation as conventional imaging has varied accuracy in response assessment particularly in defining regenerative nodules from active cancer. The radiologic response to TACE by mRECIST was 80%, and by PET was 73%, however there was no concordance between imaging modalities. This may reflect differences in the biophysical and biochemical measures derived from the different imaging techniques, and/or the small studied sample size. In addition we selected a 20% reduction in SUV_{60max} to indicate response, a larger study may define a more accurate cut-off.

A key strength of this study is the use of dynamic PET imaging data that allows us to further derive predictive biomarkers of outcome in HCC. We report a significant reduction in K_i and K_1 following TACE, illustrating abrupt reduction in blood supply to the tumour that will affect tissue perfusion. This is sharp contrast with some standard chemotherapy where we would have expected an increase in the K_1 due to a reorganization and normalization in the vascular structure of the tissue [135]. K_i is the metabolic flux constant and it is related to the phosphorylation of the thymidine in the tissue [136]. It has previously found to be correlated to [^{18}F]FLT uptake and our results illustrate correlation with SUV uptake [102]. Moreover, we report baseline K_i and v_B to be

predictive of response to treatment suggesting that these tumours are more actively proliferating and have increased vascularity which would be predictive of TACE response.

Response to TACE has been shown to be predictive of PFS both in our cohort within this manuscript and by other authors, therefore accurate response assessment is important. Conventional RECIST response criteria using change in size has limitations for targeted therapies which can induce tumour necrosis without overall change in size. Therefore, mRECIST criteria based on changes in size of the 'viable' tumour which is considered to be the arterially enhancing component of the tumour on contrast CT or MRI, was introduced [122]. The mRECIST criteria has been validated in the assessment of locoregional therapies for HCC, such as TACE/ TACE, with a recent meta-analysis of seven studies reporting strong prognostic value of mRECIST criteria in terms of overall survival ([137]). However, these imaging modalities have limited sensitivity 68 – 80% and have been shown to underestimates pathologic staging of disease [110,138].

Although there are some reports of FDG PT/CT being useful in assessment of response post TACE, the low tumour to background is a limitation [139].

We have firstly shown that [^{18F}]FLT-PET can be used to accurately predict response to TACE in this small case series, and promisingly, was able to able detect extrahepatic disease. Whilst this study is a pilot study, the results generated are provocative and should be taken forward to larger prospective trials.

References

1. Ziegler SI. Positron emission tomography: principles, technology, and recent developments. *Nuclear Physics A.* 2005;752:679-687.
2. Townsend D. Physical principles and technology of clinical PET imaging. *Annals-Academy of Medicine Singapore.* 2004;33(2):133-145.
3. Zanzonico P. Positron emission tomography: a review of basic principles, scanner design and performance, and current systems. Paper presented at: Seminars in nuclear medicine2004.
4. Cherry SR, Sorenson JA, Phelps ME. *Physics in nuclear medicine e-Book.* Elsevier Health Sciences; 2012.
5. Eckerman KF, Endo A. *MIRD: radionuclide data and decay schemes.* Snmmi; 1989.
6. Humm JL, Rosenfeld A, Del Guerra A. From PET detectors to PET scanners. *European journal of nuclear medicine and molecular imaging.* 2003;30(11):1574-1597.
7. Muehllehner G, Karp J, Surti S. Design considerations for PET scanners. *The Quarterly Journal of Nuclear Medicine and Molecular Imaging.* 2002;46(1):16.
8. Jones W, Reed J, Everman J, Young J, Seese R. Next generation PET data acquisition architectures. *IEEE Transactions on Nuclear Science.* 1997;44(3):1202-1207.
9. Lundqvist H, Lubberink M, Tolmachev V. Positron emission tomography. *European journal of physics.* 1998;19(6):537.
10. Kinahan P, Defrise M. Theoretical aspects of medical image reconstruction. *Physica Medica.* 1996;12(SUPPL. 1):33-42.
11. Defrise M, Kinahan PE, Townsend DW, Michel C, Sibomana M, Newport DF. Exact and approximate rebinning algorithms for 3-D PET data. *IEEE transactions on medical imaging.* 1997;16(2):145-158.
12. Hudson HM, Larkin RS. Accelerated image reconstruction using ordered subsets of projection data. *IEEE transactions on medical imaging.* 1994;13(4):601-609.
13. Cal-Gonzalez J, Rausch I, Shiyam Sundar LK, et al. Hybrid Imaging: Instrumentation and Data Processing. *Frontiers in Physics.* 2018;6(47).
14. Bendriem B, Trebossen R, Frouin V, Syrota A. A PET scatter correction using simultaneous acquisitions with low and high lower energy thresholds. Paper presented at: Nuclear Science Symposium and Medical Imaging Conference, 1993., 1993 IEEE Conference Record.1993.
15. Ciarmiello A. MR-based attenuation correction in brain PET/MR studies: A short review. *Journal of Diagnostic Imaging in Therapy.* 2017;4(1):29-34.
16. Conti P, Strauss L. The applications of PET in clinical oncology. *J Nucl Med.* 1991;32(4):623-648.
17. Tomasi G, Turkheimer F, Aboagye E. Importance of quantification for the analysis of PET data in oncology: review of current methods and trends for the future. *Molecular Imaging and Biology.* 2012;14(2):131-146.
18. Boellaard R. Standards for PET image acquisition and quantitative data analysis. *J Nucl Med.* 2009;50(Suppl 1):11S-20S.
19. Kety SS, Schmidt CF. The nitrous oxide method for the quantitative determination of cerebral blood flow in man: theory, procedure and normal values. *The Journal of clinical investigation.* 1948;27(4):476-483.
20. Sokoloff L, Reivich M, Kennedy C, et al. The [14C] deoxyglucose method for the measurement of local cerebral glucose utilization: theory, procedure, and normal values in the conscious and anesthetized albino rat. *Journal of neurochemistry.* 1977;28(5):897-916.
21. Mintun MA, Raichle ME, Kilbourn MR, Wooten GF, Welch MJ. A quantitative model for the in vivo assessment of drug binding sites with positron emission tomography. *Annals of neurology.* 1984;15(3):217-227.

22. Morris ED, Endres CJ, Schmidt KC, Christian BT, Muzic RF, Fisher RE. Kinetic modeling in positron emission tomography. *Emission Tomography: The Fundamentals of PET and SPECT Academic, San Diego.* 2004.
23. Herscovitch P, Markham J, Raichle M. Brain blood flow measured with intravenous H215O. I. Theory and error analysis. *Journal of Nuclear Medicine.* 1983;24(9):782-789.
24. Phelps M, Huang S, Hoffman E, Selin C, Sokoloff L, Kuhl D. Tomographic measurement of local cerebral glucose metabolic rate in humans with (F-18) 2-fluoro-2-deoxy-D-glucose: validation of method. *Annals of neurology.* 1979;6(5):371-388.
25. Schuier F, Orzi F, Suda S, Lucignani G, Kennedy C, Sokoloff L. Influence of plasma glucose concentration on lumped constant of the deoxyglucose method: effects of hyperglycemia in the rat. *Journal of Cerebral Blood Flow & Metabolism.* 1990;10(6):765-773.
26. Cobelli C, Saccomani M, Ferrannini E, Defronzo RA, Gelfand R, Bonadonna R. A compartmental model to quantitate in vivo glucose transport in the human forearm. *American Journal of Physiology-Endocrinology And Metabolism.* 1989;257(6):E943-E958.
27. Bertoldo A, Vicini P, Sambuceti G, Lammertsma AA, Parodi O, Cobelli C. Evaluation of compartmental and spectral analysis models of [/sup 18/F] FDG kinetics for heart and brain studies with PET. *IEEE transactions on biomedical engineering.* 1998;45(12):1429-1448.
28. Cobelli C, Finkelstein L, Carson E. Mathematical modelling of endocrine and metabolic systems: Model formulation, identification and validation. *Mathematics and Computers in Simulation.* 1982;24(6):442-451.
29. Schiepers C, Chen W, Dahlbom M, Cloughesy T, Hoh CK, Huang SC. 18F-fluorothymidine kinetics of malignant brain tumors. *Eur J Nucl Med Mol Imaging.* 2007;34(7):1003-1011.
30. Schiepers C, Dahlbom M, Chen W, et al. Kinetics of 3'-deoxy-3'-18F-fluorothymidine during treatment monitoring of recurrent high-grade glioma. *J Nucl Med.* 2010;51(5):720-727.
31. Wardak M, Schiepers C, Cloughesy TF, Dahlbom M, Phelps ME, Huang SC. ^{18}F-FLT and ^{18}F-FDOPA PET kinetics in recurrent brain tumors. *Eur J Nucl Med Mol Imaging.* 2014;41(6):1199-1209.
32. Muzi M, Spence AM, O'Sullivan F, et al. Kinetic analysis of 3'-deoxy-3'-18F-fluorothymidine in patients with gliomas. *J Nucl Med.* 2006;47(10):1612-1621.
33. Sugawara Y, Zasadny KR, Grossman HB, Francis IR, Clarke MF, Wahl RL. Germ cell tumor: differentiation of viable tumor, mature teratoma, and necrotic tissue with FDG PET and kinetic modeling. *Radiology.* 1999;211(1):249-256.
34. Nishiyama Y, Yamamoto Y, Monden T, et al. Diagnostic value of kinetic analysis using dynamic FDG PET in immunocompetent patients with primary CNS lymphoma. *European Journal of Nuclear Medicine and Molecular Imaging.* 2007;34(1):78-86.
35. Doot RK, Muzi M, Peterson LM, et al. Kinetic analysis of 18F-fluoride PET images of breast cancer bone metastases. *J Nucl Med.* 2010;51(4):521-527.
36. Aboagye EO, Price PM. Use of positron emission tomography in anticancer drug development. *Investigational new drugs.* 2003;21(2):169-181.
37. Patlak CS, Blasberg RG, Fenstermacher JD. Graphical evaluation of blood-to-brain transfer constants from multiple-time uptake data. *Journal of Cerebral Blood Flow & Metabolism.* 1983;3(1):1-7.
38. Patlak CS, Blasberg RG. Graphical evaluation of blood-to-brain transfer constants from multiple-time uptake data. Generalizations. *Journal of Cerebral Blood Flow & Metabolism.* 1985;5(4):584-590.
39. Logan J, Fowler JS, Volkow ND, et al. Graphical analysis of reversible radioligand binding from time—activity measurements applied to [N-11C-methyl]-(−)-cocaine PET

studies in human subjects. *Journal of Cerebral Blood Flow & Metabolism.* 1990;10(5):740-747.
40. Cunningham VJ, Jones T. Spectral analysis of dynamic PET studies. *Journal of Cerebral Blood Flow & Metabolism.* 1993;13(1):15-23.
41. Phelps ME. *PET: molecular imaging and its biological applications.* Springer Science & Business Media; 2004.
42. Veronese M, Rizzo G, Bertoldo A, Turkheimer FE. Spectral analysis of dynamic PET studies: a review of 20 years of method developments and applications. *Computational and mathematical methods in medicine.* 2016;2016.
43. Slifstein M, Laruelle M. Models and methods for derivation of in vivo neuroreceptor parameters with PET and SPECT reversible radiotracers. *Nuclear medicine and biology.* 2001;28(5):595-608.
44. Aboagye EO, Bhujwalla ZM. Malignant transformation alters membrane choline phospholipid metabolism of human mammary epithelial cells. *Cancer research.* 1999;59(1):80-84.
45. Exton J. Phosphatidylcholine breakdown and signal transduction. *Biochimica et Biophysica Acta (BBA)-Lipids and Lipid Metabolism.* 1994;1212(1):26-42.
46. George T, Morash S, Cook H, Byers D, Palmer FSC, Spence M. Phosphatidylcholine biosynthesis in cultured glioma cells: evidence for channeling of intermediates. *Biochimica et Biophysica Acta (BBA)-Lipids and Lipid Metabolism.* 1989;1004(3):283-291.
47. Teegarden D, Taparowsky EJ, Kent C. Altered phosphatidylcholine metabolism in C3H10T1/2 cells transfected with the Harvey-ras oncogene. *Journal of Biological Chemistry.* 1990;265(11):6042-6047.
48. Fuccio C, Rubello D, Castellucci P, Marzola MC, Fanti S. Choline PET/CT for prostate cancer: main clinical applications. *European journal of radiology.* 2011;80(2):e50-e56.
49. Kenny L, Coombes R, Contractor K, et al. [11C] Choline-PET imaging of breast cancer. *Journal of Clinical Oncology.* 2009;27(15S):1110-1110.
50. Torizuka T, Kanno T, Futatsubashi M, Okada H. Imaging of gynecologic tumors: comparison of (11) C-choline PET with (18) F-FDG PET. *The Journal of Nuclear Medicine.* 2003;44(7):1051.
51. Terauchi T, Tateishi U, Maeda T, et al. A case of colon cancer detected by carbon-11 choline positron emission tomography/computed tomography: an initial report. *Japanese journal of clinical oncology.* 2007;37(10):797-800.
52. DeGrado TR, Coleman RE, Wang S, et al. Synthesis and evaluation of 18F-labeled choline as an oncologic tracer for positron emission tomography: initial findings in prostate cancer. *Cancer Research.* 2001;61(1):110-117.
53. Oprea-Lager DE, Vincent AD, van Moorselaar RJ, et al. Dual-phase PET-CT to differentiate [18F] fluoromethylcholine uptake in reactive and malignant lymph nodes in patients with prostate cancer. *PLoS One.* 2012;7(10):e48430.
54. Janzen T, Tavola F, Giussani A, et al. Compartmental model of 18 F-choline. Paper presented at: Medical Imaging 2010: Biomedical Applications in Molecular, Structural, and Functional Imaging2010.
55. Verwer EE, Oprea-Lager DE, van den Eertwegh A, et al. Quantification of 18F-fluorocholine kinetics in patients with prostate cancer. *J Nucl Med.* 2015;56(3):365-371.
56. Smith G, Zhao Y, Leyton J, et al. Radiosynthesis and pre-clinical evaluation of [18F] fluoro-[1, 2-2H4] choline. *Nuclear medicine and biology.* 2011;38(1):39-51.
57. Witney TH, Alam IS, Turton DR, et al. Evaluation of deuterated 18F-and 11C-labeled choline analogs for cancer detection by positron emission tomography. *Clinical Cancer Research.* 2012;18(4):1063-1072.
58. Leyton J, Smith G, Zhao Y, et al. [18F] fluoromethyl-[1, 2-2H4]-choline: a novel radiotracer for imaging choline metabolism in tumors by positron emission tomography. *Cancer research.* 2009;69(19):7721-7728.

59. Challapalli A, Sharma R, Hallett WA, et al. Biodistribution and radiation dosimetry of deuterium-substituted 18F-fluoromethyl-[1, 2-2H4] choline in healthy volunteers. *J Nucl Med.* 2014;55(2):256-263.
60. Khalighi MM, Engström M, Fan A, et al. Validation of an image derived input function estimation method on PET/MR. Paper presented at: Journal of Nuclear Medicine2017.
61. Just N. Improving tumour heterogeneity MRI assessment with histograms. *British journal of cancer.* 2014;111(12):2205.
62. Veronese M, Rizzo G, Aboagye E, Bertoldo A. Parametric imaging of 18 F-fluoro-3-deoxy-3-l-fluorothymidine PET data to investigate tumour heterogeneity. *European journal of nuclear medicine and molecular imaging.* 2014;41(9):1781-1792.
63. Kenny LM, Vigushin DM, Al-Nahhas A, et al. Quantification of cellular proliferation in tumor and normal tissues of patients with breast cancer by [18F] fluorothymidine-positron emission tomography imaging: evaluation of analytical methods. *Cancer research.* 2005;65(21):10104-10112.
64. Turkheimer F, Moresco R, Lucignani G, Sokoloff L, Fazio F, Schmidt K. The use of spectral analysis to determine regional cerebral glucose utilization with positron emission tomography and [18F] fluorodeoxyglucose: theory, implementation, and optimization procedures. *Journal of Cerebral Blood Flow & Metabolism.* 1994;14(3):406-422.
65. Janardhan S, Srivani P, Sastry GN. Choline kinase: an important target for cancer. *Current medicinal chemistry.* 2006;13(10):1169-1186.
66. Brown RS, Leung JY, Kison PV, Zasadny KR. Glucose transporters and FDG uptake in untreated primary human non-small cell lung cancer. *The Journal of Nuclear Medicine.* 1999;40(4):556.
67. Kubota K, Ishiwata K, Kubota R, et al. Tracer feasibility for monitoring tumor radiotherapy: a quadruple tracer study with fluorine-18-fluorodeoxyglucose or fluorine-18-fluorodeoxyuridine, L-[methyl-14C] methionine,[6-3H] thymidine, and gallium-67. *Journal of Nuclear Medicine.* 1991;32(11):2118-2123.
68. Bos R, van der Hoeven JJ, van der Wall E, et al. Biologic correlates of 18fluorodeoxyglucose uptake in human breast cancer measured by positron emission tomography. *Journal of Clinical Oncology.* 2002;20(2):379-387.
69. de Molina AR, Rodríguez-González An, Gutiérrez R, et al. Overexpression of choline kinase is a frequent feature in human tumor-derived cell lines and in lung, prostate, and colorectal human cancers. *Biochemical and biophysical research communications.* 2002;296(3):580-583.
70. Sarri E, Garcia-Dorado D, Abellan A, Soler-Soler J. Effects of hypoxia, glucose deprivation and acidosis on phosphatidylcholine synthesis in HL-1 cardiomyocytes. CTP: phosphocholine cytidylyltransferase activity correlates with sarcolemmal disruption. *Biochemical Journal.* 2006;394(1):325-334.
71. Bansal A, Shuyan W, Hara T, Harris RA, DeGrado TR. Biodisposition and metabolism of [18 F] fluorocholine in 9L glioma cells and 9L glioma-bearing fisher rats. *European journal of nuclear medicine and molecular imaging.* 2008;35(6):1192-1203.
72. Shukla-Dave A, Lee NY, Jansen JF, et al. Dynamic contrast-enhanced magnetic resonance imaging as a predictor of outcome in head-and-neck squamous cell carcinoma patients with nodal metastases. *International Journal of Radiation Oncology• Biology• Physics.* 2012;82(5):1837-1844.
73. King AD, Chow K-K, Yu K-H, et al. Head and neck squamous cell carcinoma: diagnostic performance of diffusion-weighted MR imaging for the prediction of treatment response. *Radiology.* 2013;266(2):531-538.
74. Bentourkia Mh. PET kinetic modeling of 11C-acetate from projections. *Computerized medical imaging and graphics.* 2003;27(5):373-379.

75. Marshall RC, Powers-Risius P, Reutter BW, et al. Kinetic analysis of 18F-fluorodihydrorotenone as a deposited myocardial flow tracer: comparison to 201Tl. *Journal of Nuclear Medicine.* 2004;45(11):1950-1959.
76. Meikle SR, Eberl S, Iida H. Instrumentation and methodology for quantitative pre-clinical imaging studies. *Current pharmaceutical design.* 2001;7(18):1945-1966.
77. Myers JF, Rosso L, Watson BJ, et al. Characterisation of the contribution of the GABA-benzodiazepine α1 receptor subtype to [11C] Ro15-4513 PET images. *Journal of Cerebral Blood Flow & Metabolism.* 2012;32(4):731-744.
78. Hammers A, Asselin M-C, Turkheimer FE, et al. Balancing bias, reliability, noise properties and the need for parametric maps in quantitative ligand PET:[11C] diprenorphine test–retest data. *Neuroimage.* 2007;38(1):82-94.
79. Price JC, Klunk WE, Lopresti BJ, et al. Kinetic modeling of amyloid binding in humans using PET imaging and Pittsburgh Compound-B. *Journal of Cerebral Blood Flow & Metabolism.* 2005;25(11):1528-1547.
80. Miederer I, Ziegler SI, Liedtke C, et al. Kinetic modelling of [11C] flumazenil using data-driven methods. *European journal of nuclear medicine and molecular imaging.* 2009;36(4):659-670.
81. Zanotti-Fregonara P, Leroy C, Roumenov D, Trichard C, Martinot J-L, Bottlaender M. Kinetic analysis of [11 C] befloxatone in the human brain, a selective radioligand to image monoamine oxidase A. *EJNMMI research.* 2013;3(1):78.
82. Zanotti-Fregonara P, Xu R, Zoghbi SS, et al. The PET radioligand 18F-FIMX images and quantifies metabotropic glutamate receptor 1 in proportion to the regional density of its gene transcript in human brain. *Journal of Nuclear Medicine.* 2016;57(2):242-247.
83. Gullberg GT, Reutter BW, Sitek A, Maltz JS, Budinger TF. Dynamic single photon emission computed tomography—basic principles and cardiac applications. *Physics in Medicine & Biology.* 2010;55(20):R111.
84. Pencek RR, Bertoldo A, Price J, Kelley C, Cobelli C, Kelley DE. Dose-responsive insulin regulation of glucose transport in human skeletal muscle. *American Journal of Physiology-Endocrinology and Metabolism.* 2006;290(6):E1124-E1130.
85. Puri T, Blake GM, Frost ML, et al. Comparison of six quantitative methods for the measurement of bone turnover at the hip and lumbar spine using 18F-fluoride PET-CT. *Nuclear medicine communications.* 2012;33(6):597-606.
86. Murase K, Tsuda T, Mochizuki T, Ikezoe J. A simplified method for the quantitative analysis of 99Tc (m)-GSA liver scintigraphy using spectral analysis. *Nuclear medicine communications.* 1998;19(3):219-227.
87. Tomasi G, Kenny L, Mauri F, Turkheimer F, Aboagye EO. Quantification of receptor-ligand binding with [18 F] fluciclatide in metastatic breast cancer patients. *European journal of nuclear medicine and molecular imaging.* 2011;38(12):2186-2197.
88. Verwer EE, Bahce I, van Velden FH, et al. Parametric methods for quantification of 18F-FAZA kinetics in non–small cell lung cancer patients. *Journal of Nuclear Medicine.* 2014;55(11):1772-1777.
89. Gapstur SM, Morrow M, Sellers TA. Hormone replacement therapy and risk of breast cancer with a favorable histology: results of the Iowa Women's Health Study. *Jama.* 1999;281(22):2091-2097.
90. Nakhlis F, Morrow M. Ductal carcinoma in situ. *Surgical Clinics.* 2003;83(4):821-839.
91. Mossa-Basha M, Fundaro GM, Shah BA, Ali S, Pantelic MV. Ductal carcinoma in situ of the breast: MR imaging findings with histopathologic correlation. *Radiographics.* 2010;30(6):1673-1687.
92. Rostom A, Powe J, Kandil A, et al. Positron emission tomography in breast cancer: a clinicopathological correlation of results. *The British journal of radiology.* 1999;72(863):1064-1068.

93. Avril N, Rose C, Schelling M, et al. Breast imaging with positron emission tomography and fluorine-18 fluorodeoxyglucose: use and limitations. *Journal of clinical oncology.* 2000;18(20):3495-3502.
94. Mavi A, Urhan M, Jian QY, et al. Dual time point 18F-FDG PET imaging detects breast cancer with high sensitivity and correlates well with histologic subtypes. *Journal of nuclear medicine.* 2006;47(9):1440-1446.
95. Azuma A, Tozaki M, Ito K, Fukuma E, Tanaka T, O'uchi T. Ductal carcinoma in situ: correlation between FDG-PET/CT and histopathology. *Radiation medicine.* 2008;26(8):488-493.
96. Shreve PD, Anzai Y, Wahl RL. Pitfalls in oncologic diagnosis with FDG PET imaging: physiologic and benign variants. *Radiographics.* 1999;19(1):61-77.
97. Shields AF, Grierson JR, Dohmen BM, et al. Imaging proliferation in vivo with [F-18] FLT and positron emission tomography. *Nature medicine.* 1998;4(11):1334.
98. Rasey JS, Grierson JR, Wiens LW, Kolb PD, Schwartz JL. Validation of FLT uptake as a measure of thymidine kinase-1 activity in A549 carcinoma cells. *Journal of Nuclear Medicine.* 2002;43(9):1210-1217.
99. Kenny L, Coombes RC, Vigushin DM, Al-Nahhas A, Shousha S, Aboagye EO. Imaging early changes in proliferation at 1 week post chemotherapy: a pilot study in breast cancer patients with 3′-deoxy-3′-[18F] fluorothymidine positron emission tomography. *European journal of nuclear medicine and molecular imaging.* 2007;34(9):1339-1347.
100. Pio BS, Park CK, Pietras R, et al. Usefulness of 3′-[F-18] fluoro-3′-deoxythymidine with positron emission tomography in predicting breast cancer response to therapy. *Molecular Imaging and Biology.* 2006;8(1):36-42.
101. Herrmann K, Wieder HA, Buck AK, et al. Early response assessment using 3′-deoxy-3′-[18F] fluorothymidine-positron emission tomography in high-grade non-Hodgkin's lymphoma. *Clinical Cancer Research.* 2007;13(12):3552-3558.
102. Muzi M, Vesselle H, Grierson JR, et al. Kinetic analysis of 3′-deoxy-3′-fluorothymidine PET studies: validation studies in patients with lung cancer. *Journal of Nuclear Medicine.* 2005;46(2):274-282.
103. Turkheimer F, Sokoloff L, Bertoldo A, et al. Estimation of component and parameter distributions in spectral analysis. *Journal of Cerebral Blood Flow & Metabolism.* 1998;18(11):1211-1222.
104. Badruddoja M. Ductal carcinoma in situ of the breast: a surgical perspective. *International journal of surgical oncology.* 2012;2012.
105. Riedl CC, Ponhold L, Flöry D, et al. Magnetic resonance imaging of the breast improves detection of invasive cancer, preinvasive cancer, and premalignant lesions during surveillance of women at high risk for breast cancer. *Clinical Cancer Research.* 2007;13(20):6144-6152.
106. Söderqvist G, Isaksson E, von Schoultz B, Carlström K, Tani E, Skoog L. Proliferation of breast epithelial cells in healthy women during the menstrual cycle. *American Journal of Obstetrics & Gynecology.* 1997;176(1):123-128.
107. Hoque A, Menter DG, Sahin AA, Sneige N, Lippman SM. No increased Ki67 expression in ductal carcinoma in situ associated with invasive breast cancer. *Cancer Epidemiology and Prevention Biomarkers.* 2001;10(2):153-154.
108. Teo N, Shoker B, Jarvis C, Martin L, Sloane J, Holcombe C. Vascular density and phenotype around ductal carcinoma in situ (DCIS) of the breast. *British journal of cancer.* 2002;86(6):905.
109. IARC. http://www-dep.iarc.fr/. Accessed 10/10/2013, 2013.
110. Chapman WC, Majella Doyle MB, Stuart JE, et al. Outcomes of neoadjuvant transarterial chemoembolization to downstage hepatocellular carcinoma before liver transplantation. *Ann Surg.* 2008;248(4):617-625.

111. Llovet JM, Real MI, Montana X, et al. Arterial embolisation or chemoembolisation versus symptomatic treatment in patients with unresectable hepatocellular carcinoma: a randomised controlled trial. *Lancet.* 2002;359(9319):1734-1739.
112. Bieze M, Klumpen HJ, Verheij J, et al. Diagnostic accuracy of 18F-methyl-choline PET/CT for intra- and extrahepatic hepatocellular carcinoma. *Hepatology.* 2013.
113. Trojan J, Schroeder O, Raedle J, et al. Fluorine-18 FDG positron emission tomography for imaging of hepatocellular carcinoma. *Am J Gastroenterol.* 1999;94(11):3314-3319.
114. Yamamoto Y, Nishiyama Y, Kameyama R, et al. Detection of hepatocellular carcinoma using 11C-choline PET: comparison with 18F-FDG PET. *J Nucl Med.* 2008;49(8):1245-1248.
115. Toyohara J, Waki A, Takamatsu S, Yonekura Y, Magata Y, Fujibayashi Y. Basis of FLT as a cell proliferation marker: comparative uptake studies with [3H]thymidine and [3H]arabinothymidine, and cell-analysis in 22 asynchronously growing tumor cell lines. *Nuclear medicine and biology.* 2002;29(3):281-287.
116. Van Waarde A, Jager PL, Ishiwata K, Dierckx RA, Elsinga PH. Comparison of sigma-ligands and metabolic PET tracers for differentiating tumor from inflammation. *The Journal of Nuclear Medicine.* 2006;47(1):150.
117. van Waarde A, Cobben DC, Suurmeijer AJ, et al. Selectivity of 18F-FLT and 18F-FDG for differentiating tumor from inflammation in a rodent model. *J Nucl Med.* 2004;45(4):695-700.
118. Eckel F, Herrmann K, Schmidt S, et al. Imaging of proliferation in hepatocellular carcinoma with the in vivo marker 18F-fluorothymidine. *J Nucl Med.* 2009;50(9):1441-1447.
119. Pinato DJ, Sharma R. An inflammation-based prognostic index predicts survival advantage after transarterial chemoembolization in hepatocellular carcinoma. *Translational research : the journal of laboratory and clinical medicine.* 2012;160(2):146-152.
120. Bruix J, Sherman M. Management of hepatocellular carcinoma. *Hepatology.* 2005;42(5):1208-1236.
121. Edeline J, Boucher E, Rolland Y, et al. Comparison of tumor response by Response Evaluation Criteria in Solid Tumors (RECIST) and modified RECIST in patients treated with sorafenib for hepatocellular carcinoma. *Cancer.* 2012;118(1):147-156.
122. Lencioni R, Llovet JM. Modified RECIST (mRECIST) assessment for hepatocellular carcinoma. Paper presented at: Seminars in liver disease2010.
123. Kenny LM, Vigushin DM, Al-Nahhas A, et al. Quantification of cellular proliferation in tumor and normal tissues of patients with breast cancer by [18F]fluorothymidine-positron emission tomography imaging: evaluation of analytical methods. *Cancer research.* 2005;65(21):10104-10112.
124. Contractor KB, Kenny LM, Stebbing J, et al. [18F]-3'Deoxy-3'-fluorothymidine positron emission tomography and breast cancer response to docetaxel. *Clinical cancer research : an official journal of the American Association for Cancer Research.* 2011;17(24):7664-7672.
125. Eisenhauer EA, Therasse P, Bogaerts J, et al. New response evaluation criteria in solid tumours: revised RECIST guideline (version 1.1). *European journal of cancer.* 2009;45(2):228-247.
126. Kenny L, Coombes RC, Vigushin DM, Al-Nahhas A, Shousha S, Aboagye EO. Imaging early changes in proliferation at 1 week post chemotherapy: a pilot study in breast cancer patients with 3'-deoxy-3'-[18F]fluorothymidine positron emission tomography. *European journal of nuclear medicine and molecular imaging.* 2007;34(9):1339-1347.
127. Contractor K, Challapalli A, Tomasi G, et al. Imaging of cellular proliferation in liver metastasis by [18F] fluorothymidine positron emission tomography: effect of therapy. *Physics in Medicine & Biology.* 2012;57(11):3419.

128. European Association for the Study of the Liver. Electronic address eee, European Association for the Study of the L. EASL Clinical Practice Guidelines: Management of hepatocellular carcinoma. *J Hepatol.* 2018;69(1):182-236.
129. Chalaye J, Costentin CE, Luciani A, et al. Positron emission tomography/computed tomography with 18F-fluorocholine improve tumor staging and treatment allocation in patients with hepatocellular carcinoma. *J Hepatol.* 2018;69(2):336-344.
130. van Waarde A, Cobben DC, Suurmeijer AJ, et al. Selectivity of 18F-FLT and 18F-FDG for differentiating tumor from inflammation in a rodent model. *J Nucl Med.* 2004;45(4):695-700.
131. Kenny LM, Vigushin DM, Al-Nahhas A, et al. Quantification of cellular proliferation in tumor and normal tissues of patients with breast cancer by [18F]fluorothymidine-positron emission tomography imaging: evaluation of analytical methods. *Cancer Res.* 2005;65(21):10104-10112.
132. Francis DL, Freeman A, Visvikis D, et al. In vivo imaging of cellular proliferation in colorectal cancer using positron emission tomography. *Gut.* 2003;52(11):1602-1606.
133. Buck AK, Halter G, Schirrmeister H, et al. Imaging proliferation in lung tumors with PET: 18F-FLT versus 18F-FDG. *J Nucl Med.* 2003;44(9):1426-1431.
134. Eckel F, Herrmann K, Schmidt S, et al. Imaging of proliferation in hepatocellular carcinoma with the in vivo marker 18F-fluorothymidine. *Journal of Nuclear Medicine.* 2009;50(9):1441.
135. Jain RK. Normalization of tumor vasculature: an emerging concept in antiangiogenic therapy. *Science.* 2005;307(5706):58-62.
136. Muzi M, Spence AM, O'Sullivan F, et al. Kinetic analysis of 3′-deoxy-3′-18F-fluorothymidine in patients with gliomas. *Journal of Nuclear Medicine.* 2006;47(10):1612-1621.
137. Vincenzi B, Di Maio M, Silletta M, et al. Prognostic relevance of objective response according to EASL criteria and mRECIST criteria in hepatocellular carcinoma patients treated with loco-regional therapies: a literature-based meta-analysis. *PLoS One.* 2015;10(7):e0133488.
138. Colli A, Fraquelli M, Casazza G, et al. Accuracy of ultrasonography, spiral CT, magnetic resonance, and alpha-fetoprotein in diagnosing hepatocellular carcinoma: a systematic review. *Am J Gastroenterol.* 2006;101(3):513-523.
139. Song MJ, Bae SH, Yoo IR, et al. Predictive value of 18F-fluorodeoxyglucose PET/CT for transarterial chemolipiodolization of hepatocellular carcinoma. *World journal of gastroenterology: WJG.* 2012;18(25):3215.

CHAPTER 3

The basics of MRI

The basis of magnetic resonance (MR) technique is the measurement of radiofrequency radiation resulting from transitions induced between nuclear spin states of tissue hydrogen atoms (protons) in the presence of a strong external magnetic field [1]. The behaviour of a tissue subjected to a magnetic field relies on quantum mechanics and pixel intensities, in MR images, are a function of proton densities and tissue relaxation times [2]. For clinical imaging, hydrogen is the most frequently used nucleus, but other possible nuclei are carbon-13, sodium, and phosphorus. Under normal circumstances these tiny magnets are randomly distributed in space, the magnetic moments cancel each other out, and thus the net magnetic vector is zero (Figure 26A). However, when the patient is submitted to a strong external magnetic field (B_0) the nuclei adopt one of two possible orientations: parallel or antiparallel to the external field (Figure 26B).

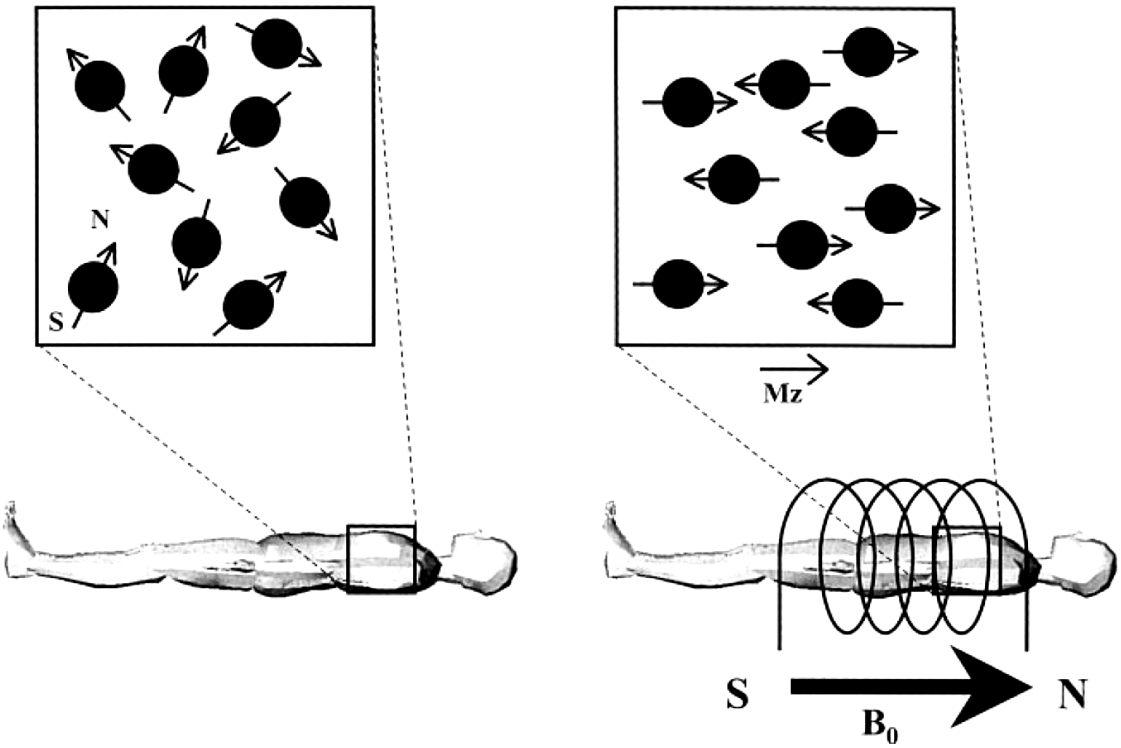

Figure 26**: A) Without a magnetic field the magnetic moments of the nuclei are distributed at random and thus the net magnetization factor is zero. (B) When there is a strong external magnetic field the spinning nuclei align parallel or antiparallel to the external field (B0) with a few more parallel than antiparallel. This results in a net magnetization vector (M_Z) parallel to the external magnetic field**.

Parallel alignment is the lower energy state and is thus the preferred alignment, whereas antiparallel alignment is the higher energy state [2]. M_z is the net magnetization vector aligned to the external magnet. Individual nuclei do not actually line up with the magnetic field but precess around the direction of the external field (Figure 27A) at the Larmor frequency F:

$$F = \gamma B_0/2\pi \quad 17)$$

where γ is the gyromagnetic ratio of the nucleus. In the frequently used commercial systems of 1.5 Tesla (T), the Larmor frequency is 63.75 MHz for hydrogen but the phase of precession around the axis of the magnetic field is different for each individual nucleus (Figure 27B) [2].
The net magnetization vector from the nuclei inside the magnet in its equilibrium state is static and does not produce a measurable signal. To obtain information from the spins, the direction of the net magnetization vector has to be altered: the precessing spins are excited by applying energy in the form of radiofrequency (RF) energy pulses of exactly the Larmor frequency (resonance frequency). When an RF signal is given at the resonance frequency into the patient, two phenomena occur: first, enough protons absorb energy to jump from the parallel state to the higher level of the antiparallel state, and second, the spins are ‘‘whipped’’ to precess in phase [2]. As a consequence, M_z flips 90° from the positive z-axis to transverse plane, it rotates around B_0 at the Larmor frequency. This rotating transverse magnetization can be measured, because it will induce an alternating current (AC) in the receiver coil placed around the patient (Figure 27).

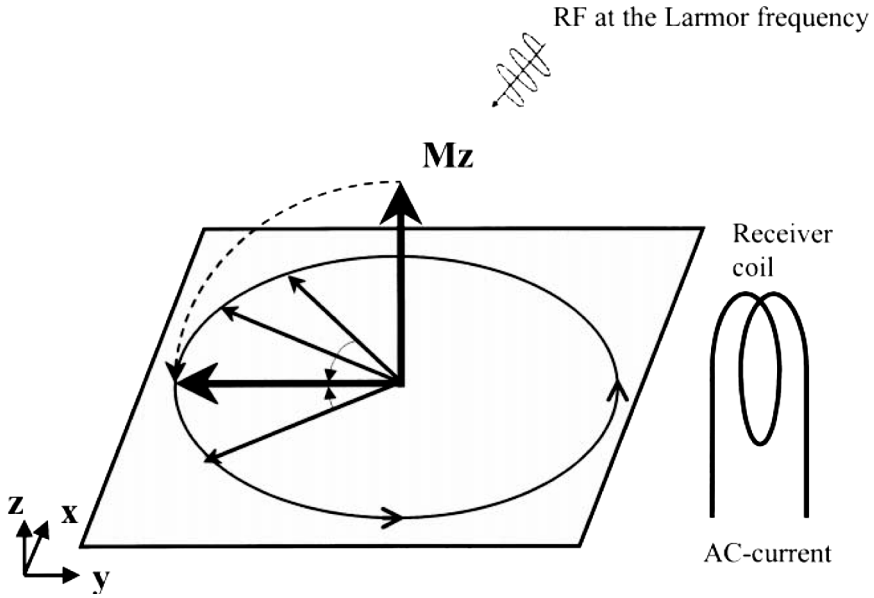

Figure 27: When the spins are exited with an RF pulse of exactly the Larmor frequency, the net magnetization flips 90° and the spins are ‘‘whipped’’ to precess in phase. The rotating net magnetization vector induces an AC in a receiver coil.

After the RF frequency transmitter is switched off, M_z decays over time and, consequently, the induced signal in the receiver coil. This decreasing signal is called the free induction decay (FID) (Figure 28) and the time required for the signal to return to equilibrium is the relaxation time [2].

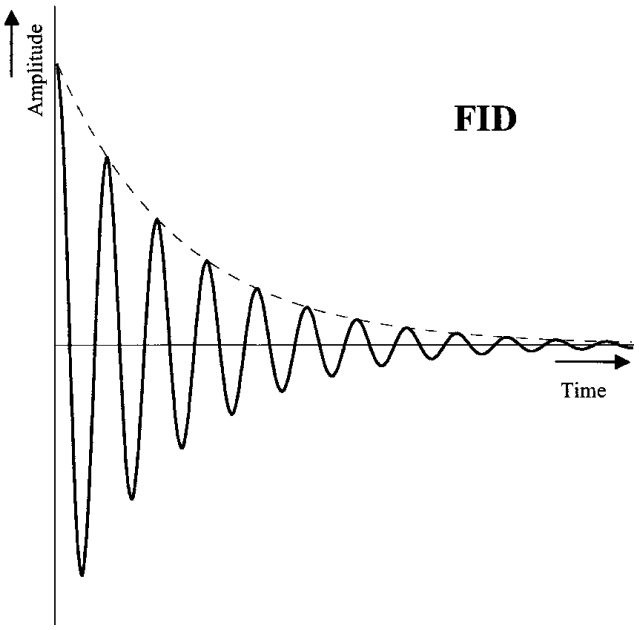

Figure 28: The received signal detected by the receiver coil, the FID, decreases over time when the net magnetization vector returns to its original orientation.

Two relaxation processes exist: transverse relaxation and longitudinal relaxation. Both processes are independent. The process of realignment to the external magnetic field is called the longitudinal relaxation process (Figure 29) and it is characterized by the relaxation time T_1. It is defined as the time required for the system to recover to 63% of its equilibrium value after it has been exposed to a 90° RF pulse (Figure 29).

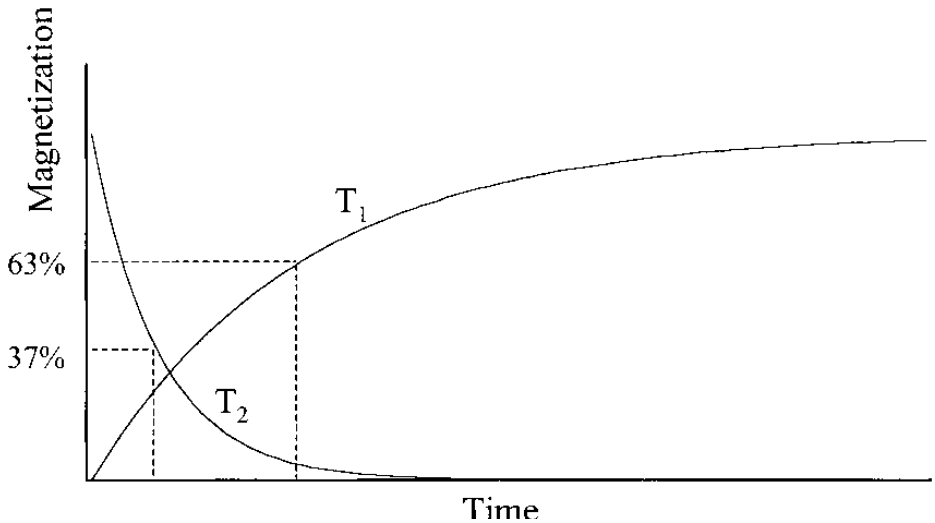

Figure 29: Longitudinal relaxation is characterized by theT1 relaxation time, which is the time to recover 63% of the original net magnetization vector. Transverse relaxation is characterized by the T2 time, which is the time it takes to decay the signal to 37% of the original signal.

Various human tissues have different T_1 values (Table 12).

Table 12: Relaxation times T1 and T2 and proton density in different tissues at different magnetic field strength.

Field strength (T)	Tissue	T1 (ms)	T2 (ms)	T2* (ms)	Proton Density
1.5	White matter	510	67	78	0.61
	Gray matter	760	77	69	0.69
	Arterial blood	1441	290	55	0.72

3.0	CSF	2650	280	na	1.0
	White matter	1080	70	50	0.61
	Gray matter	1820	100	50	0.69
	Arterial blood	1932	275	46	0.72
	CSF	3817	1442	na	1.0

The second process of relaxation, the transverse relaxation, depends on the spins precessing around the magnetization vector. Initially, after the excitation by the RF pulse, the spins precess completely in phase. However, as time passes, the observed signal starts to decrease because the spins begin to diphase due to small differences in the Larmor frequency induced by random local magnetic inhomogeneities, due to spin-spin interaction and inhomogeneity of the main static magnetic field B_0.
The spin-spin relaxation and is characterized by the relaxation time T_2, which is the time required by the signal to decay to 37% of its original value (Figure 29). There is also a reversible bulk field dephasing effect caused by local field inhomogeneities, and its characteristic time is referred to as T2* relaxation [3]. These additional dephasing fields come from the main magnetic field inhomogeneity, the differences in magnetic susceptibility among various tissues or materials, chemical shift, and gradients applied for spatial encoding (Figure 30).

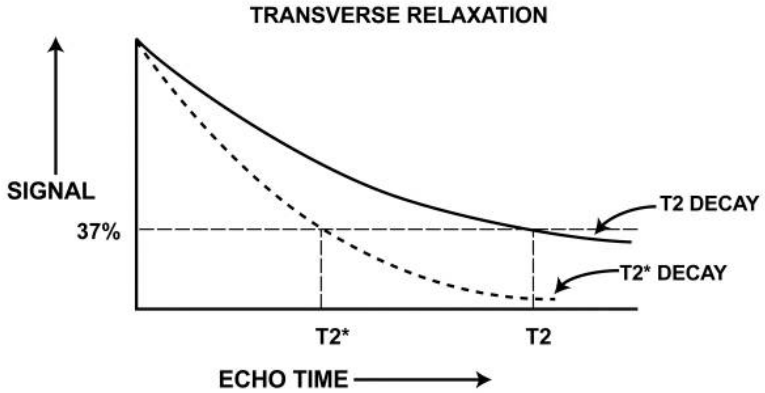

Figure 30: Graph shows T2 and T2* relaxation curves. T2* is shorter than T2.

MRI depends on the signal derived from the H-protons. It contains information about the position of these protons in the patient. The image is created in three steps:

1) slice selection
2) frequency encoding and
3) phase encoding.

The *slice selection* is done with the application of a magnetic gradient (for example 25 mT/m) in addition to the main magnetic field (usually in the caudal to cranial direction - G_z). Because the frequency of precession, and thus the frequency at which the spins can be excited, is dependent on the local strength of the magnetic field, a narrow band of frequencies will only excite a thin slice (3 to 8mm) of spins through the body. With a change in the excitation frequency another parallel slice can be acquired later. It is possible to obtain slices in other directions as the direction of gradients for the slice encoding are combinations of gradients in all three directions. The *frequency and phase encoding* are used to obtain information for the individual points within a slice, the pixels.
Since the frequency of the spins procession in the presence of a gradient field is a linear function of frequency and thus a linear function of position, the location of a given group of spins (in one direction at least) depends on their frequency. The time domain of the NMR signal is deconstructed into a histogram of the frequencies present in the signal (a spectrum) via Fourier

transform. The frequency encoding is done with a readout gradient (G_x) whose direction (the encoding direction) is called "readout direction". As for the frequency, the phase of the MR signal form a voxel full of spins depends on their position and the entire history of the gradients applied from excitation to measurements. For the phase encoding, a short temporary change in the magnetic field is applied between the RF excitation pulse and the readout of the signal. This change in the magnetic field will shift the phase of precessing of the spins and this will be dependent on the duration of this gradient switch. By repeating this process with different duration of the temporary gradients, signals with a different phase encoding can be acquired. Combining phase and frequency information allows the creation of a grid in which each pixel has a defined combination of phase and frequency codes: the K-space. With a Fast Fourier Transform, the raw data, which represent an amplitude as a function of time, are transformed into a curve that represents an amplitude as function of the frequency. The amplitude of each frequency represents the intensity of each pixel. The Fourier Transform is performed in both the frequency and phase encoding direction [2].

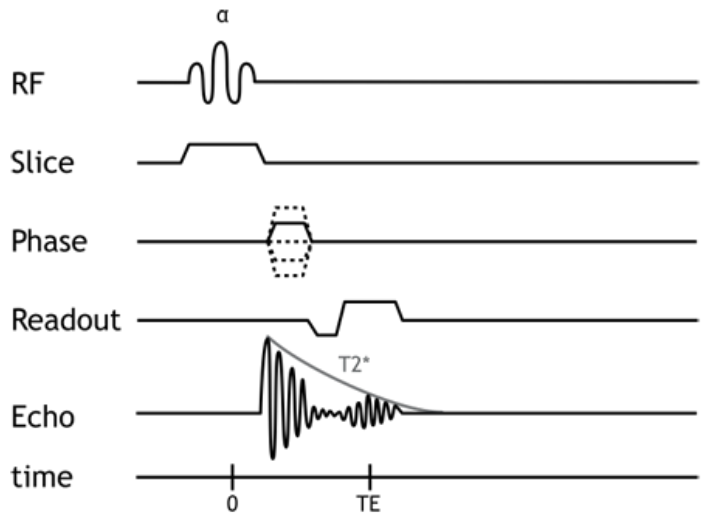

Figure 31: Pulse sequence technique.

In an MR experiment, only the RF signal can be determined by measurement, which is induced by the rotating transverse magnetization M_{xy} in the receiver coil. A defined sequence of RF pulses, which is usually repeated several times, is called a pulse sequence (*Figure 31*) [4]. The diagram of a pulse sequence is composed of several parallel lines (at least four: one for the RF pulse, and one each for the x-, y-, and z-axis gradients). The pulse sequence diagram is a schema of the timing of instructions sent to the RF generator and gradient amplifiers. There are only two fundamental types of MR pulse sequences: spin-echo (SE) and gradient recalled echo (GRE) [5].

MRI Sequences

SE Sequences - In SE sequences, a 90° pulse flips the net magnetization vector into the transverse plane. As the spinning nuclei go through T_1, T_2, and T_2*relaxation, the transverse magnetization is gradually dephased. A 180° pulse is applied at a time equal to one-half of TE to rephase the spinning nuclei. When the nuclei are again spinning in phase (at total TE), an echo is produced and read (Figure 32). Most conventional SE sequences are very long and therefore are not used frequently. However, advances in MR imaging technology have enabled a reduction in acquisition time with the use of fast SE sequences. Sequences that have a short TR and short TE are used to obtain T_1 weighting. Those with a long TR and short TE result in proton-density weighting. When

the TR is long and the TE is long, T_2 weighting is achieved. Sequentially increasing the TE of a sequence weights it more heavily toward T_2 [5].

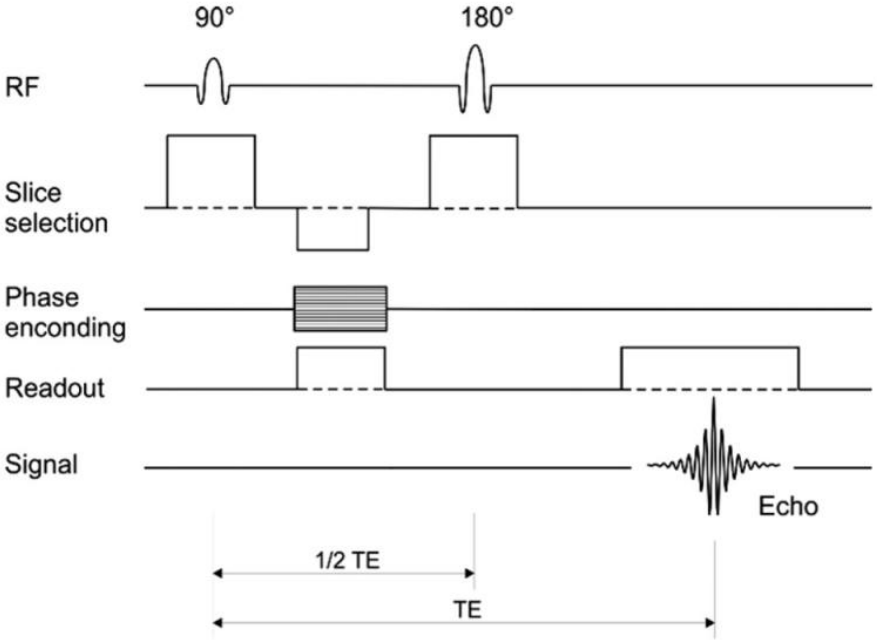

Figure 32: Time diagram of a conventional spin echo sequence

One of the first SE variant is its fast or turbo version where a single 90° pulse is applied to flip the net magnetization vector, after which multiple 180°rephasing pulses are applied, each of which creates an echo (Figure 33). All the echoes together are called an echo train, and the total number of 180° RF pulses and echoes is referred to as the echo train length. The acquisition time is greatly reduced with use of a fast SE sequence as opposed to a conventional SE sequence. It is approximately proportional to 1/ETL, where ETL is the echo train length, for imaging of a single section or a small number of sections. However, at imaging of larger volumes, the reduction of acquisition time is highly dependent on the spatial coverage [5].

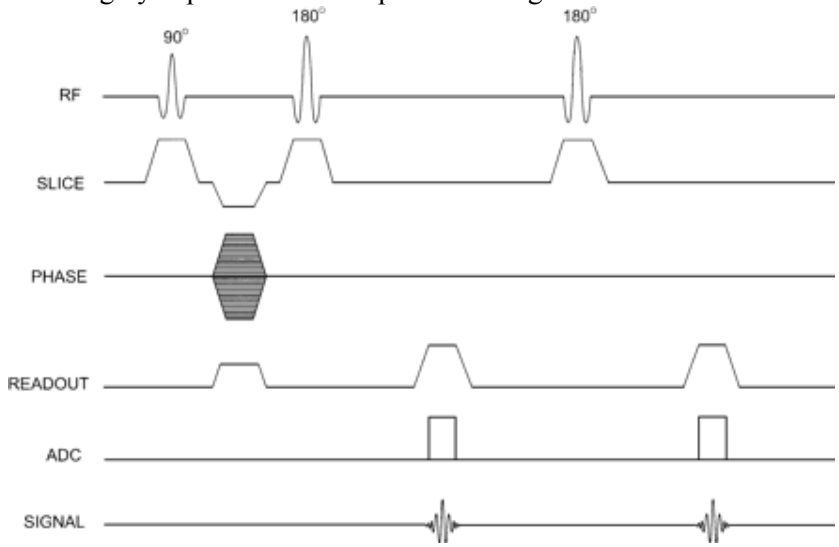

Figure 33: Time diagram of a fast spin echo sequence.

A second variant of SE is given by the inversion recovery sequence (IR) where a 180° preparatory pulse is applied to flip the net magnetization vector 180° and null the signal from a particular entity (e.g., water in tissue). When the RF pulse ceases, the spinning nuclei begin to relax. When

the net magnetization vector for water passes the transverse plane (the null point for that tissue), the conventional 90° pulse is applied, and the SE sequence then continues as before (Figure 34). The interval between the 180° pulse and the 90° pulse is the inversion time (TI). At TI, the net magnetization vector of water is very weak, whereas that for body tissues is strong [5].

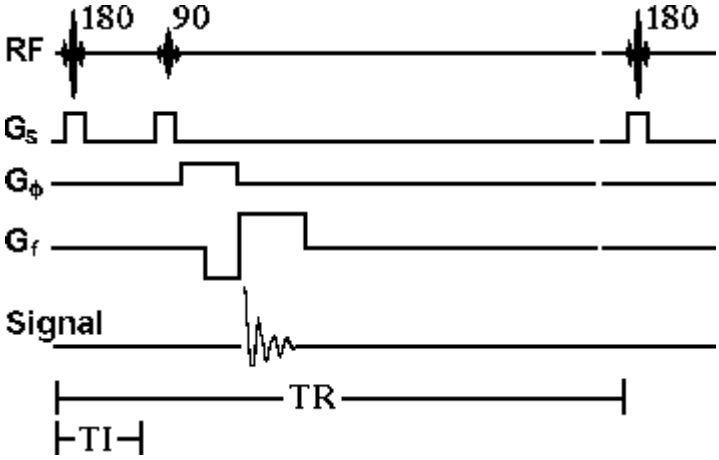

Figure 34: Time diagram of an inversion recovery sequence.

When the net magnetization vectors are flipped by the 90° pulse, there is little or no transverse magnetization in water, so no signal is generated (fluid appears dark), whereas signal intensity ranges from low to high in tissues with a stronger net magnetization vector. Two important clinical implementations of the inversion recovery concept are the short TI inversion-recovery (STIR) sequence and the fluid-attenuated inversion-recovery (FLAIR) sequence [5].

GRE Sequences - In a GRE sequence, an RF pulse is applied that partly flips the net magnetization vector into the transverse plane (variable flip angle). Gradients, as opposed to RF pulses, are used to gradients) transverse magnetization (Figure 35). Because gradients do not refocus field inhomogeneities, GRE sequences with long TEs are T_2*weighted (because of magnetic susceptibility) rather than T_2 weighted like SE sequences. GRE sequences are sensitive to magnetic field inhomogeneity secondary to magnetic susceptibility differences between tissues. Magnetic susceptibility–related signal loss, or susceptibility artefact, is caused by magnetic field (B_0) inhomogeneity and can be described in terms of T_2*signal decay. This inhomogeneity (local variation in B_0) usually occurs at the interface between entities (e.g., tissue and air) that have different magnetic susceptibilities. Because magnetic fields vary locally, some spinning nuclei precess faster than others; so when the individual vectors are added to obtain the net magnetization vector, there is a progressive decrease in the magnitude of the net magnetization vector over time. This decrease results in a progressive decrease in signal intensity, which eventually leads to a signal void [5]. Magnetic susceptibility imaging is the basis of cerebral perfusion studies, in which the T_2* effects (i.e., signal decrease) created by gadolinium (a metal injected intravenously as a chelated ion in aqueous solution, typically in the form of gadopentetate dimeglumine) are sensitively depicted by GRE sequences. Magnetic susceptibility is also used in blood oxygenation level–dependent (BOLD) imaging, in which the relative amount of deoxyhemoglobin in the cerebral vasculature is measured as a reflection of neuronal activity.

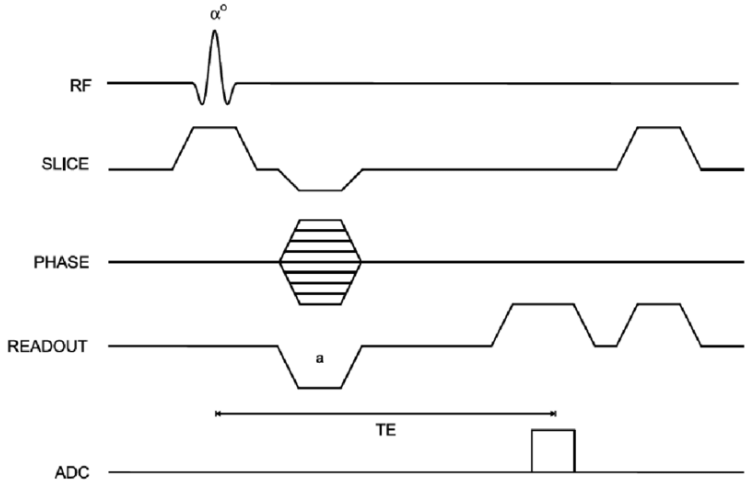

Figure 35: Time diagram of a gradient echo sequence.

A variant of the conventional GRE is the spoiled GRE where a spoiler RF pulse or gradient is used to eradicate any remaining transverse magnetization after each echo, thereby producing the same effect as T_1 or proton-density weighting. Spoiled GRE sequences are especially useful for contrast material–enhanced MR imaging and cardiac imaging [5].

Recently, multiband or simultaneous multi-slice EPI technique has been introduced[6]. It effectively shortens acquisition time without decreasing TE and, principally, without sacrificing SNR by simultaneous acquisition of multiple slices. Similar to parallel imaging, spatial encoding critically relies on the spatially varying sensitivities of RF receive coil arrays. The technique requires multiband RF pulses which achieve simultaneous excitation of multiple slices, and reconstruction is most easily done by means of the SENSE algorithm. This method facilitates a considerable shortening of volume acquisition times because the number of simultaneously acquired slices, i.e. the multiband factor, directly translates into a reduced number of excitations and thus measurement time. Similar to parallel imaging the specified spatial resolution is preserved but there is no direct SNR penalty $\sim 1/\sqrt{R}$ due to a reduced number of acquisitions with acceleration factor R[6].

Artefacts in MRI

Artefacts in magnetic resonance imaging may be caused by the MR scanner hardware itself or by the interaction of the patient with the hardware[7]. Artefacts and foreign bodies within the patient's body may be confused with a pathology or just reduce the quality of examinations. The knowledge of the artefacts and their sources is extremely important in order to avoid false diagnoses and to learn how to eliminate them. Depending on their origin, one can classify them into the following groups:

1) Truncation artefacts which occur near sharp high-contrast boundaries and are also known as the Gibbs phenomenon. They appear as multiple, alternating bright and dark lines – "ringing".

2) Motion artefacts caused by breathing, cardiac movement, CSF pulsation/blood flow, patient's movement, which create ghost artefacts. They can be reduced by patient immobilization, cardiac/respiratory gating, saturation bands, or drugs that slow down the intestinal peristalsis. One can also reduce motion artefacts by using echo-planar imaging, a very fast MR imaging technique.

3) Aliasing artefacts occur when the anatomical structures located outside the field of view are mapped at the opposite end of the image. One can eliminate them by increasing the field of view.

4) Chemical shift artefacts appear as dark or bright bands at the lipid-water interface and are seen especially in case of fluid-filled structures surrounded by fat (e.g. eye balls in the orbits, bladder). They tend to by less prominent on T1-weighted images than on T2-weighted images.

5) Others – technical literature uses many different names for artefacts, e.g. banding artefact, pile-up artefact, peripheral signal artefact, spike noise artefact, blurring artefact, suppression artefact etc.[8]

Perfusion imaging

Perfusion is one of the most important physiologic and pathophysiologic parameters and can be assessed non-invasively with MRI [9]. There are several techniques to derive perfusion-related parameters which can be mainly grouped in three categories. The first approach is called dynamic contrast enhanced (DCE-) MRI and acquires a series of rapid (less than 20 seconds per image) T_1-weighted imaging studies following the bolus administration of a gadolinium-based contrast agent. These images are typically acquired using spoiled gradient echo, T_1-weighted magnetization prepares or echo planar techniques. The second approach is called dynamic susceptibility contrast (DSC-) MRI and is useful if the contrast agent remains in the blood vessels (such as in cerebral tissues with an intact blood brain barrier). In this case, the paramagnetic nature of the contrast agent increases the local tissue susceptibility, causing an increase in the T_2* dephasing of the nearby tissues. Serial T_2*-weighted gradient echo or echo planar sequences are acquired, and the well-perfused tissue exhibits a reduction of signal relative to the pre-contrast images or the poorly perfused tissues. The third approach does not use any contrast media to highlight the flowing spins and is called arterial spin labelling (ASL). It acquires two set of images: one set following a region selective inversion pulse that inverts or "tags" the spins outside the slice of interest, whereas the other set of images serves as a reference [4].

We will focus on the quantification of dynamic contrast enhanced MRI data.

DCE-MRI

Dynamic contrast enhanced magnetic resonance imaging is based on dynamic T_1-weighted imaging of contrast reagent (CR) extravasation over several minutes in order to track the first-pass bolus [10]. The acquired signal is used to generate a so-called time intensity curve for the tissue, which mirrors the response of the tissue to the arrival of CR in enhancement values. The analysis of this curve allow the estimation of physiological properties related to the microvascular blood flow, such as vessel permeability, vessel surface area product and tissue volume fractions [11]. The underlying principal of all variations of DCE-MRI studies is rather simple: as a paramagnetic particle enters and disperses through the tissue, it alters the MR signal intensity of the tissue depending on its local concentration. MR images are acquired every few seconds before, during, and after a CR is intravenously injected. Each image acquired corresponds to one time point, and each pixel in each set of images generates its own curve of intensity values. Since the induced variation in signal intensity (correlating to the CR concentration in the tissue) at every time point after injection depends on tissue vascularization, the permeability of the vessels, the vessels' surface area product, extraction fraction, blood flow, etc., parametric maps of specific microvascular biomarkers can be derived. Moreover, absolute values of these parameters can be extracted using appropriate mathematical models. These parameters reflect the two-compartment pharmacokinetics exhibited by CRs, which are distributed between the intravascular and extravascular spaces [11].

- Image acquisition

The number of measurements required for data acquisition is dependent on the quantification method chosen. These measurements include:

1) Recording a map of pre-contrast native T_1 values (T_{10} map): this map is necessary for the calculation of CR concentrations [12].

2) Acquisition of heavily T_1-weighted images prior and following CR introduction: at a reasonably high temporal resolution in order to be able to characterize the kinetics of the CR entry and exit out of the tissue [13].

3) Acquiring the arterial input function (AIF): estimation of the CR concentration in the blood plasma of a feeding artery as a function of time. Obtaining the AIF is essential for nearly all quantitative analysis methods and remains technically the most challenging part in the process of data acquisition.
For simple semi-quantitative analysis of signal intensity (SI) curves measurement will suffice. For additional CA-concentration values measurement must also be included. For quantitative pharmacokinetic analysis, which is able to yield absolute metrics, all three measurements are necessary [11].

- The arterial input function

When calculating the various vascular parameters, mathematical pharmacokinetic models assume that the CR arrives in a vessel entering the tissue in the form of an ultra-narrow bolus (i.e., impulse input of tracer also known as the *residue* or *residual response*) [11]. Only this curve can be used to extract quantitative information pertaining intrinsic tissue properties. In reality however, the concentration time course of the CA in a vessel entering the tissue (the AIF) differs substantially from the ideal form, therefore the residual function cannot be measured directly. To solve this problem concentration time courses of both the tissue and a feeding artery (AIF) are measured whereupon these two curves can be used to reconstruct the sought after residual function [14].
Three main approaches have been developed for AIF estimation (I-III) and two further approaches (IV,V) eliminate the requirement for its measurement: (I) invasive [15]; (II) assuming an average AIF for all subjects; (III) acquiring the AIF from the DCE-MRI data sets [16]; (IV) reference region models [17] and the (V) step input method [18].

DCE-MRI data analysis

The arrival of CR and thus the enhancement pattern of the tissue depend on a wide variety of factors including vascularity, capillary permeability, perfused capillary surface area, volume and composition of extracellular fluid, renal clearance and perfusion. The analysis of DCE data can provide valuable information concerning the vascular status and perfusion. Analysis of the data can be performed using either: simple semi-quantitative methods, analysis of curve morphology or quantitative methods [11].

- Semi-quantitative analysis

Simple semi-quantitative metrics are derived directly from the signal intensity curve alone. They are easy to calculate and do not have any rigorous requirements in terms of data acquisition [19].
Semi-quantitative analysis has several advantages: it obviates the need for the measurement of the AIF, it is robust, and several parameters such as AUC are relatively independent of injection protocols (36). One challenging aspect, however, is the fact that semi-quantitative parameters do not necessarily have any obvious physiological correlates. Since they represent a mixture of microcirculatory and tissue properties, the degree to which each of these physiological parameters contributes to the MR-signal, remains unknown [11]. A further limitation is that most Model-free parameter extraction methods remain sensitive to variations between different acquisition protocols. Parameter metrics will depend on factors such as sequence parameters, hardware settings, scan duration, amount of administered CR [20], CA properties, injection protocol and so on. This will occur even if identical sequences are used since the baseline signal for any given tissue, using a particular sequence, will differ by the choice of imager. As a consequence, comparison of semi-quantitative studies is difficult at best. Semi-quantitative analysis has demonstrated clear diagnostic value in a number of areas. For instance, in oncological studies [21,22] including the assessment of tumour angiogenesis [23] but also in studies of rheumatoid illnesses [24], the heart [25] and of musculoskeletal perfusion evaluation.

- **Morphologic analysis**

This method attempt to assign physiological and pathological findings based on tissue activity curve patterns [11]. Though not quantitative, this approach offers some appealing advantages: (I) it is less sensitive to variations in sequence parameters and scanner calibrations; (II) it is not computationally demanding as fitting is not involved; (III) it does not rely on any assumptions (some more, some less physiological) as model based methods do [11]. For example, in the skeletal muscle a rapid signal intensity increase followed by a narrow peak and consequent washout is evident of an adequate vascular reserve. But if the time intensity curve (TIC) displays a shallow increment, a delayed peak and only a weak or absent washout after exercise, this indicates a limited vascular reserve [26].

- **Quantitative analysis**

DCE-MRIs' greatest appeal is its ability to produce parameters, directly related to the physiological (and pathophysiological) properties of the vascular environment and the surrounding tissue, in absolute terms [11]. In order to describe and analyse the temporal and physical distribution of an inert tracer, the classical pharmacokinetics usually utilizes linear compartmental models. A compartment is defined as a distinguishable tracer distribution space (anatomic, functional or fictive) within a biological system. Inside this space, the tracer spreads rapidly whereas the transport between adjacent compartments is hindered in some way, resulting in individual time concentration courses of the tracer in the different compartments. As CRs distribute at different rates in blood and tissue, a two-compartment model considers the intravascular-extracellular volume fraction (blood plasma) to be the central compartment, and the extravascular-extracellular volume fraction (v_e) as the peripheral compartment. The fundamental physiological variables governing CR movement across the vascular endothelium include vessel wall permeability, vessel surface area, blood flow (i.e., perfusion), ratios of the CR concentrations across the endothelium as well as intravascular and extracellular-extravascular volume fractions [11].

The purpose of the model is to describe the underlying physiological phenomenon in mathematical terms in order to enable the estimation of specific tissue parameters from the measured signal.

We will consider the main four pharmacokinetic models implemented in the analysis of DCE-MRI data.

-- ***Tofts Model (TM)***

The Tofts model, also known as the standard model, assumes a linear dependence of R_1 on [CR] (that is the equivalent of assuming the equilibrium transcytolemmal water exchange kinetics in the fast exchange limit (FXL)):

$$R_1(t) = r_1[CR(t)] + R_{10} \qquad 18)$$

where r_1 is the CR relaxivity. The extravasation of the contrast from the plasma to the extravascular extracellular space (EES) is accounted by the Kety-Schmidt rate law [27]:

$$[CR_o(T)] = K^{trans} \int_0^t [CR_p(t)] e^{\frac{K^{trans}(T-t)}{v_e}} dt \qquad 19)$$

where K^{trans} is the first order rate constant for plasma to interstitium CR transport ([1/min]) and v_e is a measure of the EES volume fraction. The ratio between K^{trans} and v_e results in the third pharmacokinetic parameter k_{ep}, that is the back flux rate constant [1/min]. [CR_0] and [CR_p] are the concentration of CR in the 'outside' space and in the plasma, respectively [CR_p] is the arterial input function.

-- ***Shutter speed model (SSM)***

Applying equation 1 to the distribution of the CR in the blood, the longitudinal relaxation rate results:

$$R_{1b}(t) = r_{1p}(1-h)\left[CR_p(t)\right] + R_{10p} \quad 20)$$

where b is for the whole blood, p for the plasma and h is the haematocrit. However, about half the water in blood is intracellular and cannot be accessed directly by the CR molecules [28]. The transport outside the erythrocytes is then required. This is described by these two equilibriums:

$$H_2O_i \leftrightarrow H_2O_p \quad 21)$$
$$H_2O_p + CR_p \leftrightarrow H_2O{\cdot}CR_p \quad 22)$$

Usually, the mean water molecule lifetime on common CRs is $< 10^{-7}$ s, leading to the linear equation 1 suitable for homogeneous solutions. In case of erythrocytes, (22) is also fast at some practical $[CR_p]$ values [28,29]. After extravasation, CRs commonly distribute into the interstitial extracellular space:

$$R_1^*(t) = r_{10}p_0[CR_0(t)] + R_{10} \quad 23)$$

R_1*(t) is the rate constant of the extravascular water signal, r_{10} is the interstitial CR relaxivity and p_0 is the fraction of the extracellular tissue water. The application of (23) to biological tissues assumes that the interstitium is a homogeneous solution and that the system remains in the fast exchange limit. On the contrary, many studies have shown that, even though the equilibrium in (22) is fast, it is insufficiently frequent for the FXL assumption to be true at all $[CR_0]$ values following a bolus injection [28]. This depends on the dimensions of the parenchymal cells that are generally much larger than erythrocytes and have a less water-permeable cytolemmae. Therefore, tissue parenchyma cannot be considered as a single homogeneous solution. It is compartmentalized on the scale of the MRI voxel. The main result of this compartmentalization is given by:

$$R_{1L}(t) = (1/2)\{2R_{1i} + r_{1o}[CR_o(t)] + (R_{10} + R_{1i} + 1/\tau_i)/p_o - \{(2/\tau_i - r_{1o}[CR_o(t)] - (R_{10} + R_{1i} + 1/\tau_i)/p_o)^2 + 4(1-p_o)/\tau_i^2 p_o\}^{\frac{1}{2}}\} \quad 24)$$

where $R_{1L}(t)$ is the long relaxation rate constant of the shutter speed model. R_{1i} is the H_2O rate constant in the absence of exchange and τi is the average intracellular water lifetime of a water molecule.

-- ***Extended Tofts model (ETM)***

While the TM assumes a negligible volume for the plasma compartment, the extended Tofts model introduces the fractional plasma volume v_p. This model is able to distinguish enhancement effects due to contrast leakage from those due to intravascular contrast. Eq. (19) becomes:

$$[CR_o](T) = v_p C_p(t) + K^{trans}\int_0^T C_p(t)\, e^{-K^{trans}(T-t)/v_e} dt \quad 25)$$

-- ***Extended shutter speed model (ESSM)***

The extended shutter speed model allows the evaluation of the blood water exchange effect on the overall signal decrease. The contribution of the water signal from the three compartments

(whole blood, EES and intracellular space) is described by the matrix format of the Bloch equation [30].

$$\frac{d\boldsymbol{M}}{dt} = \boldsymbol{XM} + \boldsymbol{C} \quad 26)$$

where the column vectors are $\mathbf{M} = (M_b, M_o, M_i)$ and $\mathbf{C} = (M_{b0}R_{1b}, M_{o0}R_{1o}, M_{io}R_{1i})$ where $\mathbf{M} \sim$ to the signal **S**. The exchange matrix **X** is:

$$\boldsymbol{X} = \begin{pmatrix} -(R_{1b} + k_{bo}) & k_{ob} & 0 \\ k_{bo} & -(R_{1o} + k_{ob} + k_{oi}) & k_{io} \\ 0 & k_{oi} & -(R_{1i} + k_{io}) \end{pmatrix} 27)$$

The subscripts *b*, *o* and *i* stand for *blood*, *outside* space and *intracellular* space, respectively. **M** is the ^1H_2O magnetization vector and k_{bo} ($= 1/\tau_b$) represents the blood to interstitium transfer; k_{io} ($= 1/\tau_i$) represents the interstitium to EES transfer; k_{ob} ($\sim 1/\tau_o$) the EES to blood transfer and k_{oi} the EES to intracellular transfer [30]. The general solution to eq. 26 is the matrix form of the Ernst-Anderson relationship [31] which assumes that, if the [CR] change is relatively small during the acquisition, at every discrete data acquisition time point, the relaxation time can be well estimated:

$$\boldsymbol{S} = [\mathbf{I} - e^{-\boldsymbol{X}T_R}(\cos\alpha)]^{-1}(\mathbf{I} - e^{-\boldsymbol{X}T_R})\boldsymbol{S_0}(\sin\alpha) \qquad 28)$$

Applications

The application of pharmacokinetic models on DCE-MRI brain data is based on the conference paper funded in part by the National Institute for Health Research (NIHR) Imperial Biomedical Research Centre (BRC), the Brain Tumour Charity and the Brain Tumour Research Campaign:

Inglese M, Honeyfield L, Aboagye OE, Waldman AD, Grech-Sollars M *Comparison of the Tofts and the Shutter Speed Model for DCE-MRI in patients with Brain Glioma* ISMRM 2018 (magna cum laude)

I. Comparison of the Tofts and the Shutter Speed Models for DCE-MRI in patients with Brain Glioma

DCE-MRI is a powerful technique able to quantitatively measure patho-physiological environments through the passage of a contrast reagent (CR) and model-based pharmacokinetic analysis. The accuracy of quantitative measurements of perfusion parameters by DCE-MRI is crucial as it can significantly impact the clinical care of cancer patients. In this study, we provide a method to identify reliable DCE-MRI brain data for perfusion quantification with different pharmacokinetic models.
We analysed DCE-MRI data of 14 patients with primary brain tumours using the Tofts model (TM), the extended-Tofts model (ETM), the shutter speed model (SSM) and the extended shutter speed model (ESSM). Due to the presence of the blood brain barrier, which can block the leakage of the CA into the interstitium, we also implemented the no-exchange model (NEM). For each lesion, we produced a 3D model selection map with the evaluation of the Akaike Information Criteria. The variability of each pharmacokinetic parameter extracted from the fitting of the model

of choice was assessed with a noise propagation procedure, resulting in distributions of the coefficient of variation (CV).
Results showed the NEM to be the most frequent model of choice (35.5%), followed by the ETM (32%), the TM (28.2%), the SSM (4.3%) and the ESSM (<0.1%). In analysing the reliability of K^{trans}, when considering regions with a CV<20%, ≈25% of voxels were found to be stable. The remaining 75% of voxels were considered to be unreliable.
In conclusion, an appropriate model selection, considering tissue biology and its effects on BBB permeability and exchange conditions, together with an analysis on the reliability and stability of the calculated parameters, is critical in the identification of reliable brain DCE-MRI data.

1. Introduction

Dynamic contrast-enhanced magnetic resonance imaging (DCE-MRI) is a non-invasive methodology that allows tissue perfusion and permeability to be quantified through analysis of T_1-weighted MR images acquired before, during and after an intra-venous (IV) injection of a gadolinium-based contrast agent (CA). These all comprise of highly paramagnetic gadolinium (Gd) ions chelated within an organic molecule, with the structure of the latter varying between specific contrast agents[32]. They are hydrophilic compounds and do not cross cell membranes to enter the intracellular compartment, nor do they cross the intact blood brain barrier (BBB). As the CA perfuses the tissue under investigation, the paramagnetic effect of the Gd-chelate causes a decrease in tissue water longitudinal relaxation time approximately linearly-related to the local CA concentration (T_1). A set of T_1-weighted dynamic images are acquired during this time in order to extract the voxel-wise characteristic signal intensity time curves which are related to the CA concentration time curves[33]. These curves are then fitted to mathematical models to calculate physiological parameters, such as volume transfer constants and volume fractions. The most extensively used model is the Tofts model (TM), which expresses the flux of the tracer across two well-mixed compartments (blood and the extravascular, extracellular space) through the volume transfer constant K^{trans} [33]. The TM assumes negligible plasma compartment and is ideal for the description of weakly vascularized tissue. An extended version of this model was introduced by Tofts in 1999 in order to account for highly perfused tissue[34]. The Extended Tofts model (ETM) therefore fits data with an additional parameter: the fractional plasma volume, v_p [34]. Both the TM and ETM embed the implicit assumption that equilibrium transcytolemmal water exchange (between the intracellular space and extracellular extravascular space) is infinitely fast, or that the system is in, what is called, the fast exchange limit (FXL) [35]. Water exchange between the intracellular space and the extracellular extravascular space effects the degree of T_1 shortening caused by CA. This effect on the MRI signal amplitude is incorporated within the shutter speed model (SSM). The SSM thus introduces a new pharmacokinetic parameter, the mean intracellular water molecule lifetime, τ_i [35]. However, similarly to the TM, the SSM ignores any contribution of the CA from the plasma compartment. This is accounted for by the extended shutter speed model (ESSM), which includes both v_b, the fractional blood volume and τ_b, the intravascular water molecule lifetime [30].
The TM and ETM are regularly applied in the field of oncology to assess treatment response [36] and in the study of blood-brain barrier disruption [37-44]. The SSM has been mainly implemented in the study of breast cancer [45], prostate cancer [46] and hepatocellular carcinoma [47]. There are few examples of the application of SSM in brain tumours in the literature [48,49]. The ESSM, also called second generation shutter speed model, or BALDERO (blood agent level dependent and extravasation relaxation overview), has previously found applications only in hepatocellular carcinoma [50] and simulated data [30].
The above models assume that the CA passes readily between the intravascular compartment and the tissue interstitium. However, this assumption is not valid in the presence of the intact BBB, where there is negligible leakage. In this case the CA will only affect the intravascular T_1 value on first pass of the bolus. In the no-exchange model (NEM), we assume that this has negligible

effect on the overall T_1 value, and therefore the model describes those instances where the CA has no effect on the MR signal.
In this study we propose a method for the identification of reliable DCE-MRI data. DCE-MRI data can be affected by a) the acquisition protocol (trade-off between spatial and temporal resolution)[51], b) the quantification procedure, which, in this specific case of brain tumours, has to take into consideration the issue of the BBB. Following on from previous work carried out by Bagher-Ebadian et al. [42], we start with a model selection procedure using the Akaike information criteria index where we compare the five pharmacokinetic models previously described (NEM, TM, ETM, SSM and ESSM) in patients with primary brain tumours. Given that a model selection procedure alone cannot guarantee final reliable results, we evaluate the stability of each parameter extracted from the model of choice, in terms of coefficients of variations (CVs), with a noise propagation procedure.

2. Materials and Methods

2.1 Patient Population

14 patients (7 male, 7 female; aged 23-73 years, mean 40 years) with primary brain tumours were recruited to this study. Ethical approval was given by the local ethics committee and informed consent was obtained from all patients. Patients had an MRI at diagnosis, prior to receiving any treatment. Following surgery, histopathological data showed 3 patients with WHO grade IV glioblastoma, 2 patients with WHO grade III astrocytoma, 2 patients with WHO grade III oligodendroglioma, 3 patients with WHO grade II astrocytoma, 3 patients with WHO grade II oligodendroglioma, and 1 patient with a WHO grade I dysembryoplastic neuroepithelial tumour.

2.2 DCE-MRI Data Acquisition

MR images were acquired on a 3T Siemens Verio MRI system using a 32 channel head coil; including pre- and post-contrast T_1-weighted images, T_2-FLAIR images and a DCE sequence with a variable flip angle pre-contrast T_1 map acquisition. The DCE-MRI protocol included five pre-contrast spoiled gradient recalled echo (SPGRE) 3D vibe sequences at five different flip angles (2, 8, 12, 15, 20, 26), and a dynamic 3D vibe sequence (TR = 3.34 ms, TE = 0.99 ms, flip angle = 26, FOV: 240 x 240 mm, acquisition matrix 128x128, slice thickness 5 mm, slice gap 1 mm, 80 volumes). To obtain acquisitions before, during and after the injection of the contrast agent, 0.1 mmol/kg body-weight gadolinium-diethylene triaminepentacetate (Gd-DTPA, Gadovist), was injected using a power injector on the 5th acquisition using a flow rate of 3 ml/s. The 3D acquisition allowed us to cover the entire brain. 80 time points were acquired with an average temporal resolution of 2.89 s and a total acquisition time of ≈ 4 minutes.

2.3 DCE-MRI Data Analysis

Volumes of interest (VOIs) were drawn by a Radiologist and confirmed by a Consultant Neuroradiologist for each patient around T_2-FLAIR hyperintense regions and on a 2 cm diameter circular region in normal-appearing contra-lateral white matter. DCE-MRI data were analysed using a semi-automated in-house software written in MATLAB (Mathworks, R2017a). Before the application of any of the aforementioned pharmacokinetic models, we calculated the relaxation rate at baseline (R_{10}) and relaxed signal (M_0) as 3D maps, with the Ernst formula (assuming $TE \ll T_2^*$) using the set of SPGRE pre contrast images acquired at different flip angles [52].

$$S(\alpha) = M_0 \sin(\alpha) \frac{1-e^{-R_{10}T_R}}{1-\cos(\alpha)e^{-R_{10}T_R}} \qquad 1)$$

where α is the flip angle having values [2, 8, 12, 15, 20, 26] and TR is 3.34 ms. Reformulating equation 1 as a linear regression system (y = cx + d) following the method described by Liberman et al. in [53],gives:

$$\frac{S(\alpha)}{\sin(\alpha)} = E\frac{S(\alpha)}{\tan(\alpha)} + M(1-E) \quad 2)$$

where $E = e^{-R_{10}T_R}$.
The slope $c = E$ and intercept $d = M_0\ (1 - E)$ can thus be estimated and continuing from [53], R_{10} and M_0 can then be obtained through:

$$R_{10} = -\frac{\log(c)}{T_R},\ M_0 = \frac{d}{1-c} \quad 3)$$

Then, 4D (x, y, z, t) post-injection longitudinal relaxation rate $R_1(t)$ maps for each dynamic phase are calculated using signal intensity data from the post contrast dynamic series:

$$R_1(t) = -(1/T_R)log\frac{1-(A+B)}{1-\cos(\alpha)(A+B)} \quad 4)$$

where α = 26, $A = S(t) - S(0)/M_0\sin(\alpha)$, $B = (1-E)/1-E \cdot \cos(\alpha)$. S(0) and S(t) are the pre contrast injection signal intensity and the signal at the dynamic phase *t* respectively [54].

The longitudinal relaxation rate is determined in order to calculate the concentration of the contrast agent. This is done through a calibration between the concentration of contrast agent [CA] and the measured H_2O MR signal. This can be modelled by either a linear or nonlinear relationship as described below.

2.3.1 Tofts Model (TM)

DCE-MRI data were fitted with the Tofts model assuming a linear dependence of R_1 on [CA] (that is the equivalent of assuming the equilibrium transcytolemmal water exchange kinetics in the FXL):

$$R_1(t) = r_1[CA(t)] + R_{10} \quad 5)$$

where r_1 is the CA relaxivity.
The extravasation of the contrast from the plasma to the EES was accounted by the Kety-Schmidt rate law [27]:

$$[CA_o(T)] = K^{trans}\int_0^t [CA_p(t)]e^{\frac{K^{trans}(T-t)}{v_e}}dt \quad 6)$$

where K^{trans} is the first order rate constant for plasma to interstitium CA transport (min^{-1}) and v_e is a measure of the EES volume fraction.
The ratio between K^{trans} and v_e results in the third pharmacokinetic parameter k_{ep}, which is the back flux rate constant (min^{-1}). $[CA_0]$ and $[CA_p]$ are the concentration of CA in the 'outside' space (the extravascular extracellular space) and in the plasma respectively. $[CA_p]$ is also called the arterial input function (AIF). The fitting of equation 6 was performed using the inbuilt MATLAB *fminsearch* function, which uses the Nelder-Mead simplex algorithm as described in Lagarias et al. [55]. The minimization procedure is done voxel-wise in order to obtain a 3D map for each pharmacokinetic parameter. We set input values of 0.1 and 0.01 for the K^{trans} and v_e, respectively, and run the algorithm with 10,000 iterations and a tolerance of 10^{-8}. The fitting procedure was also carried out with the user developed MATLAB function *fminsearchbnd* [56]. This function takes into consideration boundaries in the output values settings, which were set so as to consider only

positive values [0, ∞]. A comparison between the two functions' results was done in terms of goodness of fit by estimating the Akaike Information Criteria (AIC) for each method using equation 7:

$$AIC = 2k + nln\left(\frac{RSS}{n}\right) + \frac{2k(k+1)}{n-k-1} \quad 7)$$

where *n* is the number of data points, *k* the number of fitted parameters and RSS is the residual sum of squares [57].
In general, when performing model selection using the AIC, the model resulting with the lowest AIC value is the model that represents the best balance between complexity (i.e., the number of parameters) and goodness of fit (i.e., lower RSS). In this case, as the number of parameters is the same, only the goodness of fit is being tested. A comparison between the AIC maps relative to the bounded and unbounded procedure allowed the estimation of final K^{trans}, k_{ep} and v_e maps where the value of each voxel was obtained from the fitting procedure with the best fit (lowest AIC) (Figure 36).

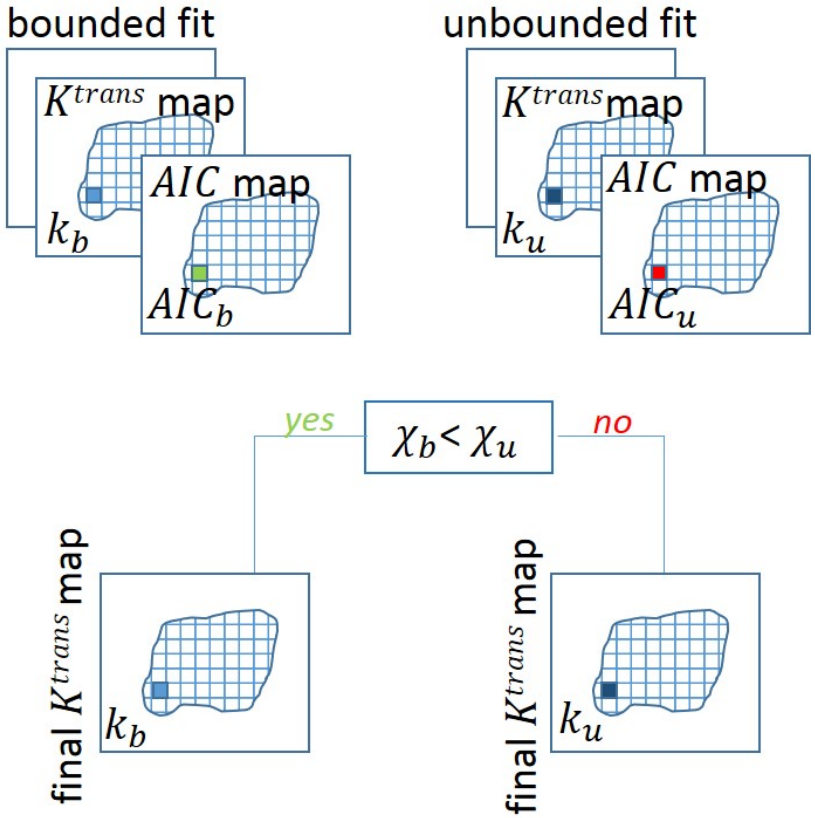

Figure 36: The fitting procedure for K^{trans}. A bounded and unbounded fitting were calculated together with the Akaike Information Criteria (AIC) map (AIC_b and AIC_u for the bounded and unbounded procedure, respectively). The final value of K^{trans}, for each voxel of the map, was the one obtained from the function with the lowest AIC (k_b when $AIC_b < AIC_u$ and k_u vice versa). The same procedure was carried out for each parameter.

2.3.2 Shutter speed model (SSM)

In the SSM, equation 5 is applied to the distribution of the CA in the blood, without assuming that the equilibrium transcytolemmal water exchange kinetics are in the FXL. The longitudinal relaxation rate is measured as:

$$R_{1b}(t) = r_{1p}(1-h)\left[CA_p(t)\right] + R_{10p} \quad 8)$$

where *b* stands for the whole blood, *p* for the plasma and *h* the blood haematocrit . However, about half of the water in the blood is intracellular and cannot be accessed directly by the CA molecules [28]. The transport outside the erythrocytes therefore needs to be considered, as described by the two equilibria:

$$H_2O_i \leftrightarrow H_2O_p \quad 9)$$
$$H_2O_p + CA_p \leftrightarrow H_2O{\cdot}CA_p \quad 10)$$

The mean water molecule lifetime in common CA is normally < 10^{-7} s, and the linear equation 5 is suitable for homogeneous solutions. In the case of erythrocytes, equation 10 is also considered fast for some commonly measured [CA_p] values [28,29]. After extravasation, the CA is commonly distributed into the interstitial extracellular space, at a rate defined by:

$$R_1^*(t) = r_{10}p_0[CA_0(t)] + R_{10} \quad 11)$$

where R_1*(t) is the rate constant of the extravascular water signal, r_{10} is the interstitial CA relaxivity and p_0 is the fraction of the extracellular tissue water. The application of equation 11 to biological tissues assumes that the interstitium is a homogeneous solution and that the system remains in the fast exchange limit. However, many studies have shown that, even though the equilibrium in equation 10 is fast, the FXL assumption is not true for all [CA_0] values following a bolus injection [28]. [CA_0] depends on the dimensions of the parenchymal cells that are generally much larger than erythrocytes and have a less water-permeable cytolemmae. Furthermore, tissue parenchyma cannot be considered as a single homogeneous solution and a single MRI voxel will constitute a number of compartments. The main result of this compartmentalization is given by:

$$R_{1L}(t) = (1/2)\Big\{2R_{1i} + r_{1o}[CA_o(t)] + (R_{10} + R_{1i} + 1/\tau_i)/p_o - \{(2/\tau_i - r_{1o}[CA_o(t)] - (R_{10} + R_{1i} + 1/\tau_i)/p_o)^2 + 4(1-p_o)/\tau_i^2 p_o\Big]^{\frac{1}{2}}\Big\} \quad 12)$$

where R_{1L}(t) is the long relaxation rate constant of the *shutter speed model*. R_{1i} is the H_2O rate constant in the absence of exchange of CA and τ_i is the average intracellular lifetime of a water molecule. The SSM was fitted by substituting equation 12 in equation 6 using the MATLAB functions *fminsearch* and *fminsearchbnd*, similarly to the TM. The initial estimates for the SSM K^{trans} and v_e where taken as the outputs of the TM, while the initial estimate for τ_i was set at 0.1 [30]. The final K^{trans}, k_{ep}, v_e, and τ_i maps were obtained from the fitting procedure with the best fit (lowest AIC value) as described in Figure 36.

2.3.3 Extended Tofts model (ETM)

While the TM assumes a negligible volume for the plasma compartment, the fractional plasma volume v_p is introduced in the ETM. This model is able to distinguish the effects due to contrast leakage from those due to intravascular contrast. Equation 6 becomes:

$$[CA_o](T) = v_p C_p(t) + K^{trans}\int_0^T C_p(t)\, e^{-K^{trans}(T-t)/v_e} dt \quad 13)$$

The ETM was fitted by substituting equation 13 in equation 6 using the MATLAB functions *fminsearch* and *fminsearchbnd*, similarly to the TM and SSM. The initial estimates for ETM K^{trans} and v_e were again taken from the output of the TM and the initial estimate for v_p was set at 0.01 [30]. The final K^{trans}, k_{ep}, v_e, and v_p maps were obtained from the fitting procedure with the best fit (lowest AIC) as described in Figure 36.

2.3.4 Extended shutter speed model (ESSM)

We implemented the ESSM to evaluate the effect of the water exchange between the vasculature and the extracellular extravascular space on the overall signal decrease. The contribution of the water signal from the three compartments (whole blood, EES and intracellular space) is described by the matrix format of the Bloch equation [30]:

$$\frac{d\boldsymbol{M}}{dt} = \boldsymbol{XM} + \boldsymbol{C} \qquad 14)$$

where the column vectors are $\mathbf{M} = (M_b, M_o, M_i)$ and $\mathbf{C} = (M_{b0}R_{1b}, M_{o0}R_{1o}, M_{i0}R_{1i})$ with the ^1H_2O magnetization vector $\mathbf{M} \approx$ to the signal $\mathbf{S}$. The exchange matrix $\mathbf{X}$ is given by:

$$\boldsymbol{X} = \begin{pmatrix} -(R_{1b} + k_{bo}) & k_{ob} & 0 \\ k_{bo} & -(R_{1o} + k_{ob} + k_{oi}) & k_{io} \\ 0 & k_{oi} & -(R_{1i} + k_{io}) \end{pmatrix} \qquad 15)$$

The subscripts *b*, *o* and *i* stand for *blood*, *outside* space and *intracellular* space, respectively. k_{bo} ($= 1/\tau_b$) represents the blood to interstitium transfer of water; k_{io} ($= 1/\tau_i$) the transfer of water from the intracellular space to the interstitium; k_{ob} (proportional to $1/\tau_o$) the EES to blood transfer and k_{oi} the EES to intracellular transfer [30]. The general solution to equation 13 is the matrix form of the Ernst-Anderson relationship [31] which assumes that if the change in [CA] is relatively small during the acquisition, at every discrete data acquisition time point, the relaxation time can be estimated using:

$$\boldsymbol{S} = [\mathbf{I} - e^{-\boldsymbol{X}T_R}(\cos\alpha)]^{-1}(\mathbf{I} - e^{-\boldsymbol{X}T_R})\boldsymbol{S_0}(\sin\alpha) \qquad (16)$$

$\mathbf{I}$ is the identity matrix and $\mathbf{S_0}$ ($= (S_{b0}, S_{o0}, S_{i0})$) is the signal at baseline.

The ESSM was fitted by considering the measured signal E(t) as a combination of the signals in the three compartments (blood, outside space and intracellular space) [50] using:

$$E(t) = \frac{S_b + S_o + S_i}{S_{b0} + S_{o0} + S_{i0}} - 1 \qquad (17)$$

Furthermore, equation 16 was simplified to:

$$\boldsymbol{S} = \sin(a) \cdot \boldsymbol{A} \cdot \boldsymbol{S_0} \qquad (18)$$

where the column vectors are $\mathbf{S} = (S_b, S_o, S_i)$ and $\boldsymbol{A} = [\mathbf{I} - e^{-\boldsymbol{X}T_R}(\cos\alpha)]^{-1}(\mathbf{I} - e^{-\boldsymbol{X}T_R})$.

The model was fitted by substituting equation 18 into equation 17 using the MATLAB function *fminsearch* function. The outputs of the SSM model were used as the initial estimates for K^{trans} and v_o and one third of the measured signal was used as the initial estimate for S_{b0}, S_{o0} and S_{i0}. Furthermore the initial estimates for k_{bo}, k_{ob}, k_{oi} and k_{io}, were taken from literature defined values as 1.2, 1.5, 1.1 and 1.2 respectively [30]. The following parameters were also derived: $\tau_b = 1/k_{bo}$, $\tau_i = 1/k_{io}$, $v_b = (k_{ob} - k_{oi} - ((k_{io}/v_o)*f_w) - k_{io})/((k_{bo}+k_{io})/v_o)$ where f_w is tissue volume fraction accessible to mobile aqueous solutes (assumed to be a constant and set to 0.8) and $v_i = 1 - (v_b + v_o)$ [30].

2.3.5 No-exchange model (NEM)

The no-exchange model describes the case where the concentration of the CA in a voxel is so low that there is no permeability or vascular filling. In this situation, the MR signal is assumed to be unperturbed by the injection of the gadolinium based CA and, as a consequence, the longitudinal

relaxation rate does not change from its baseline value (R_{10}). The system is therefore described by this value at all times such that the data is fitted by the constant R_{10}.

2.4 Arterial Input Function (AIF)

An additional ROI was drawn around the external carotid artery for the calculation of the image derived AIF (Figure 37). Signal-intensity curves were converted to R_1-time curves by using the baseline signal intensity before the first pass of the CA as a reference [58], setting the haematocrit in the blood to 0.45, and getting the baseline blood T_1 from the T_{10} map (equation 8).

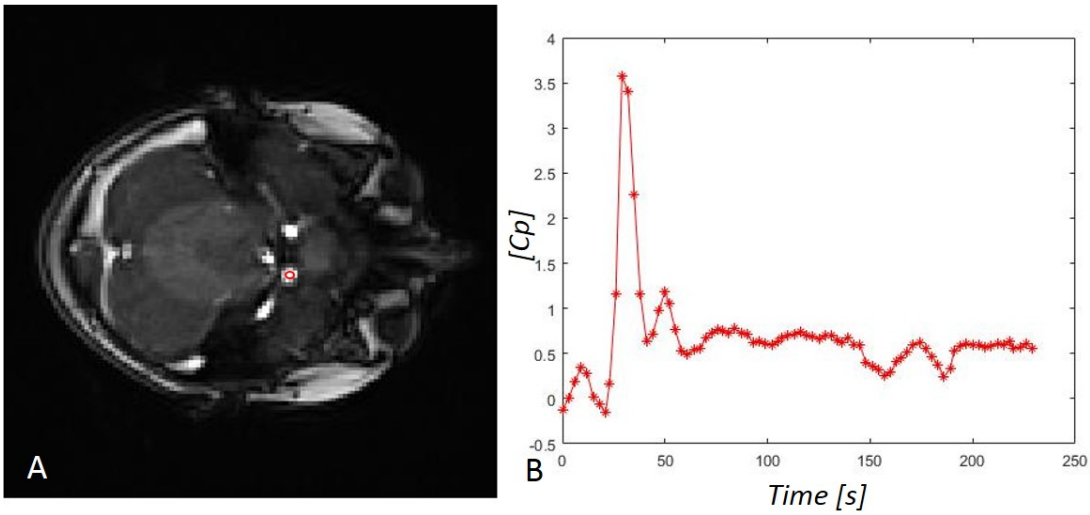

Figure 37: Measurement of the AIF. The VOI was placed in the carotid artery for the extraction of the arterial input function (AIF) as shown in the axial T1 VIBE image in (A). The time intensity curve for the concentration of contrast reagent in the plasma in the VOI indicated in red in (A) is shown in (B).

2.5 Model comparison

A model comparison was carried out using the AIC to test for the best model in a given voxel. In particular, in the presence of exchange (where the NEM fails in the description of data), a voxel-wise comparison between models was carried out (with ETM and SSM being an extension of the TM, and the ESSM an extension of the SSM) to indicate which model provided the best fit using the AIC in each voxel. The selection method is shown in the flowchart in Figure 38. The choice was expressed with a value of 1, 2, 3, 4 or 5 for the TM, ETM, SSM, ESSM and NEM respectively, in a volumetric mask (same dimensions of the original tumour volume mask). The percentage of 1s, 2s, 3s, 4s and 5s in each mask was evaluated to quantify the frequency of model choice. The model selection map was used to build final pharmacokinetic maps for the K^{trans}, k_{ep} and v_e, where, for each voxel, the value is the result of the fitting of the model of choice (lowest AIC).

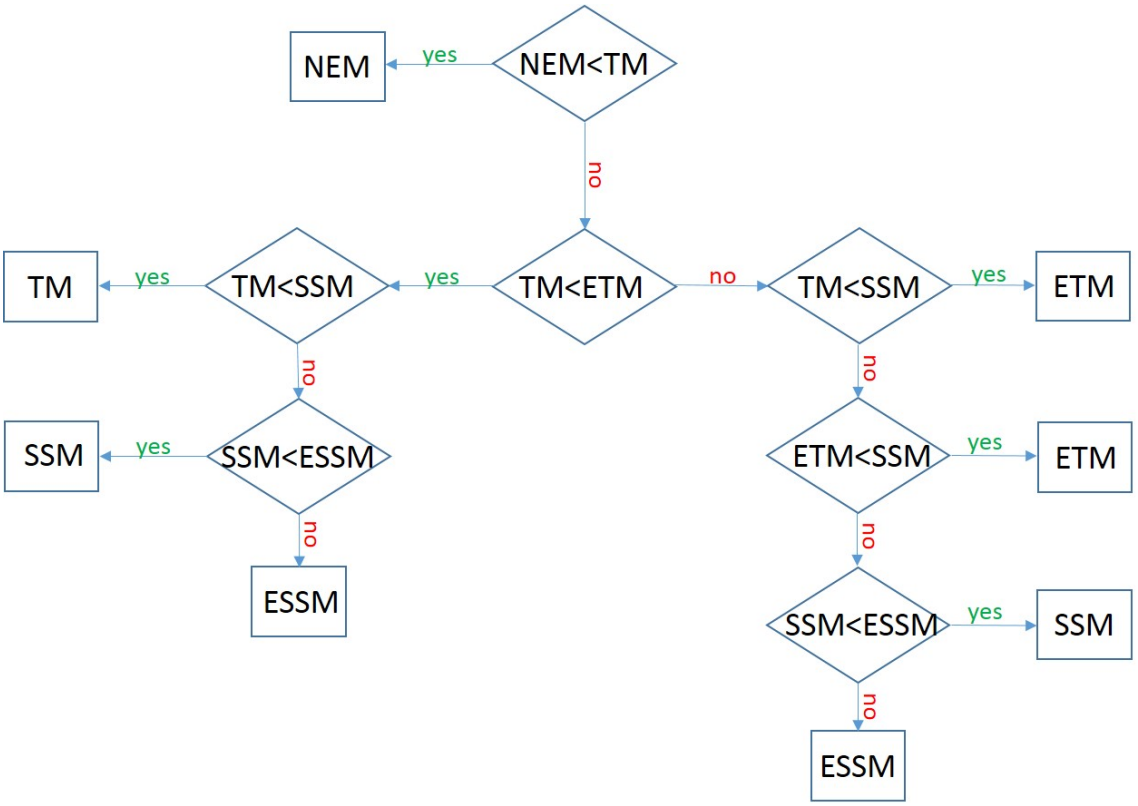

Figure 38: AIC model selection flowchart. The figure shows the hierarchical approach used to determine which model provided the best fit when using the Akaike Information Criteria (AIC).

2.5.1 Stability of pharmacokinetic parameters

Once the model selection was done, the stability of each parameter within the winning models was evaluated in a simulation environment. Tissue curves were generated back from the extracted pharmacokinetic parameters and signal intensity curves were calculated with the inverse formula of eq. 4. White Gaussian noise was added to the signal intensity curves using an SNR of 20. The SNR value for the simulated data was set by evaluating the SNR of the acquired data from the 2nd and 3rd phase of the dynamic acquisition sequence using the subtraction method[59]. The simulated noisy signal intensity curves were reconverted to noisy tissue concentration curves, and fitted to the selected pharmacokinetic model. This procedure was repeated 500 times for every kinetic parameter and the variability of each parameter was expressed in terms of coefficient of variation (CV): the percentage ratio between the standard deviation and the mean.

3. Results

3.1 Model selection and parameter variability

The behaviour of each model was assessed by studying the quality of fit for each of the models. The input data, together with the fitted curves, were normalized by the maximum value of the input data in order to compare results from the different fits. An example of a comparison of fit is shown in Figure 39.

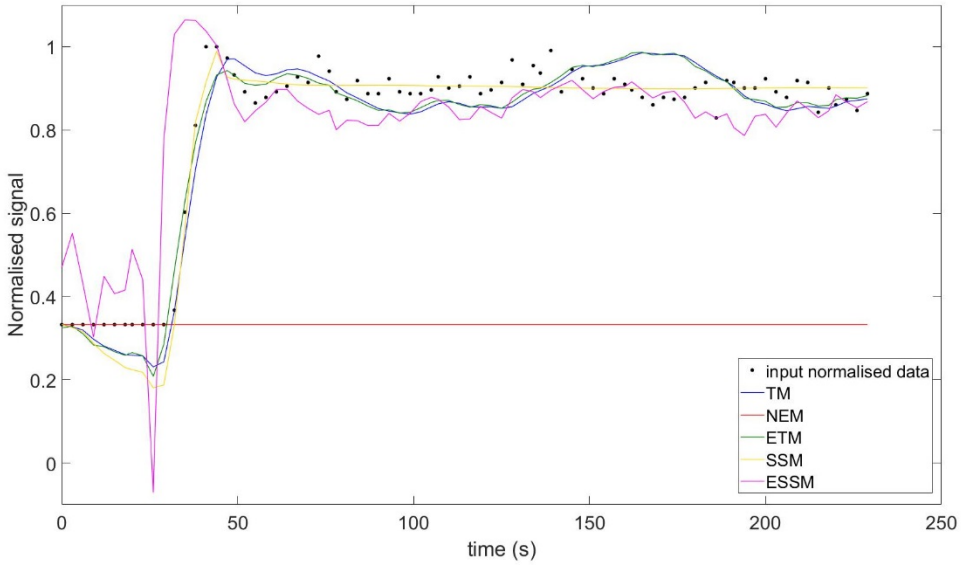

Figure 39: Normalized signal intensity curves in a voxel of an enhancing lesion fitted with the no-exchange model (red), TM (blue), ETM (green), SSM (yellow) and ESSM (pink). The quality of fitting was evaluated with the Akaike Information Criteria. AIC value: -103 for the NEM, -445 for TM, -454 for ETM, -531 for SSM and -291 for ESSM.

For each tumour, a map with the result of the statistical comparison among models was built (Figure 40). In this map, each colour represents the model for which the voxel-wise AIC value was lowest. The NEM resulted to be the model of choice by the majority of voxels (35.5 %), followed by the ETM (32 %), the TM (28.2%), the SSM (4.3%) and the ESSM (< 0.1%). Figure 40 shows the model selection map evaluated for two different lesions.

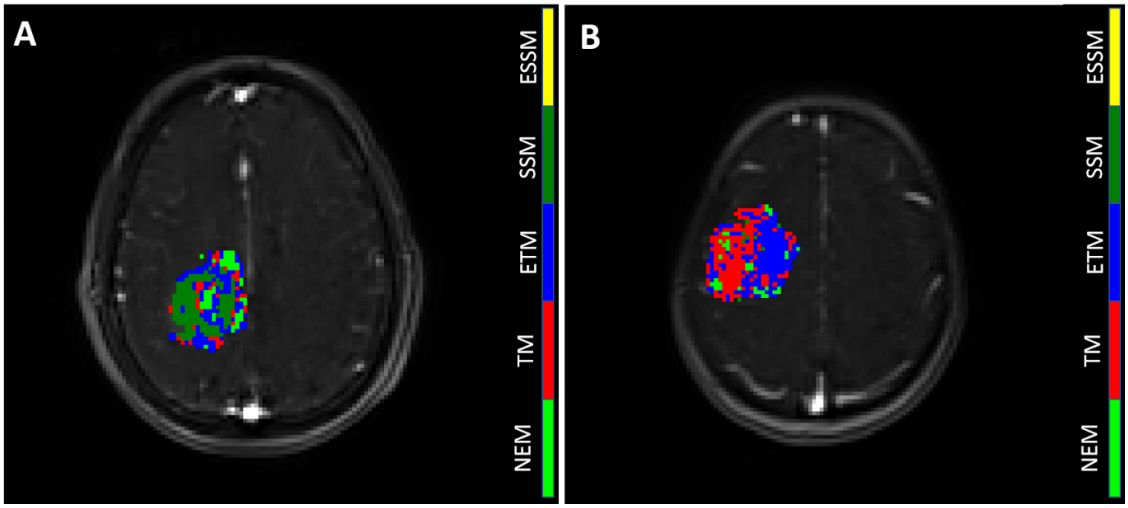

Figure 40: Statistical model comparison for two lesions. Each colour is representative of the model which best fitted the input data. An example of one slice of an enhancing (A, WHO grade IV) and non-enhancing (B, WHO grade II) lesion is shown.

Furthermore, final pharmacokinetic maps, for the K^{trans}, k_{ep} and v_e, were built considering the model selection procedure. Within the final pharmacokinetic maps, each voxel was represented by the model with the best fit (lowest AIC) within that voxel. For each of these maps, the stability of each parameter and for each lesion was presented in terms of CV maps. Figure 6 shows an example of two final K^{trans} maps with their CV map overlaid on them (A and D).

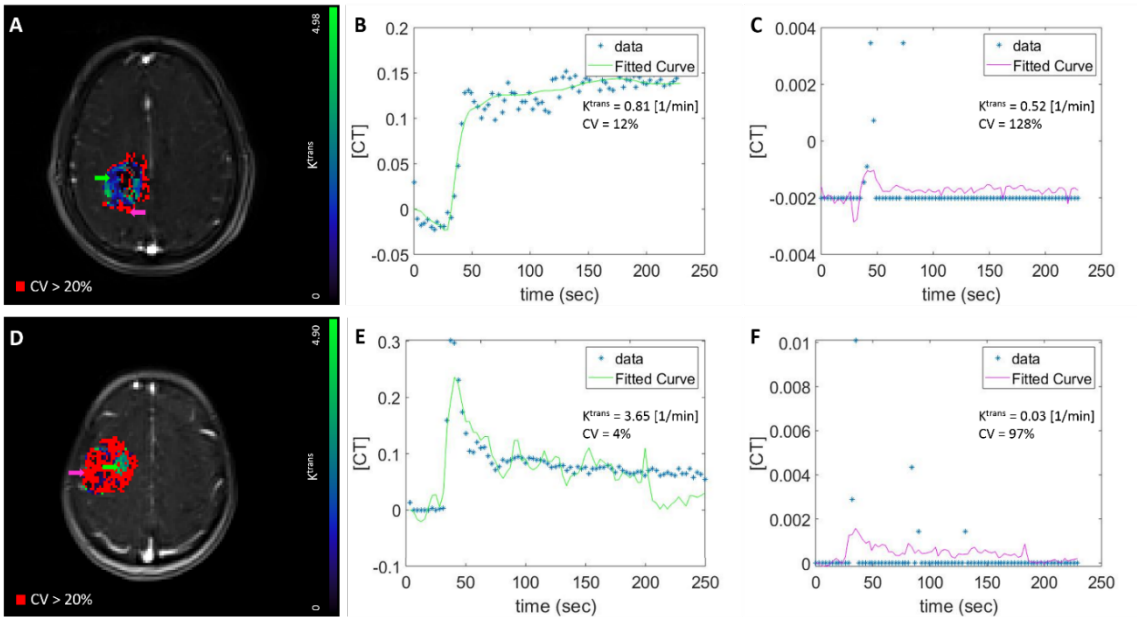

Figure 41: The stability of each pharmacokinetic parameter extracted from the fitting of the model of choice was evaluated, for each lesion, in terms of coefficient of variation in a simulation environment. A and D show two K^{trans} maps. The reliability of DCE-MRI data was evaluated by setting a threshold of 20% for the CV. This is overlaid on the K^{trans} maps in A and D, shown in red, such that only values of K^{trans} under this threshold are displayed on the blue/green colour map. Two tissue activity curves (TACs) relative to two reliable (CV = 12% and CV = 4%) voxels are plotted in B and E. C and F show the TACs relative to two unreliable voxels (CV = 128% and CV = 97%).

4. Discussion

Through an IV injection of a gadolinium-based CA, microvascular permeability is assessed by DCE-MRI. This is a powerful and valuable technique, which was found to be indicative of tumour histological grade in human brain tumours [60]. However, the accuracy of quantitative measurements of perfusion parameters by DCE-MRI is crucial as it can significantly impact the clinical care of cancer patients [61]. Usually, the reproducibility of this technique, and, as a consequence, its reliability is improved by improving the main sources of variability in quantitative DCE-MRI (the acquisition of data, the quantification software)[61]. In this retrospective study we focused on the quantification analysis taking into consideration the particularly heterogeneous nature of brain tumour vascular permeability due to the presence of the BBB. We provided a method to identify reliable DCE-MRI data based on a model selection procedure and a stability test.

4.2 DCE-MRI models

MR scanners usually employ post processing perfusion tools which fit DCE data with the TM. This model (together with its extended versions [34]) considers the system in a fast exchange limit [62,63], assuming an infinitely fast transcytolemmal water exchange between the EES and the intracellular space, which does not affect the overall signal decrease [62,63]. Therefore, many studies on the cell membrane water permeability coefficient have shown FXL to be physically unreasonable and inconsistent [64,65]. The shutter speed model was introduced to reflect a more realistic tissue environment. The model accounts for the intercompartmental water exchange effect, modelling this non-infinitely-fast exchange with the mean intracellular water molecule lifetime τ_i. In 2005, Li et al. introduced a second generation of the shutter speed model which considers also a non-infinitely-fast equilibrium transendothelial water exchange[30].

4.3 Model comparison and stability

The heterogeneity that exists in brain tumours means that one model is insufficient in explaining the different biologies that exist in different tumour regions. Different pharmacokinetic models are required for a complete description of the tissue. This variability is testified by the model selection procedure which showed how, in a single slice of one tumour, multiple models perform better. This result confirms the study of Bagher-Ebadian where they implemented a selection method based on nested models [42]. They found that in the necrotic core of the tumour, models describing vascular filling with no microvascular leakage (similar to the TM) and leakage without vascular reabsorption were selected because of the lack of blood flow. They also hypothesized that the model describing leakage with reabsorption (similar to the ETM) would be selected in the fast growing rims of the lesion. Our results show that there are a number of regions in the tumour where the CA exudation is prevented by the BBB and where the concentration of CA is so low that the evidence of permeability is missing. In this case, the use of the NEM is recommended as, the use of different models could result only in overfitting the data. In fact, our results showed that, no leakage of the CA into the interstitium (or the lack of flow of the CA through the tissue) made the NEM the model of choice for the majority of regions, particularly in the non-enhancing lesions (37.5% of voxels). The result is very close to the ETM (32%), which resulted the model of choice in the enhancing lesions (54.8%). This suggests that, in areas where there is enhancement, a model with 3 parameters performs better and that the choice is dependent on the underlying state of the tissue. In fact, both the ETM and SSM are fitted by three parameters but the third parameter is very different between the two models (v_p for the ETM describing a vascular component in the tissue, and τ_i for the SSM describing the transcytolemmal water exchange). Furthermore, with the implementation of the ESSM, we saw that the transendothelial water exchange did not have any impact on the signal (compared with parameters derived by the fitting of simpler models). It is necessary to consider that the ESSM required 9 parameters to be fitted and that the cost of fitting extra parameters is often contrary to the principle of parsimony. In fact, in fitting data to a noise-limited dataset, the estimation could be very poor and dependent on the optimization procedure itself (the initial conditions, for example) [42]. We compared the AIC values from the different fitting procedures to check whether a model with more parameters is more appropriate than a simple one. The ESSM was selected as the model of choice by <0.1% of voxels, indicating that a model with 3 parameters performed better in the description of brain tumours and further confirming the poor quality of fit observed for the ESSM model. Our outcome agreed with the results of Duan et al.[66]. Using representative in silico and clinical (cervical cancer) DCE-MRI data, they demonstrated the sensitivity of complicated models (parameters > 3) to noise and their decreasing probability of being selected in low signal-to-noise data[66].

The reliability of DCE-MRI data is not only based on the goodness of fit of the chosen pharmacokinetic model, but also on the robustness of the extracted parameters. For this reason, we assessed, for each lesion and for each parameter, the coefficient of variation. We worked in a simulation environment where we added Gaussian noise to our signal and we fitted the noisy curves 500 times. This procedure resulted with a heterogeneous distribution of CVs not linked to contrast enhancement. In fact, Figure 41 shows the plot of four different tissue activity curves together with the K^{trans} value and its CV. As we expected, CV resulted to be very high in regions where the K^{trans} was very low (figure 6, C and F): this is due to the noisy nature of the input data and its consequent high variability. On the other hand, the curves in B and C belong to the same enhancing lesion and correspond to K^{trans} values of 0.81 and 0.52 [1/min]: they correspond to CVs of 12% and 128%, respectively.

Finally, we set a threshold to differentiate between reliable and unreliable DCE-MRI data (CV=20%). We saw that K^{trans} values under this threshold of CV covered only 25% of voxels (an average percentage value evaluated among all patients). This result suggested that only this selection of voxels represents robust values, which can be used in the following statistical analyses, as, more importantly, in clinical evaluations. The selection of the threshold that makes DCE-MRI robust is, however, dependent on the effect size that is being measured and hence will vary across studies.

4.4 Limitations and future work

The main limitation of this study is the small size of the dataset. Furthermore, the sensitivity of DCE-MRI data to water exchange effect was reduced by the 26° flip angle acquisition (exchange-minimized approach) [67,68]. As a consequence, the precision of the τ_i parameter extracted is low. Another limitation of the study is related to the long computational time for the CV evaluation in the simulation environment (500 iterations). This could be improved by implementing the technique using other programming languages or through the implementation of an alternative method, such as the Cramer Rao lower bounds[69].

Finally, future work needs to assess the physiological basis for selecting a particular model in the reliable selection of DCE-MRI data. The applicability of each model depends on the physiology, anatomy and heterogeneity of the tumour and the tumour microenvironment. Future studies will also need to assess the textural features of the TM and SSM parameters in heterogeneous regions of the tumour in order to validate the model selection results.

5. Conclusion

In conclusion, DCE-MRI methods hold great promise for quantitative *in vivo* evaluation of permeability and vascular properties under different pathophysiological conditions. It allows us to identify, and quantitatively measure, smaller changes in permeability for pathological conditions effecting the BBB, than would be observed through visual assessment of post-contrast T_1-weighted images. Different models yield different pharmacokinetic parameters and, for this reason, a model selection is critical for the appropriate analysis of DCE-MRI time courses based on the regional tissue biology, specifically permeability and vasculature. However, due to the unreliable nature of DCE-MRI data, a model selection procedure alone is not enough: pharmacokinetic parameters need to be validated with a stability test in order to give only robust results for statistical analyses and clinical evaluations.

References

1. Khoo VS, Dearnaley DP, Finnigan DJ, Padhani A, Tanner SF, Leach MO. Magnetic resonance imaging (MRI): considerations and applications in radiotherapy treatment planning. *Radiotherapy and Oncology.* 1997;42(1):1-15.
2. Van Geuns R-JM, Wielopolski PA, de Bruin HG, et al. Basic principles of magnetic resonance imaging. *Progress in cardiovascular diseases.* 1999;42(2):149-156.
3. Chavhan GB, Babyn PS, Thomas B, Shroff MM, Haacke EM. Principles, techniques, and applications of T2*-based MR imaging and its special applications. *Radiographics.* 2009;29(5):1433-1449.
4. Brown M, Semelka R, Nishino TK. MRI: basic principles and applications. *Medical Physics.* 2004;31(1):170-170.
5. Bitar R, Leung G, Perng R, et al. MR pulse sequences: what every radiologist wants to know but is afraid to ask. *Radiographics.* 2006;26(2):513-537.
6. Preibisch C, Castrillón GJ, Bührer M, Riedl V. Evaluation of Multiband EPI Acquisitions for Resting State fMRI. *PLoS One.* 2015;10(9):e0136961.
7. Krupa K, Bekiesińska-Figatowska M. Artifacts in magnetic resonance imaging. *Polish journal of radiology.* 2015;80:93-106.
8. Graves MJ, Mitchell DG. Body MRI artifacts in clinical practice: a physicist's and radiologist's perspective. *Journal of magnetic resonance imaging : JMRI.* 2013;38(2):269-287.
9. Essig M, Shiroishi MS, Nguyen TB, et al. Perfusion MRI: The Five Most Frequently Asked Technical Questions. *AJR American journal of roentgenology.* 2013;200(1):24-34.
10. Nielsen T, Wittenborn T, Horsman MR. Dynamic contrast-enhanced magnetic resonance imaging (DCE-MRI) in preclinical studies of antivascular treatments. *Pharmaceutics.* 2012;4(4):563-589.
11. Gordon Y, Partovi S, Müller-Eschner M, et al. Dynamic contrast-enhanced magnetic resonance imaging: fundamentals and application to the evaluation of the peripheral perfusion. *Cardiovascular diagnosis and therapy.* 2014;4(2):147.
12. Yankeelov TE, Gore JC. Dynamic Contrast Enhanced Magnetic Resonance Imaging in Oncology: Theory, Data Acquisition, Analysis, and Examples. *Current medical imaging reviews.* 2009;3(2):91-107.
13. Brix G, Kiessling F, Lucht R, et al. Microcirculation and microvasculature in breast tumors: pharmacokinetic analysis of dynamic MR image series. *Magn Reson Med.* 2004;52(2):420-429.
14. Koh TS, Bisdas S, Koh DM, Thng CH. Fundamentals of tracer kinetics for dynamic contrast-enhanced MRI. *Journal of magnetic resonance imaging : JMRI.* 2011;34(6):1262-1276.
15. Fritz-Hansen T, Rostrup E, Larsson HB, Sondergaard L, Ring P, Henriksen O. Measurement of the arterial concentration of Gd-DTPA using MRI: a step toward quantitative perfusion imaging. *Magn Reson Med.* 1996;36(2):225-231.
16. McIntyre DJ, Ludwig C, Pasan A, Griffiths JR. A method for interleaved acquisition of a vascular input function for dynamic contrast-enhanced MRI in experimental rat tumours. *NMR Biomed.* 2004;17(3):132-143.
17. Kovar DA, Lewis M, Karczmar GS. A new method for imaging perfusion and contrast extraction fraction: input functions derived from reference tissues. *Journal of magnetic resonance imaging : JMRI.* 1998;8(5):1126-1134.
18. Thompson RB, Aviles RJ, Faranesh AZ, et al. Measurement of skeletal muscle perfusion during postischemic reactive hyperemia using contrast-enhanced MRI with a step-input function. *Magn Reson Med.* 2005;54(2):289-298.
19. Jaspers K, Leiner T, Dijkstra P, et al. Optimized pharmacokinetic modeling for the detection of perfusion differences in skeletal muscle with DCE-MRI: effect of contrast agent size. *Med Phys.* 2010;37(11):5746-5755.
20. Lavini C, de Jonge MC, van de Sande MG, Tak PP, Nederveen AJ, Maas M. Pixel-by-pixel analysis of DCE MRI curve patterns and an illustration of its application to the imaging of the musculoskeletal system. *Magn Reson Imaging.* 2007;25(5):604-612.

21. Kuhl CK, Mielcareck P, Klaschik S, et al. Dynamic breast MR imaging: are signal intensity time course data useful for differential diagnosis of enhancing lesions? *Radiology.* 1999;211(1):101-110.
22. Mayr NA, Yuh WT, Arnholt JC, et al. Pixel analysis of MR perfusion imaging in predicting radiation therapy outcome in cervical cancer. *Journal of magnetic resonance imaging : JMRI.* 2000;12(6):1027-1033.
23. Hawighorst H, Knapstein PG, Knopp MV, et al. Uterine cervical carcinoma: comparison of standard and pharmacokinetic analysis of time-intensity curves for assessment of tumor angiogenesis and patient survival. *Cancer Res.* 1998;58(16):3598-3602.
24. Cimmino MA, Innocenti S, Livrone F, Magnaguagno F, Silvestri E, Garlaschi G. Dynamic gadolinium-enhanced magnetic resonance imaging of the wrist in patients with rheumatoid arthritis can discriminate active from inactive disease. *Arthritis and rheumatism.* 2003;48(5):1207-1213.
25. Panting JR, Gatehouse PD, Yang GZ, et al. Abnormal subendocardial perfusion in cardiac syndrome X detected by cardiovascular magnetic resonance imaging. *The New England journal of medicine.* 2002;346(25):1948-1953.
26. Leppek R, Hoos O, Sattler A, et al. [MR-Imaging of lower leg muscle perfusion]. *Herz.* 2004;29(1):32-46.
27. Kety SS. Observations on the validity of a two compartmental model of the cerebral circulation. *Acta Neurol Scand Suppl.* 1965;14:85-87.
28. Landis CS, Li X, Telang FW, et al. Equilibrium transcytolemmal water-exchange kinetics in skeletal muscle in vivo. *Magn Reson Med.* 1999;42(3):467-478.
29. Donahue KM, Burstein D, Manning WJ, Gray ML. Studies of Gd-DTPA relaxivity and proton exchange rates in tissue. *Magn Reson Med.* 1994;32(1):66-76.
30. Li X, Rooney WD, Springer CS, Jr. A unified magnetic resonance imaging pharmacokinetic theory: intravascular and extracellular contrast reagents. *Magn Reson Med.* 2005;54(6):1351-1359.
31. Buckley DL. Uncertainty in the analysis of tracer kinetics using dynamic contrast-enhanced T1-weighted MRI. *Magnetic resonance in medicine.* 2002;47(3):601-606.
32. Tofts PS. T1-weighted DCE imaging concepts: modelling, acquisition and analysis. *signal.* 2010;500(450):400.
33. Tofts PS, Kermode AG. Measurement of the blood-brain barrier permeability and leakage space using dynamic MR imaging. 1. Fundamental concepts. *Magn Reson Med.* 1991;17(2):357-367.
34. Tofts PS, Brix G, Buckley DL, et al. Estimating kinetic parameters from dynamic contrast-enhanced T(1)-weighted MRI of a diffusable tracer: standardized quantities and symbols. *Journal of magnetic resonance imaging : JMRI.* 1999;10(3):223-232.
35. Yankeelov TE, Rooney WD, Li X, Springer CS, Jr. Variation of the relaxographic "shutter-speed" for transcytolemmal water exchange affects the CR bolus-tracking curve shape. *Magn Reson Med.* 2003;50(6):1151-1169.
36. O'Connor JP, Jackson A, Parker GJ, Jayson GC. DCE-MRI biomarkers in the clinical evaluation of antiangiogenic and vascular disrupting agents. *Br J Cancer.* 2007;96(2):189-195.
37. Jelescu IO, Leppert IR, Narayanan S, Araújo D, Arnold DL, Pike GB. Dual-temporal resolution dynamic contrast-enhanced MRI protocol for blood–brain barrier permeability measurement in enhancing multiple sclerosis lesions. *Journal of Magnetic Resonance Imaging.* 2011;33(6):1291-1300.
38. Singh A, Haris M, Rathore D, et al. Quantification of physiological and hemodynamic indices using T(1) dynamic contrast-enhanced MRI in intracranial mass lesions. *Journal of magnetic resonance imaging : JMRI.* 2007;26(4):871-880.
39. Haris M, Gupta RK, Singh A, et al. Differentiation of infective from neoplastic brain lesions by dynamic contrast-enhanced MRI. *Neuroradiology.* 2008;50(6):531-540.
40. Jia Z, Geng D, Xie T, Zhang J, Liu Y. Quantitative analysis of neovascular permeability in glioma by dynamic contrast-enhanced MR imaging. *J Clin Neurosci.* 2012;19(6):820-823.
41. Thompson EM, Guillaume DJ, Dosa E, et al. Dual contrast perfusion MRI in a single imaging session for assessment of pediatric brain tumors. *J Neurooncol.* 2012;109(1):105-114.
42. Bagher-Ebadian H, Jain R, Nejad-Davarani SP, et al. Model selection for DCE-T1 studies in glioblastoma. *Magnetic resonance in medicine.* 2012;68(1):241-251.

43. Ferl GZ, Xu L, Friesenhahn M, Bernstein LJ, Barboriak DP, Port RE. An automated method for nonparametric kinetic analysis of clinical DCE-MRI data: application to glioblastoma treated with bevacizumab. *Magn Reson Med.* 2010;63(5):1366-1375.
44. Zhu XP, Li KL, Kamaly-Asl ID, et al. Quantification of endothelial permeability, leakage space, and blood volume in brain tumors using combined T1 and T2* contrast-enhanced dynamic MR imaging. *Journal of magnetic resonance imaging : JMRI.* 2000;11(6):575-585.
45. Huang W, Li X, Morris EA, et al. The magnetic resonance shutter speed discriminates vascular properties of malignant and benign breast tumors in vivo. *Proceedings of the National Academy of Sciences.* 2008;105(46):17943-17948.
46. Li X, Priest RA, Woodward WJ, et al. Feasibility of shutter-speed DCE-MRI for improved prostate cancer detection. *Magnetic resonance in medicine.* 2013;69(1):171-178.
47. Jajamovich GH, Huang W, Besa C, et al. DCE-MRI of hepatocellular carcinoma: perfusion quantification with Tofts model versus shutter-speed model—initial experience. *Magnetic Resonance Materials in Physics, Biology and Medicine.* 2016;29(1):49-58.
48. Rooney WD, Li X, Sammi MK, Bourdette DN, Neuwelt EA, Springer CS, Jr. Mapping human brain capillary water lifetime: high-resolution metabolic neuroimaging. *NMR Biomed.* 2015;28(6):607-623.
49. Li X, Rooney WD, Varallyay CG, et al. Dynamic-contrast-enhanced-MRI with extravasating contrast reagent: rat cerebral glioma blood volume determination. *J Magn Reson.* 2010;206(2):190-199.
50. Lee SH, Hayano K, Zhu AX, Sahani DV, Yoshida H. Water-exchange-modified kinetic parameters from dynamic contrast-enhanced MRI as prognostic biomarkers of survival in advanced hepatocellular carcinoma treated with antiangiogenic monotherapy. *PloS one.* 2015;10(9):e0136725.
51. Guo Y, Zhu Y, Goud LS, Lebel RM, Shiroishi M. High-resolution whole-brain dynamic contrast-enhanced MRI using compressed sensing. *Biomedical Optics & Medical Imaging*: SPIE Newsroom; 2015.
52. Yuan J, Chow SK, Yeung DK, Ahuja AT, King AD. Quantitative evaluation of dual-flip-angle T1 mapping on DCE-MRI kinetic parameter estimation in head and neck. *Quant Imaging Med Surg.* 2012;2(4):245-253.
53. Liberman G, Louzoun Y, Ben Bashat D. T(1) mapping using variable flip angle SPGR data with flip angle correction. *Journal of magnetic resonance imaging : JMRI.* 2014;40(1):171-180.
54. Li KL, Zhu XP, Waterton J, Jackson A. Improved 3D quantitative mapping of blood volume and endothelial permeability in brain tumors. *Journal of magnetic resonance imaging : JMRI.* 2000;12(2):347-357.
55. Lagarias JC, Reeds JA, Wright MH, Wright PE. Convergence properties of the Nelder--Mead simplex method in low dimensions. *SIAM Journal on optimization.* 1998;9(1):112-147.
56. *fminsearchbnd* [computer program]. Version 1.4.0.0. MathWorks File Exchange2012.
57. Akaike H. A new look at the statistical model identification. *IEEE transactions on automatic control.* 1974;19(6):716-723.
58. Buckley DL, Roberts C, Parker GJ, Logue JP, Hutchinson CE. Prostate cancer: evaluation of vascular characteristics with dynamic contrast-enhanced T1-weighted MR imaging--initial experience. *Radiology.* 2004;233(3):709-715.
59. McRobbie DW, Moore EA, Graves MJ, Prince MR. *MRI from Picture to Proton.* 2 ed. Cambridge: Cambridge University Press; 2006.
60. Roberts HC, Roberts TP, Brasch RC, Dillon WP. Quantitative measurement of microvascular permeability in human brain tumors achieved using dynamic contrast-enhanced MR imaging: correlation with histologic grade. *American Journal of Neuroradiology.* 2000;21(5):891-899.
61. Kim H. Variability in Quantitative DCE-MRI: Sources and Solutions. *Journal of nature and science.* 2018;4(1).
62. Bergamino M, Bonzano L, Levrero F, Mancardi G, Roccatagliata L. A review of technical aspects of T1-weighted dynamic contrast-enhanced magnetic resonance imaging (DCE-MRI) in human brain tumors. *Physica Medica: European Journal of Medical Physics.* 2014;30(6):635-643.
63. Heye AK, Culling RD, Hernández MdCV, Thrippleton MJ, Wardlaw JM. Assessment of blood–brain barrier disruption using dynamic contrast-enhanced MRI. A systematic review. *NeuroImage: Clinical.* 2014;6:262-274.

64. Quirk JD, Bretthorst GL, Duong TQ, et al. Equilibrium water exchange between the intra-and extracellular spaces of mammalian brain. *Magnetic resonance in medicine.* 2003;50(3):493-499.
65. Nordhøy W, Anthonsen HW, Bruvold M, et al. Intracellular manganese ions provide strong T1 relaxation in rat myocardium. *Magnetic resonance in medicine.* 2004;52(3):506-514.
66. Duan C, Kallehauge JF, Bretthorst GL, Tanderup K, Ackerman JJ, Garbow JR. Are complex DCE-MRI models supported by clinical data? *Magn Reson Med.* 2017;77(3):1329-1339.
67. Li X, Priest RA, Woodward WJ, et al. Cell membrane water exchange effects in prostate DCE-MRI. *Journal of Magnetic Resonance.* 2012;218:77-85.
68. Buckley DL. Shutter-speed dynamic contrast-enhanced MRI: Is it fit for purpose? *Magn Reson Med.* 2018.
69. Naeyer DD, Ceelen WP, Verdonck P. In vivo validation of Cramer-Rao lower bounds for evaluating the reproducibility of Tofts kinetic modeling of DCE-MRI data. *Clinical Cancer Research.* 2010;16(19 Supplement):B7-B7.

CHAPTER 4

Multiparametric imaging

Tumours are frequently heterogeneous in their presentation and behaviour. Multiparametric imaging allows investigation of this heterogeneity in a comprehensive way with the identification of tumour sub-volumes with distinct properties [1]. Nowadays it is possible to gather of a large amount of information from the available advanced imaging techniques. CT and MRI both provide morphological information. In particular, dynamic contrast-enhanced CT or MRI (DCE CT/MRI) allows investigation of the vasculature (e.g. tumour permeability and blood flow) typically following injection of a contrast agent over time as it passes through the tumour blood vessels. Furthermore, diffusion-weighted MRI (DWI MRI) facilitates mapping of diffusion patterns of water molecules, a characteristic related to cellular density. These advanced MRI techniques have a role in the standard guidelines for distinguishing malignant involvement from benign conditions, for instance in prostate cancer and pleural mesothelioma [1].
On the other hand, biological processes, which are disregulated in cancer cells and distinguish malignant tissue from healthy tissue, can be visualized using nuclear medicine-based techniques. The general PET approach includes the use of FDG, a glucose analogue, whose uptake is upregulated in tumours as an indicator of their metabolism. There are many tumour hallmarks that can be visualized using PET imaging. One of them is the activity of thymidine kinase 1, an enzyme involved in DNA synthesis, as a surrogate for most cell proliferation: it is studied with Fluorothymidine (FLT). Low oxygen levels, i.e. hypoxia, are imaged with tracers based on 2-nitroimidazoles (e.g. FMISO, FAZA, HX4), which allow the visualization of increased reductase activity in cells with insufficient oxygen.

Until recently, these imaging techniques have mostly been used in isolation. However, functional molecular imaging techniques are now increasingly being performed in combinations. Multifunctional imaging is becoming an important means for biologic investigation because of its multidimensional (multispectral, multispatial and temporally resolved) nature. Combined approaches have been made possible by (a) the development of hybrid imaging technologies such as single photon emission computed tomography (SPECT)/CT and PET/CT and PET/MR imaging, (b) technologic advancements within individual imaging modalities that enable multifunctional data acquisitions within short periods of time including the use of PET isotopes with very short half-lives, (c) advances in software enabling both fusion of imaging data between imaging modalities and derivation of quantitative biologically relevant biomarker data that can be coregistered with anatomic images, and last, (d) bioinformatics allowing integration of quantitative imaging parameters with other biologic data such as serum cytokines, circulating cells, and tissue genomic and protein expressions [2].

A review of the literature shows that the multiparametric approach has been used in a number of ways, including:
1) Improving the depiction of tumour biology: multifunctional imaging makes it possible to correlate observations between techniques at the tumour or voxel level. Such cross-correlations have been used (a) to refine the accuracy of imaging observations, (b) to validate an emerging biomarker against an accepted standard (by ascertaining the strength of relationships between them and by exploring the circumstances under which the strength of relationships may be changed), and finally (c) to clarify the nature of relationships between biologic functions at the voxel and patient levels [2].

2) Clinical characterization of known disease: functional imaging is often used to clarify the nature of abnormalities seen at imaging examinations. Multifunctional evaluations are an extension of this approach that have been used for the characterization of lesions at a variety of anatomic sites including the brain (23,24) and the parotid (25) and prostate gland (26–28). When multifunctional assessments are used for disease characterization, it is often found that results from individual modalities are discordant at the regional or whole-tumour level [2].
3) Assessment of therapy response: monitoring changes with multiparametric imaging can provide invaluable information on the in vivo mechanisms of action of therapeutics and so can be of use in drug development [2].

Hybrid PET/MRI system

Both positron emission tomography and magnetic resonance imaging are well-established imaging modalities that have been clinically available for more than 30 years. However, the combination of PET and computed tomography (CT) into PET/CT has heralded a new era of hybrid imaging driven by the rapid ascend of PET/CT and the decline of stand-alone PET. The integration of PET and CT into a hybrid system has provided added value that exceeds the sum of its parts, in particular fast and accurate attenuation correction and the combination of anatomical and molecular information. This has been the inspiration for the combined PET/MRI [3]. While the integration of PET and CT into a hybrid system was challenging but technically feasible, the integration of PET and MRI was considered extremely demanding, if not impossible. Two main technical challenges had to be solved: in the first place the development of a PET insert that is compatible to high magnetic field strengths normally used in MRI, and vice versa the development of a magnetic resonance scanner that guarantees a stable and homogenous magnetic field in the presence of a PET insert [3]. Conventional PET detectors consist of scintillation crystals and photomultipliers, and the latter, being very sensitive to magnetic fields, cannot be used in integrated PET/MRI systems. Hence, one approach was to replace photomultipliers by avalanche photodiodes (APDs), which are insensitive to even strong magnetic fields. The scintillation crystals used in PET/MRI scanners are usually composed of lutetium ortho-oxysilicate, with the advantage of only minor disturbances of magnetic field homogeneity. Next generation PET/MRI scanners could be based on silicon photomultiplier PET detectors, which showed better performance characteristics than the APDs and, in contrast to these, are capable of time-of-flight imaging [4, 5]. Secondly, the development of MR-based attenuation correction methods is necessary, as the commonly used method for attenuation correction in PET/CT systems, which is based on the absorption of X-rays, is not transferable to MRI. In principle, the MR-based attenuation map is created with a two-point Dixon sequence, providing water-only and fat-only images, which are combined and segmented to form an MR-based attenuation map. The method proved its technical feasibility with the limitation that in bone tissue and in its vicinity standardized uptake values (SUV) derived from PET/MRI systems should be interpreted carefully until a larger experience with the new method of PET/MRI exists [3]. In 2010, the first fully integrated whole-body PET/MR hybrid imaging system based on APD technology and MR-based attenuation correction became commercially available (Biograph mMR, Siemens Healthcare, Erlangen, Germany) [3].
As discussed before, in addition to anatomical images, MRI provides functional and quantitative data like diffusion-weighted imaging (DWI), spectroscopy, blood oxygenation level-dependent imaging in functional MRI, T_1/T_2 mapping and dynamic contrast-enhanced imaging. Consequently, valuable applications of PET/MRI emerge in the field of multiparametric and quantitative imaging. In fact, tumour characterization and response evaluation can benefit from multiparametric imaging as tumours are spatially heterogeneous and dynamically evolving entities that are often not sufficiently characterized by size-based assessment only [3]. PET/MRI offers some unique features like real parallel PET and MRI acquisition that enable imaging protocols like integrated functional MRI and dynamic PET after presentation of a stimulus or cardiac stress PET/MRI. In combination with the ionizing radiation-free nature of MRI, parallel acquisition also allows for the continuous acquisition of anatomical images that can be used for motion correction of PET data. Thus, the quality of PET images in applications like cardiac, lung, or bowel imaging can be increased while respiratory and/or electrocardiography-gating can be potentially omitted [3].

In addition, PET/MRI offers practical advantages for patients requiring both PET and MRI examinations for oncologic assessment by providing both modalities within a single appointment and imaging session. Radiation exposure is also reduced because CT is not used in the imaging protocol. Finally, PET/MRI allows accurate, temporally and spatially aligned multiparametric imaging that combines high-contrast anatomic MR images with the quantitative power of molecular imaging of both PET and MRI, including DWI, perfusion MRI, and MR spectroscopy.

This potential creates numerous opportunities for characterizing tumour biology across all of the dimensions of imaging offered by PET and MRI [6]. Examples of clinical application include, in brain glioma, the localization of focal targets for surgical biopsy planning, especially in spatially heterogeneous gliomas, with an improved gross tumour volume and tumour margin delineation for radiotherapy planning, and improved detection of post-treatment recurrences [6]. Furthermore, FDG PET/MRI may offer improvements in both breast imaging and whole-body staging for patients with breast cancer.

Applications

My analysis has mainly focused on the clinical characterization of a known disease with the integration of information derived by CT, PET and MR imaging (the latter two in combination or not). In particular, I applied pharmacokinetic analysis on dynamic PET data acquired on a PET/CT scanner and on dynamic MRI data acquired on a hybrid PET/MRI scanner. The section will open with a brief introduction on the characteristics of the scanner and the results of the multiparametric study done on breast cancer data acquired on the hybrid PET/MRI scanner based on the published article:

Inglese M, Cavaliere C, Monti S, Forte E, Incoronato M, Nicolai E, Salvatore M, Aiello M *A multi-parametric PET/MRI study of breast cancer: evaluation of DCE-MRI pharmacokinetic models and correlation with diffusion and functional parameters* NMR in Biomedicine 2018;e4026

The same dataset has been used for a predictive study, with the relationship also with himmunoistochemical markers. I will show the results of this study based on the published article:

Incoronato M, Grimaldi AM, Cavaliere C, **Inglese M**, Mirabelli P, Monti S, Ferbo U, Nicolai E, Soricelli A, Aiello M, Salvatore M *Relationship between functional imaging and immunohistochemical markers and prediction of breast cancer subtype: a PET/MRI study* European journal of nuclear medicine and molecular imaging (2018): 1-14.

I will then show the results of a multiparametric study done on brain data acquired both on a PET/CT scanner and on an MR scanner, separately. This is based on the conference paper:

Inglese M, Grech-Sollars M, Ordidge K, Vaja V, Honeyfield L, Khan S, Barwick T, Aboagye OE, Waldman AD *Association between pharmacokinetic parameters from DCE-MRI and metabolic parameters from dynamic 18F-fluoromethylcholine PET in human brain glioma* ISMRM 2018 (second place winner)

I have applied pharmacokinetic analysis on a small dataset of breast and lung cancer patients, who have joined a translation study of the 18F-ICMT-11 PET tracer for the evaluation of chemotherapy-induced caspase 3/7 activation. I will briefly show the results, based on the published article:

Dubash S, Merchant S, Mauri F, Lavdas I, **Inglese M**, Kozlowski K, Rama N, Masrour N, Steel JF, Thornton A, Lim AK, Lewanski C, Cleator S, Coombes RC, Kenny L, Aboagye EO *Clinical translation of [18 F] ICMT-11 for measuring chemotherapy-induced caspase 3/7 activation in breast and lung cancer."* European journal of nuclear medicine and molecular imaging (2018): 1-15.

Finally, my kinetic analyses have been part of a radiomic study on patients with prostate cancer. I will show the results, based on the conference paper:

Monti S, Aiello M, **Inglese M**, Diomaiuti CT, Ragozzino A, Cavaliere C *Multiparametric MRI in prostate cancer: a radiomics study on different diffusion and perfusion models* ECR 2018

I. A multi-parametric PET/MRI study of breast cancer: evaluation of DCE-MRI pharmacokinetic models and correlation with diffusion and functional parameters

The objective of this study is to compare perfusion parameters, as measured by both the shutter speed and the Tofts model in malignant breast lesions. Also, to investigate the relationship between perfusion, morphological and functional parameters extracted by simultaneous acquisition of the positron emission tomography (PET) and magnetic resonance imaging (MRI).
46 patients with histologically confirmed breast cancer were enrolled and imaged with a 3T hybrid PET/MRI system, at staging. ^{18}F-FDG PET images were acquired simultaneously to MRI, which included DW- and DCE-MRI protocols. Standardized uptake value (SUV), apparent diffusion coefficient (ADC) and pharmacokinetic maps (from the Tofts and shutter speed model applied on dynamic MRI data) were calculated for each primary lesion and reference area. Wilcoxon and Spearman tests were chosen for the statistical analysis.
Results showed that MRI derived measurements (perfusion and diffusion) and PET SUV_{mean} resulted able to statistically discriminate between tumour and reference tissue ($p < 0.05$). Significant correlations were found between the two pharmacokinetic models ($p < 0.01$) and between SUV and pharmacokinetic parameters (K^{trans}, k_{ep}, v_e and τ_i). No correlation was observed between ADC and SUV, as well as between ADC and pharmacokinetic parameters.
In conclusion, PET/MRI allows for the characterization of primary lesions. Simultaneous analysis of perfusion, morphological and functional markers shows good agreement between different pharmacokinetic models. Perfusion parameters showed a good correlation with the SUV in breast lesions. In particular, the shutter speed τ_i was found to be significantly correlated to ^{18}F-fluorodeoxyglucose (FDG) uptake (negative correlation) meaning an association with tumour metabolic mechanisms.

1. Introduction

Recent technological developments and advanced imaging techniques can provide early diagnosis in breast cancer. However, breast cancer is still the most frequently diagnosed cancer among women in 140 of 184 countries worldwide and remains the most common cause of cancer death (322,600 breast cancer deaths have been averted in US women through 2015)[7].

In the past decades, the significant improvements of integrated and advanced imaging techniques, mainly in MRI and PET, have made both modalities clinically relevant in breast cancer staging, management and follow-up [8-11]. In particular, the multimodal, combined PET/MRI approach allows the integration of anatomic and functional information, thus providing a higher registration accuracy when compared to retrospectively coregistered images acquired on separate scanners. Thanks to the integration of MRI, excellent soft tissue contrast is combined with the molecular information from PET and this approach has been shown to provide a comprehensive clinical view for many tissues, including the breast [12-17]. In fact, the imaging parameters derived from the two different modalities can give complementary information with regards to the tumour environment as they relate to different imaging properties (functional, morphologic). ^{18}F-fluorodeoxyglucose (FDG)-PET measures the in vivo radiotracer distribution [kBq/ml], which,

in the case of FDG -an analogue of glucose- provides functional information based on the increased glucose uptake and glycolysis of cancer cells [18, 19]. On the other hand, diffusion weighted (DW)-MRI, quantified by the apparent diffusion coefficient (ADC), estimates the rate of water diffusion in tissues. It has been shown that the diffusivity of water molecules is restricted to environments of high cellularity, where tumour cell proliferation occurs. This results in low ADC values within tumours [20-22]. Finally, dynamic contrast enhanced (DCE)-MRI data, fitted to an appropriate pharmacokinetic model, results in quantitative physiological parameters, relating to tumour permeability and perfusion.

DCE-MRI data are usually quantified with the application of the pharmacokinetic two-compartment Tofts model (also known as the *standard model*), which represents the system with the plasma and tissue (extravascular extracellular space) compartments and with the contrast reagent exchange rates between them. This model considers the system in, what-is-known as, the fast exchange limit (FXL)[23] assuming infinitely fast transcytolemmal water exchange kinetics. Several measurements done on the cell membrane water permeability coefficient have shown the FXL to lead to non physiological and inconsistent results and in particular to pharmacokinetic parameters' misestimation[24, 25]. The shutter-speed model (SSM) admits the system to leave the FXL, at rising values of concentration of the contrast media, and to enter the what-is-called fast exchange regime (FXR). This model accounts for the effect of finite transcytolemmal water exchange kinetics on the overall MR signal decrease. It provides the additional pharmacokinetic parameter τ_i (mean intracellular water molecule lifetime), which has been suggested to be associated with tissue metabolic activity [26, 27].

Several studies investigated the relationship between these two models in the description of perfusion mechanisms in breast cancer. For example, Li et al. found that the transient departure from FXL to FXR is significant only in malignant tumours, presumably because of angiogenic capillary leakiness; they also found FXR models to provide the most complete statistical description of dynamic contrast-enhanced MRI with a Bayesian information criteria approach [28, 29]. Furthermore, the relationship between parameters resulting from the Tofts model and the ADC, or the SUV have been also examined: Arlinghaus et al. found no statistically significant correlation between ADC and extravascular extracellular volume fraction on either a voxel-by-voxel or a region-of-interest (ROI) basis; Semple et al. found a significant association ($p < 0.05$) between pre-therapy DCE-MRI vascular parameters and the reduction in PET metabolism resulting from administration of one cycle of chemotherapy in seventeen patients with large or locally advanced invasive ductal carcinomas of the breast [30, 31].

The aim of the study is to investigate the relationship between pharmacokinetic parameters derived by the application of both Tofts and SSM to DCE–MRI data and also the relationship between perfusion, diffusion and metabolic characteristics of breast tumour estimated by MRI. In particular, we investigate SSM DCE-MRI parameters in combination with FDG-PET metabolic activity measurements in breast cancer. Data is acquired on a hybrid PET/MR scanner: that guarantees, not only the a priori spatial coregistration of the acquired volumes, but also the convenience of the patient. Most importantly, the assessment of the lesion is done with morphological and metabolic data acquired at the same physiological condition.

2. Materials and methods

2.1 Patient population

46 patients with positive mammographic reports and histologically proven primary breast cancer were enrolled between September 2012 and December 2015 (Table 13), following institutional review board and Ethical Committee approval and written informed consent. Exclusion criteria

were: blood glucose levels greater than 150 mg/dL, pregnancy, concurrent severe renal failure, and standard contraindications for MRI.

Table 13: Population clinical parameters.

N	Age median [range]	Lesion size (cm) median [range]	pT				Tumour types		Grading		Histological Subtypes			
			T0	T1	T2	T3	IDC	ILC	G2	G3	l-A	l-B	b-l	h-l
46	58 [41, 85]	2.50 [0.2, 7]	3	7	21	15	39	7	31	15	11	29	3	3

Note: Lesion size measured by MR in the axial slice with major lesion extension; pT: histological tumour staging; l-A: luminal A; l-B: luminal B; b-l: basal like; h-l: HER2 like.

2.2 PET-MRI Data Acquisition

Data were acquired on a 3T mMR Biograph hybrid PET-MR system (Siemens, Erlangen).
All patients fasted at least six hours before PET imaging. 401 ± 32 MBq (mean ± std) of ^{18}F-FDG were administered intravenously. After a 60-minute equilibration period, during which the patients were at rest, PET images (4 mm spatial resolution) over the tumour were acquired simultaneously with MRI.

DW-MRI was acquired in the axial plane with a single shot spin-echo echo-planar imaging sequence in three orthogonal diffusion encoding directions with b-values of 0-50-400-800 s/mm^2, TR/TE = 14500 ms/ 66 ms, FOV 340 mm, base resolution 192, slice thickness 4 mm.

DCE-MRI was performed with an 8 channel dedicated breast coil. Images were acquired in the axial plane and included, for all examinations, six pre contrast spoiled gradient recalled echo (SPGRE) 3D vibe sequences at six different flip angles (2, 5, 8, 12, 15, 20) and a dynamic 3D vibe sequence (TR=5.5 ms, TE=1.7 ms, flip angle = 20, FOV 320 mm, base resolution 192, slice thickness 3.6 mm, parallel imaging acceleration factor 2, 36 slices per DCE-MRI image frame) to obtain images before, during and after the injection of the contrast agent (0.1 mmol/kg body-weight gadolinium-diethylene triaminepentacetate (Gd-DTPA), Magnevist). The contrast agent was administered using a power injector on the 3rd acquisition with a flow rate of 3 ml/s. Full breast coverage was achieved with the 3D acquisition. 60 time points were acquired with an average temporal resolution of 9.5 s and a total acquisition of ~9 minutes. Patients were allowed to breathe freely.

For clinical evaluation, the protocol included also axial and coronal T2 turbo inversion recovery magnitude sequences (TR = 4220 ms, TE = 61 ms, FOV 340 mm, base resolution 256, slice thickness 4 mm) and a T2 turbo spin echo (TR = 5440 ms, TE = 81 ms, FOV 340 mm, base resolution 448, slice thickness 4 mm).

Following acquisition, PET images were automatically corrected for the tissue attenuation with the attenuation maps generated by using the 2-point Dixon MRI sequences[32]. Emission data were corrected for randoms, dead time, scatter, and attenuation. A 3-dimensional attenuation-weighted ordered-subsets expectation maximization iterative reconstruction algorithm (AW OSEM 3D) with 3 iterations and 21 subsets, Gaussian smoothing of 4 mm in full width at half maximum, was used.

3. Image post-processing: background

3.1 Pharmacokinetic modelling

DCE-MRI data were analysed using in house code written in Matlab (Mathworks, R2015b). Relaxation rate at baseline (R_{10}) and relaxed signal (M_0) were calculated, as 3D maps, with the Ernst formula (assuming TE<<T2*) using the set of SPGRE pre contrast images at different flip angles[33]:

$$S(\alpha) = M_0 \sin(\alpha) \frac{1-e^{-R_{10}T_R}}{1-\cos(\alpha)\cdot e^{-R_{10}T_R}} \qquad 29)$$

where α is the flip angle and can assume values belonging to [2, 5, 8, 12, 15, 20] and T_R = 5.5 ms. Following the method described by Liberman et al., the problem is reformulated as a linear regression system ($y = ax + b$), as follows:

$$\frac{S(\alpha)}{\sin(\alpha)} = E \cdot \frac{S(\alpha)}{\tan(\alpha)} + M \cdot (1 - E) \qquad 30)$$

where E = exp(-R_{10}*T_R)[34]. The slope $a = E$ and intercept $b = M(1-E)$ can be estimated, from which R_{10} and M_0 can be obtained as:

$$R_{10} = -\frac{\log(a)}{T_R}, M = \frac{b}{1-a} \qquad 31)$$

4D (x, y, z, t) post-injection longitudinal relaxation rate, $R_1(t)$ maps are calculated for each dynamic phase using signal intensity data from pre and post contrast T_1 weighted gradient recalled echo (T_1w-GRE) dynamic series:

$$R_1(t) = -\frac{1}{T_R} \cdot log \frac{1-(A+B)}{1-\cos(\alpha)\cdot(A+B)} \qquad 32)$$

where α = 20, A = [S(t) - S(0)]/($M_0 \cdot \sin(\alpha)$), B = (1-E)/(1-E· cos(α)). S(0) and S(t) are respectively the pre contrast injection signal intensity (the first baseline scan) and the signal at the t^{th} dynamic phase[35].

Data was then fitted with the Tofts and the shutter speed model, as described in *Chapter 3*.

3.2 Apparent diffusion coefficient computation

ADC maps were automatically computed by the scanner via Eq. ($ADC = -\ln[\frac{S(b)}{S(0)}]/b$ 33):

$$ADC = -\ln[\frac{S(b)}{S(0)}]/b \qquad 33)$$

where *S(0)* denotes signal intensity in the absence of diffusion gradients, *b* reflects the strength and the duration of a diffusion-sensitizing gradient and *S(b)* is the signal intensity at non-zero *b* value. Having measured a set of images at four different *b*-value, the system calculates, pixel-by-pixel, the ADC using linear regression. On a half logarithmic scale, the signal decay is a straight line whose slope provides the ADC. The faster the signal decay the steeper the slope and, so, the higher the ADC[36].

3.3 SUV computation

The FDG uptake in tumours is related to the proliferative activity of a malignant tissue and to the number of viable tumour cells. Even though quantification is straightforward in PET imaging, it is subject to the variability introduced by differences in patient size, the amount of FDG injected and the radiotracer decay. The quantification of FDG uptake is preferably done with the SUV, which ideally removes those sources of variability and has a specific role in assessing patient response to cancer therapy. The body-weighted SUV is given by the following equation:

$$SUV = \frac{r}{(a\prime/w)} \qquad 34)$$

where r is the radioactivity concentration [kBq/ml] measured by the PET scanner, a' is the decay-corrected amount of injected radio-labelled FDG [kBq], and w is the weight of the patient [g].

4. Image Analysis

Free-hand regions of interest (ROIs) were drawn around the area of maximal tumour extension for each of the 46 subjects by one senior radiologist experienced in breast imaging (CC, 6 years of experience) and one nuclear medicine specialist (EN, 7 years of experience). Primary tumour location was outlined on the subtracted T_1 post-contrast slices, with consideration to avoid necrotic areas and/or large feeding vessels[37]. An additional 1-cm^2 ROI was drawn in the reference area (the contralateral healthy breast).

In order to propagate the drawn ROIs onto the ADC maps and PET images- coregistered to the subtracted T_1 contrast-enhanced sequence but of different spatial resolution- they were resampled to the 1.9 × 1.9 × 3.6 mm MRI voxel size using a fourth degree B-spline interpolation. However, DW images are affected by geometrical distortion due to echo planar acquisition[38]: we visually double confirmed the traced boundaries, after the ROI propagation onto the ADC maps and, when necessary, we made a manual correction to assure a correspondence between the lesion and the ADC map.

Then, pharmacokinetic measures for perfusion, diffusion and glucose metabolism evaluation were performed across each ROI (maximum and mean values were extracted for each parameter). The incremental area under the concentration curve (iAUC) was estimated for each ROI with the trapezoidal rule and its mean value was evaluated. An additional ROI was drawn in the aorta for the individual evaluation of the concentration of the contrast reagent in the plasma (Figure 42)[39].

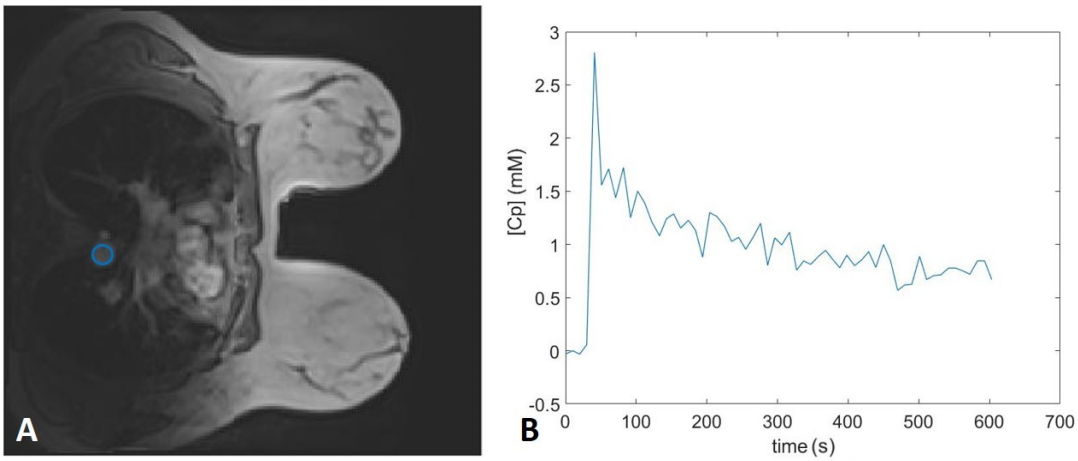

Figure 42: A) Contrast enhanced breast MR image of patient n. 1. The ROI is placed in the aorta for the evaluation of the arterial input function. B) Mean plasma contrast reagent concentration time course from the ROI placed in the aorta.

The Tofts and shutter speed models fitting of DCE-MRI data was performed using an in-house software written in Matlab (MathWorks, R2015b). In particular we chose the *fminsearch* function, which uses the Nelder-Mead simplex algorithm as described in Lagarias et al.[40]. The minimization procedure was performed voxelwise in order to obtain a 2D map for each pharmacokinetic parameter. We set input values of 0.1 and 0.01 for the K^{trans} and v_e, respectively, and run the algorithm with 10000 iterations and a tolerance of 10^{-8}. Figure 43 shows an example of the fitting results for one voxel of the lesion and reference for a representative patient. Data are expressed as mean (evaluated averaging the voxel values within the tumour ROI drawn on the single image slice with the maximal tumour extension) ± standard deviation. For the following analyses, non normative values (negative values and K^{trans}, $k_{ep} > 5$, $v_e > 1$) [41] were discarded. This resulted with an average loss of 4.26 (±13.42) % of voxels per map.

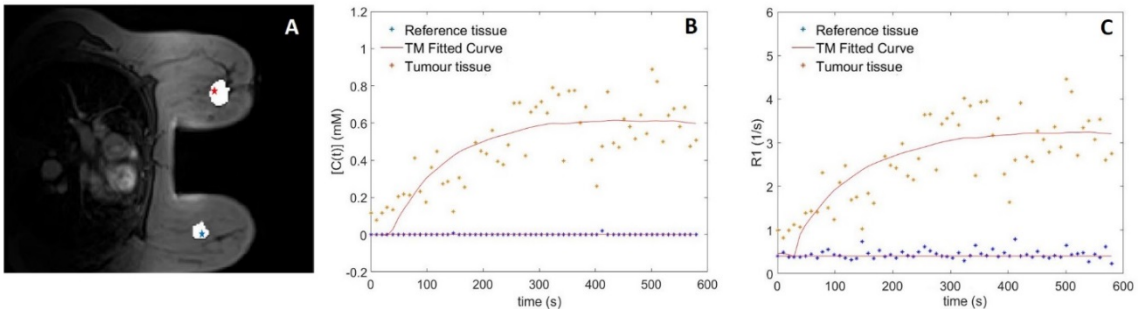

Figure 43: A) Contrast enhanced axial breast MR image of patient n. 14. Two voxels have been selected for showing the results of the Tofts and shutter speed model fitting procedure. In particular, the red star is related to the lesion where the blue one belongs to the reference area. B, C) Fitting curves (in red) resulted from the application of the Tofts and shutter speed model to tumour tissue data (red dots) and reference tissue input data (blue dots).

5. Statistical Analysis

Statistical analysis was performed in Matlab (Mathworks, R2015b). The Kolmogorov - Smirnov test was used to assess the normality of each parameter distribution; the Wilcoxon Sum Rank test was used to evaluate significant differences between tumorous and reference areas and between estimated perfusion parameters obtained with the Tofts and Shutter-speed model; the non-

parametric Spearman test was used to verify the correlation between parameter distributions. A false discovery rate < 0.05 was used for multiple comparison correction. A correlation coefficient ρ < 0.35 was considered to represent low correlation, values between 0.36 and 0.67 were characterised as low correlation, between 0.68 and 0.90 to high correlation, ρ > 0.90 represented excellent correlation[31].

6. Results

Figure 44 shows an example of the parametric maps used in this study. In particular, in the first row a post contrast MRI T_1-weighted image (8th phase), the MRI subtraction of the baseline scan from the 8th phase, the attenuation corrected PET image and the ADC map are shown. Following, there are the pharmacokinetic maps evaluated with the Tofts model (K^{trans}, k_{ep} and v_e), the iAUC and the pharmacokinetic maps evaluated with the shutter speed model (K^{trans}, k_{ep}, v_e and τ_i). Non-normal distributions were observed for all the parameters.

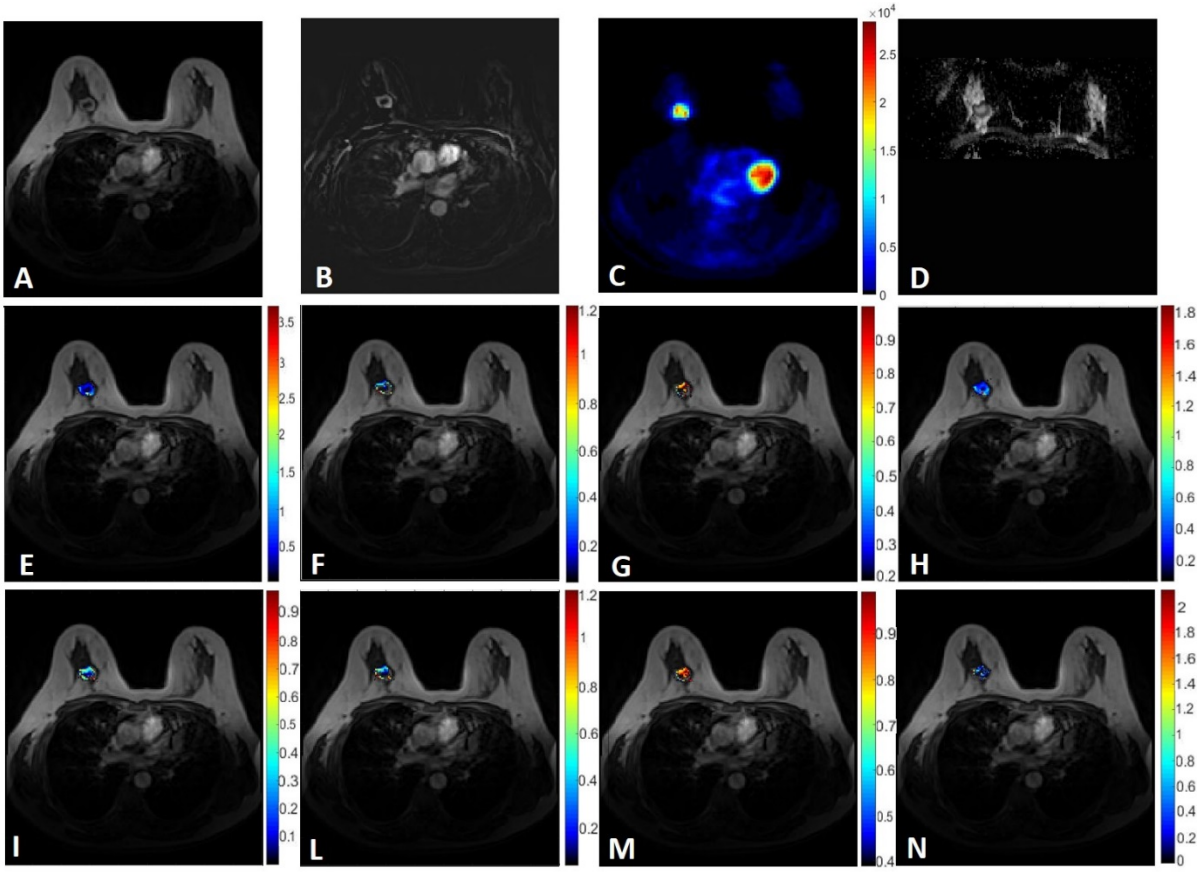

Figure 44: Patient n. 2; 45 years old, IDC. Representative axial images of a) post contrast MRI T1-weighted image (8th phase); b) MRI subtraction of the baseline scan from the 8th phase; c) attenuation corrected PET image; d) ADC map; e - g) Pharmacokinetic maps evaluated with the Tofts model: K^{trans}, K_{ep} and v_e; h) iAUC; i - n) Pharmacokinetic maps evaluated with the shutter speed model: K^{trans}, K_{ep}, v_e and τ_i.

6.1 Comparison between lesion and reference area

Table 14 shows mean and standard deviation values for K^{trans}, k_{ep}, v_e (_Tofts and _SSM) and τ_i (_SSM) in the tumour and reference area. Significantly higher SUV and lower ADC values were observed in the lesion when compared to reference area (p < 0.01).

Furthermore, the analysis of perfusion parameters derived from the application of the pharmacokinetic Tofts and shutter speed models to breast lesions showed significant differences when compared to the contralateral reference area for the following parameters: K^{trans}_Tofts, $p < 0.01$; v_e_Tofts, $p < 0.01$; K^{trans}_SSM, $p < 0.01$; v_e_SSM, $p < 0.01$; τ_i, $p < 0.01$ (Table 14).

Table 14: Mean and standard deviation of pharmacokinetic estimates, ADC and SUV in tumour and reference tissue. A significant statistical difference is marked in bold: * p < 0.05, ** p < 0.01

	Tumour		**Reference tissue**	
ADC [mm^2/s]	**1115 □ 312****		1453 ± 270	
SUV [kBq/ml / kBq/g]	**5.50 □ 3.69****		0.71 ± 0.10	
	Tofts model	*SSM*	*Tofts model*	*SSM*
K^{trans} [1/min]	**0.57 □ 0.48****	**0.69 □ 0.61****	0.04 ± 0.09	0.14 ± 0.20
k_{ep} [1/min]	1.14 □ 0.76	1.14 □ 0.75	0.91 ± 0.73	1.03 ± 1.12
v_e	**0.50 □ 0.14****	**0.68 □ 0.09****	0.06 ± 0.12	0.26 ± 0.24
τ_i [s]		**0.31 □ 0.15****		1.27 ± 1.06

6.2 Multiparametric evaluation

All patients (n = 46) showed a positive and low correlation between the SUV_{mean} and the pharmacokinetic K^{trans}_SSM, k_{ep}_Tofts ($p < 0.05$) and a negative high correlation with v_e_SSM ($p < 0.01$). The PET SUV showed a negative low correlation also with the shutter speed derived τ_i ($p < 0.05$). A high and positive correlation was found between the pharmacokinetic parameters estimated with the two different models ($p < 0.01$) (Table 15).

Table 15: Results of the Spearman correlation test applied on the distribution of each parameter. Only the correlations for which p resulted < 0.05 have been reported.

Variable 1	***Variable 2***	***p value***	***Spearman ρ***
SUV	K^{trans} _SSM	< 0.05	0.32
SUV	K^{trans} _Tofts	< 0.05	0.32
SUV	τ_i	< 0.01	-0.29
K^{trans} _Tofts	K^{trans} _SSM	< 0.01	0.94
k_{ep} _Tofts	k_{ep} _SSM	< 0.01	0.83
v_e _Tofts	v_e _SSM	< 0.01	0.80

Finally, no significant correlation was found between the ADC and both the SUV and pharmacokinetic parameters derived from the application of TM and SSM to DCE-MRI data ($p > 0.05$). Scatterplots in Figure 45 demonstrate some examples of the relationship between different imaging parameters. In particular the relationship between: SUV from PET imaging and ADC from DW-MRI; the SUV and k_{ep} evaluated with the Tofts model; the ADC and the K^{trans} evaluated with the Tofts model; and the SUV and τ_i derived from the application of the shutter-speed model to DCE-MRI data.

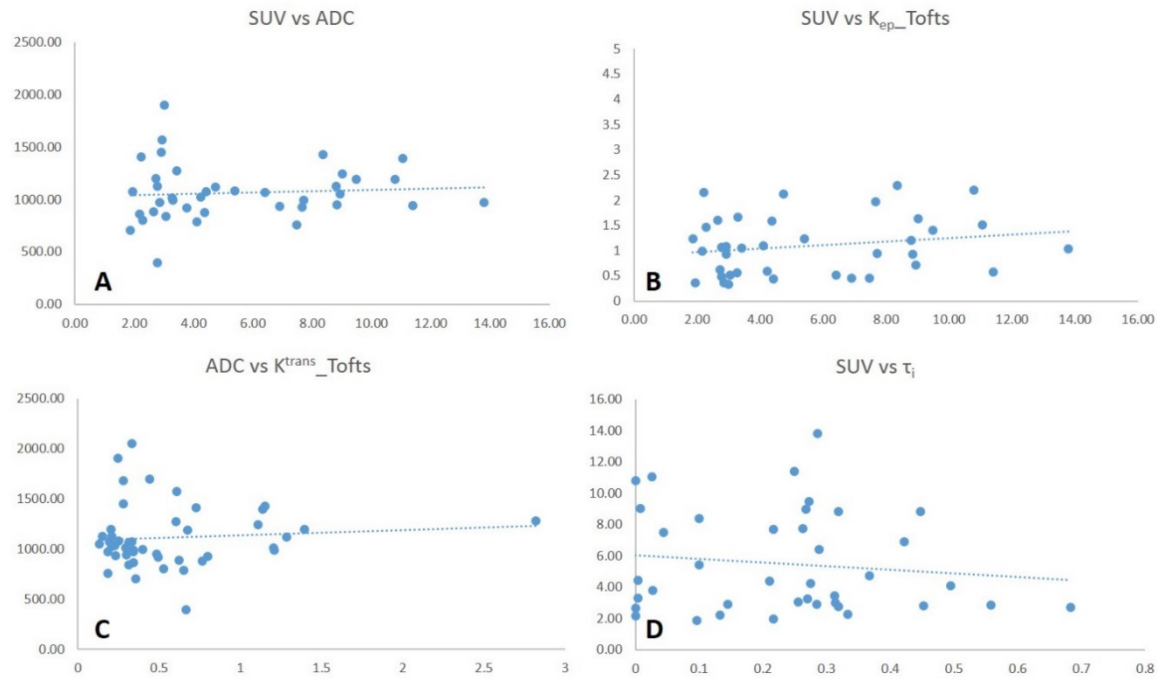

Figure 45: Scatterplots showing some relationship between different imaging techniques, with their correspondent trend-lines. A) SUV from PET imaging and ADC from DW-MRI; B) SUV and k_{ep} evaluated with the Tofts model; C) ADC and the K^{trans} evaluated with the Tofts model; D) SUV and τ_i derived from the application of the shutter-speed model to DCE-MRI data.

7. Discussion

The aim of this study was to investigate the relationship between pharmacokinetic, microstructural and metabolic features in breast tumours, simultaneously evaluated using DCE-MRI (fitted with the Tofts and the shutter speed model), DW-MRI and ^{18}F-FDG-PET imaging. Both Tofts and shutter speed derived perfusion parameters showed a significant correlation with the PET SUV, which is typically used in the evaluation of oncological lesions. Although similar in correlation coefficients, comparisons with the shutter speed model resulted in lower p values suggesting a higher significance.

The uptake of MRI contrast media and PET radiotracers is based on different physiological mechanisms, so the application of DCE-MRI and ^{18}F-FDG-PET usually provides complementary findings [42-44]. Nevertheless, the metabolism of tumours tissues is highly linked to the related neoangiogenesis, and hence, to the delivery of both contrast and/or radiopharmaceuticals to the lesion [45]. An et al. have recently demonstrated a significant correlation between the SUV_{max} and k_{ep} and v_e estimated with the Tofts model in non-triple negative breast cancer[46]. In our population, we confirmed this significant positive correlation between the mean SUV value and perfusion K^{trans}_SSM and K^{trans} _Tofts ($p < 0.05$). This finding is of particular interest, not only for staging but, in perspective, for follow-up and treatment response evaluation, considering that perfusion parameters, such as K^{trans}, have been demonstrated to be potentially predictive of patients' response to therapy [26, 47].

On the contrary, no significant correlation between mean values of metabolic (SUV) and diffusion (ADC) parameters were found (Figure 45). The literature results in this, are contradictory. Kitajima et al. found a significant, but weak inverse correlation between the SUV_{max} and ADC_{mean}

values[48]. Two other research groups demonstrated a mild correlation between the SUV_{max} and ADC_{mean} values [49, 50]. On the other hand, no correlation between ADC and SUV was found by Choi et al. [51], together with other published studies[52-54]. Different tumour tissues have different cellular structures, which lead to different ADC values. Literature reports ADC values to be inversely correlated with tumour cellularity [55-58]. Therefore, the positive correlation between FDG uptake and cellularity[59, 60] suggests SUV and ADC to be inversely proportional, confirming Kitajima et al's study[47]. In our study, the absence of significant correlation between SUV and ADC could be attributed to both the small size of the sample and the big dimension (and resulting heterogeneity) of many of our lesions. We saw an inverse correlation between the SUV and the volume fraction of extracellular extravascular space, which is usually related to tissue cellularity, suggesting that regions with high level of glucose metabolism may be characterized by high cellularity. Kim et al. [61] and An et al.[44] also found a negative correlation between the SUV and the v_e. This makes evident that tumour blood flow and vessel permeability are important for the FDG intracellular uptake. It certainly needs to be further investigated, possibly with additional histological information.

As for perfusion analysis, the standard approach for DCE-MRI employs the Tofts pharmacokinetic model, which assumes an infinitely fast equilibrium transcytolemmal water exchange kinetics. This assumption has been proven to cause pharmacokinetic parameters miscalculations[62, 63]. These results were confirmed by our analysis where the Tofts K^{trans} (mean and standard deviation, 0.57 □ 0.48 [1/min]) were lower that the shutter speed one (mean and standard deviation, 0.69 □ 0.61 [1/min]). In fact, in order to reflect a more realistic tissue environment, pharmacokinetic models should consider the intercompartimental water exchange effect, even though this involves more complex models with more parameters to be estimated. The cellular metabolic activity, evaluated by the SSM parameter τ_i, has been shown to relate to the energetic metabolism driven cell membrane water permeability[64]. In our study, we found this parameter to be significantly higher in the reference tissue, confirming an inner lower metabolic activity in these tissues, as supported also by SUV values. We also found a negative and weak correlation between τ_i and SUV_{mean}. This contradicts the results of Hectors et al. in the assessment of hepatocellular carcinoma[28]. FDG-PET measures cellular uptake of glucose, whereas τ_i is mainly dictated by Na^+, K^+-ATPase activity sustained by ATP production[26]. This negative correlation could mean that, when the metabolic activity of the cell is very high, and it takes place when a greater nutrient delivery is present, the metabolism of the cell is faster and, as a consequence, lower values of τ_i are observed[65].

The main limitation of this study is the limited size of the examined dataset. Moreover, any histological characterization was present for the evaluation of the performance of each pharmacokinetic model compared to a tissutal ground truth. This was mainly due to the heterogeneity of the sample as few Basal Like subjects were available. Finally, the sensitivity of DCE-MRI data to water exchange effect was reduced by the 20◦ flip angle acquisition. Li et al. suggest that data τ_i sensitivity can be enhanced by reducing the flip angle (~8°)[66]. This can possibly affect the precision of the τ_i parameter and, as a consequence, the accuracy of the correlation with other imaging metrics. The strength of the analysis is related to the simultaneous acquisition of PET and MRI data, because of the soft-tissue contrast resolution of MRI, particularly useful in this body area and the acquisition of both metabolic and morphological data at the same physiological conditions. Furthermore, pharmacokinetic parameters were evaluated with the application of an individual arterial input function, which avoids many problems related to the widely used population averaged one[67].

Further work is required to assess the combined information from DCE-MRI, DW-MRI and PET, together with biological/histological data, in order to conduct an advanced analysis in a radiogenomic framework[68].

8. Conclusions

PET/MRI allows breast lesions characterization when using multiparametric analysis of perfusion, morphological and functional markers with a good agreement between different pharmacokinetic models. Perfusion parameters showed a good correlation with the SUV in breast lesions, and, in particular, the shutter speed τ_i was found to be significantly associated with FDG uptake (negative correlation). On the contrary, DW-MRI derived parameters did not correlate with either PET or DCE-MRI parameters. These findings give new insights in the use and interpretation of quantitative imaging markers in breast cancer, especially when predicting response to treatment.

II. Relationship between functional imaging and immunohistochemical markers and prediction of breast cancer subtype: a PET/MRI study

1. Introduction

Breast cancer (BC) is an international public health concern characterized by high tissue heterogeneity and complexity that make clinical management a very challenging task. Based on gene expression, BC is classified in different subtypes, and their identification may contribute to treatment planning. As reported by St. Gallen 2013 guidelines[69], there are four major BC molecular subtypes: luminal A (estrogen receptor positive [ER+] and/or progesterone receptor positive[PR+], human epidermal growth factor receptor 2 negative [HER2-]); luminal B (ER+, and/or PR+, HER2+); HER2-like (ER-, PR-, HER2+); and basal-like/triple negative (ER-, PR-, HER2-). The main reason for attempting to distinguish between 'luminal A' (more endocrine sensitive, indolent, better prognosis) and 'luminal B' (less endocrine sensitive, more aggressive, worse prognosis) tumours is because they respond differently to treatment.

In the last several decades, advanced and integrated imaging techniques (mainly magnetic resonance imaging [MRI] and positron emission tomography/computed tomography [PET/CT]) have boosted diagnostic accuracy in several stages of cancer management. Histopathologic findings still play important roles in BC diagnosis and clinical management, but this approach presents limitations related to the invasive bioptic approach, inter- and intra-observer variability, limited field of view (FOV), and tissue alteration during the pre-analytical phase (fixation). Increasing evidence has suggested a role for imaging-derived morpho-functional parameters for predicting tumour malignancy and treatment response. Indeed, many studies have demonstrated relationships between ^{18}Fluoro-fluorodeoxyglucose (^{18}F-FDG) uptake on PET/CT and the clinicopathological characteristics of tumour lesions [70-77], as well as the role of maximum standardized uptake value (SUV_{max}) in the primary tumour as a predictor of molecular subtype [78], and of relapse/survival in BC patients [79]. Similarly, the correlation between imaging parameters obtained by dynamic contrast-enhanced MRI (DCE-MRI) and histopathologic findings have been reported [80-89]. FDG-PET and DCE-MRI are both functional modalities that indirectly represent the biological characteristics of cancer. For prognostic purposes, few studies have explored the association between PET and MRI parameters with the clinicopathologic subtype of BC [90-95], and the diagnostic power of hybrid PET/MRI system in this field has also not been extensively investigated [96, 97]. Several studies have demonstrated PET/MRI performance in terms of qualitative lesion detection and semi-quantitative measurement, establishing a comparable diagnostic value with PET/CT imaging, the gold standard technique for oncologic assessment [8, 98, 99].

The purpose of this study was to evaluate the association between imaging biomarkers extracted from the hybrid PET/MRI system with histopathologic findings of breast tumours, and to determine their ability to predict BC subtypes.

2. Material and Methods

2.1 Participants

This study was approved by the institutional Ethics Committee (Prot2-11, IRCCS Fondazione SDN). For study enrollment, all participants provided written informed consent. Between June 2012 and November 2015 at the IRCCS SDN Institute, 221 patients with bioptic-proven diagnosis of BC were enrolled for same-day contrast enhanced (CE)-FDG-PET-CT and CE-FDG-PET-

MRI. Inclusion criteria were: diagnosis of BC by immunohistochemistry (IHC), absence of previous oncological diseases, > 18 years of age, and lesions of at least 0.2 cm for a comprehensive imaging characterization. Exclusion criteria were: pregnancy, blood glucose levels > 140 mg/dl (7.77 mM), and standard contraindications for MRI and/or for contrast agent injection, artefacts affecting PET-CT and/or PET-MRI, and the absence of structured IHC reports. On the basis of these criteria, only n° 50 patients with invasive ductal (ID) BC diagnosis were included in this study.

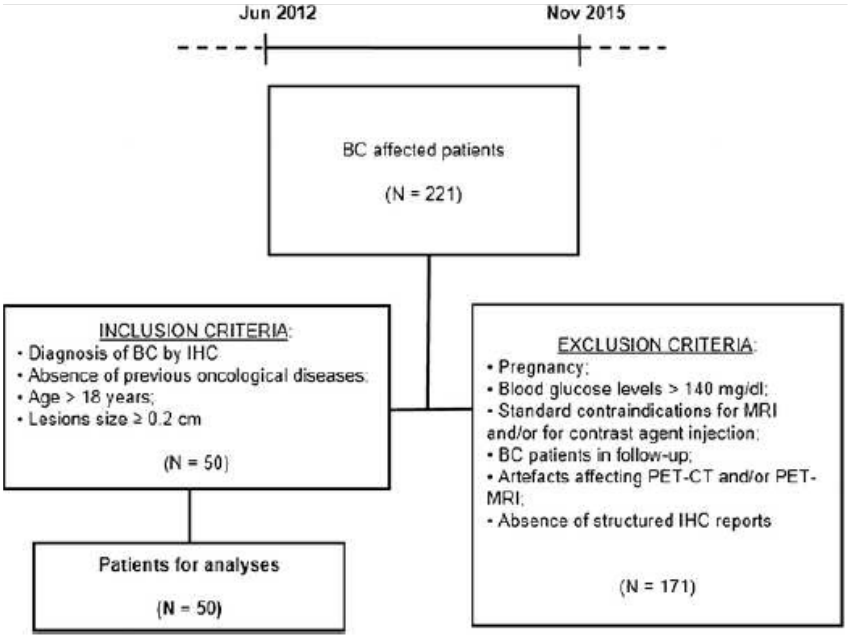

Figure 46: Inclusion and exclusion criteria for eligible patients.

2.2 Immunohistochemistry

Core needle biopsies were performed under ultrasound guidance by a radiologist with more than 15 years of experience. Biopsies were fixed in 10% neutral buffered formalin at the time of biopsy. Mastectomy specimens, obtained from patients who underwent mastectomy, were sent to the department of pathology immediately after resection. Expression of ER, PR, HER2, and Ki67 (marker of cellular proliferation) was determined by IHC analysis. Each tumour sample was classified as ER+, PR+, and/or HER2+, or being triple-negative if negative for all three. Positivity for ER and PR was defined as the presence of 1% or more positively stained nuclei. The histological grade (G) was determined using the method of Elston and Ellis. Histological subtype was determined according to St. Gallen 2013 guidelines [69].

2.3 PET-MRI data acquisition

Data were acquired on a 3T hybrid PET-MR system mMR Biograph (Siemens, Erlangen, Germany). For PET, all patients fasted at least 6 hours before the procedure. Then they received 401 ± 32 MBq (mean ± standard deviation [SD]) of ^{18}F-FDG intravenously. After a 60 min equilibration period during which the patients were at rest, PET images of the tumour were acquired with simultaneous acquisition of an MRI scan. For MRI, breast protocol was optimized for accurate detection and staging, providing images acquired with a dedicated breast coil. The DCE-MRI protocol for all of the examinations included six axial pre-contrast spoiled gradient recalled echo (SPGRE) 3D vibe sequences at six different flip angles (2, 5, 8, 12, 15, 20) and a dynamic 3D vibe sequence (repetition time [TR]=5.5ms, echo time [TE]=1.7 ms, flip angle=20, FOV of 320mm, base resolution of 192, slice thickness of 3.6 mm) to obtain acquisitions before, during, and after injection of the contrast agent (0.1 mmol/kg body weight gadolinium-diethylene

triamine pentacetate [Gd-DTPA], Magnevist). The 3D acquisition allowed us to cover the entire breast. A total of 60 time points were acquired with an average temporal resolution of 9.5s and a total acquisition of ~9 min. Patients were allowed to breathe freely. Axial diffusion-weighted (DW)MRI was acquired with a single shot spin-echo echo-planar imaging sequence in three orthogonal diffusion encoding directions with b-values of 0, 50, 400, and 800 s/mm^2, TR/TE = 14,500ms/66ms, FOV of 340 mm, base resolution of 192, and slice thickness of 4mm.For clinical evaluation, the protocol also included axial and coronal T2 turbo inversion recovery magnitude sequences (TR=4220 ms, TE= 61 ms, FOV of 340 mm, base resolution of 256, slice thickness of 4mm) and an axial T2 turbo spin echo (TR=5440ms, TE=81 ms, FOV of 340 mm, base resolution of 448, slice thickness of 4mm). Following the acquisition, PET images were automatically corrected for tissue attenuation with the attenuation maps generated on the basis of the 2-point Dixon MRI sequences [100]. Emission data were corrected for random events, dead time, scatter, and attenuation. A three-dimensional attenuation- weighted ordered-subsets expectation-maximization (3D AW OSEM) iterative reconstruction algorithm with 3 iterations and 21 subsets, Gaussian smoothing of 4 mm in full width at half maximum was used.

2.4 Image processing

DCE-MRI data were analysed using semi-automated software written in house in MATLAB (MathWorks, R2015b, Natick, MA, USA). Relaxation rate at baseline (R_{10}) and relaxed signal (M_0) were calculated, as 3D maps, with the Ernst formula (assuming TE << T_2*) using the set of SPGRE pre-contrast images at different flip angles [101].The Tofts pharmacokinetic model, which is also called the "standard model" as it is the standard approach for the post processing of MRI perfusion data, was applied to DCE-MR images to extract different perfusion maps. K^{trans} is the first order rate constant for plasma to interstitium transport ([1/min]); v_e is a measure of the extravascular extracellular space (EES) volume fraction; the ratio between K^{trans} and v_e results in the third pharmacokinetic parameter k_{ep}, that is the back flux rate constant [1/min]. DW-MRI data were automatically computed for the estimation of apparent diffusion coefficient (ADC) maps. Regarding PET activity, FDG uptake in tumours is related to the proliferative activity of a malignant tissue and to the number of viable tumour cells. Even though its quantification is direct, it is subject to the variability introduced by differences in patient size, the amount of FDG injected, and radiotracer decay. For this purpose, SUV was used.

2.5 Statistical analysis

Two groups, each composed by one senior radiologist experienced in breast imaging (more than 15 years of experience) and one nuclear medicine specialist (more than 20 years of experience), reviewed local tumour staging on PET/MRI in consensus. Free-hand region of interest (ROI) boundary was manually drawn around the area of maximal tumour extension for each of the 50 subjects on the subtracted T_1 post contrast image slice, avoiding necrotic areas and large feeding vessels. An additional ROI (1 cm^2) was drawn on the reference contralateral tissue. After data resampling, pharmacokinetic (K^{trans}, k_{ep}, and v_e), ADC, and SUV measures for perfusion, diffusion, and glucose metabolism evaluation, respectively, were calculated across each ROI (maximum and mean values were extracted for each parameter). All statistical analyses were performed using SPSS (IBM SPSS statistics, 20). All p-values were two-sided, and $p<0.05$ was considered statistically significant. For multiple comparisons $p < 0.017$ was considered statistically significant.

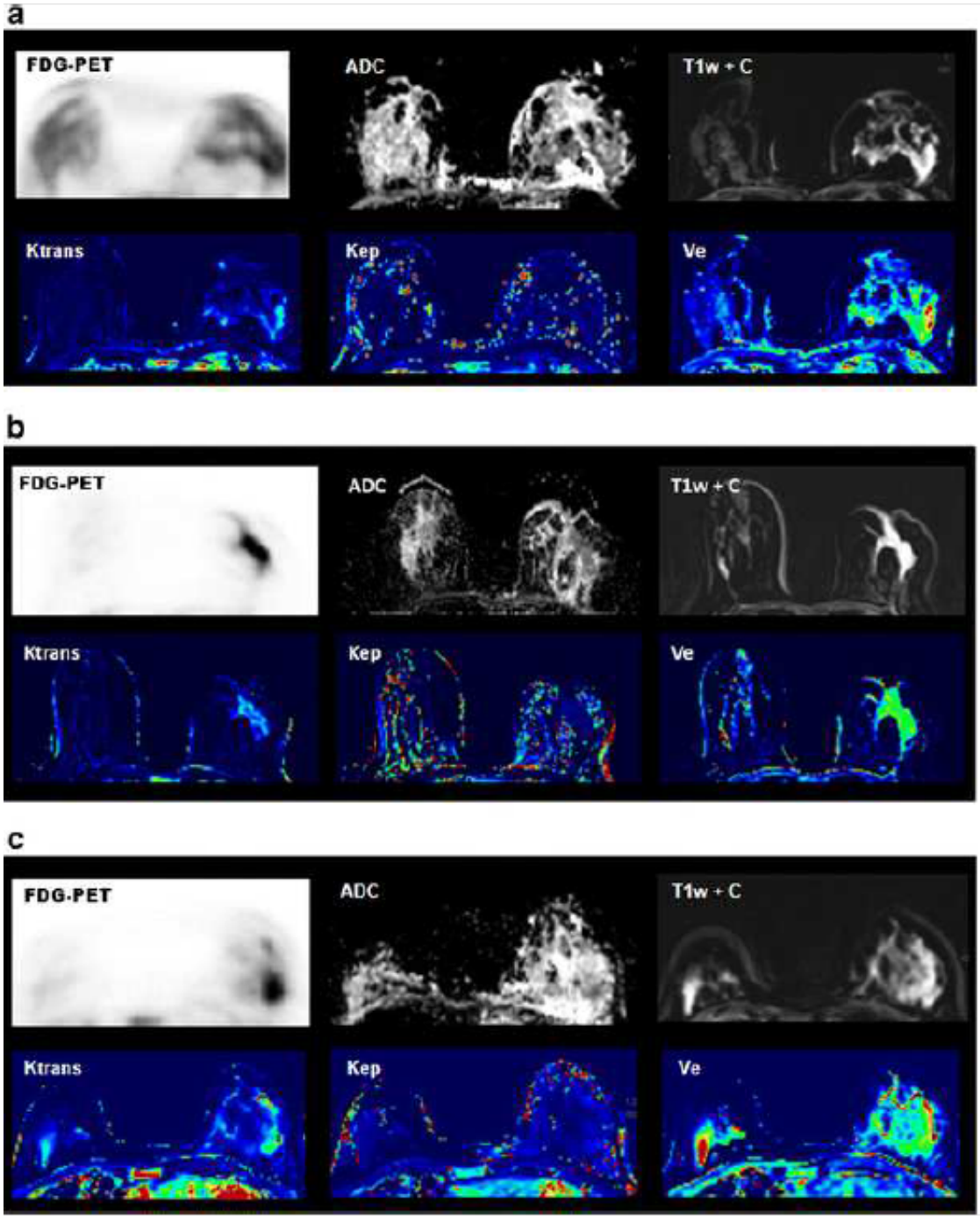

Figure 47: Examples of multiparametric analysis in women with breast ductal carcinoma. Multiparametric imaging evaluation of metabolic (PET), morphological (T1w + C), and functional (ADC, K^{trans}, v_e , k_{ep}) parameters in a luminal A BC (a), a luminal B BC (b) and a nonluminal BC (c). With increases in perfusion parameters, FDG uptake increases at the tumour site, enhancement increases in the morphological acquisitions, and diffusivity decreases in the ADC map.

In particular, the tests chosen were: Cohen's kappa, to evaluate the agreement between the two groups of observers in primary tumour detection and extension assessment; Shapiro–Wilk analyses to assess the normal distribution of each parameter; Wilcoxon rank-sum test for statistically significant difference between tumours and reference area values; and the non-parametric Spearman's rank-order correlation and Mann–Whitney U test to verify the correlation/association among biological markers as well as between imaging parameters and

biological markers. To assess the association between molecular and imaging parameters, data were grouped according to: positive (+) or negative (-) expression of ER, PR, and HER2 receptors; low or high expression of Ki67 (low ≤ 20% and high > 20%); low or high grade (low: G1–G2, high: G3); and tumour-node-metastasis (TNM) classification as T1/T2 versus T3/T4, according to BC guidelines. Tests were applied on maximum and mean values obtained for each parameter, except for ADC (only ADC_{mean}). The receiver operating characteristic (ROC) curve test was performed to evaluate the performance of a binary classifier system. The optimal cut-off able to distinguish between two BC subtypes was calculated from the data distribution on the ROC curves. Multivariate logistic regression analyses were used to determine if independent imaging parameters were able to predict BC subtypes.

3. Results

3.1 Clinicopathological features

Patient and tumour characteristics are summarized in Table 17. St. Gallen 2013 guidelines[69]were used to classify BC tumour subtypes (Table 18). In comparing St. Gallen 2013 guidelines to St. Gallen 2011 guidelines [102], no differences were found in tumour subtype classification, with the exception of one patient (luminal B according to St. Gallen 2011 vs. luminal A according to St. Gallen 2013). In addition, applying aforementioned criteria, in one case it was not possible to determine the tumour subtype. The subtypes of the 49ID-BC cases were as follows: 13 (26.5%) luminal A, 29 (59.2%) luminal B, 4 (8.2%) HER2 enriched, and 3 (6.1%) basal-like. For each patient enrolled, the lesion size was calculated by MRI. The mean tumour size and relative range for each subtype is summarized in Table 18.

Table 16: Clinical features of tumour lesions in the 50 selected patients

Clinical feature	value
Age (years), mean (range)	52.3 (35-80)
Receptor status, n	
ER+	42
ER-	8
PR+	43
PR-	7
HER+	19
HER-	31
Proliferation index (Ki67), n	
≤20%	12
>20%	38
Grade, n	
1	1
2	27
3	22

Table 17: Molecular subtypes and relative lesion sizes

	Subtype			
	Luminal A	**Luminal B**	**HER2 enriched**	**Basal Like**
Number	13	29	4	3
Lesion size (cm), mean	3.8 (0.7 – 5.0)	4.1 (2.3 – 7.8)	4.2 (2.9 – 6.6)	4.2 (2.6 – 7.1)

3.2 Correlation among immunohistochemical biomarkers

To assess the relationship between hormonal receptors, Spearman analysis and Mann–Whitney U test were performed. For this study, n°50 IHC reports were analysed. We found that the expression status of PR and ER was significantly correlated ($p < 0.001$, $\rho = 0.557$) meaning that ERs and PRs were frequently co-expressed. The expression level of ER was also significantly associated with HER2 expression ($p = 0.010$) and with grade ($p = 0.015$). In addition, Ki67 was associated with HER2 status ($p = 0.009$), and with grade ($p = 0.006$).

3.3 PET/MRI assessment in breast cancer

Excellent agreement between the two observer groups was found in anatomic allocation and extension of lesions by PET/MRI (97%, Cohen's kappa 0.9). All lesions were identified in both FDG-PET and DCE-MR images. The comparison between tumours and reference area provided significantly higher SUV values in the lesion ($p < 0.0001$). Conversely, the mean ADC value in tumours was significantly lower than the reference area ($p < 0.0001$) (Fig 50). Moreover, analysis of the perfusion parameters derived from the application of the pharmacokinetic Tofts model to the breast lesion showed significant differences for each parameter compared to the reference region (mean values): K^{trans}, $p < 0.001$; k_{ep}, $p < 0.001$; v_e, $p = 0.02$ (Fig. 50).

3.4 Association between immunohistochemical markers of tumour lesions and PET/MRI parameters

Correlation analysis between imaging parameters and histological biomarkers was made, categorizing IHC biomarkers. In Figure 51 we only report the significant results, and the absence of the box plot indicates non-significant results:

- ER: ER status (ER+ and ER-) was significantly associated with perfusion imaging parameters (panel a: K^{trans}_{max}, $p = 0.003$; panel b:K^{trans}_{mean}, $p = 0.009$; panel c:k_{epmax}, $p < 0.001$; panel d: k_{epmean}, $p = 0.002$) and metabolic parameters (panel e: SUV_{max}, 0.026; panel f: SUV_{mean}, 0.031)
- PR: PR receptor status (PR+ and PR-) was associated with both perfusion (panel a: K^{trans}_{max}, $p = 0.019$; panel c: k_{epmax}, $p = 0.021$; panel d: k_{epmean}, $p = 0.016$) and diffusion (panel g: ADC_{mean}, $p = 0.011$,) imaging parameters. Unlike ER status, PR status was not associated with glucose uptake (panels e and f).
- HER2 receptor: Regarding the association of HER2 status (HER2+ and HER2-) with imaging parameters, we found that this receptor was related to K^{trans}_{max} (panel a:$p = 0.024$), k_{epmax} (panel c: $p < 0.001$), and k_{epmean} (panel d: $p = 0.006$). HER2 status, like PR status, was not associated with glucose uptake (panels e and f). Ki67 index was associated with k_{epmax} (panel c: $p = 0.021$), glucose uptake as SUV_{max} (panel e: $p < 0.001$), and SUV_{mean}(panel f: $p < 0.001$).
- Tumour grade was only associated with k_{epmax} (panel c: $p = 0.017$) and ADC_{mean} (panel g: $p = 0.045$).
- TNM was associated with SUV_{max} (panel e: $p = 0.018$) and SUV_{mean} (panel f: $p = 0.020$), and lesion size (panel h: p = 0,006).

Taken together, these results suggested that ER-/PR-tumour lesions were characterized by higher values of perfusion parameters. In addition, only ER status correlated with tumour metabolism, while only PR- tumour lesions exhibited increased values of diffusion parameters. Conversely, decreased values of some perfusion parameters (K^{trans}_{max}, k_{epmax}, and k_{epmean}) were associated with HER2- tumour lesions. In addition, tumour lesions with a high proliferation index (≥20%) showed higher k_{epmax} and SUV values, and tumours with low cellular differentiation (Grade 3) were associated with a higher k_{epmax} and ADC_{mean}. Finally, more severe tumour staging was associated with both a higher lesion size and glucose uptake.

3.5 Association between BC subtypes and PET/MRI parameters

The ability of PET/MRI parameters to discriminate between BC molecular subtypes was evaluated. Because of small groups size (see Table 18), we merged HER2-like and basal-like subtypes to create a group named non-luminal subtype (n°7 patients), and the Kruskal–Wallis test and pairwise comparisons were performed. We found that K^{trans}_{max} (p=0.006), k_{epmax} (p=0.004), SUV_{max} (p=0.001), SUV_{mean} (p=0.002), and ADC_{mean} (p=0.024) were differently distributed across the three subgroups. As reported in Figure 3, the non-luminal subtype showed higher values of K^{trans}_{max} (panel a), k_{epmax} (panel b), SUV_{max} (panel c), and SUV_{mean} (panel d) than the luminal A subtype. The luminal B subtype showed higher values of k_{epmax} (panel b), SUV_{max} (panel c), and SUV_{mean} (panel d) than the luminal A subtype. We did not find any imaging parameters that were able to significantly discriminate between non-luminal and luminal B subtypes ($p > 0.017$, see Materials and Methods).

3.6 Prediction of BC subtypes

ROC curves of the imaging parameters significantly correlating with BC subtype (see Fig.52) were calculated with the relative AUC. As reported in Figure 4, k_{epmax}, SUV_{mean}, and SUV_{max} parameters were able to discriminate luminal A from luminal B subgroups (panel a).All of the analysed imaging parameters, except ADC_{mean}, were able to discriminate luminal A from non-luminal subgroups (panel b), and K^{trans}_{max}, and ADC_{mean} were able to discriminate luminal B from non-luminal subgroups (panel c). The AUC, p-value, and cut-off values are reported in the tables of Figure 4 (right panels). Multivariate analyses were performed to explore the association between molecular subtypes and imaging parameters. Luminal A, luminal B, and non-luminal subtypes were defined as dependent variables. Among the different independent variables analysed (data not shown), the best model came from using K^{trans}_{max} and SUV_{max} (Table 19). The results of the multivariate logistic regression analysis are summarized in Table 4. Logistics estimation of the variables was performed for luminal A, luminal B, and non-luminal subtypes. As reported, this model was able to correctly identify tumour subtypes in 38/49 biopsies (77.6%, $p < 0.001$), with higher accuracy for the luminal B subtype (86.2%).

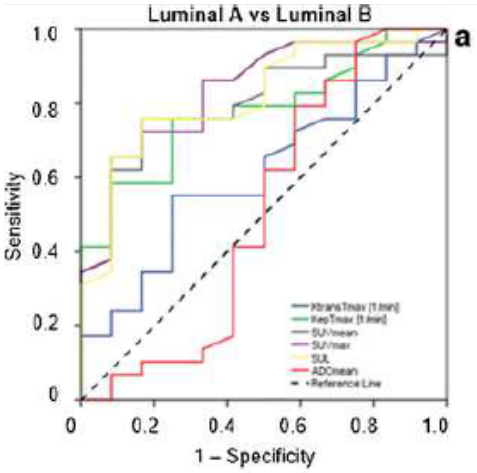

Imaging parameters	AUC	Std. Error	p-value
$Ktrans_{max}$ [1/min]	0.614	0.09	0.258
Kep_{max} [1/min]	0.779	0.07	0.005*
SUV_{mean}	0.799	0.07	0.003*
SUV_{max}	0.833	0.07	<0.001*
SUL	0.813	0.07	0.001*
ADC_{mean}	0.509	0.12	0.931

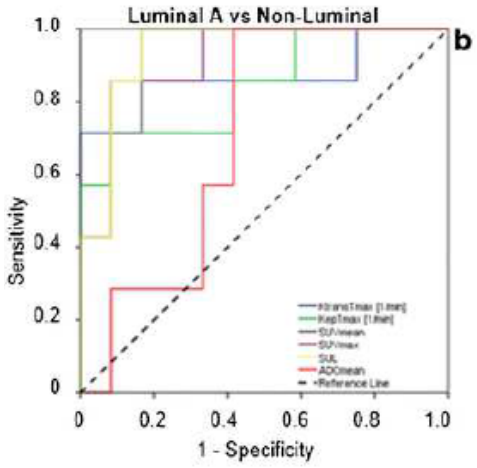

Imaging parameters	AUC	Std. Error	p-value
$Ktrans_{max}$ [1/min]	0.881	0.10	0.007*
Kep_{max} [1/min]	0.845	0.10	0.014*
SUV_{mean}	0.929	0.06	0.002*
SUV_{max}	0.917	0.07	0.003*
SUL	0.945	0.50	0.001*
ADC_{mean}	0.702	0.12	0.151

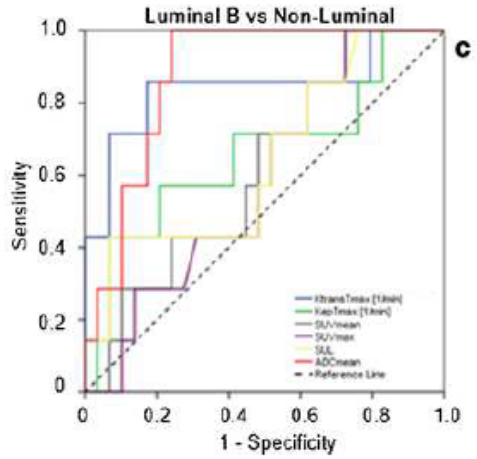

Imaging parameters	AUC	Std. Error	p-value
$Ktrans_{max}$ [1/min]	0.842	0.10	0.005*
Kep_{max} [1/min]	0.660	0.13	0.194
SUV_{mean}	0.616	0.11	0.349
SUV_{max}	0.589	0.11	0.472
SUL	0.643	0.12	0.246
ADC_{mean}	0.877	0.06	0.002*

Figure 48: ROC curve analysis showing the ability of each imaging parameter to discriminate among BC subtypes: a) luminal A vs. luminal B, b) luminal A vs. nonluminal, c) luminal B vs. nonluminal. The tables on the right show the AUCs, p values, and cut-off values of the imaging parameters taking into account the ROC curve analyses (*p < 0.05).

Table 18: Estimation parameters summary of variables significantly associated with molecular subtypes.

	Estimate	Std. Error	Wald	df	Sig.	95% Confidence Interval	
						Lower Bound	Upper Bound
$K^{trans}T_{max}$	1.17	0.37	10.073	1.00	0.002	0.44	1.89
SUV_{max}	0.23	0.08	8.28	1.00	0.004	0.075	0.39

Table 19: Multivariate analyses.

	Number of predicted subtype (%)		
Subtypes defined by IHC (n°)	**Luminal A**	**Luminal B**	**Non-luminal**
Luminal A (13)	True	False	False
	9 (69.2%)	4 (30.8%)	0 (0%)
Luminal B (29)	False	True	False
	3 (10.3%)	25 (86.2%)	1 (3.5%)
Non-luminal (7)	False	False	True
	0 (0%)	3 (42.9%)	4 (57.1%)

True: correctly predicted cases; *False*: not correctly predicted cases.

4. Discussion

The usefulness of imaging parameters to identify BC subtypes has become of great interest among scientists. Nevertheless, because this methodology has not been validated in clinical practice, additional studies are needed to verify its reliability for diagnostic and prognostic purposes. In recent years, the hybrid PET/MRI system has proven to be very useful in the diagnostic screening of different human pathologies including BC [103]. Integration of the two methods (PET and MRI) allows spatial and temporal co-registration of the examined body regions, extracting multiple tumour parameters in the same pathophysiological condition. To date, only one study using the hybrid PET/MRI system has been performed to predict BC subtypes [104]. In that study, the authors analysed 21 IDC patients and found that PET/MR biomarkers (k_{epmean}, ADC_{mean} and SUV_{max}) predicted IHC phenotype in 13 of 21 patients (62%; p = 0.001). Therefore, the purpose

of our study was to deepen our knowledge in a wider population, to better understand if imaging markers extracted through the simultaneous acquisition of FDG-PET and DCE-MRI (PET/MRI technology) correlated with prognostic biomarkers of BC, and were able to predict BC subtypes. To this end, 50 BC patients at diagnosis were enrolled in this study and underwent PET/MRI before pharmacological and surgical treatments. IHC of the core biopsy was used to determine the pathological status of tumour lesions. To determine whether there was a correlation among prognostic biomarkers (ER, PR, HER2, Ki67, and grade) and imaging parameters (SUV, K^{trans}, k_{ep}, v_e, and ADC), association studies were performed. We found that ER status correlated with both metabolic (SUV max and mean) and perfusion imaging parameters (K^{trans} and k_{ep}, max and mean). Specifically, levels of SUV (SUV_{max} and SUV_{mean}) in the ER- group were significantly higher than those in the ER+ group. These results were in agreement with other groups that used PET/CT technology [70, 72, 73, 76, 78, 105, 106]. Neither SUV_{max} nor SUV_{mean} was found to be associated with PR status [73, 107].

DCE-MRI-derived parameters, including K^{trans}, v_e, and k_{ep}, reflect the extent of tumour angiogenesis, so their increase correlates with disease severity. Interestingly, we found that the highest values of Ktrans (max and mean) and k_{ep} (max and mean) correlated with the ER- group. Similarly, the highest values of K^{trans}_{max} and k_{ep} (max and mean) also correlated with the PR- group. Taken together, our results suggest that perfusion parameters of tumours increase when ER and PR are not expressed, and that ER- lesions have increased metabolic activity. Among the analysed receptors, only PR status correlated with the diffusion parameter ADC_{mean}, which significantly increased when the PR was not expressed (PR- group). To date, the results of association between ADC and PR are somewhat controversial; some groups found a correlation between the highest ADC values with the PR- group [85, 108], whereas others did not find a correlation between PR status and ADC [84, 109, 110].In this study, we found significant correlations between grade and ADC_{mean}, with values increasing in Grade 3 tumour tissues. This result is discordant with those reported by Molinari et al.[111], in which lower ADC values were associated with more aggressive pathological features. However, Shin et al.[18] demonstrated that more and stronger correlations between ADC and prognostic biomarkers were found when the ADC tumour boundary was considered, suggesting that the result may change according to the lesion outline approach. In addition, the highest k_{epmax} values were associated with Grade 3 tumours, which is in accordance with other studies [88, 112]. Moreover, we found that a high proliferation index (Ki67 $\geq$ 20) correlated with the highest values of k_{epmax} and SUV [105, 107].

It is worth noting that proving a biological relationship between imaging and tissue biological markers is not simple, above all when many and different parameters are analysed, and when the results reported in the literature are still discordant. However, compared with ER+/PR+ cancer, ER-/PR- cancer has a poorer clinical outcome and shorter median survivor, as determined by the presence of a high proliferation index and high grade. It should also be that BC with higher perfusion parameters related to tumour angiogenesis and elevated metabolism has poor prognostic factors and is more aggressive. Based on these factors and globally considering the data obtained from our association studies, we found that tumours with low metabolic activity and low angiogenesis are more differentiated, less proliferative, and express both ER and PR, conditions that reflect a better prognosis.

The second part of our study focused on the ability to select imaging parameters to predict BC subtypes. Because of small size groups, we merged HER2-like and basal-like subtypes creating the non-luminal subtype group; therefore, the diagnostic accuracy of the selected imaging parameters was calculated to find the best prognostic model able to identify a specific BC subtype (luminal A, luminal B, and non-luminal subtypes). By ROC curve analyses, we found that both

SUV_{max} and SUV_{mean} were able to significantly discriminate luminal A from luminal B and luminal A from non-luminal subtypes. Interestingly, the lowest SUV values correlated with the luminal A subtype, suggesting that SUV values lower than the extracted cut-offs correlated with a better prognosis. Our data support the suitability of SUV_{max} as an imaging parameter that predicts the luminal A subtype[78, 90] and discriminates it from non-luminal BC [76]. Similarly, by ROC curve analyses, we found that K^{trans}_{max} was able to significantly discriminate luminal A from non-luminal subtypes, with a diagnostic accuracy of 88.1% and with the lowest K^{trans}_{max} values (cut-off = 2.76). In addition, k_{epmax} was able to discriminate luminal A from non-luminal subtypes and luminal A from luminal B subtypes, with a diagnostic accuracy of 84.5% and 77.9%, respectively. The ADC can be used to assess the biological characteristics of tumours based on tissue microstructure and cell density. We found that this parameter was able to discriminate luminal B from non-luminal subtypes with a diagnostic accuracy of 87.7% and a cut-off value of 1098.5, with the highest values in non-luminal subtype tumours. This result is in agreement with [113], showing that higher ADC values were associated with non-luminal BC subtype. These results indicate that the lowest values of metabolism, perfusion, and diffusion markers were found in BC subtypes with a better prognosis. Based on these results, we decided to develop a prognostic model that was able to predict BC subtypes; to this end, multivariate analyses were performed. Among the different independent variables analysed, the best performance came from using K^{trans}_{max} and SUV_{max}, which were able to correctly predict 38/49 tumour subtypes (77.6%, $p < 0.001$). In addition, this model seemed to work well for discriminating luminal B from the other analysed subtypes with a diagnostic accuracy of 86.2%.

Because we had a low sample size, we consider the results of this study to be preliminary; thus further studies are needed with a larger sample and a more homogeneous distribution of tumour subtypes, considering the prevalence of luminal B in our study. Moreover, BC classification was based on IHC, which may have a lower sensitivity and specificity for gene expression profiles than other molecular biology methods, although it is cheaper and easier to perform.

The heterogeneity and complexity of BC make challenging to create a unique predictive model that uses multiple imaging parameters to discriminate among each tumour subtype with high diagnostic accuracy. To this end, we proposed a model that separately analysed each imaging parameter. We evaluated the cut-off values of each parameter, based on their ability to significantly discriminate among subtypes. The model, schematized in Figure 3, used in a first step K^{trans}_{max}, SUV_{mean}, and ADC_{mean} parameters. Based on our results obtained by ROC curve analyses, we proposed the following hypothesis: if the lesion had K^{trans}_{max}, SUV_{mean}, and ADC_{mean} values < 2.9, < 2.97, and < 1098, respectively, the subtype was luminal (A or B) rather than a non-luminal subtype. In the second step, k_{epmax}, SUV_{mean}, and/or SUV_{max} parameters were evaluated to determine if the luminal subtype (identified in the first step) was luminal A or luminal B. Specifically, $k_{epmax} < 2.64$, $SUV_{mean} < 2.93$, and/or $SUV_{max} < 4.43$indicated that the subtype was luminal A. In this way, using a separate analysis of the imaging parameters, we were able to predict the three analysed subtypes. We are aware that this is just a hypothesis, as the diagnostic validity of a cut-off value is strictly related to the sample size that should exceed hundreds of samples per tumour subtype, and in our case the number of samples was too low to make cut-off hypotheses. Nevertheless, it is plausible to hypothesize an alternative strategy when the imaging parameters are numerous and cannot be exclusively used for discriminating all BC subtypes with high specificity and sensitivity.

III. Association between pharmacokinetic parameters from DCE-MRI and metabolic parameters from dynamic 18F-fluoromethylcholine PET in human brain glioma.

The purpose of the study is to compare pharmacokinetic parameters resulting from the modelling of dynamic contrast enhanced (DCE-) MRI data (using the Tofts model (TM) and the shutter speed model (SSM)) with metabolic macroparameters derived from the application of the spectral analysis (SA) to dynamic 18F-fluoromethylcholine (FMC) PET data.
14 patients with primary untreated glioma were imaged dynamically with DCE-MRI and ^{18}F-FMC PET, on the same day. Images were registered and analysed for kinetics on a voxel basis. FMC-PET images were analysed with spectral analysis. Additionally, tumour-to-background ratio (TBR) maps were evaluated. DCE-MRI data was analysed with the TM and SSM. Voxel-wise Spearman's coefficients were calculated for each patient to assess pairwise pharmacokinetic parameter correlations. Pearson's correlation coefficients were evaluated to assess TBR vs. pharmacokinetic parameters correlations.
The non-parametric Spearman correlation test showed strong correlations between spectral K_1 and K_i and pharmacokinetic TM-v_e ($\rho = 0.88$, $\rho = 0.93$), SSM-v_e ($\rho = 0.92$, $\rho = 0.94$) and SSM-τ_i ($\rho = 0.92$, $\rho = 0.97$). Pearson correlation test between TBR and DCE pharmacokinetic results showed a significant correlation for TM-K^{trans}, TM-v_e, SSM-v_e and SSM-τ_i.
In conclusions, the combination of DCE-MRI and FMC PET, two imaging modalities commonly used in the clinical management of brain cancer, provides a practical and attractive combination that may predict treatment response better than either modality alone. Results showed a high correlation between the irreversible trapping of the tracer in the tissue and the volume of distribution of the gadolinium based contrast agent.

1. Introduction

Primary brain tumours are a heterogeneous group of benign and malignant tumours arising from the brain parenchyma and its surrounding structures. These tumours are an important cause of morbidity and mortality in both adults and children, often generating severe disabilities and producing high burden in both families and health care systems[114]. 23770 new cases have been estimated in the United States in 2016 (including both sexes)[115].

Imaging plays a central role in diagnosis, characterisation, surveillance and therapeutic monitoring of intracranial tumours. Magnetic resonance imaging (MRI) is the gold standard in the diagnosis of brain lesions. However, this technique only reflects biological activity of the tumour indirectly by detecting the breakdown of the blood–brain barrier. The direct characterization of tumour metabolism, and in particular of cell proliferation, is given by dynamic choline-based positron emission tomography (PET) data acquisition.

In this study, we compared pharmacokinetic parameters resulted from the modelling of dynamic PET data with spectral analysis (SA) to dynamic contrast enhanced (DCE) MRI data. The multimodal analysis allows the integration of anatomic and functional information provided by a coregistration between the PET and the MRI. Imaging parameters derived from the two different modalities give complementary information with regards to tumour environment as they relate to different imaging properties (functional, morphologic). Choline is the precursor for the biosynthesis of phosphatidylcholine, a key component of the cell membrane phospholipids. It is transported intracellularly and phosphorylated by the enzyme choline chinase (ChKα) to phosphocholine and it is trapped within the cell. Most types of cancer are characterized by increased choline transport and by the overexpression of choline kinase in highly proliferating

cells in response to enhanced demand of phosphatidylcholine [116-119]. In particular, this has been reported in prostate, breast, lung, ovarian and colon cancers [120-123]. ^{11}C-choline has been widely used to study metabolic activity in vivo but its short physical half-life (20.4 min) is disadvantageous for its routine clinical use. The longer half-life of fluorine 18 (^{18}F) (109.8 min) overcomes this limitation allowing also late imaging of tumours when sufficient clearance of the parent tracer in systemic circulation occurs.
Dynamic 18F-FMC PET data, quantified with spectral analysis (SA) result in the expression of the uptake and the retain of the tracer in the tissue. In particular, this analysis, introduced by Cunningham et al. in the early 90s, allows the extraction of two macroparameters of interest: K_1, the net uptake of the tracer in the tissue, and the K_i, for irreversible tracers, which is the rate at which the tracer is irreversibly trapped by the tissue[124].
DCE-MRI is a non-invasive methodology that measures tissue perfusion through the acquisition of T_1-weighted MR images before, during and after an intra-venous (IV) injection of a gadolinium-based contrast reagent (CR)[23]. As the CR perfuses into the tissue under investigation, the concentration of the contrast in the tissue increases and the tissue water relaxation times decrease. A set of T_1-weighted dynamic images are acquired during this time in order to extract the voxel-wise characteristic signal intensity time curves which are related to the CR concentration time curves[65]. These curves are then fit to appropriate mathematical models to calculate physiological parameters, such as volume transfer constants and volume fractions. The standard model used is the Tofts model (TM), which expresses the flux of the tracer across two well-mixed compartments (blood and extravascular extracellular space) through the volume transfer constant K^{trans}[65]. The TM assumes negligible plasma compartment and is ideal for the description of weakly vascularized tissue. The TM embeds the implicit assumption that equilibrium transcytolemmal water exchange (between the intracellular space and extracellular extravascular space) is infinitely fast, or that the system is in, what is called, the fast exchange limit (FXL)[125]. The effect of the CR on the water exchange between the intracellular space and the extracellular extravascular space and therefore on the MRI signal amplitude is incorporated within the shutter speed model (SSM). The SSM thus introduces a new pharmacokinetic parameter, the mean intracellular water molecule lifetime, τ_i[125].

The aim of the study is to investigate the relationship between pharmacokinetic parameters derived by the application of both Tofts and SSM to DCE-MRI data, and metabolic characteristics of brain glioma described by PET imaging.

2. Materials and Methods

2.1 Subjects and imaging

14 patients (7 male, 7 female; aged 23-73 years, mean 40 years) with suspected primary supratentorial glioma were recruited to this study. Ethical approval was given by the local ethics committee and informed consent was obtained from all patients. PET/CT and MR imaging were performed prior to surgery. Imaging was acquired on the two modalities on the same afternoon in 12 of the 14 patients. Tracer production failed for two patients and in one patient it was possible to rescan them the following week prior to surgery, while in the other analysis was carried out solely on MR data.

2.1.1 FMC-PET imaging

PET/CT was performed on a Siemens Biograph 6 scanner with 285 MBq of 18F-methylcholine (PETNET Solutions Inc., UK), using a dedicated 45 minute brain dynamic list mode acquisition. The administration of radioactivity for the PET scans was approved by the Administration of Radioactive Substances Advisory Committee, United Kingdom. In one patient 154MBq of 18F-FMC were injected and in another patient the acquisition was halted after 38 minutes.

Discrete venous blood samples of 5mL were taken during the scan in 8 of the 14 patients. Samples were taken at 2.5, 5, 7.5, 10 and 45 minutes post-injection in the first two patients and at 1, 2, 3, 4, 5, 10 and 45 minutes post-injection in the next 6 patients. The start and end withdrawal times for the venous sampling were recorded.

2.1.2 DCE-MRI imaging

MR images were acquired on a 3T Siemens Verio MRI system using a 32 channel head coil; including pre- and post-contrast T1-weighted images, T2-FLAIR images and a DCE sequence with a variable flip angle pre-contrast T1 map acquisition. The DCE-MRI protocol included five pre-contrast spoiled gradient recalled echo (SPGRE) 3D vibe sequences at five different flip angles (2, 8, 12, 15, 20, 26), and a dynamic 3D vibe sequence (TR = 3.34 ms, TE = 0.99 ms, flip angle = 26, FOV: 240 x 240 mm, acquisition matrix 128x128, slice thickness 5 mm, slice gap 1 mm, 80 volumes). To obtain acquisitions before, during and after the injection of the contrast agent, 0.1 mmol/kg body-weight gadolinium-diethylene triaminepentacetate (Gd-DTPA), Gadovist, was injected using a power injector on the 5th acquisition using a flow rate of 3 ml/s. The 3D acquisition allowed us to cover the entire brain. 80 time points were acquired with an average temporal resolution of 2.89 s and a total acquisition time of ≈ 4 minutes.

2.2 Image registration and analysis

Volumes of interest (VOIs) were drawn by a Radiologist and confirmed by a Consultant Neuroradiologist for each patient around T2-FLAIR hyperintense regions. An additional ROI was drawn around the external carotid artery for the calculation of the image derived AIF (for both the PET and MRI post processing, as described above).

2.2.1 DCE-MRI kinetic analysis

DCE-MRI data were analysed using a semi-automated software written in house in MATLAB (Mathworks, R2017a). Before the application of any pharmacokinetic model, we calculated the relaxation rate at baseline (R_{10}) and relaxed signal (M_0) as 3D maps, with the Ernst formula (assuming TE<<T_2*) using the set of SPGRE pre contrast images acquired at different flip angles[126]:

$$S(\alpha) = M_0 \sin(\alpha) \frac{1-e^{-R_{10}T_R}}{1-\cos(\alpha)e^{-R_{10}T_R}} \qquad 1)$$

where α is the flip angle having values [2 8 12 15 20 26] and TR is 3.34 ms. Reformulating equation 1 as a linear regression system (y = cx + d) following the method described by Liberman et al. in[34], gives:

$$\frac{S(\alpha)}{\sin(\alpha)} = E\frac{S(\alpha)}{\tan(\alpha)} + M(1-E) \quad 2)$$

where $E = e^{-R_{10}T_R}$.

The slope $c = E$ and intercept $d = M_0 (1 - E)$ can thus be estimated and continuing from [34], R_{10} and M_0 can then be obtained through:

$$R_{10} = -\frac{\log(c)}{T_R},\ M_0 = \frac{d}{1-c} \qquad 3)$$

Then, 4D (x, y, z, t) post-injection longitudinal relaxation rate $R_1(t)$ maps for each dynamic phase are calculated using signal intensity data from the post contrast dynamic series:

$$R_1(t) = -(1/T_R) log \frac{1-(A+B)}{1-\cos(\alpha)(A+B)} \qquad 4)$$

where α = 26, $A = S(t) - S(0)/M_0 \sin(\alpha), B = (1-E)/1-E \cdot \cos(\alpha)$. S(0) and S(t) are the pre contrast injection signal intensity and the signal at the dynamic phase t respectively[35].

The longitudinal relaxation rate is determined in order to calculate the concentration of the contrast reagent. This is done through a calibration between the concentration of contrast reagent [CR] and the measured H_2O MR signal. This can be modelled by either a linear or nonlinear relationship as described below.

2.2.1.1 Tofts Model (TM)

DCE-MRI data were fitted with the Tofts model assuming a linear dependence of R_1 on [CR] (that is the equivalent of assuming the equilibrium transcytolemmal water exchange kinetics in the FXL):

$$R_1(t) = r_1[CR(t)] + R_{10} \qquad 5)$$

where r_1 is the CR relaxivity.
The extravasation of the contrast from the plasma to the EES was accounted by the Kety-Schmidt rate law[127]:

$$[CR_o(T)] = K^{trans} \int_0^t [CR_p(t)] e^{\frac{K^{trans}(T-t)}{v_e}} dt \qquad 6)$$

where K^{trans} is the first order rate constant for plasma to interstitium CR transport (min^{-1}) and v_e is a measure of the EES volume fraction.
The ratio between K^{trans} and v_e results in the third pharmacokinetic parameter k_{ep}, which is the back flux rate constant (min^{-1}). [CR_0] and [CR_p] are the concentration of CR in the 'outside' space (the extravascular extracellular space) and in the plasma respectively. [CR_p] is also called the arterial input function (AIF). The fitting of eq. 6 was performed using the inbuilt MATLAB *fminsearch* function, which uses the Nelder-Mead simplex algorithm as described in Lagarias et al.[40]. The minimization procedure is done voxel-wise in order to obtain a 3D map for each pharmacokinetic parameter. We set input values of 0.1 and 0.01 for the K^{trans} and v_e, respectively, and run the algorithm with 10,000 iterations and a tolerance of 10^{-8}.

2.2.1.2 Shutter speed model (SSM)

In the SSM, equation 5 is applied to the distribution of the CR in the blood, without assuming that the equilibrium transcytolemmal water exchange kinetics are in the FXL. The longitudinal relaxation rate is measured as:

$$R_{1b}(t) = r_{1p}(1-h)\left[CR_p(t)\right] + R_{10p} \qquad 8)$$

where b stands for the whole blood, p for the plasma and h the fraction of haematocrit in the blood. However, about half of the water in the blood is intracellular and cannot be accessed directly by the CR molecules[128]. The transport outside the erythrocytes therefore needs to be considered, as described by the two equilibriums:

$$H_2O_i \leftrightarrow H_2O_p \qquad 9)$$
$$H_2O_p + CR_p \leftrightarrow H_2O \cdot CR_p \qquad 10)$$

The mean water molecule lifetime in common CR is normally < 10^{-7} s, and the linear equation 5 is suitable for homogeneous solutions. In the case of erythrocytes, equation 10 is also considered

fast for some commonly measured [CR_p] values [128, 129]. After extravasation, the CR is commonly distributed into the interstitial extracellular space, at a rate defined by:

$$R_1^*(t) = r_{10}p_0[CR_0(t)] + R_{10} \quad 11)$$

where R_1*(t) is the rate constant of the extravascular water signal, r_{10} is the interstitial CR relaxivity and p_0 is the fraction of the extracellular tissue water. The application of equation (11) to biological tissues assumes that the interstitium is a homogeneous solution and that the system remains in the fast exchange limit. However, many studies have shown that, even though the equilibrium in equation 10 is fast, the FXL assumption is not true for all [CR_0] values following a bolus injection[128]. [CR_0] depends on the dimensions of the parenchymal cells that are generally much larger than erythrocytes and have a less water-permeable cytolemmae. Furthermore, tissue parenchyma cannot be considered as a single homogeneous solution and a single MRI voxel will constitute a number of compartments. The main result of this compartmentalization is given by:

$$R_{1L}(t) = (1/2)\Big\{2R_{1i} + r_{1o}[CR_o(t)] + (R_{10} + R_{1i} + 1/\tau_i)/p_o - \{(2/\tau_i - r_{1o}[CR_o(t)] - (R_{10} + R_{1i} + 1/\tau_i)/p_o)^2 + 4(1 - p_o)/\tau_i^2 p_o]^{\frac{1}{2}}\Big\} \quad 12)$$

where R_{1L}(t) is the long relaxation rate constant of the shutter speed model. R_{1i} is the H_2O rate constant in the absence of exchange of CR and τ_i is the average intracellular lifetime of a water molecule. The SSM was fitted by substituting equation 12 in equation 6 using the MATLAB functions fminsearch and fminsearchbnd, similarly to the TM. The initial estimates for the SSM K^{trans} and v_e where taken as the outputs of the TM, while the initial estimate for τ_i was set at 0.1[27].

2.2.2 Spectral analysis

Dynamic FMC-PET data were quantified with spectral analysis (SA)[124], which considers the tissue tracer activity in a given volume of observation at time t $C_{tissue}(t)$ as the convolution of the plasma time activity curve $C_p(t)$ with the IRF:

$$C_{tissue}(t) = \sum_{j=0}^{M} C_p(t) \times \alpha_j e^{-b_j t} \quad 13)$$

α_j and b_j are assumed to be real and non-negative values. We fixed a grid of 100 b_j values covering a spectral range of [1/3T_f 1/T_i/3] (where T_f is the end time of the experiment and T_i is the duration of the first scan) and then estimated the amplitudes α_j (the spectral contents). Only a few values of $\alpha_j > 0$ (correspondent to non-zero b values) are detected and they constitute the spectrum of the kinetic components of the tracer. The components of the spectrum have different meaning depending on their position in the spectrum, hence on their correspondent b_j value. Components with very large b_j are proportional to $C_p(t)$ and are seen as high frequency components, while components corresponding to $b_j = 0$ become proportional to $\int C_p(\tau)d\tau$ and are seen as low frequency components. In other words, they account for a slower kinetic, for the trapping of the tracer in the tissue (irreversible trapping). Lastly, the components with intermediate b_j values are referred to as the equilibrating components and their number corresponds to the number of tissue compartments that exchange material with the plasma.

The information given by the spectrum allow the estimation of some macro parameters of interest. They are: the influx rate constant $K_1 = \sum_{j=0}^{M} \alpha_j$ [mL/cm^3/min]; the net uptake of the tracer in the tissue, which, for irreversible tracers, can be derived by the limit of the IRF→ ∞, $K_i =$

$\lim_{n\to\infty} IRF(t) = \alpha_0$ [mL/cm^3/min], and the volume of distribution, which, for reversible tracers, can be derived as the integral of IRF, $V_T = \int_0^\infty IRF(\tau)d\tau$[124] [mL/$cm^3$]. The algorithm setting was implemented in MATLAB, based on the SAKE software by Veronese et al.[130].

2.3 Arterial input function (AIF)

Kinetic analysis of both dynamic PET and MRI data requires the quantification of the concentration of the tracer and the CR, respectively, in the blood. This function is also called arterial input function and has been derived drawing an additional ROI around the carotid artery. The correction of the image derived AIF is different for PET and MRI kinetic analysis as described below.

2.3.1 DCE-MRI AIF

Figure 1 shows the additional ROI placed in the external carotid artery for the calculation of the image derived AIF. Signal-intensity curves were converted to R_1-time curves by using the baseline signal intensity before the first pass of the CR as a reference [131], setting the haematocrit in the blood to 0.45, and getting the baseline blood T_1 from the T_{10} map.

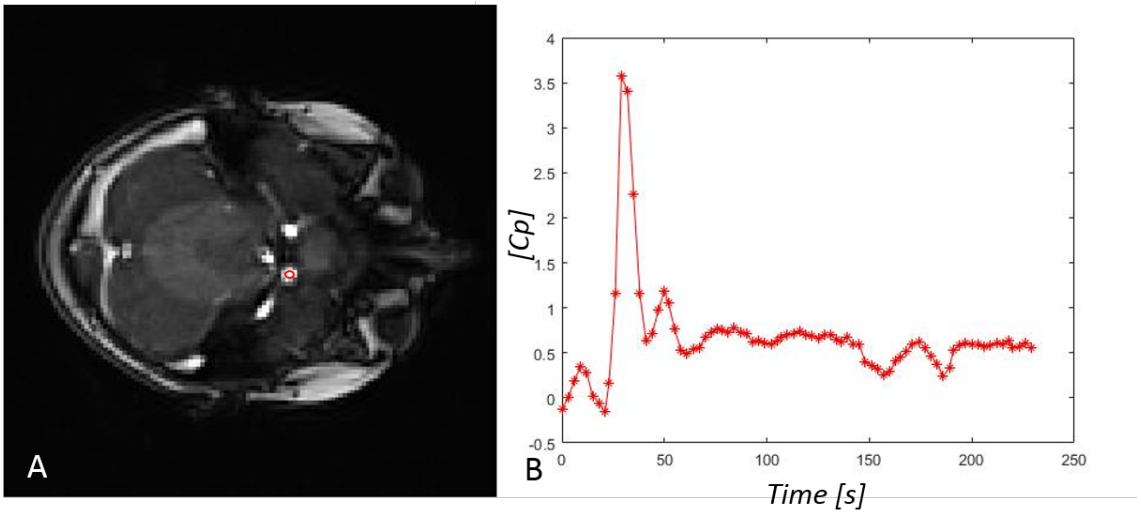

Figure 49: Measurement of the AIF. The VOI was placed in the carotid artery for the extraction of the arterial input function (AIF) as shown in the axial T1 VIBE image in (A). The time intensity curve for the concentration of contrast reagent in the plasma in the VOI indicated in red in (A) is shown in (B).

2.3.2 FMC-PET AIF

For each patient, total FMC activity in each blood sample was used to fit the plasma-over-blood (pob) ratio to a monoexponential curve to provide a continuous pob representation. Then, a total plasma activity curve was obtained by multiplying the pob by our tissue derived input function. Finally, the average fraction of parent compound measured in the plasma in each sample was fitted to obtain a continuous representation of the parent tracer concentration which was then multiplied by the total plasma function. Our result was a tissue derived parent plasma input function for each patient, which was used in SA.

2.4 Statistical Analysis

Pharmacokinetic analysis produced tumour 3D parametric maps of the Tofts model K^{trans} (TM-K^{trans}), k_{ep} (TM-k_{ep}) and v_e (TM-v_e) and the shutter speed model K^{trans} (SSM-K^{trans}), k_{ep} (SSM-k_{ep}), v_e (SSM-v_e) and τ_i (SSM-τ_i). Spectral analysis produced tumour 3D parametric maps of K_1 and K_i. Pearson's and Spearman's correlation coefficients were evaluated for each patient and all available pairwise combinations of parametric maps and FMC TBR. Mean and standard deviation

values for the patient cohort were reported. All statistical analysis were performed in MATLAB (MathWorks R2017a).

3. Results

3D parametric maps of TM and SSM estimates of K^{trans}, v_e and τ_i and of spectral K_1 and K_i for one axial slice of a non-enhancing tumour are shown in Figure 50.

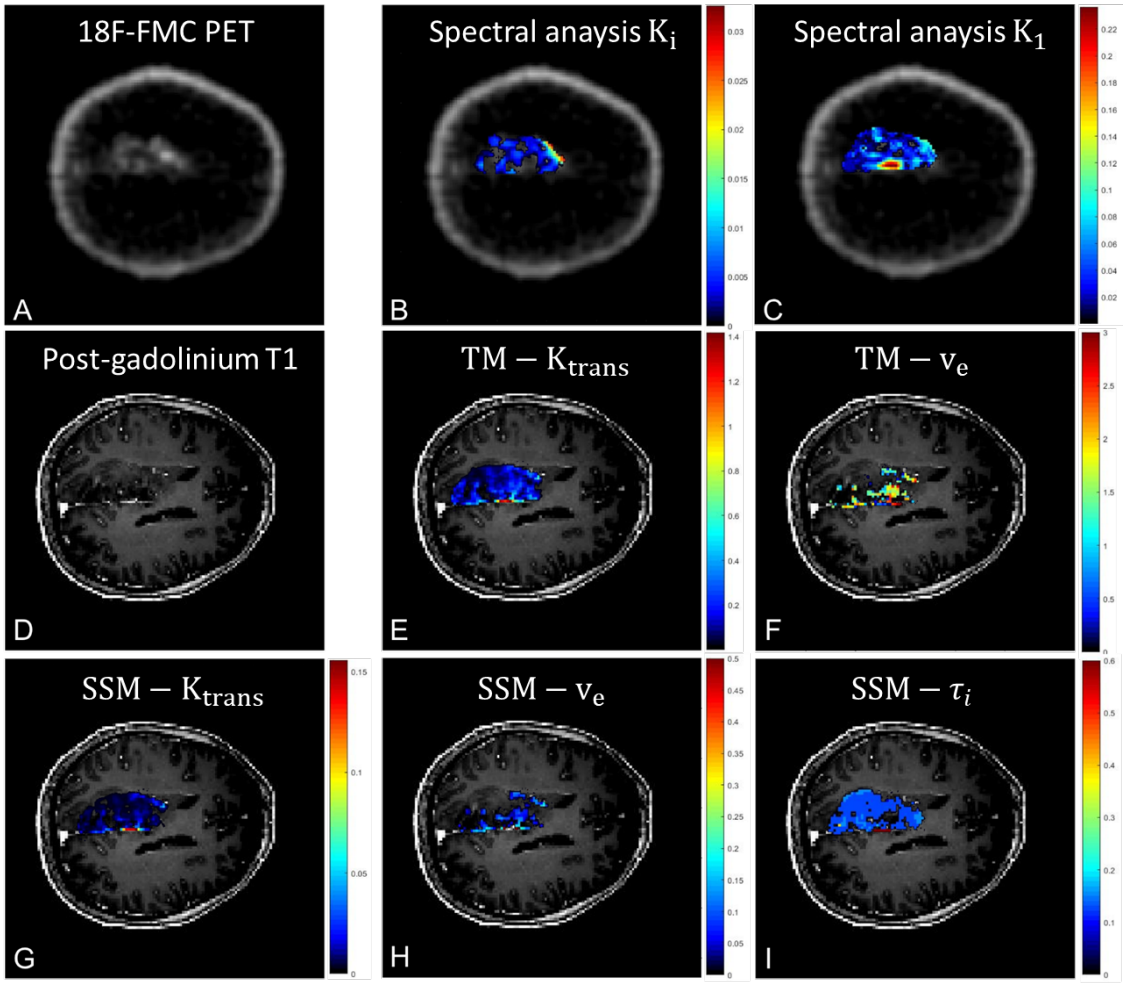

Figure 50: Patient n. 3 (WHO grade III). A) 18F-FMC PET; B) Spectral analysis K_1 and C) K_i; D) Post gadolinium T1 MR image; E) TM-K^{trans} and F) TM- v_e; G) SSM-K^{trans}, H) SSM-v_e and I) τ_i.

Table 21 shows the results of the application of TM and SSM to DCE-MRI data and SA to dynamic PET data (mean and standard deviations).

Table 20: Estimates of the mean and standard deviation for derived parameters in tumour tissue. The table shows the volume transfer constant K^{trans}, the intravasation rate constant k_{ep}, the EES volume fraction v_e, the intracellular water molecule lifetime τ_i obtained with the application of the Tofts model (TM) and shutter speed model (SSM). It also shows the net influx rate K_1 and in irreversible uptake rate of the tracer K_i evaluated with spectral analysis (SA). Results are expressed in terms of mean and standard deviation ($\mu \pm \sigma$).

Variables	$\mu \pm \sigma$
TM-K^{trans}	0.27 ± 0.17
TM-k_{ep}	0.74 ± 1.047
TM-v_e	0.023 ± 0.025
SSM-K^{trans}	0.51 ± 0.44
SSM-k_{ep}	0.52 ± 0.71
SSM-v_e	0.084 ± 0.090
SSM-τ_i	0.41 ± 0.33
K_1	0.14 ± 0.14
K_i	0.028 ± 0.058

3.1 Comparison between dynamic PET and MRI pharmacokinetic parameters

The non-parametric Spearman correlation test showed strong correlations between spectral K_1 and K_i with pharmacokinetic TM-v_e ($\rho = 0.88$, $\rho = 0.93$), SSM-v_e ($\rho = 0.92$, $\rho = 0.94$) and SSM-τ_i ($\rho = 0.92$, $\rho = 0.97$) as shown in Table 22.

Table 21: Results of the non parametric Spearman correlation test applied between DCE MRI pharmacokinetic results and spectral analysis perfusion parameters.

Parameters			p	ρ
TM-v_e	vs	K_i	0.0070	0.93
SSM-v_e	vs	K_i	0.0060	0.94
SSM-τ_i	vs	K_i	0.0010	0.97
TM-v_e	vs	K_1	0.021	0.88
SSM-v_e	vs	K_1	0.0090	0.92
SSM-τ_i	vs	K_1	0.0080	0.92

3.2 Comparison between static PET and MRI pharmacokinetic parameters

Pearson correlation test between TBR and DCE pharmacokinetic results showed significant correlation (Table 23).

Table 22: Results of the Pearson correlation test applied between DCE MRI pharmacokinetic results and TBR

Parameters			p	ρ
TM-K^{trans}	vs	TBR	0.015	0.65
TM-v_e	vs	TBR	<<0.01	0.86
SSM-v_e	vs	TBR	<<0.01	0.79
SSM-τ_i	vs	TBR	<<0.01	0.78

4. Discussion

The aim of this study was the investigation of the relationship between pharmacokinetic and metabolic features in brain tumours, evaluated using DCE-MRI data (fitted with the Tofts and the shutter speed model) and dynamic (and static) ^{18}F-FMC PET data. The comparison with the two pharmacokinetic models resulted in correlations with both the TBR and SA related parameters. A higher significance of the correlations with the SSM is suggested by the resulting lower p values (Tables 22 and 23).

The present literature shows ^{18}F-FDG to be the tracer of choice for the management of several diseases for its extreme versatility as a glucose analogue. Despite the advantage of that, it has been largely demonstrated the possibility of false-positive case of ^{18}F-FDG uptake due to non-oncological processes as inflammation or benign tumours or false-negative findings associated with the low glucose metabolism rate of the examined diseases [132]. In the brain, the ^{18}F-FDG is usually highly enhanced in the normal grey and white matters, due to the specific glucose metabolism of the neurons, that allows the diagnosis of degenerative diseases [133, 134]. Despite this feature, this tracer plays a limited role in the detection or monitoring of brain tumours. In fact, brain primitive lesions or metastases usually show a very different pattern of uptake of ^{18}F-FDG, generally classified as low, mild, or high, being often barely identified from the high gradient of physiological tracer uptake in the brain[135]. The choline is a precursor of phosphatidylcholine, an important element of cell membrane. The peculiar physiopathologic pathway of choline allows to use this tracer as a marker of lipogenesis and synthesis of cell membrane, helping to detect tumours with a high synthesis of cellular wall[136]. Therefore, since 1997, preclinical[137] and clinical settings[138] started to deepen the knowledge about the usefulness of radiolabeled choline PET in diagnosing brain tumours. In particular, Coleman et al.[139] showed that patients with suspected recurrent brain tumours had more clearly defined abnormal accumulation on the choline PET than with the ^{18}F-FDG PET, while the choline uptake observed in normal cortex was corresponding only to 10 % of the uptake registered with ^{18}F-FDG[136]. The kinetic analysis of dynamic ^{18}F-FMC PET data has been mainly done on patients with prostate cancer [140-142] but results of the combination between PET and MRI quantitative parameters are not available in the present literature.
The results of the correlation between SA K_1 and K_i with TM and SSM parameters is shown in table 2. No correlation was found between K^{trans} and both K_1 and K_i testifying: the delivery of the radiotracer and of the gadolinium based contrast agent is based on different physiological mechanisms and, as usually happens with the FDG, PET and MR related rate constants provide complementary findings[42]. A part form the different permeability over surface area of the choline and on the Gd-based CA, the uptake of these two is driven by active[143] and passive[144] mechanisms, respectively. On the other hand, we found significant correlations between K_1, K_i (and TBR) and k_{ep} and v_e (from both TM and SSM). v_e is the volume fraction of extravascular extracellular space. Many studies on breast cancer show inverse correlation between v_e and the SUV, suggesting that regions with high level of glucose metabolism, in these particular examples, may be characterized by high cellularity[44, 61]. In our study, we found a positive significant correlation between v_e and both the delivery rate constant and the rate at which the choline is irreversibly trapped by the tissue. This might be related to a different interpretation of the v_e, as an expression of the space available for the choline to be uptaken and then phosphorilated. Finally, PET parameters were found to be correlated to the SSM-τ_i. This parameter is the result of the extension of the Tofts model, which is the standard model for the analysis of DCE-MRI data. In the brain, the feasibility of the SSM DCE-MRI pharmacokinetic analysis was investigated by Rooney et al. on 6 healthy subjects, 6 patients with multiple sclerosis and 5 patients with glioblastoma[145]. Cerebral τ_i maps were said to represent metabolic activity in the brain as τ_i is

proportional to water permeability [145]. It has been suggested that τ_i may be related to the NKA pump, driven by the P-type ATPase ion pump[146, 147]. In our study, we found a positive correlation between τ_i and the PET related parameters. This contradicts the results of Hectors et al. in the assessment of hepatocellular carcinoma with ^{18}F-FDG PET and DCE-MRI[28]. Choline PET measures cellular proliferation, whereas τ_i is mainly dictated by Na^+, K^+-ATPase activity sustained by ATP production[26]. This correlation could mean that the metabolism of the cell is faster[65] as cell membrane synthesize their cellular wall. Correlations with the TBR are shown in table 3 and confirm the previous results, with the additional moderate correlation with TM-K^{trans}. This finding might be of particular interest as K^{trans} has been shown to be predictive of patients' response to therapy, in other types of cancer [47, 148].
The main limitation of this study is the limited size of the examined dataset. Moreover, any histological characterization was present for the evaluation of the performance of each pharmacokinetic model compared to a tissutal ground truth. The sensitivity of DCE-MRI data to water exchange effect was reduced by the 26° flip angle acquisition. Li et al. suggest that data τ_i sensitivity can be enhanced by reducing the flip angle (~8°)[66]. This can possibly affect the precision of the τ_i parameter and, as a consequence, the accuracy of the correlation with other imaging metrics. Furthermore, statistical analyses are based on mean quantitative values, which cannot be good description of a heterogeneous tissue, such as the tumour one. On the other hand, DCE- pharmacokinetic parameters were evaluated with the application of an individual arterial input function, which avoids many problems related to the widely used population averaged one[67].

5. Conclusions

In conclusion, dynamic contrast-enhanced MRI and dynamic FMC PET are two imaging modalities that can provide valuable insight to the characterization of tumour tissue.
The two imaging techniques are functionally very different and the extent of their agreement or discordance is not well understood. Therefore, the primary purpose of this study was to evaluate the association between pharmacokinetic parameters resulted from the analysis of DCE MRI data with TM and SSM and metabolic parameters derived from the application of the SA to dynamic PET data. Results showed a high correlation between the irreversible trapping of the tracer in the tissue and the volume of distribution of the gadolinium based contrast agent. The study is a novel co-analysis of kinetic MRI and choline PET, which will benefit from a spatial correlation with DWI-MRI and tissue biology.

IV. Clinical translation of [^{18}F]ICMT-11 for measuring chemotherapy-induced caspase 3/7 activation in breast and lung cancer

1. Introduction

Cell death, is recognised for the constant regulation and harmony of biological systems and is known to occur by several mechanisms, predominantly necrosis and apoptosis. Necrotic cell death is characterised by a non-specific process of events resulting in plasma membrane rupture and a localised inflammatory response around the surrounding cells and tissues. Apoptosis (programmed cell death, first described by Kerr and colleagues [149, 150], however, is a precise series of well executed events with upstream regulators and downstream effector components [3, 4], leading to the systematic dismemberment of the cell by Bapoptotic triggers. The Bapoptotic triggers^ are kept in balance by pro- and anti-apoptotic regulatory proteins, including members of the Bcl-2 family [151]. One of the key players in the execution of apoptosis is a family of caspases (cysteine aspartate specific proteases) [152]. Caspases 8 and 9, known as the initiator caspases, are responsible for initiating a cascade of proteolysis by cleavage of procaspases 3, 6, and 7 to their activated form. The controlled demolition of cellular components resulting in DNA fragmentation is unique to apoptosis, and one that is driven by caspase 3, a central effector caspase. It is this unique feature of caspase-3 that permits its potential use as a non-invasive biomarker of apoptosis [153]. Imaging the apoptotic process may prove to be invaluable for the following reasons: a) by enabling anti-cancer therapy response assessment at earlier time-points than current response criteria allows with conventional imaging, apoptosis imaging may aid the decision to implement changes to treatment in the context of drug resistance sparing the unwanted side-effects of ineffective treatment, and b) secondly, by allowing for the pharmacodynamic assessment of drugs that target the apoptotic machinery in early-phase trials during drug development. There has been a handful of pre-clinical and clinical PET imaging studies attempting to image molecular and biochemical events of the apoptotic process [154-162]. Studies with [^{18}F]ML-10 [163-165] and [99mTc]Annexin V [166-168] showed promising results in humans. A study of [^{18}F]ML-10 — a member of the aposense family of biomarkers that measures 'apoptotic imprint' — in human subjects reported favourable dosimetry and biodistribution, and binding to apoptotic sites in testicular tissue of mice, confirmed by terminal deoxynucleotidyl transferase (TdT) dUTP nick-end labeling (TUNEL) of apoptotic cells; initial studies reported correlation of early changes of tumour [^{18}F]ML-10, and later changes in anatomical tumour dimension following radiotherapy. Annexin V, a 36 kDa calcium-dependent protein with the ability to bind to cells during all stages of the apoptotic process, has high affinity for phosphatidylserine (a phospholipid, normally located on the inner leaflet of cell membranes). During apoptosis, phosphatidylserine is exposed to the extracellular surface and provides an opportunity for annexin V binding. To date, [99mTc]HYNIC-annexin V has been investigated widely for the imaging of apoptosis, and has provided invaluable information in several disease settings. Both [^{18}F]ML-10 and [99mTc]Annexin V imaging, however, pose limitations. [^{18}F]ML-10 remains undefined in its specific target and [99mTc]Annexin V in its non-specific uptake, which has proved difficult in distinguishing between apoptosis and necrosis. Clinical studies evaluating apoptosis in breast cancer therapy have shown an increase in apoptosis within biopsies taken at 24 h post-chemotherapy (comparing six cycles of epirubicin, cisplatin, and fluorouracil with six cycles of doxorubicin and cyclophosphamide) compared to baseline [169-172], as well as at 48, 72, and 96 h post-treatment (combination of epirubicin, cisplatin, and fluorouracil, doxorubicin and cyclophosphamide and weekly paclitaxel) [173]. In the small numbers of patients studied, the authors highlighted the wide variation of changes in apoptosis and or/necrosis and importantly, no correlation of the changes with clinical response to treatment. Breast cancer is, to

an extent, the ideal clinical setting to obtain tissue pre- and post-therapy. Biopsies offer a snapshot of caspase activation at microscopic levels; however, PET and MRI provide dynamic and perhaps more robust non-invasive methods for assessment of apoptosis across the entire lesion volume. The fundamental requirements of any PET radiolabeled probe are ease of synthesis, robust and reproducible facile radiolabelling procedure, and high specificity and selectivity. [^{18}F](S)-1-((1-(2-fluoroethyl)-1H-[1,2,3]-triazol4-yl)methyl)-5-(2(2,4-difluorophenoxymethyl)-pyrrolidine-1-sulfonyl), [18F]ICMT-11 (Figure 51a), an activated caspase-3/7 specific PET imaging radiotracer, was designed from a library of isatin-5-sulfonamides, a chemical class known to have caspase inhibitory activity. With regard to the mechanism of action in relation to selectivity for binding activated caspase-3/7, the dicarbonyl functionality of isatin sulfonamides, including [^{18}F]ICMT-11, is thought to form an intracellular enzyme– tracer complex with the cysteine residue of the active site of caspase-3/7 — forming a thiohemiketal via the electrophilic C-3 carbonyl of the isatin sulfonamide and the nucleophilic cysteine thiol functionality [174]. [^{18}F]ICMT-11 was selected for further evaluation, due to its subnanomolar affinity for activated caspase-3, high metabolic stability, reduced lipophilicity, and facile radiolabelling [175]. Here, we report the results of the first clinical study investigating [^{18}F]ICMT-11 as a noninvasive biomarker to assess tumour apoptosis in locally advanced breast cancer pre- and post-first-cycle of - and in locally advanced lung cancer patients receiving chemotherapy as first-line treatment.

2. Materials and methods

2.1 Radiopharmaceutical preparation

[^{18}F]ICMT- 11 synthesis and radiolabelling was performed by Imanova Ltd., as previously described [176].

2.2 Patients

Two independent phase 1 non-randomised open-label prospective feasibility studies (breast and lung cancer) were recruited from 2013 to 2016. The aim of this study was to assess the effect of chemotherapy on [^{18}F]ICMT-11 uptake by PET and relationship between this variable and blood and tissue activated caspase-3/7 markers. Inclusion criteria in the breast cohort required patients 18 years or older, newly diagnosed with locally advanced potentially operable breast cancer receiving NCT followed by surgery. At least one measurable breast lesion ≥ 20 mm was required on conventional imaging. Patients were excluded from the study if they had received any chemotherapy, immunotherapy, biologic therapy, or investigational therapy within 14 days prior to the first dose of [^{18}F]ICMT-11 injection. Exclusion also applied if the subject was undergoing occupational monitoring of ionising radiation exposure, was lactating or pregnant, or was taking any anticoagulation therapy, a prolonged prothrombin time, or had a positive Allen's test. All breast patients, as per standard routine diagnostic and staging procedures, had a pre-treatment core-needle biopsy and ultrasound (USS) for histological confirmation with characterisation of hormone receptor status alongside imaging with mammogram, and if indicated an MRI of the breasts. Patients had a sentinel lymph node biopsy prior to NCT if deemed appropriate by their clinical team. NCT consisted of six cycles of FEC-T (5-fluorouracil, epirubicin, cyclophosphamide and docetaxel) alongside trastuzumab (Herceptin) in those with HER2-positive breast cancer. Patients were treated at Imperial College Healthcare NHS Trust, and one patient was treated at their local oncology unit. Clinical response using RECIST 1.1 after three cycles of NCT using USS and after six cycles of chemotherapy on surgical histopathology specimens (post wide local excision or mastectomy ± axillary lymph node clearance) was documented. Patients underwent a baseline dynamic [^{18}F]ICMT-11 PET/ CT prior to start of NCT for 65 min followed by a repeat PET/CT scan performed 24–48 h (early) or within 2–14 days (late) post-chemotherapy and repeat breast biopsy within 24 h of the second PET/CT to correlate apoptosis in breast tissue utilising cleaved (active) caspase-3 staining by immunohistochemistry.

In the small cohort of lung patients (n = 2), subjects diagnosed with non-small cell lung cancer undergoing platinumbased chemotherapy treatment (both patients were treated with pemetrexed and cisplatin) were enrolled. At least one measurable lung lesion ≥ 20 mm was required on conventional imaging. Patients were required to have a PET/CT, as well as DW- and DCE-MRI at baseline and post-chemotherapy (24–48 h (early) and within 6–8 days (late) post-treatment). A baseline DW- or DCE-MRI over the area of interest was followed by a 61-min dynamic [^{18}F]ICMT-11 PET/CT scan. The Harrow and Westminister London Research Ethics Committees approved the breast and lung study, respectively. All subjects signed a written informed consent form. The study was conducted according to the Declaration of Helsinki. The administration of radioactivity was approved by the Administration of Radioactive Substances Advisory Committee, U.K.

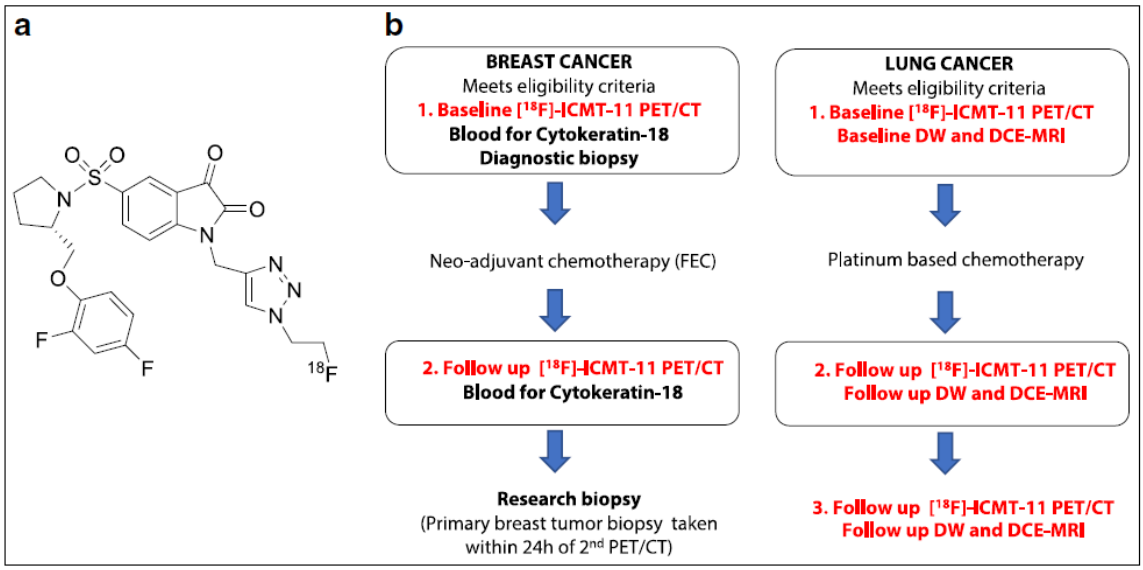

Figure 51: Chemical structure of [^{18}F]ICMT-11 and) study design in breast and lung cancer cohorts. a Schematic diagram of chemical structure of [^{18}F]ICMT-11. b Study design in breast cancer patients receiving neoadjuvant chemotherapy. Patients underwent a baseline and follow-up scan with a repeat second breast biopsy under USS guidance, within 24 h of the second PET/CT scan. The cohort of lung cancer patients recruited to study all received first-line chemotherapy (combination chemotherapy with a platinum-based compound — Cisplatin). [^{18}F]ICMT-11 PET/CT and MRI (DWand DCE) were performed at three time-points (baseline, follow-up at 24–48 h, and within 6–8 days post-chemotherapy. FEC= 5- fluorouracil, epirubicin and cyclophosphamide, USS = ultrasound, MRI magnetic resonance imaging, DW= diffusion-weighted, DCE= dynamic contrast-enhanced.

2.3 Imaging acquisition

Images were acquired on a Biograph 6 TruePoint PET/CT scanner (with TrueV; extended field of view [Siemens]) with 21.6 cm axial and 60.5 cm transaxial fields of view. Patients in both studies underwent an attenuation CT scan (CT settings: tube potential, 130 kV; exposure, 15 effective mAs; pitch 1.5; slice thickness, 5 mm; rotation time, 0.6 s; effective dose of 2.5 mSv) of the thorax before administration of [^{18}F]ICMT-11 injection. [^{18}F]ICMT-11 was injected with a target dose of 300 MBq (maximum dose 370 MBq) as a slow bolus in 1– 20 mls of saline over 30s.

Dynamic PET imaging was performed in a single bed position over 65 min with blood and plasma radioactivity measurements at specified time-points. Data were binned into 35 frames and reconstructed using the ordered subset expectation maximization algorithm (3 iterations and 21 subsets). In the lung cohort, dynamic PET imaging was performed in a single bed position over 61 min. Data were binned into 36 frames and reconstructed using the ordered subset expectation

maximization algorithm (3 iterations and 21 subsets). Radioactive blood data were taken but were not analysed in this study.

Lung MRI was performed on a moving-table 3T system (Siemens Verio with Syngo MR B17, Erlangen, Germany), using the body coil for transmission and a matrix phased array coil as receive coil. Axial slices were acquired during free-breathing for DW-MRI, while DW-MRI slice-matched T2-w imaging was also performed. Dynamic contrast enhanced MRI (DCE-MRI) was performed on the sagittal plane using a VIBE acquisition (0.1mmol/Kg) DOTAREM®.

2.4 Image analysis

All volumes of interest on PET/CT were outlined manually on Hermes (Hermes Diagnostics, Stockholm, Sweden) by a single investigator (SD) to avoid any interobserver variation. For the breast study, volumes of interest (VOIs) were drawn on fused PET/CT datasets by outlining the whole primary breast tumour and any involved axillary lymph nodes [regions of interest (ROIs) over several slices]. VOIs were also drawn using a 2-cm fixed sphere to outline contralateral breast tissue, normal lung, bone, muscle, and aorta. In the lung study, VOIs were drawn outlining the primary lung tumour lesion, normal contralateral lung, bone, muscle, and aorta. SUV60ave, SUV60max, tumour to breast ratio (TBR_{60max}) and tumour to muscle ratio (TMR_{60max}) were obtained at baseline and postchemotherapy in both studies. In both studies, all VOIs were also outlined on fused PET/ CT images to create binary object masks using Analyze software (version 11; Biomedical Imaging Resource, Mayo Clinic). The object masks created for tumour and lymph nodes, alongside respective dynamic PET data, were used within Matlab 16a (The MathWorks®) for analysis and characterisation of the VOIs by voxel intensities sorting. Voxelwise analysis of PET data was done as previously described [177]. Briefly, this involved extraction of all the voxels within each VOI and sorting as per their intensity frequency. PET-based voxel intensity sorting (PVIS) identifies any shifts in voxels, as would otherwise be difficult to observe by using only ROI analyses, where any spatially discrete areas of effect may be averaged. Any shifts observed (higher intensity voxels) were presumed to be in keeping with apoptosis and shifts to lower intensity voxels representing necrosis. The highest voxel intensities (taken as a cut-off at the 95th percentile) are more indicative of high radiotracer retention than the voxel mean, and were taken to biologically represent apoptotic cells. Histogram analysis was then performed using in-house software developed in Matlab 15a (The MathWorks(R)), to calculate first-order statistics.

2.4.1 DW-MRI and DCE MRI

ADC maps were generated in Matlab 15a (The MathWorks(R)) using monoexponential, non-linear fittings to the equation: $S=S0 \cdot exp(-b \cdot ADC)$ and all ten b-values (0, 10, 20, 30, 50, 80, 100, 150, 400 and 800 s/mm2). ADC values are expressed in $\mu m^2/s$. For voxels in which the ADC calculation software failed to converge or returned negative values, the ADC value was set to zero (processing software: Medical Image Processing, Analysis and Visualisation, National Institutes of Health, US), where the regions of interest (ROIs) were drawn, with consideration to avoid regions affected by artefacts and partial volume effects. Multiple-slice ROIs were used (i.e. volumes of interest-VOIs), as opposed to single-slice ones for the analysis, to avoid observer bias and reduce ADC measurement variability. Volumetric assessment is also expected to capture lesion heterogeneity more effectively than single-slice assessment and, as a result, is better suited for voxel-wise characterisation with histogram analysis. VOIs were drawn by an MRI physicist (IL) on the b=800 s/mm2 images and then copied to the ADC maps. Histogram analysis was then performed using in-house software developed in Matlab 15a (The MathWorks(R)), to calculate mean, skewness, kurtosis, 25th, 50th and 75th percentiles. Voxels with zero ADC values were excluded from the analysis.

For DCE-MRI, the shutter speed model was used (as described in *Chapter 3*). VOIs were drawn by a single investigator (SD) on the dynamic scan of the lung patients DCE MRI data using the Analyze software (Biomedical Imaging Resource, Mayo Foundation, Rochester, MN). All 3D parametric maps were generated in Matlab R2015a (The MathWorks(R)) using a standard non-linear least square curve fitting algorithm. Mean, standard deviation, kurtosis and skewness values were evaluated for each parameter. Voxels with biologically implausible results were excluded from the analysis (e.g. $K^{trans} > 5$ 1/min, $v_e > 1$, $\tau_i > 3$ s as any negative value). Implicit in the analysis is the requirement of the AIF which, in this study, has been evaluated, for each subject, drawing a region of interest in the aorta.

2.5 Cytokeratin-18 measurements

Blood samples were taken in breast patients to measure CK18. Two samples, each 7.5 mls, of blood from all patients were taken at baseline and at follow-up scan to measure M65 (measuring caspase-cleaved and intact CK-18) and M_{30} (measuring caspase-cleaved CK-18) using ELISA kits obtained by PEVIVA (BIOAXXESS, UK).

2.6 Cleaved (active) caspase-3 immunohistochemistry

A core biopsy was taken post-chemotherapy by a consultant interventional radiologist within 24 h of the second [^{18}F]ICMT-11 PET/CT scan. All diagnostic and research breast biopsies obtained were processed as previously described [177].

3. Results

3.1 Radiopharmaceutical

The radiolabelling of [^{18}F]ICMT-11 was performed as previously described [176]. Radiochemical purity was > 99% on completion of synthesis with a mean (± SD) specific activity of 1373 ±1605 GBq/μmol (range, 199-9317 GBq/μmol) and pH of 5.02 ± 0.22 (range 4.57–5.66). The mean (range) doses injected in all breast patients pre- and post-chemotherapy were 335.6 MBq (278.4–353.3 MBq) and 343.1 MBq (282.4– 359.1 MBq).

3.2 Patients

The study was designed: (a) in breast cancer to assess the effect of chemotherapy on [^{18}F]ICMT-11 uptake correlated with blood cytokeratin-18 assessment and biopsy-derived caspase-3/7 tissue expression within 24 h of the first dose of neoadjuvant FEC-T treatment, and (b) in lung cancer to measure the longitudinal effect of first-line chemotherapy on [^{18}F]ICMT-11 correlated with diffusion-weighted and dynamic contrast-enhanced magnetic resonance imaging (DW- and DCE-MRI) at each time point; notably, the latter was more difficult to recruit to, as a result only descriptive data are presented. A total of 23 patients were recruited, 20 breast cancer patients and three lung cancer patients. Seventeen patients were evaluable (15 breast cancer patients, all of whom were female, and two lung cancer patients, both male). Five breast patients withdrew from the study (two due to tracer failure, two due to patient's personal decision, and one due to needle phobia), and one lung patient also withdrew (due to extreme fatigue). Study design and patient characteristics are shown in Figure 51b and Table 23 respectively. All breast patients had a diagnosis of invasive ductal carcinoma. Ten patients were found to have positive axillary lymph nodes on ultrasound (USS) and/or sentinel lymph node biopsy. All 15 patients completed a total of six cycles of FEC-T (three cycles of 5- fluorouracil, epirubicin, and cyclophosphamide, followed by three cycles of docetaxel). Four patients then commenced trastuzumab (Herceptin) concomitantly with docetaxel, after the first three cycles of FEC chemotherapy, for 1 year, as per standard local hospital guidelines. Fourteen patients received radiotherapy post-surgery, and one patient did not require radiotherapy. Oestrogen (ER), progesterone (PR), and human epidermal growth factor (HER2/neu) receptor status are documented in Table 23. Response was measured after three cycles of NCT by USS and after six cycles on histopathology at surgery. Fourteen out of 15 patients were classified as responders — partial response (PR) or complete response (CR) post-

treatment — and one patient had stable disease (SD); no patient showed evidence of disease progression. Both lung cancer patients had a diagnosis of non-small cell carcinoma (adenocarcinoma). Clinical response in the patients with lung cancer were reported with computerized tomography (CT) using RECIST 1.1 [178] midway through their chemotherapy and at the end. One lung patient had a PR post four cycles of chemotherapy and proceeded to radiotherapy treatment (55Gy in 20 fractions over 4 weeks), the second patient, had a PR after three cycles and completed five cycles with SD after initial PR. This patient subsequently died due to infection, unrelated to tumour or treatment received.

3.3 [^{18}F]ICMT-11 uptake in breast tumours at baseline and post-chemotherapy

[^{18}F]ICMT-11 was well tolerated by all patients, with no immediate or delayed complications observed. The median time (range) between baseline [^{18}F]ICMT-11 PET/CT and start of NCT in breast patients was 6 days (1–14 days), and that between first cycle of NCT and post-treatment [^{18}F]ICMT-11 PET/CT was 12 days (24 h–14 days). All primary tumours and involved axillary lymph nodes were visible on conventional imaging and PET; however, not all lesions demonstrated uptake on [^{18}F]ICMT-11 PET (Figure 52a). For analysis, patients were divided into early (24– 48 h) and late (2–14 days) imaging post-chemotherapy. There were four patients in the early imaging group and 11 in the late imaging group. The mean and maximum SUV at 60 min (SUV_{60ave} and SUV_{60max}) pre- and post-chemotherapy are illustrated in Figure 52b and c. The median (range) pre-treatment SUV_{60ave} and pre-treatment SUV_{60max} were 0.56 (0.33–0.94) and 0.91(0.53–1.24) respectively. Post-treatment SUV60ave and post-treatment SUV_{60max} were 0.50 (0.38– 1.07) and 0.75 (0.41–1.59) respectively. Pre- and post chemotherapy ratios (± standard deviation, SD) of tumour o-normal breast tissue (TBR_{60max}), were 3.65 (± 1.71), 3.34 (± 1.52); corresponding tumour-to-muscle ratios (TMR_{60max}) were 1.63 (± 0.43), 1.57 (± 0.49) respectively. Seven first-order statistics were extracted (mean, standard deviation, min, max, range, skew, and kurtosis), and none showed a change in the variables, irrespective of whether they were in the early or late imaged breast tumour group (Figure 52d).

3.4 Voxel-wise analysis of [^{18}F]ICMT-11 PET imaging data

As previously described, the analysis of apoptosis in PET imaging at the tumour level using a PET-based voxel intensity sorting (PVIS) approach allows for the overall spatial distribution of voxel intensities within the tumour to be assessed; higher Δ intensity in treated tumours compared to baseline (right shift) is assigned PVIS apoptosis-dominant signature (PADS), while lower Δ intensity (left shift) is assigned PVIS necrosis-dominant signature (PNDS). Four patients (e.g., patients 1 and 2 in Figure 52) displayed PADS (Figure 53a); patient 3 in particular had a substantial right shift in voxel intensities. Mean percentage shift in voxel intensities for all four patients was 71%, and all had a PR after three cycles of chemotherapy on USS and after six cycles confirmed on histopathological correlation at surgery. The area under the curve (AUC) differences for all patients (numbered 1–15) are shown (Figure 53c). Thus, it appears that despite a lack of change in SUV_{60ave} there were regional changes in tumour radiotracer uptake. Of the 11 patients that did not demonstrate PADS, nine displayed ≥ 25% lower voxel intensities post-treatment indicating a PNDS. Examples of patients with PNDS — patients 5 (with post-treatment imaging at 24 h) and 6 (post-treatment imaging at 6 days) are shown in Figure 53b. The mean percentage shift in voxel intensities was 68%; eight out of the nine patients had either a PR or CR post-chemotherapy, while one patient (patient 10) had SD (Figure 53d), suggesting that either PADS or PNDS can be associated with response to therapy The remaining two patients (exemplified by patient 14) showed no change in voxel intensity Figure 53b), despite showing PR to therapy. Notably, a snapshot of tumour [^{18}F]ICMT-11 localisation is detected by our methodology; thus, presently we do not know whether the necrosis-dominant signature or indeed the no change in voxel intensities despite PR/CR, represents outright necrosis or a dynamic transition of cell death via an apoptosis dominant signature. In the cohort of patients studied, no patients demonstrated progressive disease.

Table 23: Patient characteristics.

Breast

Patient	Age	Tumour	Tumour size (mm)	Grade	Nodal status	TNM*	Hormone receptor status
1	47	IDC	120mm	G3	-	T3NoMo	ER+/PR+/HER2-
2	37	IDC	20mm	G2	-	T2N2M1	ER+/PR+/HER2-
3	44	IDC	50MM	G2	-	T2NoMo	ER+/PR+/HER2-
4	55	IDC	17MM	G3	N1	T1N1Mo	ER+/PR+/HER2-
5	60	IDC	48MM	G3	N1	T2N1Mo	ER+/PR+/HER2+
6	54	IDC	87MM	G3	N2	T3N2Mo	ER+/PR+/HER2-
7	40	IDC/HG DCIS	32MM	G2	N1	T2N1Mo	ER-/PR-/HER2+
8	63	IDC	50MM	G3	N1	T2N1Mo	ER-/PR-/HER2-
9	42	IDC/ IM DCIS	40MM	G2	N2	T2N2Mo	ER+/PR+/HER2-
10	67	IDC	18MM	G3	N1	T1N1Mo	ER+/PR+/HER2-
11	45	IDC	40MM	G3	-	T2NoMo	ER-/PR- /HER2-
12	61	IDC (2 lesions within breast)	25MM	G2	-	T2NoMo	ER-/PR-/HER2+
13	58	IDC	25MM	G3	N1	T2N1Mo	ER-/PR-/HER2+
14	68	IDC	20MM	G3	N1	T2N1Mo	ER-/PR-/HER2+
15	43	IDC	26MM	G2	N1	T2N1Mo	ER+/PR+/HER2-

Lung

Patient	Age	Tumour	Nodal status	TNM	
16	54	Adenocarcinoma	-	T4NoMo	-
17	42	Adenocarcinoma	N3	T4N3Mo	-

The median age (mean; range) of all patients: 54y (52; 37-67y), median weight 71.9 kg (73; 52.3-95.3 kg)
- Light grey shading (patients 1-4, found to show a predominant apoptotic signature)
- Mid-grey shading (patients 5-13, found to show a predominant necrotic and/or necrotic/apoptotic signature)
- Dark grey shading (patients 14 and 15, found to show neither a predominant apoptotic nor necrotic shift)
IDC Invasive ductal carcinoma, HG DCIS High grade ductal carcinoma in-situ, IM DCIS Intermediate grade ductal carcinoma in-situ, ER Oestrogen receptor, PR Progesterone receptor, HER2 Human epidermal growth factor receptor 2
***AJCC staging (7th edition) used for TNM staging in breast and lung cancer**

3.5 Cytokeratin-18 and caspase cleaved cytokeratin-18

All breast patients had blood taken for cytokeratin-18 (CK-18) analysis. Circulating full-length (M65) and caspase-cleaved CK 18 (M_{30}) fragments were assessed by ELISA pre- and post-treatment at the time of the PET scan. Typical data are shown in Figure 53e. Ratios of cleaved to total CK-18 varied considerably in this cohort of breast patients, with the lowest ratio post-chemotherapy 0.27 observed in patient 10, in whom there was no response to NCT. The median pre- and post-chemotherapy values of M_{65} were 141.5 U/l (range 50.3–359.7), and 180.8 U/l (range 66.9–369.7), and those for M_{30} were 78.8 U/l (range 32.2–207.9) U/L and 102.7 U/l (range 47.8–207.7) respectively. Overall M_{30} or M_{65} did not correlate with PADS or PNDS (*Figure 53*f).

Patient 3, who had the highest PADS, also showed the only consistent increase of M_{30}/M_{65} ratio, increasing from 0.35 pre-chemotherapy to 0.52 post-chemotherapy, perhaps suggesting that the levels of apoptosis or necrosis were not sufficiently high to generate robust changes of M30/M65 in blood.

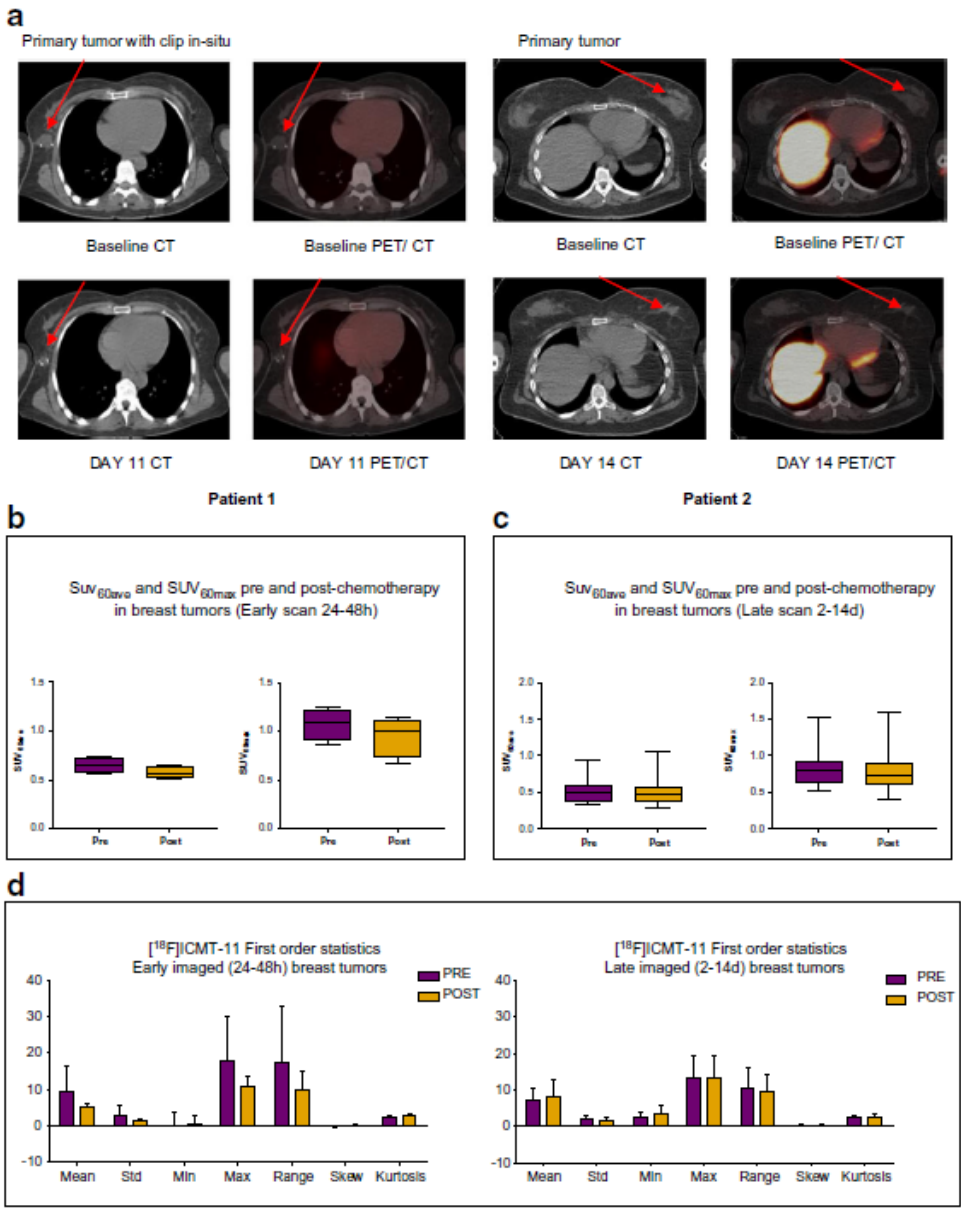

Figure 52: [^{18}F]ICMT-11 uptake in primary breast tumours. a Axial CT and fused [^{18}F]ICMT-11 PET/CT images of primary breast tumours in two patients, 1 and 2,at baseline (pre-) and post-chemotherapy. Low-level uptake is noted. b Pre- and postchemotherapySUV60ave andSUV60max values of breast tumours imaged at an early time point(24–48 h) or c late time point(2–14 days). Small changes were seen pre- and post-chemotherapy. d First-order statistics were extracted using in house software under Matlab 15a [The MathWorks(R)], and a subset of features were selected to detect changes in early and late imaged breast tumours

3.6 Cleaved caspase-3 expression

Acknowledging that pre- and post-treatment biopsies could have been taken from different parts of the tumour, we assessed if there was some general association between the PVIS data and histopathology in the breast patients. All diagnostic (pre-) and post-chemotherapy biopsies were stained for cleaved (active) capsase-3 expression. The diagnostic tumour blocks of two patients (patients 2 and 5) were not available. Typical cleaved caspase-3 immunostains in patients

assigned PADS and PNDS are shown in *Figure 54*a and b. Whole tissue mount analysis of percentage cleaved caspase-3 showed variable baseline and posttreatment expression. Cleaved caspase-3 expression was low at baseline with levels below 0.45%; expression increased from a mean of 0.13% (95% CI 0.12–0.13) to 0.81% (95% CI 0.79– 0.83). Such low levels of caspase-3 activation despite a mean fold-change of 15.7% may prove difficult to detect by PET.

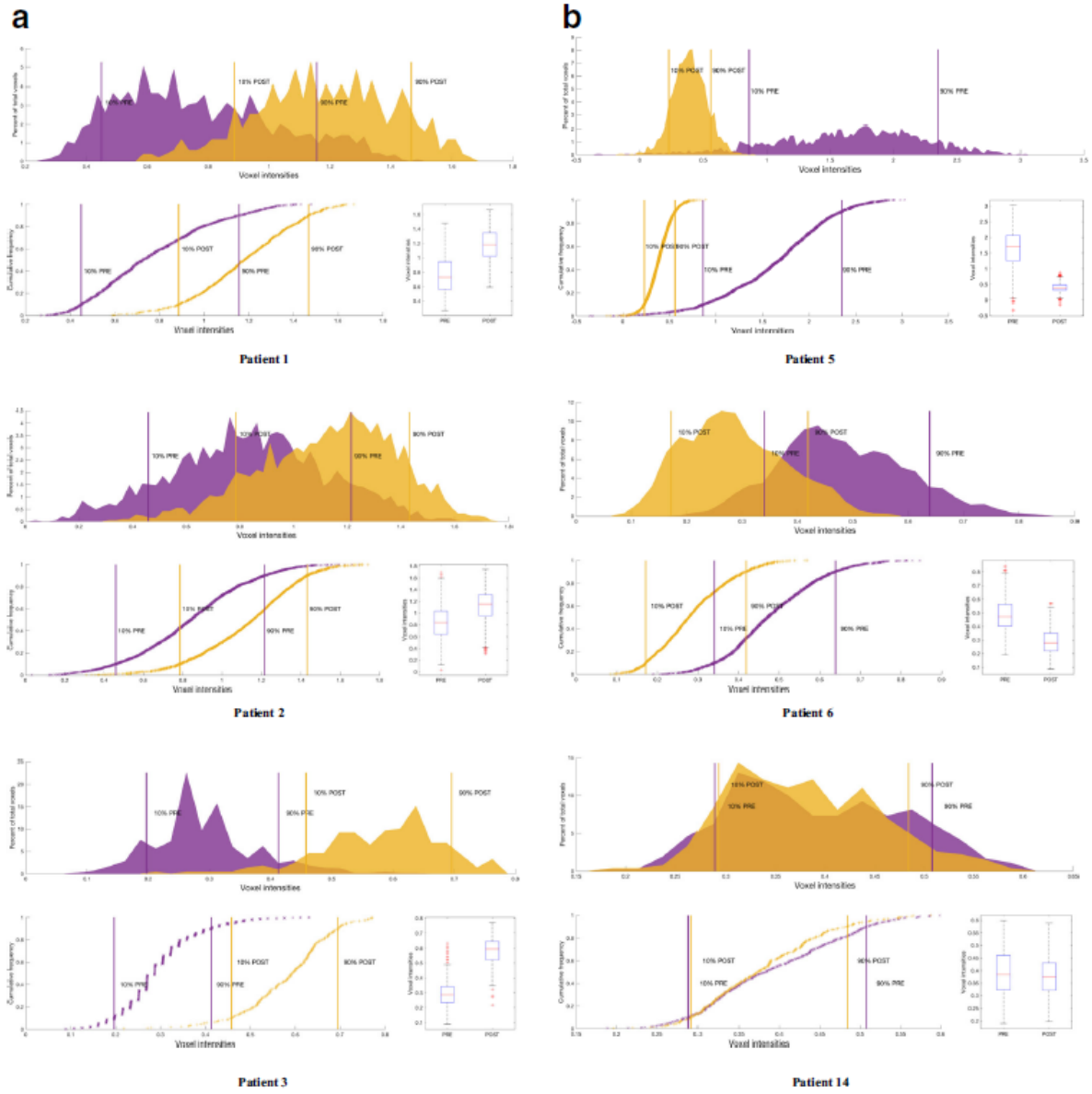

Figure 53: Voxel–wise tumour [^{18}F]ICMT-11 intensity histogram analysis and blood cytokeratin-18 in all breast cancer patients. a PET-based voxel intensity sorting (PVIS) histogram analysis in patients 1, 2, and 3. All patients are late-imaged, (2–14 days) except patient 5* (early imaged 24–48 h). The intensities of all voxels within the tumour volume of interest (VOI) have been expressed as histogram plots of normalised voxel intensities pre-and post-chemotherapy. These patients demonstrated a predominant PVIS apoptotic signature with right shifts of all voxel intensities within the tumour VOI post-chemotherapy. b PVIS histogram analysis inpatients 5 and 6, showing a predominant PVIS necrotic signature with shift in voxel intensities to the left. Patient 14, showing no dominant signature on PVIS histogram analysis. These results have been analysed statistically and are represented through box-plot diagrams (minimum, maximum, median, 10th and 90th percentile statistical parameters). The differences in AUC shifts noted in each patient are shown in c, demonstrating tumours with a predominant dominant PVIS apoptotic signature (black) or dominant PVIS necrotic signature (white), and d associated outcomes in all fifteen breast patients post 3 and 6 cycles of NCT. Patients are shown as having SD (stable disease), PR (partial response) or CR (complete response). * denotes patients who received trastuzumab alongside their 4th–6th cycle of chemotherapy. Light grey shading (patients1–4, who showed a predominant

PVIS apoptotic signature). Mid grey shading (patients 5–13, who showed a predominant PVIS necrotic signature). Dark grey shading (patients 14 and 15, who showed neither a predominant apoptotic nor necrotic shift). e Corresponding CK-18 analysis(M65 and M30) pre-and post-chemotherapy in patients 1, 2, and 3.Graphs highlight the variation in levels, with only patient 3 demonstrating an increase in post-chemotherapy levels ofM65 andM30. f CK-18 (M65and M30) analysis in patients 5 and 6, showing no clear increase post-chemotherapy, and patient 14, who despite showing no dominant signature on PVIS histogram analysis, was found to have an increase in M65and M30 levels post-chemotherapy.

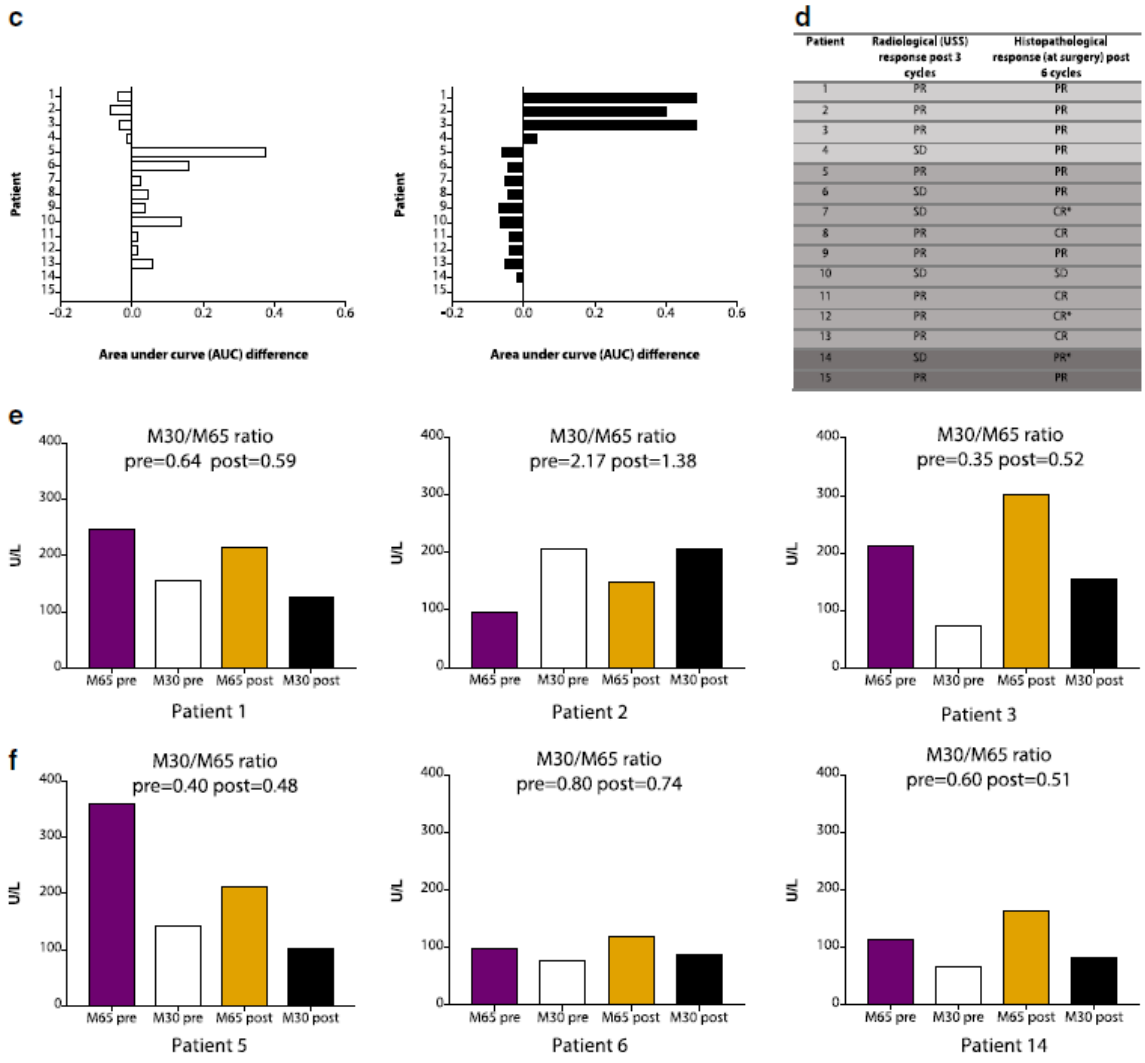

Patient	Radiological (USS) response post 3 cycles	Histopathological response (at surgery) post 6 cycles
1	PR	PR
2	PR	PR
3	PR	PR
4	SD	PR
5	PR	PR
6	SD	PR
7	SD	CR*
8	PR	CR
9	PR	PR
10	SD	SD
11	PR	CR
12	PR	CR*
13	PR	CR
14	SD	PR*
15	PR	PR

Figure 57 (continued)

3.7 Longitudinal studies in lung cancer patients

3.7.1 [^{18}F]ICMT-11 uptake in lung tumours at baseline and post-chemotherapy

Three lesions from two lung cancer patients (a large left upper lobe tumour in patient 16; a primary lesion in the right upper thoracic mediastinum and a mediastinal lymph node in patient 17) were analysed at three time-points; the lesions were all visible on PET (Figure 55a). The interval between baseline [^{18}F]ICMT-11 PET/CT/MRI and start of chemotherapy in both lung cancer patients was between 2 and 8 days. Patients were scanned at 24 h and at 7 days after the first cycle

of chemotherapy. Median (range) SUV60ave and SUV60max were 0.41 (0.33–0.61) and 0.85 (0.52–0.87) at baseline, 0.39 (0.35–0.62) and 0.87 (0.47–0.88) early after chemotherapy, and 0.45 (0.42–0.66) and 0.94 (0.64–0.98) late after chemotherapy. First-order statistics showed no differences in the features extracted. With regard to voxel-wise analysis, patient 16 demonstrated an initial PNDS shift followed by a PADS shift (61%) to higher voxel intensities at 7 days post-chemotherapy (*Figure 55*a and b). Patient 17, had a PNDS in the primary thoracic lesion, at 24 h and 7 days post-chemotherapy (*Figure 55*c and d). Both patients had a partial response to combination platinumbased chemotherapy (*Figure 55*e and f).

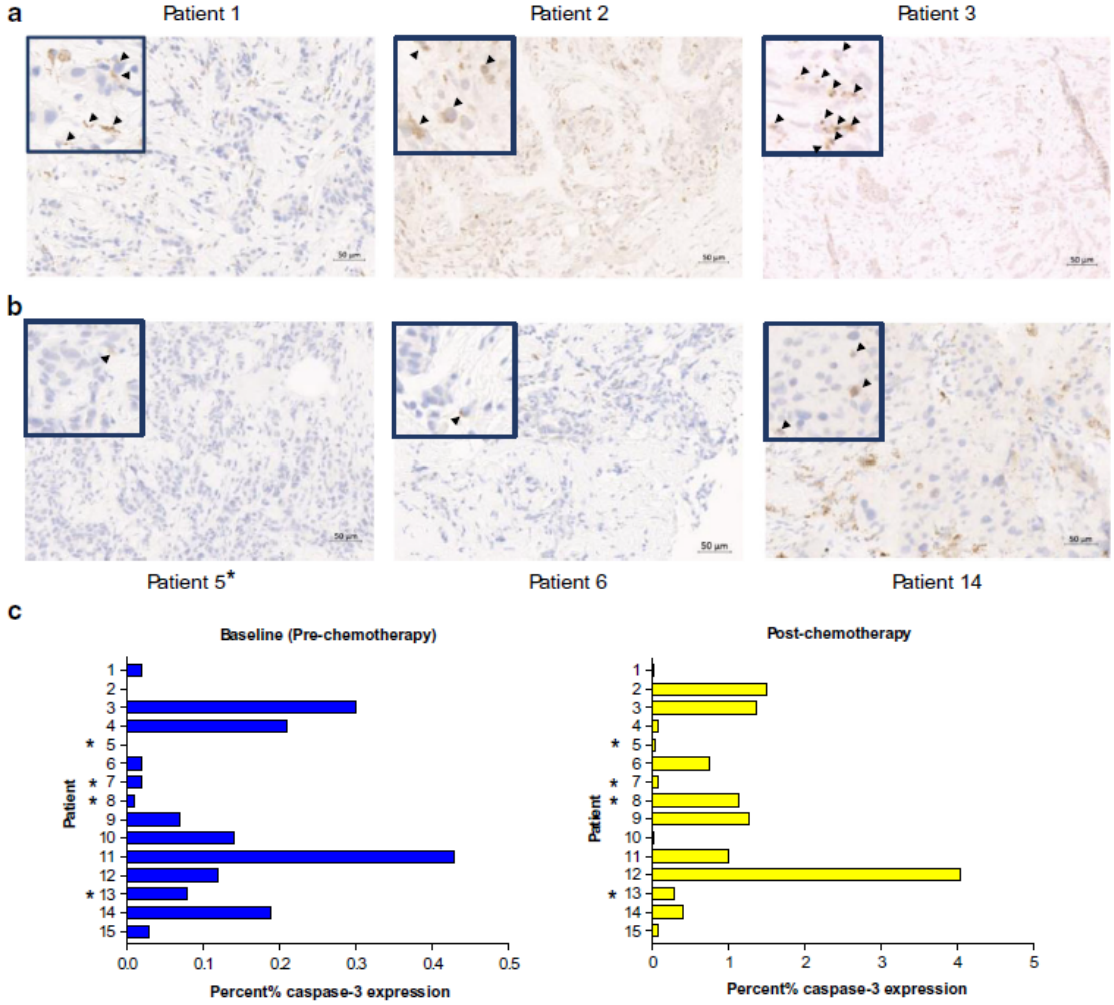

Figure 54: Cleaved caspase-3 expression in breast patients. a Expression of cleaved caspase-3 detected by immunohistochemistry in breast tissue taken by USS-guided biopsy post-chemotherapy in patients with a predominant PVIS apoptotic signature. b Similar cleaved caspase-3expression in patients with a predominant PVIS necrotic signature no change on PVIS. Arrows (black) demonstrate cleaved caspase-3staining on tissue biopsy post-chemotherapy. c Graph indicates the percentage (%) cleaved caspase-3 expression in breast tissue in all patients taken at baseline (blue bars) and post-chemotherapy (yellow bars). * denotes early imaged (24–48 h) breast patients.

3.7.2 Diffusion-weighted (DW) and dynamic contrast enhanced (DCE) MRI in lung cancer

The diffusion of water molecules embodied in the variable Apparent Diffusion Coefficient (ADC; mean and percentiles), increased in patient 16 but not in patient 17 (*Table 24*) consistent with cell death-related increase in extracellular space in the former after the initiation of therapy (*Figure 55*A and B). Histogram analysis demonstrated increase in skewness and kurtosis in patient 16, particularly at 7d, while these variables decreased or were unchanged in patient 17 (*Figure 55*C and D). A reduction of ADC and skewness could be related to increases in extracellular matrix

(ECM) constituents, which introduces additional obstructions and hydrogen-bonding sites to the tumour microenvironment, thus reducing the ADC.

Table 24: ADC histogram analysis results of lung cancer patients 16 and 17.

	Patient 16						
	#Voxels	Mean	Skew	Kurtosis	25th perc.	50th perc.	75th perc.
Baseline	10274	998.2	0.27	4.71	881.0	995.0	1111.0
24 h	10261	1109.0	0.67	5.74	986.0	1099.0	1214.0
7 d	3781	1343.2	2.14	26.5	1105.0	1309.0	1546.0
	Patient 17						
	#Voxels	Mean	Skew	Kurtosis	25th perc.	50th perc.	75th perc.
Baseline	2157	1743.5	0.68	2.79	1263.7	1614.0	2131.5
24 h	1976	1315.5	0.25	3.12	1104.0	1291.5	1521
7 d	1781	1459.5	0.15	3.54	1264.7	1454	1645

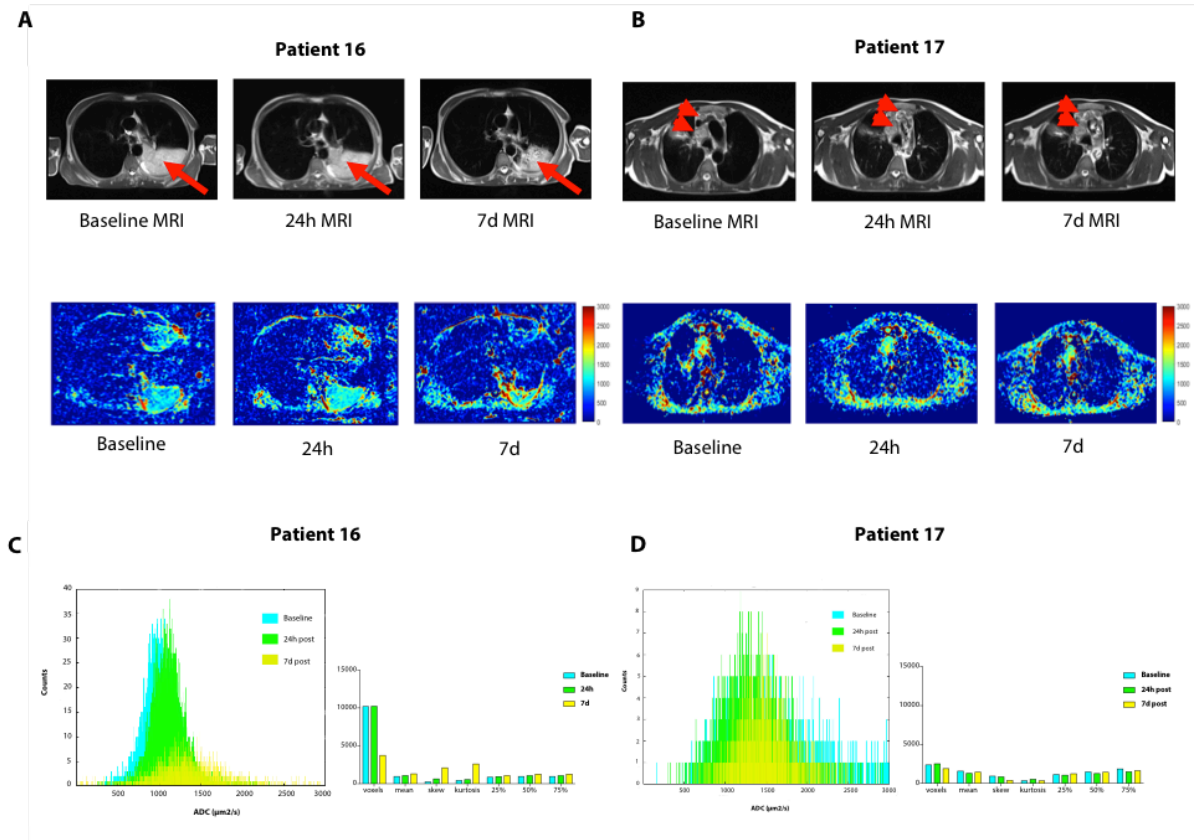

Figure 55: Detection of tumour cell death in lung cancer by DW-MRI. (A and B) DW-MRI images for patient 16 and 17 at baseline, 24h and 7d post-chemotherapy. Corresponding apparent diffusion coefficient (ADC) maps in jet colour scale (µm2/s) are shown. (C and D) ADC tumour histograms in patient 16 and 17 depicting the distribution of the voxels as per their intensities at baseline, 24h and 7d post-chemotherapy with histogram

analysis using in-house software developed in Matlab 15a (The MathWorks(R)), to calculate mean, skewness, kurtosis, 25th, 50th and 75th percentiles. Voxels with zero ADC values were excluded from the analysis.

DCE-MRI pharmacokinetic analysis using the shutter speed model was conducted to verify whether large changes in perfusion/permeability accompanied [18F]ICMT-11. K^{trans} is a variable that reflects permeability and blood flow, and measured as the accumulation of contrast agent into the extravascular-extracellular space. In general, K^{trans} increased at 24h followed by a decrease to below baseline values at 7d (*Table 25*), suggesting that changes in [18F]ICMT-11 tumour uptake in the lung patients could not be explained by perfusion/permeability changes. Other DCE variables including K_{ep}, v_e and τ_i (mean and histogram values) are summarised in Table 25.

Table 25: Results of the application of the shutter speed model on DCE-MRI data.

Shutter Speed Model

	Patient #1															
	K^{trans}				K_{ep}				v_e				τ_i			
	Mean	Std	Kurtosis	Skewness	Mean	Std	Kurtosis	Skewness	Mean	Std	Kurtosis	Skewness	Mean	Std	Kurtosis	Skewness
Baseline	0.76	1.12	5.78	1.90	1.53	1.38	2.49	0.85	0.79	0.14	10.99	-2.14	0.22	0.32	18.04	3.48
24 hours	0.94	1.27	4.44	1.65	2.05	1.52	1.76	0.48	0.81	0.11	8.74	-1.15	0.18	0.21	28.66	4.08
7 days	0.57	0.70	12.018	2.80	0.78	0.87	7.76	2.19	0.68	0.20	2.091	-0.30	0.19	0.13	4.59	0.45
Variation	-0.39	-0.45	1.70	0.69	-0.62	-0.43	3.41	3.53	-0.16	0.88	-0.760	-0.74	0.09	-0.37	-0.83	-0.88
	Patient #2															
	K^{trans}				K_{ep}				v_e				τ_i			
	Mean	Std	Kurtosis	Skewness	Mean	Std	Kurtosis	Skewness	Mean	Std	Kurtosis	Skewness	Mean	Std	Kurtosis	Skewness
Baseline	1.26	1.19	4.016	1.3075	1.98	1.29	1.90	0.29	0.74	0.24	2.83	-1.088	0.087	0.35	176.37	12.62
24 hours	1.18	1.16	3.75	1.3269	1.45	0.96	4.16	1.07	0.69	0.25	2.12	-0.79	0.10	0.075	4.82	0.90
7 days	1.12	1.32	3.77	1.4103	0.80	0.74	4.80	1.65	0.68	0.28	3.0041	-1.087	0.15	0.29	11.066	2.84
Variation	-0.05	0.13	0.0031	0.062	-0.44	-0.23	0.15	0.53	-0.02	0.13	0.42	0.36	0.51	2.88	1.29	2.15

4. Discussion

In the first patient study of the caspase 3/7-specific isatin sulphonamide PET radiotracer, we show that the lack of significant global tumour [^{18}F]ICMT-11 dependent PET changes, despite some regional voxel changes, reflect a lack of significant apoptosis induction following chemotherapy. This study to our knowledge is the first to investigate the use of a caspase 3/7-specific PET radiotracer for imaging of chemotherapyinduced apoptosis in cancer Chemotherapy response has often been associated with cell death via apoptosis [169, 171, 172]; however, such studies have often been semi-quantitative and based on biopsy samples with variable output. Several studies have reported that spatial and temporal heterogeneity exist in breast and other cancers [179, 180]. Repeat biopsy of breast tissue at a single point in time is not representative of the whole tumour. Thus, approaches aiming to image whole-tumour apoptosis for the purposes of assessing therapeutic response (to chemotherapy, targeted therapies, and radiotherapy) were embraced. These imaging methods include MRI [181], magnetic resonance spectroscopy (MRS) [182], USS [183], novel fluorescence imaging [184], scintigraphy [159, 166]and PET [158, 164, 165]. Studies using [99mTc]Annexin V, in particular, led the way for nuclear imaging of apoptosis [159, 166, 167]. In the current study, we report that caspase-3/7 activation as determined by [^{18}F]ICMT-11 was not a dominant mechanism of pharmacological activity following chemotherapy in breast cancer. Two pieces of information enabled us to reach this conclusion.

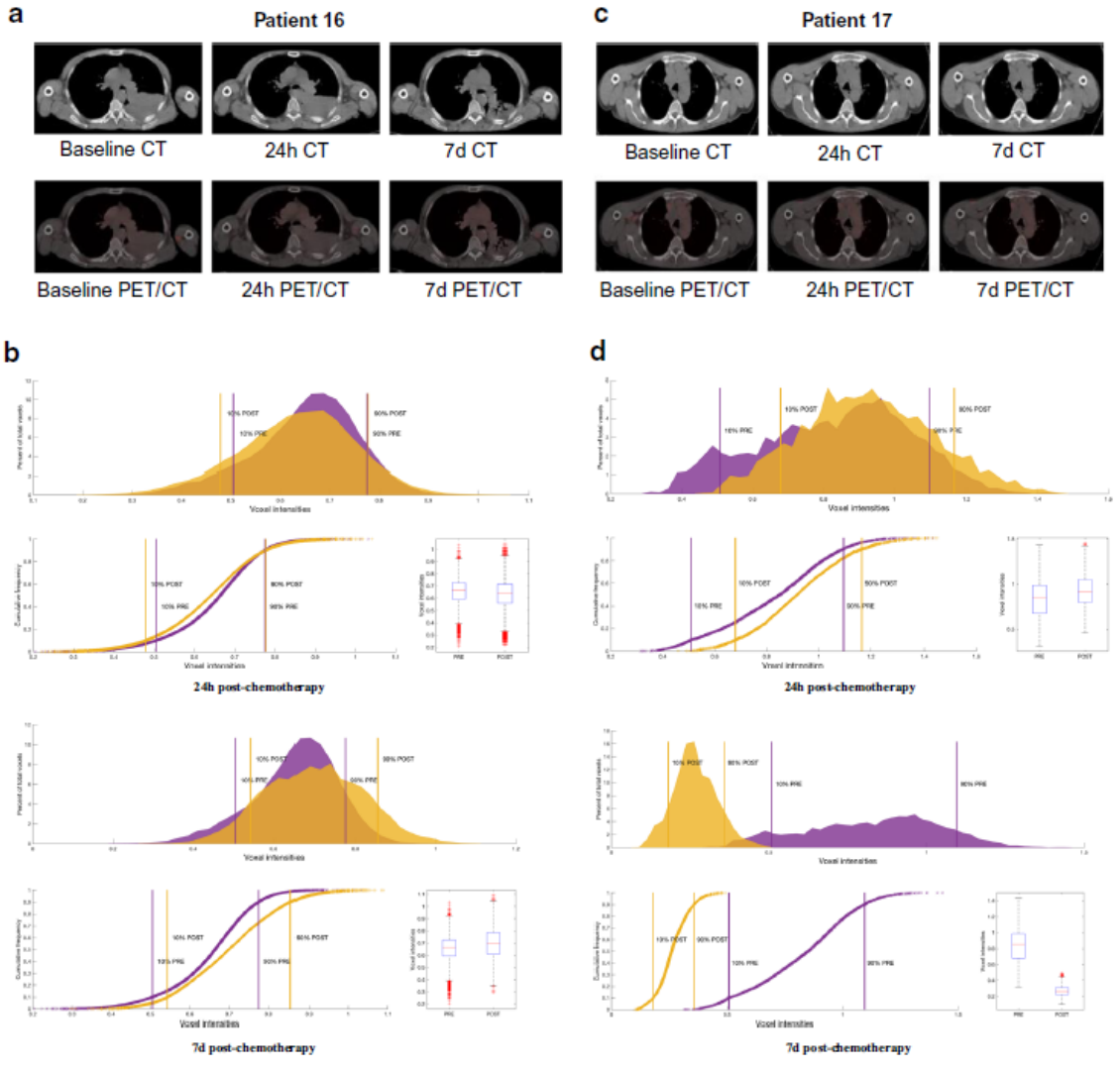

e

Patient	Radiological response (RECIST 1.1)	
	Post 3 cycles	Post 4 cycles
16	PR	PR

f

Patient	Radiological response (RECIST 1.1)	
	Post 3 cycles	Post 5 cycles
17	PR	PR

Figure 56: Detection of tumour cell death in lung cancer by [^{18}F]ICMT-11PET/CT. Patient 16 (a) and Patient 17 (c) axial CT and fused [^{18}F]ICMT-11 PET/CT images of primary lung cancer at cancer at baseline, 24 h and7 days post-chemotherapy. PVIS histogram analysis at 24 h and 7 days post-chemotherapy in patient 16 (b) and 17 (d), with clinical outcomes (e and f).

First, cytokeratin-18 analysis in blood samples, a method that has been previously reported to have high sensitivity and specificity for detecting apoptosis [185, 186], showed a positive change — increased M30/M65 ratio — only in one patient (patient 3). Indeed, Olofsson et al. indicated based on their M30/M65 data that FEC chemotherapy, also used by us, causes predominantly necrotic death compared for instance to taxane-based therapy [186]. Whether necrotic death was secondary to apoptosis was not determined. Furthermore, the absolute proportion of apoptotic cells in biopsy samples obtained from patients soon after [^{18}F]ICMT-11 PET scanning was generally in the 1% range, albeit an increase from pretherapy levels (*Figure 54*c). This low proportion of apoptotic cells may not generally lead to detection by nuclear methods. While cytokeratin-18 methodology can be influenced by apoptosis of chemotherapy-sensitive healthy tissue [187], we were surprised by the low proportion of apoptosis from histology. In comparison to routine oncology nuclear medicine radiotracers, the (baseline) pre-chemotherapy uptake of

[^{18}F]ICMT-11 in tumour was low, with SUV60max values around 1. With simultaneous acquisition of anatomical information, by CT in our case, segmentation of tumour is still possible and in view of this, low baseline uptake presumably representing the no/low apoptosis state is inconsequential. However, SUV parameters did not change following treatment, attributed to the low level of apoptosis seen in these tumours. In preclinical studies, [^{18}F]ICMT-11 demonstrated high specificity to apoptosis versus necrosis [177]; thus, it is unlikely that the lack of changes is a reflection of lack of specificity. It is possible to rationalise a highly heterogeneous response of tumours to chemotherapy whereby clusters of tumours respond more avidly to the therapy than the bulk of the tumour. Indeed, we demonstrate this phenomenon in preclinical models of lung cancer imaged with [^{18}F]ICMT-11 PET, whereby the global tumour tracer normalised uptake value returned no changes following effective therapy. In contrast, PVIS histogram analysis showed a clear right shift over 48 h post-treatment, with a 1.5-fold increase in the number of voxels having high intensity uptake [188]. Consequently, PVIS analysis allows extraction of the Bcell-death^ signal by allowing the capture of heterogeneous [^{18}F]ICMT-11-detectable activated caspase-3/7 within the tumour, compared with simple uptake values derived from the volume of interest. The over-reliance on voxel-based analysis for apoptosis data is predicated on pre-clinical studies for ICMT-11 [188] and clinical studies with [^{18}F]ML-10 [164, 165], intimating a manner in which apoptosis data should be presented in view of its heterogeneous presentation. All patients, except one, responded to treatment; hence, we were unable to correlate PADS in particular, but also PANS to clinical outcome. All four patients with PADS responded to therapy; however, patients showing PANS or no change also responded to therapy, indicating that PADS is not a pre-requisite for response in this patient group. Notably, however, the only patient showing a positive M30/M65 also showed the highest PADS. Equally, we cannot infer a more appropriate time for [^{18}F]ICMT-11 measurement, although the second window (2-14d) is perhaps more practical. The lack of 'non-responders' is a limitation of our study; however, this could not be influenced due to the prospective nature of the study; thus, all outcomes were reported. The main aim — the investigation of the changes in ICMT-11 uptake and relationship with biochemical/histological caspase-3 activity — was, however, not compromised. It is worth considering the difficulties within this study both from a logistics and scientific perspective. The timing of apoptosis has been elusive and fraught with difficulties when using functional imaging such as PET. Parton et al. [170] reported apoptosis in tissue biopsies rising within 24 h of chemotherapy in breast patients, a finding consistent with other studies [169, 171]. Due to logistics of imaging and availability of the patient, 24 h post-chemotherapy imaging was not feasible in all patients. In our study cohort, patients underwent imaging with [^{18}F]ICMT-11 PET/CT at various time-points post-chemotherapy. Two patients imaged at 24 h post-chemotherapy failed to show an apoptotic dominant signature or significant increase in caspase-3 expression. Apoptosis may not be the sole mechanism of cell death in treatment response. Although it is known to play a key role, cell death can occur by necrosis, mitotic catastrophe, senescence, autophagy, pyroptosis, and DNA damage [189]. As the majority of patients in our study showed a dominant necrotic or mixed apoptotic/necrotic signature phenotype, the balance between apoptosis and necrosis may be one in favour of the latter. This could in part, account for the lack of a predominant apoptotic signal on PET and histology. Longitudinal, multi-parametric imaging studies in the lung cancer patients permitted us to verify simultaneously [^{18}F]ICMT-11, ADC as a measure of cell death, and DCEMRI as a measure of perfusion/permeability. The increase in ADC values seen with DW-MRI in patient 16, 24 h and 7 days post-chemotherapy, infers increased cell death induced increases in water mobility as previously reported [51]. This is consistent with the increase in tumour [^{18}F]ICMT-11 in the same patient. Conversely, the decrease in ADC variables in patient 17 may be linked to increases in ECM constituents [190] that can accompany response (necrosis, fibrosis, or mixed inflammatory infiltrate) and associated cell swelling [51]. Accordingly, in the two patients there appears to be congruence of [^{18}F]ICMT-11 and ADC data. Significant changes in perfusion/permeability could perturb PVIS measurements. Assessment of the pharmacokinetics rate constant K^{trans} from the DCE-MRI study showed that perfusion/ permeability dynamics could not explain the [^{18}F]ICMT-11 dynamics

within the time frame of the study. Beyond this proof of concept study, future prospective studies in a larger cohort should examine the role of [^{18}F]ICMT-11 in assessing chemotherapy response, to also include a fair mix of responders and non-responders. The outcome of the lung cancer cohort study when confirmed in a larger cohort may support use of combined PET-MRI in monitoring ADC-detectable cell death and [^{18}F]ICMT-11-detectable caspase-3/7 activation.

5. Conclusion

In aggregate, initial studies using [^{18}F]ICMT-11 were promising in preclinical and first-in-man healthy volunteer studies [8, 29, 41, 45]. We report the first use of [^{18}F]ICMT-11 in a small cohort of patients diagnosed with breast or lung cancer and receiving first-line chemotherapy. The results show that only a small proportion of apoptosis was induced by drug treatment and that this level did not induce global changes in tumour [^{18}F]ICMT-11 uptake. Voxel-wise analysis showed regional increases of [^{18}F]ICMT-11 intensity regions in some tumours, and while patients having this phenotype responded to therapy, it was not an exclusive marker of response. Thus, tumour response could occur in the absence of predominant chemotherapy-induced caspase-3/7 activation measured non-invasively across entire tumour lesions in patients with breast and lung cancer.

V. Multiparametric MRI in prostate cancer: a radiomic study on different diffusion and perfusion models

The aim of this study was to evaluate radiomics features extracted from T2-weighted, diffusion weighted imaging (DWI), diffusion kurtosis imaging (DKI), dynamic contrast enhanced (DCE) MRI data fitted with the Tofts (TM) and shutter speed model (SSM), benign prostatic hyperplasia (BPH), and benign peripheral zone (PZ). Furthermore, the comparison between the diagnostic performances of advanced prostate radiomics to PI-RADS v2 classification was under investigation.

1. Materials and Methods

40 foci of PCa, 48 BPH nodules, and 36 benign PZ from 40 patients who underwent multiparametric MRI of prostate, to eventually address a target-biopsy, were evaluated.

MRI exam was performed without endorectal coil with a 3T mMR Biograph scanner. DWI was performed using 7 b-values (0-2500 s/mm2): classical apparent diffusion coefficient (ADC) map was generated using b values up to 1500 s/mm2; the entire range of b values was used to compute non-Gaussian diffusion coefficient (D) and deviations from normal distribution (K) maps.
Dynamic contrast-enhanced magnetic resonance imaging (DCE-MRI) parameters (K^{trans}, v_e, k_{ep} [TM & SSM] and intracellular water molecular lifetime τ_i [SSM]) were also determined.
2D regions of interest were manually outlined on the axial T2w that was also used as reference image to coregister other maps. 13 first-order statistical features were extracted for each map.
Feature selection was performed to identify 5 features for each model [191]. A logistic regression classifiers were used to identify features discriminating clinically significant tumours (PIRADS 4-5) from benign PZ with an intra- and inter-model approach. The area under the receiving-operating characteristic curve (AUC), the sensitivity, the specificity and the accuracy were used to evaluate the performances of models. The intermodel approach was also tested to discriminate between BPH and other groups.

2. Results

Identified radiomic features differentiated PCa from benign PZ. Prediction performances were higher for diffusion features (extracted for both DWI and DKI – Fig61) than for perfusion ones (extracted for both the TM and the SSM – Fig62).

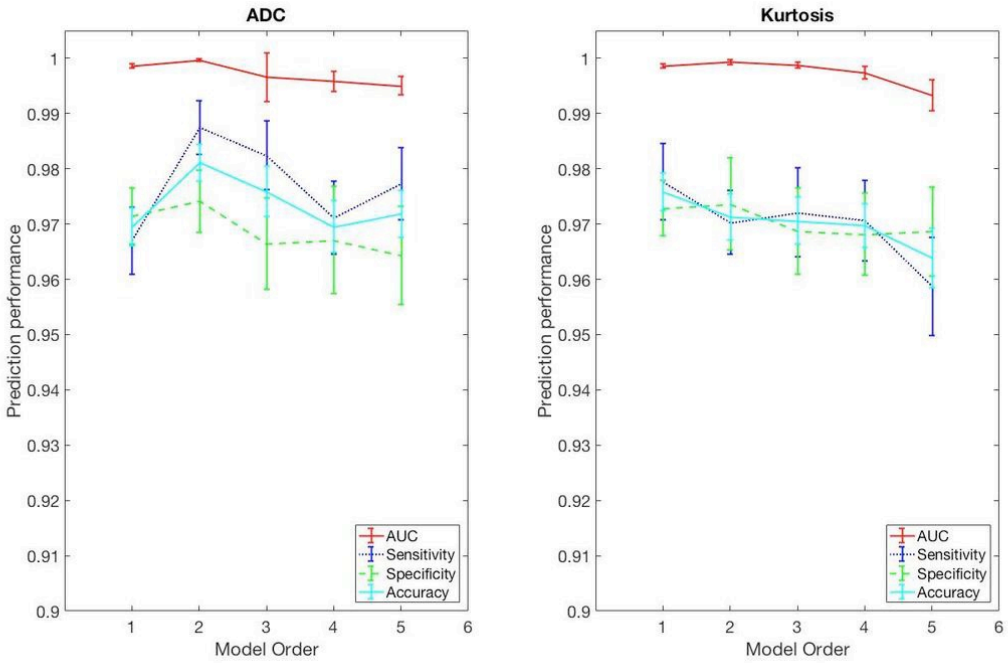

Figure 57: Prediction performances of logistic regression models for diffusion features.

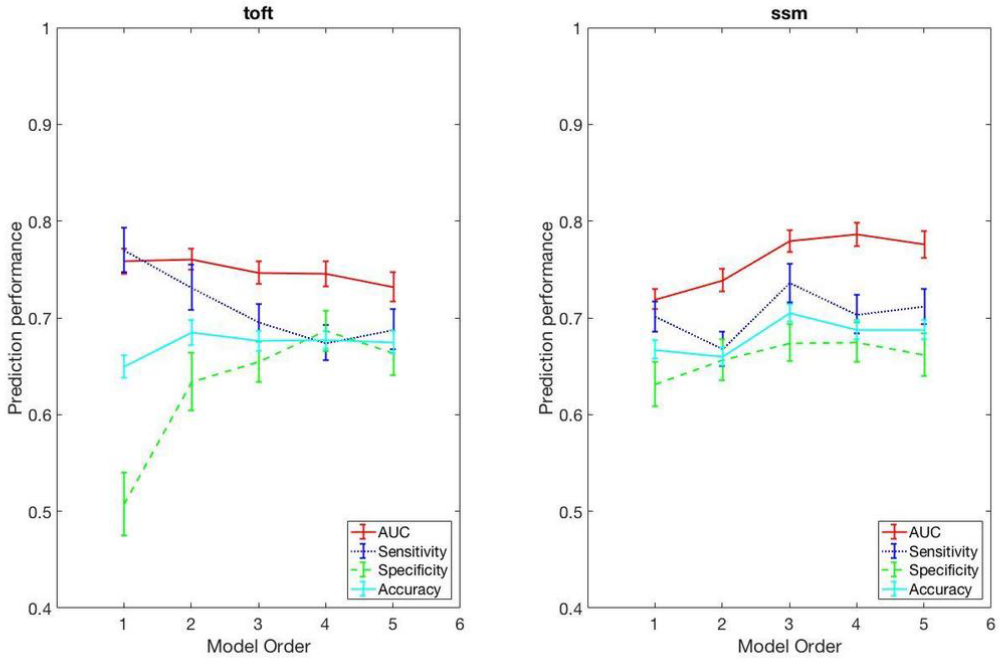

Figure 58: Prediction performances of logistic regression models for perfusion features.

These differences were confirmed independently by the number of features included in the logistic model (i.e., Model order). Intermodal approach lead to logistic regression models with very high discrimination performances (AUC values close to 1) with best results for sensitivity, specificity and accuracy (more than 0.99) in the models including 4, 5, and 7 features (Fig63,64).

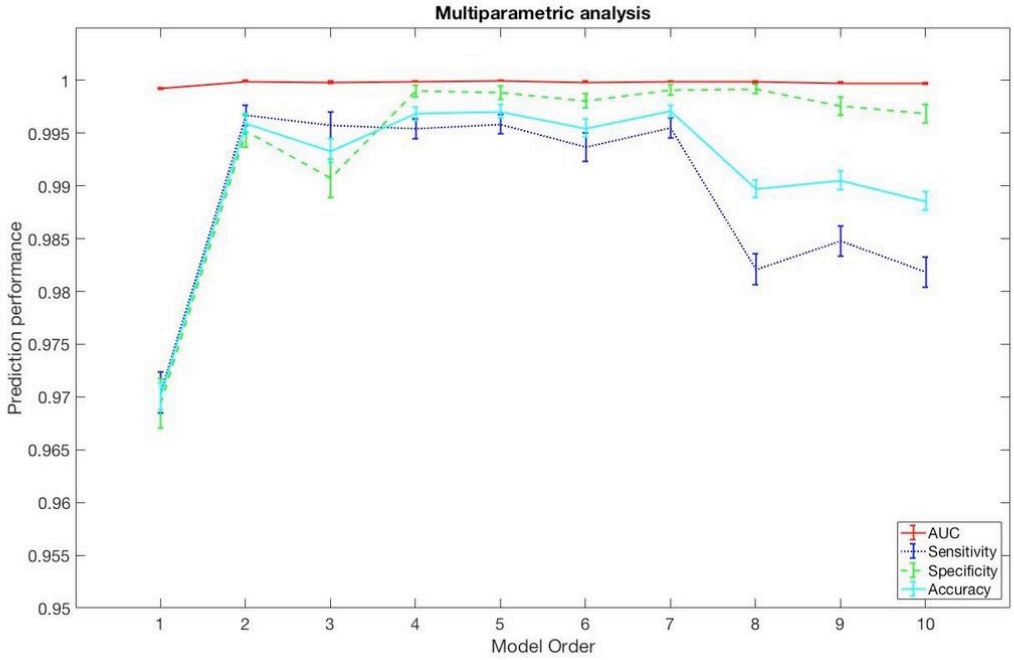

Figure 59: Prediction performances of logistic regression models for intermodel approach.

MODEL ORDER	SELECTED FEATURES	AUC	SENSITIVITY	SPECIFICITY	ACCURACY
1	T2w - median	0.99	0.97	0.97	0.97
2	T2w - median v_e (SSM) - uniformity	0.99	0.99	0.99	0.99
3	ADC - energy T2w - median v_e (SSM) - uniformity	0.99	0.99	0.99	0.99
4	D - maximum T2w - median T2w - skewness ADC - skewness	0.99	0.99	0.99	0.99
5	D - maximum T2w - median T2w - skewness ADC - skewness T2w - energy	0.99	0.99	0.99	0.99
6	T2w - mean	0.99	0.99	0.99	0.99

	v_e (SSM) - uniformity ADC - energy D - maximum k_{ep} (TM) - entropy T2w - skewness				
7	D - maximum T2w - median T2w - skewness ADC - skewness D - skewness K^{trans} (SSM) - uniformity	0.99	0.99	0.99	0.99
8	D - maximum T2w - median T2w - skewness ADC - skewness D - skewness K^{trans} - uniformity v_e (TM) - maximum	0.99	0.98	0.99	0.98
9	D - maximum T2w - median T2w - skewness ADC - skewness D - skewness K^{trans} - uniformity v_e (TM) - maximum ADC - median	0.99	0.98	0.99	0.99
10	D - maximum T2w - median T2w - skewness ADC - skewness D - skewness K^{trans} - uniformity v_e (TM) - maximum	0.99	0.98	0.99	0.98

ADC - median

k_{ep} (TM) - entropy

Figure 60: AUC, Sensitivity, Specificity and Accuracy values for intermodel approach.

These models were also able to significantly discriminate BPH from other groups ($p < 0.001$ – Fig65).

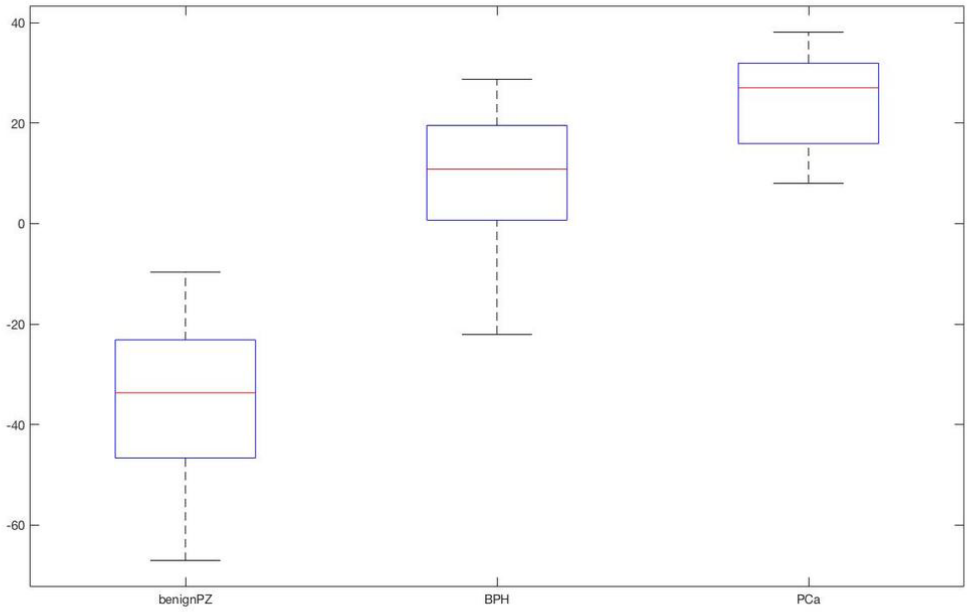

Figure 61: Discriminating power of prediction model of order 7 between BPH and other groups.

References

[1] A.J.G. Even, D. De Ruysscher, W. van Elmpt, The promise of multiparametric imaging in oncology: how do we move forward?, European Journal of Nuclear Medicine and Molecular Imaging, 43 (2016) 1195-1198.
[2] A.R. Padhani, K.A. Miles, Multiparametric Imaging of Tumor Response to Therapy, Radiology, 256 (2010) 348-364.
[3] F. Nensa, K. Beiderwellen, P. Heusch, A. Wetter, Clinical applications of PET/MRI: current status and future perspectives, Diagnostic and Interventional Radiology, 20 (2014) 438-447.
[4] B.J. Pichler, B.K. Swann, J. Rochelle, R.E. Nutt, S.R. Cherry, S.B. Siegel, Lutetium oxyorthosilicate block detector readout by avalanche photodiode arrays for high resolution animal PET, Physics in medicine and biology, 49 (2004) 4305-4319.
[5] H.S. Yoon, G.B. Ko, S.I. Kwon, C.M. Lee, M. Ito, I. Chan Song, D.S. Lee, S.J. Hong, J.S. Lee, Initial results of simultaneous PET/MRI experiments with an MRI-compatible silicon photomultiplier PET scanner, J Nucl Med, 53 (2012) 608-614.
[6] A.B. Rosenkrantz, K. Friedman, H. Chandarana, A. Melsaether, L. Moy, Y.S. Ding, K. Jhaveri, L. Beltran, R. Jain, Current Status of Hybrid PET/MRI in Oncologic Imaging, AJR. American journal of roentgenology, 206 (2016) 162-172.
[7] C.E. DeSantis, J. Ma, A. Goding Sauer, L.A. Newman, A. Jemal, Breast cancer statistics, 2017, racial disparity in mortality by state, CA: a cancer journal for clinicians, 67 (2017) 439-448.
[8] L. Pace, E. Nicolai, A. Luongo, M. Aiello, O.A. Catalano, A. Soricelli, M. Salvatore, Comparison of whole-body PET/CT and PET/MRI in breast cancer patients: lesion detection and quantitation of 18F-deoxyglucose uptake in lesions and in normal organ tissues, European journal of radiology, 83 (2014) 289-296.
[9] W.V. Vogel, U. Nestle, M.C. Valli, PET/MRI in breast cancer, Clinical and Translational Imaging, 5 (2017) 71-78.
[10] S. Taneja, A. Jena, R. Goel, R. Sarin, S. Kaul, Simultaneous whole-body 18F-FDG PET-MRI in primary staging of breast cancer: a pilot study, European journal of radiology, 83 (2014) 2231-2239.
[11] K.Z. Al-Nabhani, R. Syed, S. Michopoulou, J. Alkalbani, A. Afaq, E. Panagiotidis, C. O'Meara, A. Groves, P. Ell, J. Bomanji, Qualitative and quantitative comparison of PET/CT and PET/MR imaging in clinical practice, Journal of Nuclear Medicine, 55 (2014) 88-94.
[12] C. Cavaliere, V. Romeo, M. Aiello, M. Mesolella, B. Iorio, L. Barbuto, E. Cantone, E. Nicolai, M. Covello, Multiparametric evaluation by simultaneous PET-MRI examination in patients with histologically proven laryngeal cancer, European journal of radiology, 88 (2017) 47-55.
[13] M. Aiello, C. Cavaliere, M. Salvatore, Hybrid PET/MR imaging and brain connectivity, Frontiers in neuroscience, 10 (2016) 64.
[14] J.F. Schäfer, S. Gatidis, H. Schmidt, B. Gückel, I. Bezrukov, C.A. Pfannenberg, M. Reimold, M. Ebinger, J. Fuchs, C.D. Claussen, Simultaneous whole-body PET/MR imaging in comparison to PET/CT in pediatric oncology: initial results, Radiology, 273 (2014) 220-231.
[15] G. Antoch, A. Bockisch, Combined PET/MRI: a new dimension in whole-body oncology imaging?, European journal of nuclear medicine and molecular imaging, 36 (2009) 113-120.
[16] S. Monti, C. Cavaliere, M. Covello, E. Nicolai, M. Salvatore, M. Aiello, An evaluation of the benefits of simultaneous acquisition on PET/MR coregistration in head/neck imaging, Journal of healthcare engineering, 2017 (2017).
[17] B.J. Pichler, A. Kolb, T. Nägele, H.-P. Schlemmer, PET/MRI: paving the way for the next generation of clinical multimodality imaging applications, Journal of Nuclear Medicine, 51 (2010) 333-336.
[18] A. Almuhaideb, N. Papathanasiou, J. Bomanji, 18F-FDG PET/CT imaging in oncology, Annals of Saudi medicine, 31 (2011) 3.

[19] A. Mahajan, G. Cook, Clinical Applications of PET/CT in Oncology, Basic Science of PET Imaging, Springer2017, pp. 429-450.
[20] L. Chen, M. Liu, J. Bao, Y. Xia, J. Zhang, L. Zhang, X. Huang, J. Wang, The correlation between apparent diffusion coefficient and tumor cellularity in patients: a meta-analysis, PloS one, 8 (2013) e79008.
[21] L. Chen, J. Zhang, Y. Chen, W. Wang, X. Zhou, X. Yan, J. Wang, Relationship between apparent diffusion coefficient and tumour cellularity in lung cancer, PloS one, 9 (2014) e99865.
[22] A. Surov, H.J. Meyer, A. Wienke, Correlation between apparent diffusion coefficient (ADC) and cellularity is different in several tumors: a meta-analysis, Oncotarget, 8 (2017) 59492.
[23] P.S. Tofts, T1-weighted DCE imaging concepts: modelling, acquisition and analysis, signal, 500 (2010) 400.
[24] J.D. Quirk, G.L. Bretthorst, T.Q. Duong, A.Z. Snyder, C.S. Springer, J.J. Ackerman, J.J. Neil, Equilibrium water exchange between the intra-and extracellular spaces of mammalian brain, Magnetic resonance in medicine, 50 (2003) 493-499.
[25] W. Nordhøy, H.W. Anthonsen, M. Bruvold, H. Brurok, S. Skarra, J. Krane, P. Jynge, Intracellular manganese ions provide strong T1 relaxation in rat myocardium, Magnetic resonance in medicine, 52 (2004) 506-514.
[26] W. Huang, L.A. Tudorica, X. Li, S.B. Thakur, Y. Chen, E.A. Morris, I.J. Tagge, M.E. Korenblit, W.D. Rooney, J.A. Koutcher, Discrimination of benign and malignant breast lesions by using shutter-speed dynamic contrast-enhanced MR imaging, Radiology, 261 (2011) 394-403.
[27] X. Li, W.D. Rooney, C.S. Springer, Jr., A unified magnetic resonance imaging pharmacokinetic theory: intravascular and extracellular contrast reagents, Magn Reson Med, 54 (2005) 1351-1359.
[28] X. Li, W. Huang, E.A. Morris, L.A. Tudorica, V.E. Seshan, W.D. Rooney, I. Tagge, Y. Wang, J. Xu, C.S. Springer, Dynamic NMR effects in breast cancer dynamic-contrast-enhanced MRI, Proceedings of the National Academy of Sciences, 105 (2008) 17937-17942.
[29] X. Li, E.B. Welch, A.B. Chakravarthy, L. Xu, L.R. Arlinghaus, J. Farley, I.A. Mayer, M.C. Kelley, I.M. Meszoely, J. Means-Powell, Statistical comparison of dynamic contrast-enhanced MRI pharmacokinetic models in human breast cancer, Magnetic resonance in medicine, 68 (2012) 261-271.
[30] L.R. Arlinghaus, X. Li, A.R. Rahman, E.B. Welch, L. Xu, J.C. Gore, T.E. Yankeelov, On the relationship between the apparent diffusion coefficient and extravascular extracellular volume fraction in human breast cancer, Magnetic resonance imaging, 29 (2011) 630-638.
[31] S.I.K. Semple, R.T. Staff, S.D. Heys, T.W. Redpath, A. Welch, T.S. Ahearn, A. Hutcheon, F.J. Gilbert, Baseline MRI delivery characteristics predict change in invasive ductal breast carcinoma PET metabolism as a result of primary chemotherapy administration, Annals of oncology, 17 (2006) 1393-1398.
[32] A. Martinez-Möller, M. Souvatzoglou, G. Delso, R.A. Bundschuh, C. Chefd'hotel, S.I. Ziegler, N. Navab, M. Schwaiger, S.G. Nekolla, Tissue classification as a potential approach for attenuation correction in whole-body PET/MRI: evaluation with PET/CT data, Journal of nuclear medicine, 50 (2009) 520-526.
[33] J. Yuan, S.K.K. Chow, D.K.W. Yeung, A.T. Ahuja, A.D. King, Quantitative evaluation of dual-flip-angle T1 mapping on DCE-MRI kinetic parameter estimation in head and neck, Quantitative imaging in medicine and surgery, 2 (2012) 245.
[34] G. Liberman, Y. Louzoun, D. Ben Bashat, T(1) mapping using variable flip angle SPGR data with flip angle correction, Journal of magnetic resonance imaging : JMRI, 40 (2014) 171-180.
[35] K.L. Li, X.P. Zhu, J. Waterton, A. Jackson, Improved 3D quantitative mapping of blood volume and endothelial permeability in brain tumors, Journal of magnetic resonance imaging : JMRI, 12 (2000) 347-357.

[36] J. Graessner, Frequently Asked Questions: Diffusion-Weighted Imaging (DWI), MAGNETON Flash, DOI (2011) 6-9.
[37] M. Covello, C. Cavaliere, M. Aiello, M. Cianelli, M. Mesolella, B. Iorio, A. Rossi, E. Nicolai, Simultaneous PET/MR head–neck cancer imaging: Preliminary clinical experience and multiparametric evaluation, European journal of radiology, 84 (2015) 1269-1276.
[38] J.C. Haselgrove, J.R. Moore, Correction for distortion of echo-planar images used to calculate the apparent diffusion coefficient, Magnetic Resonance in Medicine, 36 (1996) 960-964.
[39] T. Fritz-Hansen, E. Rostrup, H.B. Larsson, L. Søndergaard, P. Ring, O. Henriksen, Measurement of the arterial concentration of Gd-DTPA using MRI: A step toward quantitative perfusion imaging, Magnetic Resonance in Medicine, 36 (1996) 225-231.
[40] J.C. Lagarias, J.A. Reeds, M.H. Wright, P.E. Wright, Convergence properties of the Nelder--Mead simplex method in low dimensions, SIAM Journal on optimization, 9 (1998) 112-147.
[41] D.S. Smith, X. Li, L.R. Arlinghaus, T.E. Yankeelov, E.B. Welch, DCEMRI. jl: A fast, validated, open source toolkit for dynamic contrast enhanced MRI analysis, PeerJ, 3 (2015) e909.
[42] I.C. Smith, A.E. Welch, A.W. Hutcheon, I.D. Miller, S. Payne, F. Chilcott, S. Waikar, T. Whitaker, A.K. Ah-See, O. Eremin, Positron emission tomography using [18F]-fluorodeoxy-D-glucose to predict the pathologic response of breast cancer to primary chemotherapy, Journal of Clinical Oncology, 18 (2000) 1676-1688.
[43] E. Bombardieri, F. Crippa, L. Maffioli, M. Greco, Nuclear medicine techniques for the study of breast cancer, European journal of nuclear medicine, 24 (1997) 809-824.
[44] Y.-S. An, D.K. Kang, Y.S. Jung, S. Han, T.H. Kim, Tumor metabolism and perfusion ratio assessed by 18F-FDG PET/CT and DCE-MRI in breast cancer patients: correlation with tumor subtype and histologic prognostic factors, European journal of radiology, 84 (2015) 1365-1370.
[45] B. Muz, P. de la Puente, F. Azab, A.K. Azab, The role of hypoxia in cancer progression, angiogenesis, metastasis, and resistance to therapy, Hypoxia, 3 (2015) 83.
[46] A. Jena, S. Taneja, A. Singh, P. Negi, S.B. Mehta, A. Ahuja, M. Singhal, R. Sarin, Association of pharmacokinetic and metabolic parameters derived using simultaneous PET/MRI: Initial findings and impact on response evaluation in breast cancer, European journal of radiology, 92 (2017) 30-36.
[47] K. Kitajima, T. Yamano, K. Fukushima, Y. Miyoshi, S. Hirota, Y. Kawanaka, M. Miya, H. Doi, K. Yamakado, S. Hirota, Correlation of the SUVmax of FDG-PET and ADC values of diffusion-weighted MR imaging with pathologic prognostic factors in breast carcinoma, European journal of radiology, 85 (2016) 943-949.
[48] A.R. Padhani, D.-M. Koh, D.J. Collins, Whole-body diffusion-weighted MR imaging in cancer: current status and research directions, Radiology, 261 (2011) 700-718.
[49] B.H. Byun, W.C. Noh, I. Lim, S.S. Lee, A.R. Cho, J.A. Park, K.M. Kim, H.-A. Kim, E.-K. Kim, B.I. Kim, A new method for apparent diffusion coefficient measurement using sequential 18 F-FDG PET and MRI: correlation with histological grade of invasive ductal carcinoma of the breast, Annals of nuclear medicine, 27 (2013) 720-728.
[50] B.B. Choi, S.H. Kim, B.J. Kang, J.H. Lee, B.J. Song, S.H. Jeong, H.W. Yim, Diffusion-weighted imaging and FDG PET/CT: predicting the prognoses with apparent diffusion coefficient values and maximum standardized uptake values in patients with invasive ductal carcinoma, World journal of surgical oncology, 10 (2012) 126.
[51] D.M. Patterson, A.R. Padhani, D.J. Collins, Technology insight: water diffusion MRI—a potential new biomarker of response to cancer therapy, Nature Reviews Clinical Oncology, 5 (2008) 220.
[52] Y. Tsushima, A. Takahashi-Taketomi, K. Endo, Magnetic resonance (MR) differential diagnosis of breast tumors using apparent diffusion coefficient (ADC) on 1.5-T, Journal of magnetic resonance imaging, 30 (2009) 249-255.

[53] C. Marini, C. Iacconi, M. Giannelli, A. Cilotti, M. Moretti, C. Bartolozzi, Quantitative diffusion-weighted MR imaging in the differential diagnosis of breast lesion, European radiology, 17 (2007) 2646-2655.
[54] A.A.K.A. Razek, G. Gaballa, A. Denewer, N. Nada, Invasive ductal carcinoma: correlation of apparent diffusion coefficient value with pathological prognostic factors, NMR in biomedicine, 23 (2010) 619-623.
[55] M. Hatakenaka, H. Soeda, H. Yabuuchi, Y. Matsuo, T. Kamitani, Y. Oda, M. Tsuneyoshi, H. Honda, Apparent diffusion coefficients of breast tumors: clinical application, Magnetic Resonance in Medical Sciences, 7 (2008) 23-29.
[56] Y. Guo, Y.Q. Cai, Z.L. Cai, Y.G. Gao, N.Y. An, L. Ma, S. Mahankali, J.H. Gao, Differentiation of clinically benign and malignant breast lesions using diffusion-weighted imaging, Journal of magnetic resonance imaging, 16 (2002) 172-178.
[57] R. Woodhams, K. Matsunaga, K. Iwabuchi, S. Kan, H. Hata, M. Kuranami, M. Watanabe, K. Hayakawa, Diffusion-weighted imaging of malignant breast tumors: the usefulness of apparent diffusion coefficient (ADC) value and ADC map for the detection of malignant breast tumors and evaluation of cancer extension, Journal of computer assisted tomography, 29 (2005) 644-649.
[58] R. Bos, J.J. van der Hoeven, E. van der Wall, P. van der Groep, P.J. van Diest, E.F. Comans, U. Joshi, G.L. Semenza, O.S. Hoekstra, A.A. Lammertsma, Biologic correlates of 18fluorodeoxyglucose uptake in human breast cancer measured by positron emission tomography, Journal of Clinical Oncology, 20 (2002) 379-387.
[59] K. Ito, T. Kato, M. Tadokoro, T. Ishiguchi, M. Oshima, T. Ishigaki, S. Sakuma, Recurrent rectal cancer and scar: differentiation with PET and MR imaging, Radiology, 182 (1992) 549-552.
[60] W. Huang, X. Li, E.A. Morris, L.A. Tudorica, V.E. Seshan, W.D. Rooney, I. Tagge, Y. Wang, J. Xu, C.S. Springer, The magnetic resonance shutter speed discriminates vascular properties of malignant and benign breast tumors in vivo, Proceedings of the National Academy of Sciences, 105 (2008) 17943-17948.
[61] T.H. Kim, J.-K. Yoon, D.K. Kang, S.J. Lee, Y.S. Jung, H. Yim, Y.-S. An, Correlation between F-18 fluorodeoxyglucose positron emission tomography metabolic parameters and dynamic contrast-enhanced MRI-derived perfusion data in patients with invasive ductal breast carcinoma, Annals of surgical oncology, 22 (2015) 3866-3872.
[62] X. Li, W. Huang, T.E. Yankeelov, A. Tudorica, W.D. Rooney, C.S. Springer, Shutter-speed analysis of contrast reagent bolus-tracking data: Preliminary observations in benign and malignant breast disease, Magnetic resonance in medicine, 53 (2005) 724-729.
[63] C.S. Springer, X. Li, L.A. Tudorica, K.Y. Oh, N. Roy, S.Y.C. Chui, A.M. Naik, M.L. Holtorf, A. Afzal, W.D. Rooney, Intratumor mapping of intracellular water lifetime: metabolic images of breast cancer?, NMR in Biomedicine, 27 (2014) 760-773.
[64] G.H. Jajamovich, W. Huang, C. Besa, X. Li, A. Afzal, H.A. Dyvorne, B. Taouli, DCE-MRI of hepatocellular carcinoma: perfusion quantification with Tofts model versus shutter-speed model—initial experience, Magnetic Resonance Materials in Physics, Biology and Medicine, 29 (2016) 49-58.
[65] P.S. Tofts, A.G. Kermode, Measurement of the blood-brain barrier permeability and leakage space using dynamic MR imaging. 1. Fundamental concepts, Magn Reson Med, 17 (1991) 357-367.
[66] X. Li, R.A. Priest, W.J. Woodward, F. Siddiqui, T.M. Beer, M.G. Garzotto, W.D. Rooney, C.S. Springer Jr, Cell membrane water exchange effects in prostate DCE-MRI, Journal of Magnetic Resonance, 218 (2012) 77-85.
[67] T.E. Yankeelov, G.O. Cron, C.L. Addison, J.C. Wallace, R.C. Wilkins, B.A. Pappas, G.E. Santyr, J.C. Gore, Comparison of a reference region model with direct measurement of an AIF in the analysis of DCE-MRI data, Magnetic resonance in medicine, 57 (2007) 353-361.
[68] S. Monti, M. Aiello, M. Incoronato, A.M. Grimaldi, M. Moscarino, P. Mirabelli, U. Ferbo, C. Cavaliere, M. Salvatore, DCE-MRI Pharmacokinetic-Based Phenotyping of Invasive Ductal

Carcinoma: A Radiomic Study for Prediction of Histological Outcomes, Contrast Media & Molecular Imaging, 2018 (2018).
[69] A. Goldhirsch, E.P. Winer, A.S. Coates, R.D. Gelber, M. Piccart-Gebhart, B. Thurlimann, H.J. Senn, M. Panel, Personalizing the treatment of women with early breast cancer: highlights of the St Gallen International Expert Consensus on the Primary Therapy of Early Breast Cancer 2013, Annals of Oncology, 24 (2013) 2206-2223.
[70] S. Ueda, H. Tsuda, H. Asakawa, T. Shigekawa, K. Fukatsu, N. Kondo, M. Yamamoto, Y. Hama, K. Tamura, J. Ishida, Y. Abe, H. Mochizuki, Clinicopathological and prognostic relevance of uptake level using F-18-fluorodeoxyglucose positron emission tomography/computed tomography fusion imaging (F-18-FDG PET/CT) in primary breast cancer, Japanese Journal of Clinical Oncology, 38 (2008) 250-258.
[71] J.R. Osborne, E. Port, M. Gonen, A.S. Doane, H. Yeung, W. Gerald, J.B. Cook, S. Larson, F-18-FDG PET of Locally Invasive Breast Cancer and Association of Estrogen Receptor Status with Standardized Uptake Value: Microarray and Immunohistochemical Analysis, Journal of Nuclear Medicine, 51 (2010) 543-550.
[72] P. Heudel, S. Cimarelli, A. Montella, C. Bouteille, T. Mognetti, Value of PET-FDG in primary breast cancer based on histopathological and immunohistochemical prognostic factors, International Journal of Clinical Oncology, 15 (2010) 588-593.
[73] D. Groheux, S. Giacchetti, J.L. Moretti, R. Porcher, M. Espie, J. Lehmann-Che, A. de Roquancourt, A.S. Hamy, C. Cuvier, L. Vercellino, E. Hindie, Correlation of high F-18-FDG uptake to clinical, pathological and biological prognostic factors in breast cancer, European Journal of Nuclear Medicine and Molecular Imaging, 38 (2011) 426-435.
[74] C.L. Wang, L.R. MacDonald, J.V. Rogers, A. Aravkin, D.R. Haseley, J.D. Beatty, Positron Emission Mammography: Correlation of Estrogen Receptor, Progesterone Receptor, and Human Epidermal Growth Factor Receptor 2 Status and F-18-FDG, American Journal of Roentgenology, 197 (2011) W247-W255.
[75] B.B. Koolen, M. Peeters, J. Wesseling, E.H. Lips, W.V. Vogel, T.S. Aukema, E. van Werkhoven, K.G.A. Gilhuijs, S. Rodenhuis, E.J.T. Rutgers, R.A.V. Olmos, Association of primary tumour FDG uptake with clinical, histopathological and molecular characteristics in breast cancer patients scheduled for neoadjuvant chemotherapy, European Journal of Nuclear Medicine and Molecular Imaging, 39 (2012) 1830-1838.
[76] H.R. Koo, J.S. Park, K.W. Kang, N. Cho, J.M. Chang, M.S. Bae, W.H. Kim, S.H. Lee, M.Y. Kim, J.Y. Kim, M. Seo, W.K. Moon, F-18-FDG uptake in breast cancer correlates with immunohistochemically defined subtypes, European Radiology, 24 (2014) 610-618.
[77] A.M.G. Vicente, A.S. Castrejon, A.L. Martin, I.C. Lopez-Muniz, V.M. Madero, M.D.M. Sanchez, A.P. Munoz, R.E. Aunion, A.G. Ageitos, Molecular subtypes of breast cancer: metabolic correlation with F-18-FDG PET/CT, European Journal of Nuclear Medicine and Molecular Imaging, 40 (2013) 1304-1311.
[78] K. Kitajima, K. Fukushima, Y. Miyoshi, A. Nishimukai, S. Hirota, Y. Igarashi, T. Katsuura, K. Maruyama, Association between F-18-FDG uptake and molecular subtype of breast cancer, European Journal of Nuclear Medicine and Molecular Imaging, 42 (2015) 1371-1377.
[79] K. Aogi, T. Kadoya, Y. Sugawara, S. Kiyoto, H. Shigematsu, N. Masumoto, M. Okada, Utility of F-18 FDG-PET/CT for predicting prognosis of luminal-type breast cancer, Breast Cancer Research and Treatment, 150 (2015) 209-217.
[80] J.H. Chen, H.M. Baek, O. Nalcioglu, M.Y. Su, Estrogen receptor and breast MR imaging features: A correlation study, Journal of Magnetic Resonance Imaging, 27 (2008) 825-833.
[81] V. Cipolla, D. Santucci, D. Guerrieri, F.M. Drudi, M.L. Meggiorini, C. de Felice, Correlation between 3T apparent diffusion coefficient values and grading of invasive breast carcinoma, European Journal of Radiology, 83 (2014) 2144-2150.
[82] J.Y. Kim, S.H. Kim, Y.J. Kim, B.J. Kang, Y.Y. An, A.W. Lee, B.J. Song, Y.S. Park, H.B. Lee, Enhancement parameters on dynamic contrast enhanced breast MRI: do they correlate with

prognostic factors and subtypes of breast cancers?, Magnetic Resonance Imaging, 33 (2015) 72-80.
[83] N. Mori, H. Ota, S. Mugikura, C. Takasawa, T. Ishida, G. Watanabe, H. Tada, M. Watanabe, K. Takase, S. Takahashi, Luminal-Type Breast Cancer: Correlation of Apparent Diffusion Coefficients with the Ki-67 Labeling Index, Radiology, 274 (2015) 66-73.
[84] S.H. Park, H.Y. Choi, S.Y. Hahn, Correlations Between Apparent Diffusion Coefficient Values of Invasive Ductal Carcinoma and Pathologic Factors on Diffusion-Weighted MRI at 3.0 Tesla, Journal of Magnetic Resonance Imaging, 41 (2015) 175-182.
[85] U. Sharma, R.G. Sah, K. Agarwal, R. Parshad, V. Seenu, S.R. Mathur, S. Hari, N.R. Jagannathan, Potential of Diffusion-Weighted imaging in the characterization of Malignant, Benign, and healthy Breast Tissues and Molecular subtypes of Breast cancer, Frontiers in Oncology, 6 (2016).
[86] H.J. Shin, J.Y. Park, K.C. Shin, H.H. Kim, J.H. Cha, E.Y. Chae, W.J. Choi, Characterization of tumor and adjacent peritumoral stroma in patients with breast cancer using high-resolution diffusion-weighted imaging: Correlation with pathologic biomarkers, European Journal of Radiology, 85 (2016) 1004-1011.
[87] T. Uematsu, M. Kasami, S. Yuen, Triple-Negative Breast Cancer: Correlation between MR Imaging and Pathologic Findings, Radiology, 250 (2009) 638-647.
[88] J.K. Shin, J.Y. Kim, Dynamic Contrast-Enhanced and Diffusion-Weighted MRI of Estrogen Receptor-Positive Invasive Breast Cancers: Associations Between Quantitative MR Parameters and Ki-67 Proliferation Status, Journal of Magnetic Resonance Imaging, 45 (2017) 94-102.
[89] M.X. Wu, J. Ma, Association Between Imaging Characteristics and Different Molecular Subtypes of Breast Cancer, Academic Radiology, 24 (2017) 426-434.
[90] K.K. Miyake, Y. Nakamoto, S. Kanao, S. Tanaka, T. Sugie, Y. Mikami, M. Toi, K. Togashi, Diagnostic Value of F-18-FDG PET/CT and MRI in Predicting the Clinicopathologic Subtypes of Invasive Breast Cancer, American Journal of Roentgenology, 203 (2014) 272-279.
[91] M. Nakajo, Y. Kajiya, T. Kaneko, Y. Kaneko, T. Takasaki, A. Tani, M. Ueno, C. Koriyama, FDG PET/CT and diffusion-weighted imaging for breast cancer: prognostic value of maximum standardized uptake values and apparent diffusion coefficient values of the primary lesion, European Journal of Nuclear Medicine and Molecular Imaging, 37 (2010) 2011-2020.
[92] B.B. Choi, S.H. Kim, B.J. Kang, J.H. Lee, B.J. Song, S.H. Jeong, H.W. Yim, Diffusion-weighted imaging and FDG PET/CT: predicting the prognoses with apparent diffusion coefficient values and maximum standardized uptake values in patients with invasive ductal carcinoma, World Journal of Surgical Oncology, 10 (2012).
[93] B.H. Byun, W.C. Noh, I. Lim, S.S. Lee, A.R. Cho, J.A. Park, K.M. Kim, H.A. Kim, E.K. Kim, B.I. Kim, C.W. Choi, S.M. Lim, A new method for apparent diffusion coefficient measurement using sequential F-18-FDG PET and MRI: correlation with histological grade of invasive ductal carcinoma of the breast, Annals of Nuclear Medicine, 27 (2013) 720-728.
[94] S. Baba, T. Isoda, Y. Maruoka, Y. Kitamura, M. Sasaki, T. Yoshida, H. Honda, Diagnostic and Prognostic Value of Pretreatment SUV in F-18-FDG/PET in Breast Cancer: Comparison with Apparent Diffusion Coefficient from Diffusion-Weighted MR Imaging, Journal of Nuclear Medicine, 55 (2014) 736-742.
[95] K. Kitajim, T. Yamano, K. Fukushima, Y. Miyoshi, S. Hirota, Y. Kawanaka, M. Miya, H. Doi, K. Yamakado, Correlation of the SUVmax of FDG-PET and ADC values of diffusion-weighted MR imaging with pathologic prognostic factors in breast carcinoma, European Journal of Radiology, 85 (2016) 943-949.
[96] O.A. Catalano, D. Daye, A. Signore, C. Iannace, M. Vangel, A. Luongo, M. Catalano, M. Filomena, L. Mansi, A. Soricelli, M. Salvatore, N. Fuin, C. Catana, U. Mahmood, B.R. Rosen, Staging performance of whole-body DWI, PET/CT and PET/MRI in invasive ductal carcinoma of the breast, International Journal of Oncology, 51 (2017) 281-288.
[97] O.A. Catalano, B.R. Rosen, D.V. Sahani, P.F. Hahn, A.R. Guimaraes, M.G. Vangel, E. Nicolai, A. Soricelli, M. Salvatore, Clinical Impact of PET/MR Imaging in Patients with Cancer

Undergoing Same-Day PET/CT: Initial Experience in 134 Patients-A Hypothesis-generating Exploratory Study, Radiology, 269 (2013) 857-869.
[98] M. Wiesmuller, H.H. Quick, B. Navalpakkam, M.M. Lell, M. Uder, P. Ritt, D. Schmidt, M. Beck, T. Kuwert, C.C. von Gall, Comparison of lesion detection and quantitation of tracer uptake between PET from a simultaneously acquiring whole-body PET/MR hybrid scanner and PET from PET/CT, European Journal of Nuclear Medicine and Molecular Imaging, 40 (2013) 12-21.
[99] R. Boellaard, M.J. O'Doherty, W.A. Weber, F.M. Mottaghy, M.N. Lonsdale, S.G. Stroobants, W.J.G. Oyen, J. Kotzerke, O.S. Hoekstra, J. Pruim, P.K. Marsden, K. Tatsch, C.J. Hoekstra, E.P. Visser, B. Arends, F.J. Verzijlbergen, J.M. Zijlstra, E.F.I. Comans, A.A. Lammertsma, A.M. Paans, A.T. Willemsen, T. Beyer, A. Bockisch, C. Schaefer-Prokop, D. Delbeke, R.P. Baum, A. Chiti, B.J. Krause, FDG PET and PET/CT: EANM procedure guidelines for tumour PET imaging: version 1.0, European Journal of Nuclear Medicine and Molecular Imaging, 37 (2010) 181-200.
[100] A. Martinez-Moller, M. Souvatzoglou, G. Delso, R.A. Bundschuh, C. Chefd'hotel, S.I. Ziegler, N. Navab, M. Schwaiger, S.G. Nekolla, Tissue Classification as a Potential Approach for Attenuation Correction in Whole-Body PET/MRI: Evaluation with PET/CT Data, Journal of Nuclear Medicine, 50 (2009) 520-526.
[101] J. Yuan, S.K.K. Chow, D.K.W. Yeung, A.T. Ahuja, A.D. King, Quantitative evaluation of dual-flip-angle T1 mapping on DCE-MRI kinetic parameter estimation in head and neck, Quantitative imaging in medicine and surgery, 2 (2012) 245-253.
[102] A. Goldhirsch, W.C. Wood, A.S. Coates, R.D. Gelber, B. Thurlimann, H.J. Senn, M. Panel, Strategies for subtypes-dealing with the diversity of breast cancer: highlights of the St Gallen International Expert Consensus on the Primary Therapy of Early Breast Cancer 2011, Annals of Oncology, 22 (2011) 1736-1747.
[103] D.M. Plecha, P. Faulhaber, PET/MRI of the breast, European Journal of Radiology, 94 (2017) A26-A34.
[104] O.A. Catalano, G.L. Horn, A. Signore, C. Iannace, M. Lepore, M. Vangel, A. Luongo, M. Catalano, C. Lehman, M. Salvatore, A. Soricelli, C. Catana, U. Mahmood, B.R. Rosen, PET/MR in invasive ductal breast cancer: correlation between imaging markers and histological phenotype, British Journal of Cancer, 116 (2017) 893-902.
[105] T. Higuchi, A. Nishimukai, H. Ozawa, Y. Fujimoto, A. Yanai, Y. Miyagawa, K. Murase, M. Imamura, Y. Takatsuka, K. Kitajima, K. Fukushima, Y. Miyoshi, Prognostic significance of preoperative F-18-FDG PET/CT for breast cancer subtypes, Breast, 30 (2016) 5-12.
[106] H.J. Yoon, K.W. Kang, I.K. Chun, N. Cho, S.A. Im, S. Jeong, S. Lee, K.C. Jung, Y.S. Lee, J.M. Jeong, D.S. Lee, J.K. Chung, W.K. Moon, Correlation of breast cancer subtypes, based on estrogen receptor, progesterone receptor, and HER2, with functional imaging parameters from Ga-68-RGD PET/CT and F-18-FDG PET/CT, European Journal of Nuclear Medicine and Molecular Imaging, 41 (2014) 1534-1543.
[107] C. De Cicco, L. Gilardi, E. Botteri, S.L.V. Fracassi, G.A. Di Dia, F. Botta, G. Prisco, D. Lombardo, N. Rotmensz, U. Veronesi, G. Paganelli, Is F-18 fluorodeoxyglucose uptake by the primary tumor a prognostic factor in breast cancer?, Breast, 22 (2013) 39-43.
[108] S.Y. Choi, Y.W. Chang, H.J. Park, H.J. Kim, S.S. Hong, D.Y. Seo, Correlation of the apparent diffusion coefficiency values on diffusion-weighted imaging with prognostic factors for breast cancer, British Journal of Radiology, 85 (2012) E474-E479.
[109] H.S. Lee, S.H. Kim, B.J. Kang, J.E. Baek, B.J. Song, Perfusion Parameters in Dynamic Contrast-enhanced MRI and Apparent Diffusion Coefficient Value in Diffusion-weighted MRI: Association with Prognostic Factors in Breast Cancer, Academic Radiology, 23 (2016) 446-456.
[110] S.K. Jeh, S.H. Kim, H.S. Kim, B.J. Kang, S.H. Jeong, H.W. Yim, B.J. Song, Correlation of the Apparent Diffusion Coefficient Value and Dynamic Magnetic Resonance Imaging Findings With Prognostic Factors in Invasive Ductal Carcinoma, Journal of Magnetic Resonance Imaging, 33 (2011) 102-109.

[111] C. Molinari, P. Clauser, R. Girometti, A. Linda, E. Cimino, F. Puglisi, C. Zuiani, M. Bazzocchi, MR mammography using diffusion-weighted imaging in evaluating breast cancer: a correlation with proliferation index, Radiologia Medica, 120 (2015) 911-918.
[112] H.R. Koo, N. Cho, I.C. Song, H. Kim, J.M. Chang, A. Yi, B.L. Yun, W.K. Moon, Correlation of perfusion parameters on dynamic contrast-enhanced MRI with prognostic factors and subtypes of breast cancers, Journal of Magnetic Resonance Imaging, 36 (2012) 145-151.
[113] J.H. Youk, E.J. Son, J. Chung, J.A. Kim, E.K. Kim, Triple-negative invasive breast cancer on dynamic contrast-enhanced and diffusion-weighted MR imaging: comparison with other breast cancer subtypes, European Radiology, 22 (2012) 1724-1734.
[114] P. de Robles, K.M. Fiest, A.D. Frolkis, T. Pringsheim, C. Atta, C. St. Germaine-Smith, L. Day, D. Lam, N. Jette, The worldwide incidence and prevalence of primary brain tumors: a systematic review and meta-analysis, Neuro-Oncology, 17 (2015) 776-783.
[115] R.L. Siegel, K.D. Miller, A. Jemal, Cancer statistics, 2016, CA: a cancer journal for clinicians, 66 (2016) 7-30.
[116] E.O. Aboagye, Z.M. Bhujwalla, Malignant transformation alters membrane choline phospholipid metabolism of human mammary epithelial cells, Cancer research, 59 (1999) 80-84.
[117] J. Exton, Phosphatidylcholine breakdown and signal transduction, Biochimica et Biophysica Acta (BBA)-Lipids and Lipid Metabolism, 1212 (1994) 26-42.
[118] T. George, S. Morash, H. Cook, D. Byers, F.S.C. Palmer, M. Spence, Phosphatidylcholine biosynthesis in cultured glioma cells: evidence for channeling of intermediates, Biochimica et Biophysica Acta (BBA)-Lipids and Lipid Metabolism, 1004 (1989) 283-291.
[119] D. Teegarden, E.J. Taparowsky, C. Kent, Altered phosphatidylcholine metabolism in C3H10T1/2 cells transfected with the Harvey-ras oncogene, Journal of Biological Chemistry, 265 (1990) 6042-6047.
[120] C. Fuccio, D. Rubello, P. Castellucci, M.C. Marzola, S. Fanti, Choline PET/CT for prostate cancer: main clinical applications, European journal of radiology, 80 (2011) e50-e56.
[121] L. Kenny, R. Coombes, K. Contractor, J. Stebbing, A. Al-Nahhas, C. Palmieri, S. Shousha, C. Lowdell, E. Aboagye, [11C] Choline-PET imaging of breast cancer, Journal of Clinical Oncology, 27 (2009) 1110-1110.
[122] T. Torizuka, T. Kanno, M. Futatsubashi, H. Okada, Imaging of gynecologic tumors: comparison of (11) C-choline PET with (18) F-FDG PET, The Journal of Nuclear Medicine, 44 (2003) 1051.
[123] T. Terauchi, U. Tateishi, T. Maeda, D. Kanou, H. Daisaki, Y. Moriya, N. Moriyama, T. Kakizoe, A case of colon cancer detected by carbon-11 choline positron emission tomography/computed tomography: an initial report, Japanese journal of clinical oncology, 37 (2007) 797-800.
[124] V.J. Cunningham, T. Jones, Spectral analysis of dynamic PET studies, Journal of Cerebral Blood Flow & Metabolism, 13 (1993) 15-23.
[125] T.E. Yankeelov, W.D. Rooney, X. Li, C.S. Springer, Jr., Variation of the relaxographic "shutter-speed" for transcytolemmal water exchange affects the CR bolus-tracking curve shape, Magn Reson Med, 50 (2003) 1151-1169.
[126] J. Yuan, S.K. Chow, D.K. Yeung, A.T. Ahuja, A.D. King, Quantitative evaluation of dual-flip-angle T1 mapping on DCE-MRI kinetic parameter estimation in head and neck, Quant Imaging Med Surg, 2 (2012) 245-253.
[127] S.S. Kety, Observations on the validity of a two compartmental model of the cerebral circulation, Acta Neurol Scand Suppl, 14 (1965) 85-87.
[128] C.S. Landis, X. Li, F.W. Telang, P.E. Molina, I. Palyka, G. Vetek, C.S. Springer, Jr., Equilibrium transcytolemmal water-exchange kinetics in skeletal muscle in vivo, Magn Reson Med, 42 (1999) 467-478.
[129] K.M. Donahue, D. Burstein, W.J. Manning, M.L. Gray, Studies of Gd-DTPA relaxivity and proton exchange rates in tissue, Magn Reson Med, 32 (1994) 66-76.

[130] M. Veronese, G. Rizzo, F.E. Turkheimer, A. Bertoldo, SAKE: a new quantification tool for positron emission tomography studies, Computer methods and programs in biomedicine, 111 (2013) 199-213.
[131] D.L. Buckley, C. Roberts, G.J. Parker, J.P. Logue, C.E. Hutchinson, Prostate cancer: evaluation of vascular characteristics with dynamic contrast-enhanced T1-weighted MR imaging--initial experience, Radiology, 233 (2004) 709-715.
[132] W. Chen, D.H. Silverman, S. Delaloye, J. Czernin, N. Kamdar, W. Pope, N. Satyamurthy, C. Schiepers, T. Cloughesy, 18F-FDOPA PET imaging of brain tumors: comparison study with 18F-FDG PET and evaluation of diagnostic accuracy, J Nucl Med, 47 (2006) 904-911.
[133] V.K. Shivamurthy, A.K. Tahari, C. Marcus, R.M. Subramaniam, Brain FDG PET and the diagnosis of dementia, American Journal of Roentgenology, 204 (2015) W76-W85.
[134] C. Rathore, J.C. Dickson, R. Teotónio, P. Ell, J.S. Duncan, The utility of 18F-fluorodeoxyglucose PET (FDG PET) in epilepsy surgery, Epilepsy Research, 108 (2014) 1306-1314.
[135] K. Manohar, A. Bhattacharya, B.R. Mittal, Low positive yield from routine inclusion of the brain in whole-body 18F-FDG PET/CT imaging for noncerebral malignancies: results from a large population study, Nuclear medicine communications, 34 (2013) 540-543.
[136] F.F. Calabria, M. Barbarisi, V. Gangemi, G. Grillea, G.L. Cascini, Molecular imaging of brain tumors with radiolabeled choline PET, Neurosurgical Review, 41 (2018) 67-76.
[137] N. Shinoura, M. Nishijima, T. Hara, T. Haisa, H. Yamamoto, K. Fujii, I. Mitsui, N. Kosaka, T. Kondo, T. Hara, Brain tumors: detection with C-11 choline PET, Radiology, 202 (1997) 497-503.
[138] T. Hara, N. Kosaka, N. Shinoura, T. Kondo, PET imaging of brain tumor with [methyl-11C] choline, Journal of Nuclear Medicine, 38 (1997) 842-847.
[139] R. Coleman, T. DeGrado, S. Wang, S. Baldwin, M. Orr, R. Reiman, D. Price, 9:30-9:45. Preliminary Evaluation of F-18 Fluorocholine (FCH) as a PET Tumor Imaging Agent, Clinical positron imaging : official journal of the Institute for Clinical P.E.T, 3 (2000) 147.
[140] E.E. Verwer, D.E. Oprea-Lager, A. van den Eertwegh, R. van Moorselaar, A.D. Windhorst, L.A. Schwarte, N.H. Hendrikse, R.C. Schuit, O.S. Hoekstra, A.A. Lammertsma, Quantification of 18F-fluorocholine kinetics in patients with prostate cancer, J Nucl Med, 56 (2015) 365-371.
[141] M. Takesh, Kinetic modeling application to 18F-fluoroethylcholine positron emission tomography in patients with primary and recurrent prostate cancer using two-tissue compartmental model, World journal of nuclear medicine, 12 (2013) 101.
[142] J.D. Schaefferkoetter, Z. Wang, M.C. Stephenson, S. Roy, M. Conti, L. Eriksson, D.W. Townsend, T. Thamboo, E. Chiong, Quantitative 18 F-fluorocholine positron emission tomography for prostate cancer: correlation between kinetic parameters and Gleason scoring, EJNMMI research, 7 (2017) 25.
[143] S. Dresel, PET in Oncology, Springer2008.
[144] Z. Zhou, Z.-R. Lu, Gadolinium-Based Contrast Agents for MR Cancer Imaging, Wiley interdisciplinary reviews. Nanomedicine and nanobiotechnology, 5 (2013) 1-18.
[145] W.D. Rooney, X. Li, M.K. Sammi, D.N. Bourdette, E.A. Neuwelt, C.S. Springer, Jr., Mapping human brain capillary water lifetime: high-resolution metabolic neuroimaging, NMR Biomed, 28 (2015) 607-623.
[146] Y. Zhang, J.A. Balschi, Water exchange kinetics in the isolated heart correlate with Na+/K+ ATPase activity: potentially high spatiotemporal resolution in vivo MR access to cellular metabolic activity, Proceedings of the 21st Annual Meeting ISMRM, Salt Lake City, UT, 2013, pp. 4045.
[147] M.W. Stefanie Hectors, Cecilia Besa, Wei Huang, Bachir Taouli, PET-MRI in hepatocellular carcinoma: Correlation of DCE-MRI perfusion quantification using shutter-speed model with FDG uptake, ISMRM, 2017.

[148] Y. Mazaheri, O. Akin, H. Hricak, Dynamic contrast-enhanced magnetic resonance imaging of prostate cancer: A review of current methods and applications, World Journal of Radiology, 9 (2017) 416-425.
[149] J.F. Kerr, A.H. Wyllie, A.R. Currie, Apoptosis: a basic biological phenomenon with wideranging implications in tissue kinetics, British journal of cancer, 26 (1972) 239.
[150] J.F. Kerr, History of the events leading to the formulation of the apoptosis concept, Toxicology, 181 (2002) 471-474.
[151] G. Ichim, S.W. Tait, A fate worse than death: apoptosis as an oncogenic process, Nature Reviews Cancer, 16 (2016) 539.
[152] J. Lopez, S. Tait, Mitochondrial apoptosis: killing cancer using the enemy within, British journal of cancer, 112 (2015) 957.
[153] D.L. Chen, J.T. Engle, E.A. Griffin, J.P. Miller, W. Chu, D. Zhou, R.H. Mach, Imaging caspase-3 activation as a marker of apoptosis-targeted treatment response in cancer, Molecular Imaging and Biology, 17 (2015) 384-393.
[154] K.J. Yagle, J.F. Eary, J.F. Tait, J.R. Grierson, J.M. Link, B. Lewellen, D.F. Gibson, K.A. Krohn, Evaluation of 18F-annexin V as a PET imaging agent in an animal model of apoptosis, Journal of Nuclear Medicine, 46 (2005) 658-666.
[155] F. Wang, W. Fang, M.-R. Zhang, M. Zhao, B. Liu, Z. Wang, Z. Hua, M. Yang, K. Kumata, A. Hatori, Evaluation of chemotherapy response in VX2 rabbit lung cancer with 18F-labeled C2A domain of synaptotagmin I, Journal of nuclear medicine: official publication, Society of Nuclear Medicine, 52 (2011).
[156] Q.-D. Nguyen, G. Smith, M. Glaser, M. Perumal, E. Årstad, E.O. Aboagye, Positron emission tomography imaging of drug-induced tumor apoptosis with a caspase-3/7 specific [18F]-labeled isatin sulfonamide, Proceedings of the National Academy of Sciences, DOI (2009) pnas. 0901310106.
[157] J. Höglund, A. Shirvan, G. Antoni, S.-Å. Gustavsson, B. Långström, A. Ringheim, J. Sörensen, M. Ben-Ami, I. Ziv, 18F-ML-10, a PET tracer for apoptosis: first human study, Journal of Nuclear Medicine, 52 (2011) 720.
[158] X. Bao, Z. Yang, S. Wang, Y. Zheng, M. Wang, B. Gu, J. Zhang, Y. Zhang, Y. Zhang, The preclinical study of predicting radiosensitivity in human nasopharyngeal carcinoma xenografts by 18F-ML-10 animal-PET/CT imaging, Oncotarget, 7 (2016) 20743.
[159] M. Kartachova, R.L. Haas, R.A.V. Olmos, F.J. Hoebers, N. van Zandwijk, M. Verheij, In vivo imaging of apoptosis by 99mTc-Annexin V scintigraphy: visual analysis in relation to treatment response, Radiotherapy and oncology, 72 (2004) 333-339.
[160] F. Hoebers, M. Kartachova, M. van den Brekel, J. de Bois, M. van Herk, C. Rasch, R.V. Olmos, M. Verheij, 99MTC hynic-RH-annexin V scintigraphy for in vivo imaging of apoptosis in patients with advanced head and neck cancer treated with concurrent cisplatin and radiotherapy, Radiotherapy and Oncology, 82 (2007) S34.
[161] T.H. Witney, A. Hoehne, R. Reeves, O. Ilovich, M. Namavari, B. Shen, F. Chin, J. Rao, S.S. Gambhir, A systematic comparison of 18F-C-SNAT to established radiotracer imaging agents for the detection of tumor response to treatment, Clinical Cancer Research, DOI (2015) clincanres. 3176.2014.
[162] H. Qin, M.-R. Zhang, L. Xie, Y. Hou, Z. Hua, M. Hu, Z. Wang, F. Wang, PET imaging of apoptosis in tumor-bearing mice and rabbits after paclitaxel treatment with 18F-Labeled recombinant human His10-annexin V, American journal of nuclear medicine and molecular imaging, 5 (2015) 27.
[163] A. Reshef, A. Shirvan, R.N. Waterhouse, H. Grimberg, G. Levin, A. Cohen, L.G. Ulysse, G. Friedman, G. Antoni, I. Ziv, Molecular imaging of neurovascular cell death in experimental cerebral stroke by PET, Journal of Nuclear Medicine, 49 (2008) 1520.
[164] A.M. Allen, M. Ben-Ami, A. Reshef, A. Steinmetz, Y. Kundel, E. Inbar, R. Djaldetti, T. Davidson, E. Fenig, I. Ziv, Assessment of response of brain metastases to radiotherapy by PET imaging of apoptosis with 18 F-ML-10, European journal of nuclear medicine and molecular imaging, 39 (2012) 1400-1408.

[165] M.J. Oborski, C.M. Laymon, F.S. Lieberman, J. Drappatz, R.L. Hamilton, J.M. Mountz, First use of 18F-labeled ML-10 PET to assess apoptosis change in a newly diagnosed glioblastoma multiforme patient before and early after therapy, Brain and behavior, 4 (2014) 312-315.
[166] T. Belhocine, N. Steinmetz, R. Hustinx, P. Bartsch, G. Jerusalem, L. Seidel, P. Rigo, A. Green, Increased uptake of the apoptosis-imaging agent 99mTc recombinant human Annexin V in human tumors after one course of chemotherapy as a predictor of tumor response and patient prognosis, Clinical Cancer Research, 8 (2002) 2766-2774.
[167] M. Kartachova, N. van Zandwijk, S. Burgers, H. van Tinteren, M. Verheij, R.A. Valdés Olmos, Prognostic significance of 99mTc Hynic-rh-annexin V scintigraphy during platinum-based chemotherapy in advanced lung cancer, Journal of Clinical Oncology, 25 (2007) 2534-2539.
[168] P.M. Kazmierczak, E. Burian, R. Eschbach, H. Hirner-Eppeneder, M. Moser, L. Havla, M. Eisenblätter, M.F. Reiser, K. Nikolaou, C.C. Cyran, Monitoring cell death in regorafenib-treated experimental colon carcinomas using annexin-based optical fluorescence imaging validated by perfusion MRI, PloS one, 10 (2015) e0138452.
[169] C. Archer, M. Parton, I. Smith, P. Ellis, J. Salter, S. Ashley, G. Gui, N. Sacks, S. Ebbs, W. Allum, Early changes in apoptosis and proliferation following primary chemotherapy for breast cancer, British journal of cancer, 89 (2003) 1035.
[170] M. Parton, S. Krajewski, I. Smith, M. Krajewska, C. Archer, M. Naito, R. Ahern, J. Reed, M. Dowsett, Coordinate expression of apoptosis-associated proteins in human breast cancer before and during chemotherapy, Clinical Cancer Research, 8 (2002) 2100-2108.
[171] P. Ellis, I. Smith, K. McCarthy, S. Detre, J. Salter, M. Dowsett, Preoperative chemotherapy induces apoptosis in early breast cancer, The Lancet, 349 (1997) 849.
[172] T.A. Buchholz, D.W. Davis, D.J. McConkey, W.F. Symmans, V. Valero, A. Jhingran, S.L. Tucker, L. Pusztai, M. Cristofanilli, F.J. Esteva, Chemotherapy-induced apoptosis and Bcl-2 levels correlate with breast cancer response to chemotherapy, The Cancer Journal, 9 (2003) 33-41.
[173] W.F. Symmans, M.D. Volm, R.L. Shapiro, A.B. Perkins, A.Y. Kim, S. Demaria, H.T. Yee, H. McMullen, R. Oratz, P. Klein, Paclitaxel-induced apoptosis and mitotic arrest assessed by serial fine-needle aspiration: implications for early prediction of breast cancer response to neoadjuvant treatment, Clinical Cancer Research, 6 (2000) 4610-4617.
[174] Q.-D. Nguyen, A. Challapalli, G. Smith, R. Fortt, E.O. Aboagye, Imaging apoptosis with positron emission tomography:'bench to bedside'development of the caspase-3/7 specific radiotracer [18F] ICMT-11, European Journal of Cancer, 48 (2012) 432-440.
[175] G. Smith, M. Glaser, M. Perumal, Q.-D. Nguyen, B. Shan, E. Årstad, E.O. Aboagye, Design, synthesis, and biological characterization of a caspase 3/7 selective isatin labeled with 2-[18F] fluoroethylazide, Journal of medicinal chemistry, 51 (2008) 8057-8067.
[176] R. Fortt, G. Smith, R.O. Awais, S.K. Luthra, E.O. Aboagye, Automated GMP synthesis of [18F] ICMT-11 for in vivo imaging of caspase-3 activity, Nuclear medicine and biology, 39 (2012) 1000-1005.
[177] Q.-D. Nguyen, I. Lavdas, J. Gubbins, G. Smith, R. Fortt, L.S. Carroll, M.A. Graham, E.O. Aboagye, Temporal and Spatial Evolution of Therapy-Induced Tumor Apoptosis Detected by Caspase-3–Selective Molecular Imaging, Clinical Cancer Research, DOI (2013).
[178] H. Watanabe, M. Okada, Y. Kaji, M. Satouchi, Y. Sato, Y. Yamabe, H. Onaya, M. Endo, M. Sone, Y. Arai, New response evaluation criteria in solid tumours-revised RECIST guideline (version 1.1), Gan to kagaku ryoho. Cancer & chemotherapy, 36 (2009) 2495.
[179] M. Gerlinger, A.J. Rowan, S. Horswell, J. Larkin, D. Endesfelder, E. Gronroos, P. Martinez, N. Matthews, A. Stewart, P. Tarpey, Intratumor heterogeneity and branched evolution revealed by multiregion sequencing, New England journal of medicine, 366 (2012) 883-892.
[180] N. Navin, J. Kendall, J. Troge, P. Andrews, L. Rodgers, J. McIndoo, K. Cook, A. Stepansky, D. Levy, D. Esposito, Tumour evolution inferred by single-cell sequencing, Nature, 472 (2011) 90.

[181] E. Papaevangelou, G. Almeida, Y. Jamin, S. Robinson, Diffusion-weighted MRI for imaging cell death after cytotoxic or apoptosis-inducing therapy, British journal of cancer, 112 (2015) 1471.
[182] J.E. Schmitz, M.I. Kettunen, D.E. Hu, K.M. Brindle, 1H MRS-visible lipids accumulate during apoptosis of lymphoma cells in vitro and in vivo, Magnetic Resonance in Medicine: An Official Journal of the International Society for Magnetic Resonance in Medicine, 54 (2005) 43-50.
[183] B. Banihashemi, R. Vlad, B. Debeljevic, A. Giles, M.C. Kolios, G.J. Czarnota, Ultrasound imaging of apoptosis in tumor response: novel preclinical monitoring of photodynamic therapy effects, Cancer research, 68 (2008) 8590-8596.
[184] G. Levin, A. Shirvan, H. Grimberg, A. Reshef, M. Yogev-Falach, A. Cohen, I. Ziv, Novel fluorescence molecular imaging of chemotherapy-induced intestinal apoptosis, Journal of Biomedical Optics, 14 (2009) 054019.
[185] E.C. de Haas, A. di Pietro, K.L. Simpson, C. Meijer, A.J. Suurmeijer, L.J. Lancashire, J. Cummings, S. de Jong, E.G. de Vries, C. Dive, Clinical evaluation of M30 and M65 ELISA cell death assays as circulating biomarkers in a drug-sensitive tumor, testicular cancer, Neoplasia, 10 (2008) 1041-1048.
[186] M.H. Olofsson, T. Ueno, Y. Pan, R. Xu, F. Cai, H. van der Kuip, T.E. Muerdter, M. Sonnenberg, W.E. Aulitzky, S. Schwarz, Cytokeratin-18 is a useful serum biomarker for early determination of response of breast carcinomas to chemotherapy, Clinical Cancer Research, 13 (2007) 3198-3206.
[187] A. Greystoke, J.P. O'Connor, K. Linton, M.B. Taylor, J. Cummings, T. Ward, F. Maders, A. Hughes, M. Ranson, T.M. Illidge, Assessment of circulating biomarkers for potential pharmacodynamic utility in patients with lymphoma, British journal of cancer, 104 (2011) 719.
[188] T.H. Witney, R.R. Fortt, E.O. Aboagye, Preclinical assessment of carboplatin treatment efficacy in lung cancer by 18F-ICMT-11-positron emission tomography, PLoS One, 9 (2014) e91694.
[189] L. Galluzzi, I. Vitale, J. Abrams, E. Alnemri, E. Baehrecke, M. Blagosklonny, T. Dawson, V. Dawson, W. El-Deiry, S. Fulda, Molecular definitions of cell death subroutines: recommendations of the Nomenclature Committee on Cell Death 2012, Cell death and differentiation, 19 (2012) 107.
[190] M.C. Tourell, A. Shokoohmand, M. Landgraf, N.P. Holzapfel, P.S. Poh, D. Loessner, K.I. Momot, The distribution of the apparent diffusion coefficient as an indicator of the response to chemotherapeutics in ovarian tumour xenografts, Scientific Reports, 7 (2017) 42905.
[191] M. Incoronato, M. Aiello, T. Infante, C. Cavaliere, A.M. Grimaldi, P. Mirabelli, S. Monti, M. Salvatore, Radiogenomic Analysis of Oncological Data: A Technical Survey, International journal of molecular sciences, 18 (2017).

Conclusions

"*If we knew what it was we were doing,*
it would not be called research, would it?"
Albert Einstein

The analysis of tissue kinetics of intravenously injected contrast agents or tracers is the most widely used technique for the evaluation of tissue perfusion and permeability. In fact, microcirculation is affected by both pathological conditions and treatment and, for this reason, the analysis of tissue microvascular network could be very informative of the state of the lesion.

This thesis shows the application of quantification methods for the analysis of dynamic PET and MRI data. It involves well known and new PET tracers as well as standard and new pharmacokinetic models for the extraction of parametric maps from DCE-MRI data.

The first application of kinetic modelling on D4-Choline and ^{18}F-FLT PET data of lung and liver tumour tissues, respectively, reinforced the idea that ^{18}F-FDG, which is the most widely used tracer in PET clinical protocols, may be inappropriate for too many reasons where the choice of more specific tracers works for both tumour assessment and treatment response evaluation. On the other hand, the analysis of DCIS with both ^{18}F-FDG and FLT showed many limitations, mainly due to the limited dataset and the inner proliferative activity of the breast, which made the detection and identification of these small lesions, complicated.

In the third chapter, the feasibility of DCE-MRI analysis in primary brain glioma was investigated. These tumours are different as in the healthy brain the blood brain barrier blocks the leakage of the contrast agent from the vessel. The implementation of multiple models (the non exchange, the Tofts, the extended Tofts, the shutter speed model) with the additional first implementation of the extended shutter speed model showed that the complexity of the model does not guarantee a fair description of the tumour. In fact, in this particular case where both the heterogeneity and the blood brain barrier play important roles in the analysis of the lesion, we showed how a model selection procedure can be crucial in the description of these tissues. In fact, different models yield different pharmacokinetic parameters and it is crucial to select the appropriate model to analyse DCE-MRI time courses based on the regional tissue biology, specifically permeability and vasculature.

The last part of the thesis involves several multiparametric studies where the kinetics of both PET tracers and MRI contrast agent have been analysed. These two imaging techniques are functionally very different and the extent of their agreement or discordance is not well understood yet. Therefore, the evaluation of the association between pharmacokinetic parameters resulted from the analysis of DCE-MRI data with multiple models and metabolic parameters derived from the application of graphical or spectral analysis to PET data, is important for the integration and validation of methods. In fact, the kinetic analysis of PET data could benefit from the pharmacokinetic parameters extracted from DCE-MRI data and vice versa. This thesis shows associations between

these two modalities in both brain and breast cancers but would benefit from a spatial correlation with DW-MRI and tissue biology.

The quantification methods used in this thesis are not currently implemented in the routine clinical practice. Additional studies are needed for the verification of the reliability of models and parameters for diagnostic and prognostic purposes with the final aim of biomarker validation.

This thesis is in agreement with a number of published works and it shows the potential of the kinetic analysis of tracers in pathological conditions and before and after treatment. It represents a step towards the validation of these models, which can finally provide a novel clinical tool to aid clinicians in tumour diagnosis, treatment planning and in the improvement of patients' outcomes.